TECHNISCHE UNIVERSITÄT MÜNCHEN

Fakultät für Medizin

Identification and in-depth characterization of SARS-CoV-2-specific $CD8^+$ T cell receptors

Laura Marlene Mateyka

Vollständiger Abdruck der von der Fakultät für Medizin der Technischen Universität München zur Erlangung eines

Doctor of Philosophy (Ph.D.)

genehmigten Dissertation.

Vorsitz: Prof. Dr. Stefan Lichtenthaler

Betreuer*in: Prof. Dr. Dirk H. Busch

Prüfer*innen der Dissertation:

1. Prof. Dr. Kathrin Schumann
2. Prof. Dr. Jürgen Ruland

Die Dissertation wurde am 07.06.2023 bei der Fakultät für Medizin der Technischen Universität München eingereicht und durch die Fakultät für Medizin am 04.09.2023 angenommen.

Abstract

Severe Acute Respiratory Syndrome CoronaVirus type 2 (SARS-CoV-2) is a novel betacoronavirus that first emerged in 2019 and causes the coronavirus disease 2019 (COVID-19). While this respiratory disease usually presents with mild symptoms (fever, cough, headache, etc.), it can also lead to a severe course of disease characterized by respiratory failure, septic shock, and multiple organ dysfunction. The high infectivity of the virus resulted in high hospitalization rates and COVID-19-related mortality worldwide, making the pandemic a public health burden. At the same time, vaccines and treatments became available at an unprecedented rate, leading to a decline in severe COVID-19 and associated deaths. However, the emergence of variants constantly challenges the therapeutic benefits achieved. This calls for a better understanding of the immune response to the virus, which could also lead to the development of alternative treatments. Although many studies have contributed to our current knowledge of SARS-CoV-2-mediated immunity, the focus has often been on B cell immunity, with limited investigation of T cell responses. It is well established that cells of the adaptive immune system, particularly $CD8^+$ T cells, play an essential role in protection against severe COVID-19. However, detailed analyses of the functionality of epitope-specific $CD8^+$ T cells, including in-depth analysis of their T cell receptor (TCR) repertoires, are lacking.

In this work, we aimed to investigate SARS-CoV-2 $CD8^+$ T cell immunity in convalescent, mild COVID-19 donors by identifying immunogenic epitopes and their corresponding TCRs, and by functionally analyzing these TCRs. To this end, we designed a 9-mer peptide pool consisting of epitopes predicted to be specific and immunogenic for SARS-CoV-2. To facilitate the detection of SARS-CoV-2-specific $CD8^+$ T cells, we further established an *in vitro* expansion protocol. Overall, we detected $CD8^+$ T cell responses to SARS-CoV-2 9-mer epitopes in 77 % of mild COVID-19 donors and in 78 % of asymptomatic seropositive donors. By deconvolution of the peptide pool, we further identified 19 immunogenic epitopes presented on eight prominent HLA types. Responses in the control cohorts, asymptomatic seronegative and pre-pandemic, were much lower and were driven by a single epitope in pre-pandemic donors. In contrast, we observed multi-epitope responses in confirmed infected individuals, demonstrating the specificity of these epitopes and their ability to reliably identify SARS-CoV-2 exposed individuals. To increase the HLA coverage, we developed an 'extended' peptide pool for which we found responses in 75 % of mild COVID-19 donors, resulting in an overall coverage of 91 %. In addition, we showed that SARS-CoV-2-specific antibody levels declined rapidly after infection, while SARS-CoV-2-specific $CD8^+$ T cells were still detectable two years after infection, supporting the generation of long-term $CD8^+$ T cell immunity and suggesting some degree of protection.

Abstract

To identify SARS-CoV-2-specific TCRs, PBMCs from mild COVID-19 donors were expanded with SARS-CoV-2 epitopes and restimulated prior to single-cell RNA sequencing to select recently activated cells. We found that SARS-CoV-2-specific TCR repertoires were highly polyclonal across epitopes. To assess TCR functionality, we then re-expressed 40 SARS-CoV-2-specific TCRs using CRISPR/Cas9-mediated orthotopic TCR replacement in PBMCs from healthy donors or in the Jurkat triple-parameter cell line for high-throughput characterization. We evaluated TCR functionality *in vitro* by measuring structural avidity, epitope sensitivity, cellular avidity, and cytotoxicity, and demonstrated that SARS-CoV-2-specific TCRs were indeed specific for their respective epitope, exhibited strong binding, and were highly functional, ultimately causing efficient and specific lysis of target cells. By analyzing signatures of recent activation in parental cells together with experimentally determined functionality of TCR-engineered T cells, we found a core of genes that reliably identified truly antigen-specific T cells from transcriptomic data. We also found genes potentially associated with TCR functionality, although these appeared to be experimentally dependent.

In summary, we showed that in mild COVID-19 donors, $CD8^+$ T cell responses were polyclonal, functional, and long-lasting. Furthermore, we have provided the basis for in-depth functional characterization of $CD8^+$ T cells, which may be useful for further development of viral T cell therapy.

Zusammenfassung

SARS-CoV-2 ist ein neues Beta-Coronavirus, das 2019 erstmals aufgetreten ist und COVID-19 verursacht. Diese Atemwegserkrankung verläuft in der Regel mit milden Symptomen (Fieber, Husten, Kopfschmerzen etc.), kann aber auch einen schweren Verlauf mit Atemversagen, septischem Schock und Multiorganversagen nehmen. Die hohe Infektiosität des Virus führte weltweit zu hohen Hospitalisierungsraten und einer hohen Sterblichkeit, wodurch die Pandemie zu einer Belastung für die öffentliche Gesundheit wurde. Gleichzeitig wurden Impfstoffe und Behandlungsmöglichkeiten in nie dagewesenem Tempo verfügbar, was zu einem Rückgang der schweren COVID-19-Erkrankungen und der damit verbundenen Todesfälle führte. Die erzielten therapeutischen Vorteile werden jedoch durch das Auftreten von Varianten ständig in Frage gestellt. Dies erfordert ein besseres Verständnis der Immunreaktionen auf das Virus, was auch zur Entwicklung alternativer Behandlungsmöglichkeiten führen könnte. Obwohl viele Studien zu einem besseren Verständnis der SARS-CoV-2-vermittelten Immunität beigetragen haben, lag der Schwerpunkt häufig auf der B-Zell-Immunität, während T-Zell-Reaktionen nur begrenzt untersucht wurden. Es ist allgemein bekannt, dass Zellen des adaptiven Immunsystems, insbesonders $CD8^+$ T-Zellen, eine wesentliche Rolle beim Schutz vor schweren COVID-19-Erkrankungen spielen. Jedoch fehlt es an einer detaillierte Analyse der Funktionsweise epitopspezifischer $CD8^+$ T-Zellen, einschließlich einer eingehenden Analyse ihrer T-Zell-Rezeptoren (TZR).

Ziel dieser Arbeit was es, die $CD8^+$ T-Zell Immunität gegen SARS-CoV-2 bei leicht erkrankten konvaleszenten COVID-19 Spendern durch die Identifizierung immunogener Epitope und ihrer korrespondierenden TZRen zu untersuchen und funktionell zu analysieren. Zu diesem Zweck haben wir einen 9-meren Peptidpool entwickelt, der aus Epitopen besteht, die als spezifisch und immunogen für SARS-CoV-2 vorhergesagt wurden. Um den Nachweis von SARS-CoV-2-spezifischen $CD8^+$ T-Zellen zu erleichtern, haben wir ein *in vitro*-Expansionsprotokoll entwickelt. Insgesamt konnten wir $CD8^+$ T-Zell-Antworten auf 9-mere Epitope von SARS-CoV-2 bei 77 % der leicht erkrankten COVID-19 Spendern und bei 78 % der asymptomatischen seropositiven Spendern nachweisen. Durch Dekonvolutierung des Peptidpools identifizierten wir 19 immunogene Epitope, die auf acht prominenten HLA-Typen präsentiert wurden. Die Reaktionen in den Kontrollkohorten, den asymptomatischen seronegativen und den präpandemischen Spendern, waren deutlich schwächer und wurden bei den präpandemischen Spendern durch ein einziges Epitop ausgelöst. Im Gegensatz dazu beobachteten wir bei bestätigten Infizierten Reaktionen auf mehrere Epitopen, was die Spezifität dieser Epitope und ihre Eignung zur zuverlässigen Identifizierung von SARS-CoV-2 exponierten Personen belegt. Um die HLA-Abdeckung zu erhöhen, entwickelten wir einen "erweiterten" Peptidpool, auf den 75 % der leicht erkrankten COVID-19 Spendern reagierten, was zu einer

Gesamtabdeckung von 91 % führte. Darüber hinaus konnten wir zeigen, dass SARS-CoV-2-spezifische Antikörperspiegel nach Infektion rasch abnahmen, während SARS-CoV-2-spezifische $CD8^+$ T-Zellen noch zwei Jahre nach der Infektion nachweisbar waren. Dies spricht für eine langfristige $CD8^+$ T-Zell-Immunität und lässt einen gewissen Schutz vermuten lässt.

Um SARS-CoV-2-spezifische TZRen zu identifizieren, wurden mononukleäre Zellen des peripheren Blutes (PBMCs) von leicht erkrankten COVID-19 Spendern mit SARS-CoV-2 Epitopen expandiert und vor der Einzelzell-RNA-Sequenzierung restimuliert, um kürzlich aktivierte Zellen zu selektieren. Wir stellten fest, dass SARS-CoV-2-spezifische TZR-Repertoires über alle Epitope hochgradig polyklonal waren. Um die Funktionalität der TZRen zu evaluieren, haben wir 40 SARS-CoV-2-spezifische TZRen durch CRISPR/Cas9-vermittelter orthotopen TZR-Substitution in PBMCs von gesunden Spendern oder in der Jurkat-Triple-Parameter-Zelllinie für Hochdurchsatz-Charakterisierungen reexprimiert. Wir evaluierten die Funktionalität der TZRen durch Messung der strukturellen Avidität, Epitopsensitivität, zellulären Avidität und Zytotoxizität und zeigten, dass SARS-CoV-2-spezifische TZRen tatsächlich spezifisch für ihr jeweiliges Epitop waren, eine starke Bindung aufwiesen und hoch funktionell waren, was letztendlich zu einer effizienten und spezifischen Lyse der Zielzellen führte. Durch die Analyse von frischen Aktivierungssignaturen in parentalen Zellen zusammen mit experimentell nachgewiesener Funktionalität in TZR-manipulierten T-Zellen konnten wir Gene identifizieren, die tatsächlich Antigen-spezifische T-Zellen anhand von Transkriptomdaten zuverlässig identifizieren. Wir haben auch Gene gefunden, die möglicherweise mit der TZR-Funktionalität in Verbindung stehen, auch wenn diese experimentell abhängig zu sein scheint.

Zusammenfassend konnten wir zeigen, dass $CD8^+$ T-Zell-Antworten bei milder COVID-19-Erkrankung polyklonal, funktionell und lang anhaltend sind. Darüber hinaus haben wir die Grundlage für eine detaillierte funktionelle Charakterisierung von $CD8^+$ T-Zellen geschaffen, die für die Weiterentwicklung der viralen T-Zelltherapie nützlich sein könnte.

Contents

List of Figures

List of Tables

Abbreviations

2019-nCoV	2019-new coronavirus
ACE2	angiotensin-converting enzyme 2
APCs	antigen presenting cells
AUC	area under the curve
Cas	CRISPR-associated protein
CCCs	common cold coronaviruses
CMV	cytomegalovirus
COVID-19	coronavirus disease 2019
CoVs	coronaviruses
CRISPR	Clustered Regularly Interspaced Short Palindromic Repeats
crRNA	CRISPR RNA
DMEM	Dulbecco's Modified Eagle medium
DMSO	dimethyl sulfoxide
DNA	deoxyribonucleic acid
E	envelope
E:T	effector to target ratio
EBV	Epstein-Barr virus
EBV+ PTLD	Epstein-Barr virus-positive posttransplant lymphoproliferative disease
FACS	fluorescent activated cell sorting
FCS	fetal calf serum
GFP	green fluorescent protein
gRNAs	guide RNAs
HDR	homology directed repair
HLA	human leucocyte antigen
HSCT	hematopoietic stem cell transplantation
IFN-γ	Interferon gamma

IL-15	interleucin-15
IL-2	interleucin-2
IL-7	interleucin-7
J-TPR	Jurkat triple parameter reporter
KI	knock in
KO	knock out
M	membrane
mAbs	monoclonal antibodes
MERS-CoV	Middle East Respiratory Syndrome CoronaVirus
mRNA	messenger RNA
N	nucleocapsid
ORFs	open reading frames
OTR	orthotopic T cell receptor replacement
PBMCs	peripheral blood mononuclear cells
PBS	phosphate-buffered saline
PCR	polymerase chain reaction
PHA	phytohaemagglutinin
pHLA	peptide human leucocyte antigen
PI	propidium iodide
RBD	receptor binding domain
RNA	ribonucleic acid
RNPs	ribonucleoproteins
RPMI	Roswell Park Memorial Institute medium
RT	room temperature
S	spike
SARS-CoV	Severe Acute Respiratory Syndrome CoronaVirus
SARS-CoV-2	Severe Acute Respiratory Syndrome CoronaVirus type 2
scRNAseq	single cell RNA sequencing
TCR	T cell receptor
TCRA	TCRα chain
TCRB	TCRβ chain
TNF-α	tumor necrosis factor alpha
tracrRNA	trans-activating crRNA

1 Introduction

1.1 Formation of a functional immune response

The immune system is divided into an innate and an adaptive immune response. The innate immune response is considered the first line of defense because it can quickly recognize and eliminate pathogens such as bacteria or parasites. It consists of different cell types with different functions to eliminate invading pathogens (neutrophils, monocytes, macrophages) and to stimulate further immune responses by releasing cytokines and inflammatory mediators (macrophages, mast cells, natural-killer cells). Some cells of the innate immune system (e.g. macrophages, neutrophils) are equipped with specific receptors that initiate inflammatory processes and defense mechanisms when they recognize common features of pathogens. Although the innate immune response can recognize many pathogens simultaneously, broad recognition is also associated with lower specificity. Because an immune response can be either rapid and unspecific or slow and specific, an important role of the innate immune response is to recruit and activate the adaptive immune response.

The adaptive immune system can recognize specific antigens and is divided into a humoral and a cellular response. The humoral immune response is mediated by B cells, which produce and secrete specific antibodies against certain surface features of the pathogen. The secreted antibodies can then bind to the pathogen, a process known as opsonization. Covering the pathogen with antibodies prevents infection of host cells by steric hindrance and helps cells of the innate immune system to better recognize and eliminate pathogens. The cellular immune response is mediated by T cells, which can recognize and kill infected host cells. This is particularly important in infections with viruses that replicate in host cells or infections with intracellular bacteria that have learned to hide from the adaptive immune system.

When a pathogen is unknown to the adaptive immune system, the formation of an antigen-specific immune response usually takes one to two weeks. After that, a lifelong immune cell memory is formed for that particular pathogen, and recognition as well as elimination of a secondary infection is much faster. Thus, effective pathogen elimination requires both, a rapid and broad response to eliminate the majority of pathogens and limit their spread, and a slow but very specific response to eventually eliminate all pathogens and infected cells. The cells of the cellular adaptive immune system and the mechanism of antigen recognition are explained below.

1.1.1 The specificity of the adaptive immunity

The cellular adaptive immune system consists of two types of T lymphocytes, the $CD4^+$ helper T cells and the $CD8^+$ cytotoxic T cells, both of which develop in the thymus. Each T cell has its own T cell receptor (TCR) that recognizes a specific peptide presented on human leucocyte antigen (HLA) molecules by professional antigen presenting cells (APCs) such as dendritic cells (DCs), B cells, macrophages, and thymic epithelial cells [1]. The TCR is composed of a TCRα chain (TCRA) and a TCRβ chain (TCRB) [2]. During thymic maturation, variable regions of the TCRA are assembled by recombination of variable (V) and joining (J) segments, whereas variable regions of the TCRB are assembled by recombination of V, diversifying (D) and J segments [3, 4]. After transcription, the sequence between the recombined V(D)J regions and the constant region is removed by splicing, resulting in complete TCR complexes with variable and constant regions [5].

The variable regions of each TCR chain contain three hypervariable loops known as complementary determining regions (CDRs), CDR1, CDR2, CDR3, which interact with HLA-loaded peptides (peptide human leucocyte antigen (pHLA)). The CDR1 and CDR2 loops are derived from the V gene, have limited diversity, and are responsible for interacting with the HLA molecule. The CDR3 region is encoded within the V(D)J junction and is highly polymorphic [5,6], as a result of somatic recombination as well as deletions and/or additions of random bases at the CDR3 recombination junction during thymic development [5]. The high diversity of these hypervariable CDR3 loops allows specific recognition of peptides from potentially any target antigen [7, 8]. Current estimates of the diversity of the TCR repertoire suggest over 100 million unique TCR sequences in naïve T cells [4]. Before being released into the periphery, naïve T cells undergo positive and negative thymic selection. During positive selection, only T cells that bind above a low-affinity threshold to HLA class I or II molecules are selected. In this way, T cells that do not recognize HLA molecules are eliminated because they cannot mount an immune response. During negative selection, T cells with high affinity for self-peptides are induced to undergo apoptosis, thereby avoiding autoimmunity [9].

As mentioned earlier, TCRs are restricted to recognize antigenic peptides presented on specific HLA molecules, a mechanism first discovered in 1974 and known as HLA restriction [10]. In humans, the HLA system is divided into two types, HLA class I and HLA class II. HLA genes are the most polymorphic loci in the human genome, and their polymorphism influences a variety of biological mechanisms, including immune recognition, susceptibility to infection, autoimmune diseases, individual odors, or mating preference [11,12]. Different HLA molecules preferentially present different peptides that have stochastically different degrees of immunogenicity. Thus, high population diversity increases the likelihood that a population will recognize and overcome infections, thereby providing a survival advantage.

HLA class I molecules are present on the cell surface of almost all cell types and present intracellular peptides to cytotoxic $CD8^+$ T lymphocytes. By binding to HLA class I molecules, $CD8^+$ T cells thus monitor intracellular proteins and, because of prior thymic negative selection, respond only to foreign peptides derived from pathogens

such as viruses or bacteria. HLA class II molecules are typically found on professional APCs, where they present extracellular peptides to $CD4^+$ T cells [1]. To this end, APCs probe their environment by ingesting extracellular bacteria or viruses by phagocytosis or receptor-mediated endocytosis and loading them onto HLA class II molecules [1]. While HLA class I molecules preferentially bind short peptides (eight to eleven amino acids) [13], HLA class II molecules usually bind longer peptides with an average peptide length of 15 amino acids [14]. The difference in binding length is due to differences in the peptide binding groove, with the binding groove of HLA class I molecules being closed at both ends and that of HLA class II molecules having open ends instead [15, 16].

When a T cell and a target cell come into contact, an immunological synapse is formed where TCR - pHLA antigen recognition, adhesion molecules, and costimulatory/checkpoint receptor signaling come together for T cell activation [17]. Once a TCR – pHLA complex is formed, CD8 and CD4 co-receptors bind to HLA class I and class II molecules, respectively [18, 19]. Thus, co-receptor binding stabilizes the extracellular TCR - pHLA interaction. In addition, co-receptor binding is important for TCR signaling by activating intracellular signaling cascades, which is then followed by phosphorylation of the cytoplasmic domains of CD3 and ζ chains [20, 21]. T cell activation is then achieved through the activation of TCR signal-triggered transcription factors and prominent signal transduction pathways (PI3K, RAS, MAPK pathway) [21].

1.1.2 The live cycle of $CD8^+$ T cells during an acute virus infection

Viral infections can be divided into acute and chronic infections. While acute infections usually resolve within a few weeks, chronic infections can last a lifetime. In chronic viral infections, once the virus has evaded complete clearance, the immune system adapts to the constant presence of the virus by down-regulating inflammation to reduce tissue damage. Examples of chronic infections include hepatitis B and C viruses, the cytomegalovirus (CMV), or the Epstein-Barr virus (EBV) [22]. Acute infections, on the other hand, are characterized by rapid disease onset and usually a quick resolution through activation of innate and adaptive immunity [23]. Examples of viruses that cause acute infections include the influenza virus, coronavirus, Ebola virus, or dengue virus [24].

For the initial activation or priming of naïve $CD8^+$ T cells, viral antigen is presented to $CD8^+$ T cells by activated cross-presenting APCs. Cross-presentation is the process by which APCs, like DCs, take up soluble molecules or cells in the tissue. Before the ingested parts can be presented to naïve $CD8^+$ T cells, DCs must receive activation signals in a process called APC licensing. When DCs are not directly infected by a virus, APC licensing functions via viral components that are part of the infected cells or via host molecules expressed by the cells in response to the virus [25]. The licensed DCs then migrate from the site of infection to peripheral lymphoid organs such as the lymph node or spleen. Naïve $CD8^+$ T cells, on the other hand, constantly circulate between the lymph nodes and the bloodstream until they encounter their specific antigen presented to them by APCs in the lymph node. Specific antigen encounter is followed by priming of $CD8^+$ T cells against exogenous antigens. Here, the response of $CD8^+$ T cells is divided

into three phases: the initial activation and expansion phase, the death phase, and the immune memory formation phase [26]. Once a naïve $CD8^+$ T cell encounters its antigen, it becomes activated and differentiates into an antiviral effector phenotype, eventually becoming an effector $CD8^+$ T cell. In addition to pHLA - TCR recognition, the help of $CD4^+$ T cells and environmental stimuli are necessary for the activation of $CD8^+$ T cells and their differentiation into effector and memory cells [27]. To eliminate infected target cells, effector T cells acquire the ability to produce proinflammatory cytokines such as Interferon gamma (IFN-γ), tumor necrosis factor alpha (TNF-α) and interleucin-2 (IL-2) and upregulate the expression of cytolytic granule proteins [28, 29]. In parallel, effector $CD8^+$ T cells also undergo extensive proliferation. One to three weeks after the initial infection, when the infection has resolved, a dramatic decrease in the number of effector T cells is observed, with the majority of effector T cells (90 % - 95 %) dying by apoptosis. This is followed by T cell memory formation [29].

1.2 Severe acute respiratory syndrome coronavirus type 2

1.2.1 Phylogenetics and structure of SARS-CoV-2

The first cases of pneumonia of unknown etiology were recorded in December 2019 in the city of Wuhan, China. The local Huanan Seafood Wholesale Market was quickly identified as the epidemiologic origin of the outbreak. This novel coronavirus, named 2019-new coronavirus (2019-nCoV) by the World Health Organization (WHO), was first genome sequenced on January 7, 2020, and the genetic sequences were made available worldwide just five days later [30]. 2019-nCoV belongs to the Coronaviridae family of viruses. According to phylogeny, taxonomy and established practice, the Coronaviridae Study Group renamed 2019-nCoV to Severe Acute Respiratory Syndrome CoronaVirus type 2 (SARS-CoV-2) due to its close relationship with severe acute respiratory coronaviruses [31].

SARS-CoV-2 consists of the positive-sense single-stranded ribonucleic acid (RNA) genome with at least 10 open reading frames (ORFs) and several structural proteins. The structural proteins are located in the 3' one-third of the genome and include the nucleocapsid (N) that encapsulates the RNA genome, the spike (S) protein that is the viral entry receptor, and membrane (M) and envelope (E) proteins that are responsible for the incorporation of viral particles during the assembly step. The first ORF, ORF1ab is about two-thirds of the genome and encodes 16 non-structural proteins, 15 of which take part in the viral replication and transcription complex and one (nsp1) that targets the host cell translation machinery [32,33]. Other ORFs encode accessory proteins, some of which are thought to play a role in inhibiting innate immune responses [33].

SARS-CoV-2 shares an overall homology with Severe Acute Respiratory Syndrome CoronaVirus (SARS-CoV) of 82 %. However, the spike receptor of both viruses, which is responsible for virus entry, shares a sequence identity of only 40 % [34]. This led many to search for other coronaviruses more closely related to SARS-CoV-2. While the direct origin of SARS-CoV-2 remains controversial, recent estimates suggest that the horseshoe bat Rhinolophus is the most likely reservoir species for the ancestral SARS-CoV-2 strain.

Whether there is a direct progenitor to SARS-CoV-2 has not yet been confirmed. More wildlife samples are needed to determine the exact origin of the SARS-CoV-2 progenitor strains [35]. Finding the direct or indirect ancestor strain of SARS-CoV-2 is important for understanding how the virus evolved to infect humans and may lead to measures that can be taken to prevent the outbreak of future pandemics.

An infection with SARS-CoV-2 can result in the coronavirus disease 2019 (COVID-19) [31]. Although SARS-CoV-2 clearly has an unprecedented prevalence, it is not the first member of the Coronaviridae family to cause infections in humans. From 2002 to 2003, an outbreak of Severe Acute Respiratory Syndrome was documented and attributed to a novel coronavirus now known as SARS-CoV [36]. Striking features of SARS-CoV were a relatively low global prevalence and a mortality rate of 13 % [37]. Also for SARS-CoV, horseshoe bats were thought to be the natural reservoir, but direct evidence is lacking [38]. Another example of a Coronaviridae family member causing a human pandemic is the Middle East Respiratory Syndrome CoronaVirus (MERS-CoV). MERS-CoV is transmitted to humans through contact with infected dromedary camels [39]. First detected in Saudi Arabia in 2012, MERS-CoV has an extremely high mortality rate of 35 % - 40 %, but fortunately little human-to-human transmission [37, 40]. As a result, the total fatality number to date is quite low, with only 858 known deaths [41].

1.2.2 Epidemiology of SARS-CoV-2

Initial estimates of the ancestral SARS-CoV-2 mortality rate were 5.6 % but because of asymptomatic and unrecorded infections, they were likely much lower [37]. Although unreported infections skew the data, the current case fatality rate in 237 countries is 1.27 % [42]. Unlike SARS-CoV and MERS-CoV, both of which were prevalent for only a year or two and spread more locally, SARS-CoV-2 spread rapidly around the world, crippling the global economy for months and is still having a massive impact on normal life, with infections and deaths reported daily. The SARS-CoV-2 outbreak has resulted in more than 762 million confirmed COVID-19 cases and more than 6.8 million deaths by April 2023 [43].

There are many reasons why SARS-CoV-2 became a pandemic, some of which are explained here. The most important factors leading to the rapid and uncontrolled spread of the virus are its ability to spread from person to person and its transmission via airborne droplets, since SARS-CoV-2 is a respiratory virus. However, this alone does not explain why the spread of SARS-CoV-2 has not been contained with similar success as the SARS-CoV pandemic of 2002/2003. There are two important factors that made the containment of SARS-CoV possible. First, only a small proportion of those infected with SARS-CoV were highly infectious to others, and second, only symptomatic patients were infectious. This made it possible to identify and isolate infected individuals and prevent further spread [44]. In addition to severe COVID-19 patients, SARS-CoV-2 can also be transmitted by pre-symptomatic, asymptomatic, and mildly symptomatic individuals [45]. Another factor contributing to infectivity is the strength of receptor binding. Like SARS-CoV, SARS-CoV-2 uses the protease angiotensin-converting enzyme 2 (ACE2) as an entry receptor, but binds to ACE2 with a 10 to 20-fold higher affinity [46].

This suggests that the binding strength of ACE2 may have played an important role in the greater infectivity of SARS-CoV-2. Initially, it was suggested that the incubation period between infection and infectivity also impacted disease progression of SARS-CoV-2, but this was quickly ruled out as a driving factor because the incubation period of SARS-CoV-2 (mean: 6 days, range: 2 – 16 days) [47] was consistent with the incubation periods reported for SARS-CoV (mean: 5 days, range: 2 – 14 days) [48] and MERS-CoV (mean: 5 – 7 days, range: 2 – 14 days) [49]. Compared to most human coronaviruses (CoVs), including common cold coronaviruses (CCCs), which usually cause mild upper respiratory tract infections [50], SARS-CoV, MERS-CoV and SARS-CoV-2 cause severe respiratory disease. This is likely due to infection of the lower respiratory tract and makes infection with these viruses more dangerous [51–53]. SARS-CoV-2 patients with upper respiratory tract infection had a much better clinical outcome than patients with lower respiratory tract infection, who also had the highest incidence of pneumonia [53].

The mutation rate of SARS-CoV-2 is estimated to be about $1 - 2 \times 10^{-6}$ mutations per nucleotide per replication cycle. The high infectivity of the ancestral SARS-CoV-2 virus resulted in a high mutation rate and also a high substitution rate, which measures the rate of mutation accumulation during virus evolution. In addition, recombination events further increased diversity, creating hybrid variants with different genetic backgrounds. While several variants of concern (VOC) were reported in the first months after the emergence of the ancestral SARS-CoV-2 strain, a first turning point in the pandemic was observed after eight months with the appearance of several divergent SARS-CoV-2 lineages with increased infectivity (Alpha, Beta, Gamma). In May 2021, the Delta lineage was identified as VOC, and its increased virulence rapidly led to an increase in reported deaths. This was followed by the appearance of the first Omicron lineages (BA.1, BA.2, BA.3) in November 2021, which quickly reached global dominance due to higher infectivity, fortunately accompanied by lower disease severity. BA.1 initially achieved global dominance, was replaced by BA.2, which in turn was replaced by BA.5, the current dominant lineage. In summary, the new lineages predominantly had mutations in the spike protein that enhanced binding to the host receptor, facilitated viral entry, and ultimately increased transmissibility. The strains prior to Omicron showed striking changes in pathology, with increased hospitalizations and higher mortality rates compared to the ancestral strain. Omicron, on the other hand, had higher infectivity with lower disease severity [54].

1.3 The immune response against SARS-CoV-2

1.3.1 Pathogenesis of SARS-CoV-2

After infection with SARS-CoV-2, the pathogenesis of COVID-19 can be divided into three stages. The first stage, the asymptomatic stage, begins with the uptake of SARS-CoV-2 through the nasal cavity and entry into ciliated epithelial cells [55]. Following S protein-mediated entry via the cellular entry receptor ACE2, the viral membrane fuses with the cellular or endosomal membrane and the positive-sense single-stranded RNA genome is released. Inside the cell, viral RNA is replicated and encapsulating proteins

are produced for the assembly of virions, which are then secreted from infected cells by exocytosis [33]. This first stage is characterized by local virus replication but limited innate immune responses. In the second stage, the upper and conducting airway response, the virus spreads further into the respiratory tract along the conducting airways [55]. Here, a stronger innate immune response is induced by infected cells through the release of pro-inflammatory cytokines and chemokines that attract innate and adaptive immune cells to the site of infection [56].

In 80 % of patients infected with SARS-CoV-2, the course of disease is mild and limited to the upper and conducting airways [57]. In 20 % of patients, the virus continues to spread to the lower respiratory tract, described as stage 3, hypoxia and progressive acute pneumonia [55]. Alveolar type II cells are infected, resulting in the release of large numbers of pro-inflammatory cytokines and chemokines and ultimately the release of viral particles and death of alveolar type II cells by apoptosis [58]. Excessive immune cell infiltration further exacerbates inflammation and leads to a systemic cytokine storm. In particular, the imbalance between an excessive innate and a delayed adaptive immune response negatively affects disease progression [59]. Uncontrolled inflammation can eventually lead to multi-organ failure [60]. Together with the continued spread of the virus, persistent inflammation can lead to diffuse alveolar damage and eventually to pulmonary edema and pneumonia [56,61]. Interestingly, the viral load does not initially correlate with early pathology, but is the cause of severe COVID-19 [62], characterized by persistent high viral load and extensive inflammation [63].

1.3.2 Dysregulation of immune responses in COVID-19 patients

Innate immune responses are critical for building the first line of defense against infection with viruses such as SARS-CoV-2. They limit viral entry, slow translation, replication and assembly within cells, and help to identify and eliminate infected cells. They also coordinate and accelerate the development of adaptive immunity. Innate immune cells (such as macrophages and DCs) sense the presence of a virus with their pattern recognition receptors (PRRs) by recognizing surface features or structural motifs of pathogens (pathogen-associated molecular patterns, PAMPs). This is followed by the activation of inflammatory pathways that promote viral clearance [64]. Hallmarks of severe COVID-19 infections include decreased innate antiviral defenses and excessive production of inflammatory cytokines (Figure 1). Specifically, COVID-19 patients have been found to have a unique and inappropriate inflammatory immune response characterized by low levels of type I and type III interferons and elevated levels of cytokines and IL-6 [65]. The interferon (IFN) pathway is a key component of the host innate immune antiviral response. Interestingly, only low levels of IFN proteins were detected in COVID-19 patients despite elevated IFN mRNAs, suggesting post-transcriptional inhibition of IFN protein production by SARS-CoV-2 [66]. Coronaviruses such as SARS-CoV-2 have developed evasion strategies to limit host cell control and enhance replication and transmission [67]. SARS-CoV-2 proteins inhibit the host cell through degradation of host mRNA and direct and indirect inhibition of antiviral mRNA biogenesis such as IFNB1 [66]. ORF3b was identified as a potent interferon agonist that efficiently suppresses the induction of type

I interferon [68]. In addition, ORF6, ORF8 and the N protein were found to inhibit type I interferon (IFN-beta) and NF-κB-responsive promoters [69]. Delayed and suboptimal activation of the type I interferon pathway is thought to contribute to a delayed and elevated adaptive immune response [70].

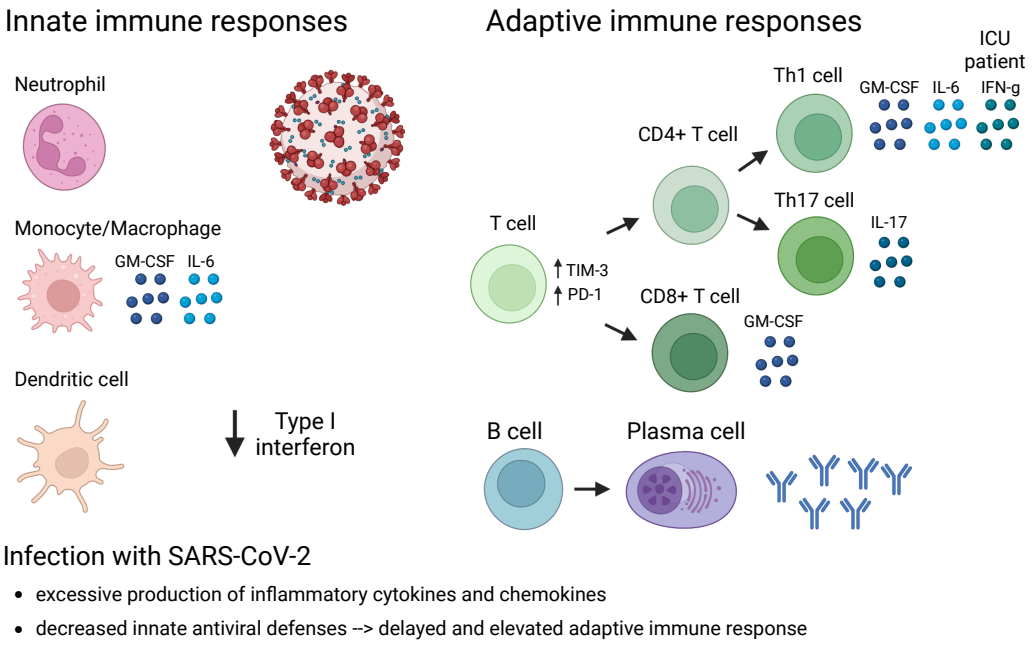

Figure 1: Dysregulation of immune responses by SARS-CoV-2. Dysregulation of chemokine and cytokines in the innate immune system (Neutrophils, Monocytes/-macrophages, and Dendritic cells) and the adaptive immune system (T cells, $CD4^+$ Th1 and Th17 and $CD8^+$ T cells, B cells) after infection with SARS-CoV-2. Adapted from [32].

Early in the pandemic, the S protein, and in particular its receptor binding domain (RBD), was found to be immunogenic and the target of most neutralizing antibodies [71, 72]. Following the kinetics of an antibody response after acute viral infection, SARS-CoV-2 neutralizing antibody titers peaked within the first few weeks after infection but declined quickly over time [73–75]. Delayed neutralizing antibody kinetics correlate with COVID-19 mortality [76]. As mentioned above, suppression of the IFN pathway by SARS-CoV-2 delays the T cell response. A moderate delay results in an asymptomatic or mild disease course. A longer delay is associated with severe COVID-19 and also with a pathological contribution of T cells to the disease. In severe COVID-19 patients, the total number of T cells was significantly reduced and correlated with elevated levels of IL-6, IL-10 and TNF-α. Both $CD4^+$ and $CD8^+$ T cells were found to contribute to the pathogenesis of COVID-19 (Figure 1). $CD4^+$ and $CD8^+$ T cells were functionally exhausted, as indicated by high expression of the exhaustion markers Tim-3 and PD-1 [77].

When the $CD8^+$ T cell response is delayed, disease severity and systemic inflammation are more pronounced [76]. $CD8^+$ T cells from severe COVID-19 patients showed higher levels of GM-CSF, suggesting their involvement in the pathogenesis of COVID-19 infection and initiation of tissue damage [78]. $CD4^+$ T helper (Th1) cells produce pro-inflammatory cytokines and mediate immune responses against intracellular pathogens by promoting the activation of macrophages, B cells, NK cells, and $CD8^+$ T cells. After SARS-CoV-2 infection, pathogenic Th1 cells were found to produce high levels of GM-CSF and IL-6. In patients on intensive care units (ICU), this was further complemented by the expression of IFN-γ, suggesting that aberrant pathogenic Th1 cells play a critical role in hyperinflammatory responses in SARS-CoV-2 pathogenesis [78]. Probably induced by the cytokine milieu, $CD14^+$ $CD16^+$ inflammatory monocytes were also found in COVID-19 patients characterized by high expression of GM-CSF and IL-6. Finally, Zhou et al. suggested that GM-CSF links the ability of pathogenic Th1 cells to initiate severe lung syndrome with the inflammatory signature of monocytes. By entering the pulmonary circulation, these cells play an immune-damaging role leading to disruption of lung function and mortality [78]. $CD4^+$ Th17 T cells have also been shown to contribute to the pathogenesis of COVID-19 by activating cytokine cascades, inducing Th2 responses, inhibiting Th1 differentiation and suppressing regulatory $CD4^+$ T cells (Treg) cells [79]. In summary, there is evidence that delayed activation of adaptive immune cells by the innate immune response together with dysregulated adaptive immune responses are significant components of severe COVID-19.

1.3.3 SARS-CoV-2 immunity shapes viral evolution

The SARS-CoV-2 virus can evade immune recognition through mutation and recombination events. Neutralizing antibodies mostly target the RBD and exert selective pressure on the S protein. Consequently, this affects the appearance of new variants that can escape neutralization [80]. An example of selective pressure is the Omicron variant (B.1.1.529), which has a greater number of mutations than previous variants. Of the 37 mutations in the S protein, 15 are in the RBD [81]. Indeed Omicron escape from neutralization was demonstrated in 85 % of 247 neutralizing antibodies tested [82]. Since immunodominant epitopes of SARS-CoV-2 were also found in ORFs other than the S protein (e.g. ORF1, ORF3, N) with multiple epitope reactivities per donor, immune escape of T cells is unlikely [83–86]. In fact, protection from infection with the ancestral strain and the Alpha, Beta, and Delta variants was high at 78.6 % at 40 weeks post infection. Protection from severe disease with these variants also remained high at 40 weeks at 90.2 %. For Omicron, protection from infection was significantly lower with initial efficacy of 45.3 % against reinfection and 36 % at 40 weeks. Encouragingly, a prior SARS-CoV-2 infection still provided protection against severe disease after infection with Omicron at 40 weeks (> 88.9 %) [87].

1.3.4 T cell cross-reactivity other coronaviruses

To understand whether there is cross-reactivity between SARS-CoV-2 and other coronaviruses, important insights can be gained by studying cross-reactivity between other coronaviruses. In a mouse model, prior infection with MERS-CoV was shown to confer protection against infection with SARS-CoV. More precisely, airway memory $CD4^+$ T cells specific for a conserved epitope shared by SARS-CoV and MERS-CoV were shown to protect against both CoVs in mice [88]. These data suggest a possible protective role of prior infection with other coronaviruses for infection with SARS-CoV-2 via shared epitopes, but this may not be the only mechanism of action. The amount of SARS-CoV-2 cross-reactive T cells found in unexposed individuals varies between studies from 35 % – 81 % [86, 89, 90]. Braun et al. further demonstrated that these cross-reactive T cells reacted against the human endemic common cold coronaviruses HCoV229E and HCoVOC43 [90]. In another study, the correlation between the cross-reactivity of CCCs and the course of COVID-19 was investigated [91]. Here, Saletti et al. found that although hCoV memory T cells can be detected in young adults, they are completely absent in old adults. Since patients older than 60 years account for more than 95 % of COVID-19 morbidity and mortality cases, they reasoned that the absence of these cross-reactive T cells might influence a more severe disease course. Saletti et al. concluded that a higher proportion of cross-reactive hCoV T cells prior to SARS-CoV-2 infection might provide protection against severe COVID-19 and death [91]. Specifically, cross-reactive memory T cells from seasonal CCCs against the SARS-CoV-2 N protein have been suggested to provide protection against infection [92].

In addition to CCCs, SARS-CoV may also provide protection against SARS-CoV-2. Since SARS-CoV shares a high sequence homology (82 %) with SARS-CoV-2 [34], protection via similar epitopes may be even more likely. While SARS-CoV IgG antibodies were undetectable in most patients six years after infection, long-lasting memory T cells were still detectable [93]. The longest tracking of memory T cells against SARS-CoV was 17 years. These T cells were specifically reactive to the N protein of SARS-CoV and were cross-reactive with the N protein of SARS-CoV-2 [94]. The exact effect of prior SARS-CoV infection on SARS-CoV-2 infection is still unclear.

In summary, although the extent or mechanism of protection by cross-reactive T cells is not well understood, current knowledge suggests that cross-reactive T cells derived from human CoVs provide some protection against SARS-CoV-2 infection or the development of severe COVID-19.

1.4 Vaccination against SARS-CoV-2

After the genome sequence of SARS-CoV-2 was made available to the public, companies began developing vaccines within weeks. Immediate large-scale vaccine production and parallel clinical trials enabled unprecedented rapid development and delivery of the first U.S. Food and Drug Administration (FDA)-approved vaccine against SARS-CoV-2 by the end of that year [95]. Since then, many other SARS-CoV-2 vaccines with different modes of action (messenger RNA (mRNA) vaccines, adenovirus vector vaccines, recom-

binant antigen vaccines, and inactivated virus vaccines) have been approved, some of which are presented below.

1.4.1 mRNA vaccines

With the development of synthetic lipid nanoparticles, mRNA vaccines had a major breakthrough as fragile mRNAs could be encapsulated and efficiently transported to their target cell. Once lipid nanoparticles reach their target cells, they are taken up and synthetic proteins encoded by the mRNA code are produced in the cytoplasm. mRNA vaccines are transient and do not interact with genomic deoxyribonucleic acid (DNA), giving them a high safety profile. In addition, mRNA vaccines are biodegradable, can be easily produced in large quantities, and induce a balanced immune response of humoral and cellular immunity. All these factors make mRNA vaccines attractive for the treatment of severe COVID-19 [96,97]. The mRNA vaccines BNT162b2 and mRNA1273 marketed by BioNTech/Pfizer and Moderna were the first approved vaccines against SARS-CoV-2 [95, 98]. Both are lipid nanoparticle formulated nucleoside-modified RNA vaccines encoding the SARS-CoV-2 S protein. Safety and efficacy studies of BNT162b2 and mRNA1273 reported 94 % and 95 % protection against COVID-19 of the ancestral strain and the Omicron variant, respectively [99–101].

1.4.2 Adenovirus vector vaccines

Adenoviruses are non-enveloped DNA viruses with a 30 - 40 kb linear double-stranded genome [102]. Unlike lentiviruses, transduction with adenoviral vectors poses no risk of insertional mutagenesis because adenoviruses remain extrachromosomal [103], making them suitable for gene delivery. Replication incompetent adenoviral vectors are widely used for gene therapy [104]. Adenoviruses induce both, innate and adaptive immunity and were therefore considered a promising therapy for vaccination against SARS-CoV-2 [105]. Two adenoviral vector vaccines containing double-stranded DNA of the S protein (CHAdOx1, AstraZeneca/Oxford; Ad26COVS1, Janssen) have been approved in the EU for vaccination against SARS-CoV-2 [106, 107] with a vaccine efficacy of 67 % for both vaccines [108, 109]. Recently, only combinatorial vaccinations with adenovirus vector vaccines have been studied, making interpretation of the efficacy of adenovirus vector vaccines against Omicron difficult [110].

1.4.3 Inactivated virus vaccines

Inactivated viruses are live viruses that have been ‘killed’ by exposure to chemical or physical agents and are unable to infect target cells or cause disease while retaining immunogenicity. Currently, inactivated viruses are approved for six pathogens: influenza, rabies, poliovirus, hepatitis A, japanese encephalitis virus, and tick-borne encephalitis virus [111]. Inactivated virus vaccines contain the entire SARS-CoV-2 protein, allowing the immune system to also mount responses against proteins other than the S protein. This could be advantageous given the continued emergence of new variants that are highly mutated in the S protein. VLM2001 is an inactivated SARS-CoV-2 virus vaccine

and the only one approved in the EU against SARS-CoV-2 [112]. VLM2001 achieved higher neutralizing antibody titers against SARS-CoV-2 than ChAdOx1-S, but efficacy studies are lacking [113].

1.4.4 Recombinant antigen vaccine

The use of highly purified recombinant antigens allows for targeted immune responses against specific proteins. The Novavax COVID-19 vaccine (NVX-CoV2373) is a recombinant nanoparticle vaccine containing full-length S glycoprotein as an S-trimer attached to polysorbate 80 (PS80) and adjuvated with saponin-based Matrix-M [114]. NVX-CoV2373 has a vaccine efficacy of 89.7 % in preventing disease and resistance to neutralization of Omicron variants BA.1 and BA.4/BA.5 of 72 % and 59 %, respectively [115].

Early reports of vaccines based on mRNA and adenoviruses suggested that neutralizing antibodies from vaccines might protect against infection [116–118]. However, hopes for long-term protection against infection by vaccination were quickly dashed by the emergence of the B.1.1.529/Omicron strain. While vaccination remained largely effective against severe disease and death, Omicron showed an escape from vaccine-induced immunity [119–121]. By comparison, the protective immunity to the four seasonal cold CoVs (HCoV-NL63, HCoV-229E, HCoV-OC43, and HCoV-HKU1) is also short-lived. Antibody levels to human CoVs are not maintained and reinfection with the same seasonal coronavirus is likely within twelve months. Considering that these CoVs belong to two different taxonomic genera and use different entry receptors, it is reasonable to assume that reinfection is a common feature of CoVs and is also common for SARS-CoV-2 [122].

1.5 Treatments against severe COVID-19

In the last three years, several therapeutic options for the treatment of severe COVID-19 have emerged. Some of these treatments are already used for other viral diseases (monoclonal antibodies, antiviral chemotherapy), while others are still experimental (convalescent plasma therapy, TCR T cell therapy) (Figure 2). Their mechanisms of action and clinical utility are discussed below.

1.5.1 Convalescent plasma and antibody therapy

Convalescent plasma refers to the practice of isolating plasma from patients who have been infected with a virus and have since recovered and developed an antibody response against the virus. Early in the pandemic, when no other therapeutic options were available, convalescent plasma therapy was approved by the FDA in August 2020 for the treatment of severe COVID-19 [123]. In the following months, several studies examined the efficacy of convalescent plasma therapy and found that it had little to no effect on clinical improvement, did not reduce the need for invasive mechanical ventilation, and

did not reduce mortality [124, 125]. Therefore, in December 2021, the WHO recommended against the use of convalescent plasma for the treatment of COVID-19 [126].

For the treatment of other viral infections, such as infections with Respiratory Syncytial Virus (RSV) or Ebola virus, monoclonal antibodes (mAbs) have been successfully used [127, 128]. Thus, the pipelines for the development of mAbs were already in place and could easily be repurposed for the treatment of severe COVID-19 (Figure 2). Specifically, peripheral blood mononuclear cells (PBMCs) were obtained from convalescent donors, and SARS-CoV-2-specific memory B cells were isolated by single-cell sorting with biotinylated RBD and SARS-CoV-2 S antigens. Paired heavy (V_H) and light variable (V_L) chains were then identified by RT-PCR, and mAbs were generated. The binding specificity to the RBD and S protein, and the neutralizing power of the SARS-CoV-2 spread were tested using a suitable ACE2 expressing cell line. This guided the selection of the mAbs to be used for therapy [129]. There are now 19 mAbs approved for the treatment of severe COVID-19, subdivided into antibodies targeting the RBD (class 1 - 4) or the N-terminal domain depending on their S protein binding position [130]. Overall, the mAbs had a good safety profile and treatment resulted in a significant reduction in the risk of hospitalization, development of severe COVID-19 symptoms, or death [131]. While mAbs remained relatively effective against the Alpha variant, with the emergence of the Beta and Gamma variants, seven mAbs have already lost efficacy. Strikingly, with the emergence of the Omicron variant, the efficacy of mAbs was drastically reduced, with 17 of 19 antibodies showing abolished or impaired activity [132]. The mutational antigen escape with Omicron is only expected to increase with future variants and will require the discovery of mAbs that do not target the RBD, or even other alternative therapeutic options.

1.5.2 Antiviral chemotherapy

Antiviral drugs are already in clinical and experimental use for a variety of different viruses, including Human Immunodeficiency Virus (HIV), CMV, and hepatitis B. Therapeutic agents can block the replication of the virus by inhibiting the viral reverse transcriptase, act on the viral protease, or may be interferon treatments [133]. The following three small molecule inhibitors, two of which are approved for the treatment of severe COVID-19, are discussed: remdesivir, nirmatrelvir, and molnupiravir [134–136] (Figure 2).

Remdesivir is a nucleotide analog prodrug that inhibits the viral RNA polymerase [137]. A three-day course of treatment improved clinical outcomes in patients with severe COVID-19 and resulted in an 87 % lower risk of hospitalization or death [138]. A retrospective study confirmed that remdesivir treatment was associated with significantly lower mortality for Delta and Omicron variants [139]. Nirmatrelvir is a main protease inhibitor that was not approved until early 2022, at which time the Omicron variant was dominant [135]. Treatment with nirmatrelvir resulted in a significant reduction in hospitalization rates and deaths following Omicron variant infection [140]. Molnupiravir is a small molecule antiviral prodrug that has not yet been approved by the EMA [136]. While the authors of the phase 3 study found that early treatment with molnupiravir

resulted in lower risk of hospitalization or death [141], a more recent study claimed that molnupiravir resulted in faster recovery but no benefit in COVID-19-associated hospitalization or death following infection with Omicron [142]. A study testing the *in vitro* antiviral activity of remdesivir, molnupiravir, and nirmatrelvir against Omicron showed that antiviral activity remained stable for all three drugs [143]. These results were expected since small molecule drugs are not affected by S protein mutations due to their mode of action.

1.5.3 Adoptive T cell therapy

Adoptive transfer of virus-specific T cells has been shown to be effective in preventing and treating serious infections in immunocompromised hosts after hematopoietic stem cell transplantation (HSCT). In fact, 11 % of deaths after HSCT are due to reactivation of latent viruses such as CMV, EBV or adenovirus. For this purpose, virus-specific T cells are isolated from a HLA-matched seropositive donor, expanded *in vitro*, and infused into the patient. Alternatively, virus-specific T cells can be isolated *ex vivo* via peptide HLA multimers and infused directly into the patient [144]. Similar clinical benefits were also observed after adoptive transfer of tumor-specific T cells. For this, patient-derived tumor-infiltrating lymphocytes (TILs) are isolated, expanded *ex vivo* and reinfused into the patient. While adoptively transferred tumor-specific T cell products have shown expansion *in vivo* and functionality in *in vitro* assays, clinical outcomes for patients have been limited [145].

The use of antigen-specific T cells may also be considered a potential treatment option for patients with active COVID-19 or at risk of developing COVID-19. Bonifacius et al. have shown that it is possible to generate clinical-grade SARS-CoV-2-specific T cell products from convalescent donors. After magnetic activated cell sorting (MACS) enrichment of IFN-γ-secreting cells following SARS-CoV-2 peptide pool stimulation, they demonstrated that isolated SARS-CoV-2-specific T cells were proliferative, functional, and able to specifically recognize and kill target cells [146]. Thus, for the treatment of severe COVID-19, allogeneic adoptive transfer of partially matched, SARS-CoV-2-specific T cells from convalescent donors may be a viable option.

A major risk of allogeneic T cell therapy is immunocytotoxicity due to only a partial HLA match. This can result in an ineffective and short-lived T cell product if the infused T cells are eliminated by the host immune system, or in graft-versus-host symptoms if the infused T cells cause non-specific cytotoxicity. A promising alternative is the engineering of autologous T cells with antigen-specific TCRs. To identify TCRs for viral TCR-T cell therapy, virus-specific T cells can be isolated from the memory repertoire of convalescent patients. In 2022, a viral TCR-T cell therapy was developed for the treatment of CMV reactivation after HSCT. Specifically, several CMV epitopes were used to identify CMV-specific TCRs from CMV^+ healthy donors. After the infusion of TCR-engineered T cells, the persistence of CMV-specific T cells was demonstrated for several months and a complete response as measured by plasma CMV DNA, was observed in most or all patients [147]. Although the number of patients in this study was small, the effects were remarkable.

With the continuous emergence of new variants, T cell therapy may be a promising approach for the treatment of severe COVID-19, since evading a diverse T cell response is more difficult compared to antibody immunity (Figure 2). Since T cells from SARS-CoV-2 convalescent patients often recognize immunodominant epitopes located in regions other than the S protein [84, 89, 94], other ORFs should also be considered for epitope selection of SARS-CoV-2-specific TCRs. After epitope selection, epitope-specific TCRs from convalescent donors need to be identified and *in vitro* functionally characterized to select the best TCR candidates for T cell therapy. Given the same HLA background, we envision that identified TCRs could also be used to generate an off-the-shelf library of TCRs to target multiple antigens and/or epitopes of the same antigen simultaneously to avoid escape.

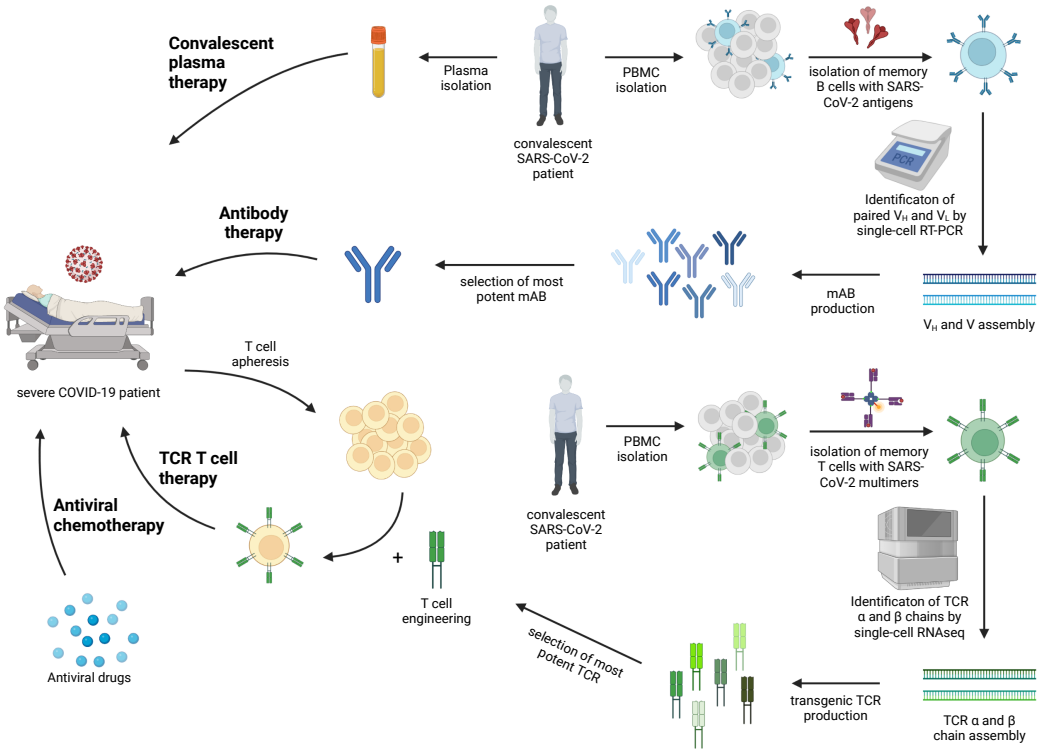

Figure 2: COVID-19 treatment options. Schematic depiction of different treatment options for a severe COVID-19 patient. Plasma and PBMCs can be isolated from a SARS-CoV-2 convalescent donor for either 'convalescent plasma therapy', 'antibody therapy', or 'T cell therapy'. For antibody or T cell therapy, SARS-CoV-2-specific B cells and T cells are first isolated and sequenced. After sequence assembly and re-expression, the best performing antibody or TCR needs to be identified. Another treatment option is 'antiviral chemotherapy' with antiviral drugs.

1.6 TCR engineering

TCR T cell therapy describes the integration of transgenic TCRs into the patient's T cells. For clinical applications, lentiviral and retroviral vectors are still the transduction method of choice due to their high efficiency and stable gene transfer. Other advantages include the large size of the genetic constructs and the integration of the target gene into the genome, which ensures stable expression. However, the use of viruses for gene transfer has several limitations. In has proven challenging to generate large quantities of viral vectors for manufacturing. In addition, safety testing to ensure the absence of residual virus is extensive and costly [148]. Finally, the presence of the endogenous TCR can lead to TCR chain mispairing between the endogenous and transgenic TCR chains with unpredictable toxicities [149].

Genome engineering of cells with non-viral approaches was taken to a new level by Jennifer Doudna and Emmanuelle Charpentier, who received the 2020 Nobel Prize in Chemistry "for the development of a method for genome editing" [150]. With Clustered Regularly Interspaced Short Palindromic Repeats (CRISPR)/CRISPR-associated protein (Cas)9, many therapeutic options opened up, including for T cell therapy [151]. In 2015, efficient genome editing of primary human $CD4^+$ T cells by knock out (KO) of CXCR4, a coreceptor for HIV entry, using the CRISPR/Cas9 system was demonstrated [152]. Following these developments, the Busch laboratory developed a protocol to perform CRISPR/Cas9-mediated orthotopic T cell receptor replacement (OTR) in primary T cells for simultaneous editing of TCRA and TCRB. By homology directed repair (HDR), the endogenous TCRA is replaced with the transgenic TCR, containing both the α and β chain. The concomitant KO of TCRB ensures complete abrogation of the endogenous TCR and, consequently, that no mispairing occurs between the endogenous TCRB and the transgenic TCR chains. Thus, the transgenic TCR underlies endogenous TCR regulation with near-physiological T cell function [149].

For efficient knock-in of the transgenic TCR, the HDR template has the following domain order (Figure 3): outside the TCR structure, the flanking regions at both ends of the HDR template need to overlap with the targeted genomic region to form the left homology arm (LHA) and the right homology arm (RHA). The LHA is followed by the self-cleaving peptide P2A, and a component that constitutes the variable part of the endogenous TCRB (variable – V, diversifying – D, joining - J). The variable part of the transgenic TCRA (VJ) is separated from the TCRB by the self-cleaving T2A element, followed by a stop codon and a poly-A tail (bGHpA). To improve TCR surface expression, the human constant domains of both TCR chains were replaced by murine constant regions containing additional cysteine bridges [153]. For CRISPR/Cas9 OTR, Cas9 proteins are loaded with a sgRNA targeting the genomic locus, resulting in Cas9-RNA complexes or ribonucleoproteins (RNPs). After *in silico* assembly and synthesis, the assembled Cas9 RNPs are electroporated together with a HDR template into target cells [149, 154, 155] (see 3.2.5). Compared to conventional TCR engineering by viral integration, CRISPR/Cas9-mediated OTR results in lower variability due to controlled gene insertion. By preventing TCR chain mispairing between the endogenous and transgenic TCR, recognition of the correct target is ensured while off-target effects

are reduced [149]. In addition, integration of the transgenic TCR by targeted TCR editing leads to homogeneous expression and thus better prediction of T cell function *in vivo* [156]. Although the efficiency of OTR still needs to be improved, the above factors support the use of OTR for the generation of TCR-engineered T cells for T cell therapy.

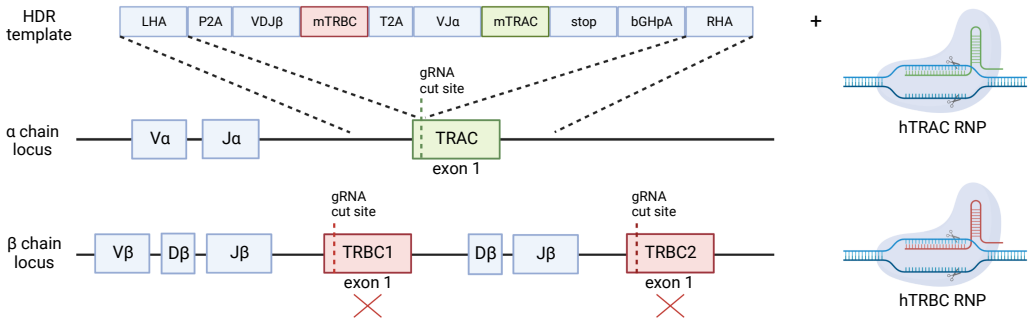

Figure 3: CRISPR-Cas9 OTR. Schematic depiction of CRISPR/Cas9 mediated OTR with knock in (KI) of the transgenic TCR containing TCRA and TCRB chains into the endogenous TCRA locus via HDR and hTRAC RNPs as well as KO of the endogenous TCRB locus with hTRBC RNPs.

In 2020, a first-in-human Phase I clinical trial demonstrated the safety and feasibility of CRISPR-engineered T cells for the treatment of patients with refractory cancer. The engineered T cells persisted for up to nine months with minimal toxicity, setting the stage for CRISPR gene editing for cancer immunotherapy [157]. Through the clinical application of CRISPR-Cas9-mediated OTR for the treatment of solid tumors, the feasibility and clinical-grade manufacturing were shown for orthotopic TCR replacement [158]. However, it is important to note that CRISPR-Cas9 KO can result in chromosome loss. Detailed analysis of CRISPR KO revealed a loss in 9 % and 10 % of chromosome 14 and chromosome 7, where TCRA and TCRB are located, respectively. Gain of chromosomes was also detected, but at lower levels. While there is certainly negative selection against truncated and aneuploid cells, chromosome loss was still detected at low levels after eleven days of culture. CRISPR/Cas9 KO could therefore lead to an increased risk of tumorigenesis [159]. Therefore, other gene editing options should also be considered for the further development of gene KO T cell therapy. How chromosomal alterations are affected after HDR is not known.

1.7 Functional TCR characterization

To select the best TCR for therapy, it is critical to relate the functionality measured *in vitro* to the actual *in vivo* performance of a TCR-engineered T cell product. For the study of human TCRs, this means extrapolation of *in vitro* TCR functionality, as informative mouse models are still limited. The functionality of a TCR can be determined at several levels, ranging from monomeric binding to a pHLA complex (affinity) to binding of multiple TCR – pHLA molecules in the presence of co-receptors (avidity)

to the measurement of T cell peptide sensitivity (TCR functional avidity). The killing of target cells *in vitro* is further evidence of TCR functionality (Figure 4).

1.7.1 TCR affinity and structural avidity

TCR affinity is defined as the binding strength of a TCR to a single pHLA molecule and it determines T cell antigen sensitivity. TCR affinity can be measured by the equilibrium dissociation constant (K_D), which is determined by the TCR – pHLA association (k_{on}) and dissociation rate (k_{off}) [160]. The most established method for measuring TCR affinity is surface plasmon resonance (SPR). In this method, one of the two proteins (TCR or pHLA) is immobilized on a biosensor surface. Binding of the soluble component (k_{on}) can be detected by changes in light intensity reflection. Dissociation of the components from their target (k_{off}) can then be followed by a gradual decrease in intensity. Since the intensity shift is proportional to the mass of bound material, SPR measurements can be related to single molecule interactions [161] (Figure 4, left). Measurement of TCR affinity by SPR requires that pHLA and TCR molecules are provided as highly purified proteins. Since the expression of correctly folded TCRs is technically challenging, SPR is not suitable for high-throughput testing of many TCRs.

The Busch laboratory has developed an alternative assay to measure k_{off} rates of monomeric TCR:pHLA interactions in the presence of the CD8 co-receptor (defined as structural avidity) based on reversible multimer staining with *Strep*Tamers [162]. This k_{off} rate assay allows the accurate measurement of monomeric pHLA dissociations from cell surface expressed TCRs. To measure k_{off} rates, *Strep*Tamers are first generated by multimerizing fluorochrome-conjugated (e.g. Atto488) pHLA molecules to fluorochrome-conjugated (e.g. APC) *Strep*Tactin backbones. This is achieved by a *Strep*-tag on the pHLA molecule that binds to *Strep*Tactin. T cells can then be stained with the resulting *Strep*Tamers. The *Strep*Tamer complex is subsequently disrupted by the addition of D-biotin, which binds to *Strep*Tactin with higher affinity than the *Strep*-tag. Dissociation of *Strep*Tactin from the pHLA molecules can be measured by a decrease in the fluorophore signal. This results in monomeric pHLA molecules that remain bound to the TCR. Dissociation of pHLA molecules (k_{off} rate) can subsequently be measured by a decrease in the pHLA fluorophore signal (Figure 4, center). K_{off} rates showed a strong correlation with the protective capacity of adoptively transferred T cells *in vivo* and may thus be a good predictor of actual TCR functionality [163].

1.7.2 TCR functional avidity

The functional avidity of a TCR describes the measurement of T cell peptide sensitivity, i.e. the degree of T cell activation at different peptide concentrations, as well as the measurement of cytotoxicity. By determining the half maximal effective concentration (EC_{50}), the functional avidity of different TCRs can be compared. The gold standard approach for peptide pulsing is to use autologous APCs from the same donor/patient. This approach is also used when the patient's HLA type is unknown. An established alternative to autologous APCs for antigen presentation is the use of tumor cell lines

with the correct HLA class I restriction, assuming the HLA type is known (Figure 4, right). If the correct HLA type is not present on the tumor cell line of interest, APCs can also be modified to express the matching HLA molecule. Antigen delivery can then be accomplished by either peptide pulsing or full-length mRNA transfection. It is important to note that EC_{50} values depend on the choice of APC and the mechanism of antigen loading [164].

A common method for detecting target cell killing of adherent cells is by measuring the change in cellular impedance as the cells are killed and detach from the surface of the well. Cellular impedance is measured using special 96-well plates with gold microelectrodes at the bottom of the wells. The gold microelectrodes act as conductors and can conduct the electrical current. By applying a small electrical current, the electrical flow from one microelectrode to the next is measured. Adherent cells act as insulators and alter the current flow. Consequently, if the addition of effector $CD8^+$ T cells results in killing of adherent cells, the detachment of dying cells can be measured by an increase in current. Furthermore, when cells undergo apoptosis, cellular proteins are degraded and nuclear DNA is fragmented. Therefore, another way to measure target cell death is by engineering target cells for the expression of a fluorescent protein. A decrease in the fluorescent signal can then be correlated with target cell killing.

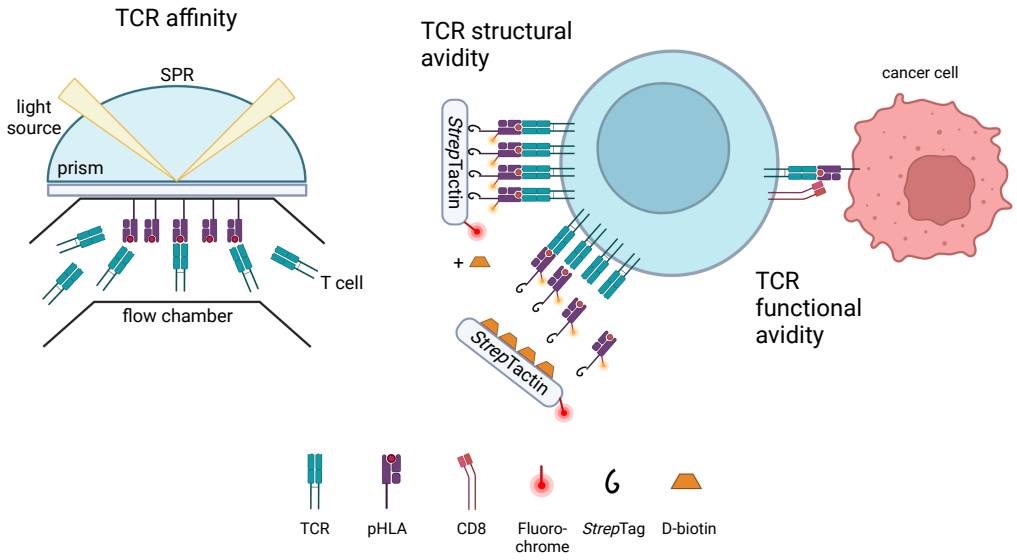

Figure 4: Functional TCR characterization. Schematic depiction of TCR affinity and TCR structural and functional avidity. SPR = surface plasmon resonance, TCR = T cell receptor, pHLA = peptide-human leucocyte antigen.

2 Aim of this thesis

Most patients infected with SARS-CoV-2 have a mild course of COVID-19. Similar to other acute viral infections, it has been found that after about two weeks the adoptive immune system has developed a functional immune response to eliminate all SARS-CoV-2-infected cells. In fact, humoral and cellular immune responses against SARS-CoV-2 are readily detectable after infection with the virus. The precise mechanisms describing $CD8^+$ T cell immunity, in particular the study of SARS-CoV-2-specific TCRs and the assessment of the quality of such a response, remain to be determined.

The aim of this work was to investigate $CD8^+$ T cell immunity against SARS-CoV-2 in convalescent COVID-19 patients with a mild course of disease. More specifically, our objectives were to:

- identify immunogenic SARS-CoV-2 epitopes
- isolate TCRs recognizing identified immunodominant SARS-CoV-2 epitopes
- decipher the quality of SARS-CoV-2-specific TCR repertoires through their re-expression and functional characterization

To study SARS-CoV-2-specific T cell responses, we first selected SARS-CoV-2 epitopes from HLA class I binding prediction tools as well as from literature, and established an antigen-specific expansion assay to facilitate the detection of low-frequency T cell populations. By monitoring responses to these epitopes over time, we were able to assess the persistence of T cell responses relative to antibody levels. Following this, we also evaluated the immunogenicity of individual epitopes.

To subsequently identify TCR sequences recognizing these epitopes, we performed single-cell RNA sequencing of SARS-CoV-2 peptide-responsive $CD8^+$ T cells. As a next step, we assembled TCR sequences *in silico*, PCR-amplified them as HDR constructs, and re-expressed them under the endogenous promoter in healthy donor PBMCs using a method known as orthotopic TCR replacement. This allowed us to functionally characterize these TCRs for affinity and avidity. For high-throughput characterization of TCR functionality, we further integrated SARS-CoV-2 TCRs into the Jurkat triple-parameter-reporter cell line and additionally analyzed the cellular avidity of TCRs. Interestingly, we found correlations between TCR functionality after re-expression and the transcriptomic profile of the parental cells from which the TCR was isolated.

Finally, we developed killing assays to evaluate the cytotoxic capacity of SARS-CoV-2-specific TCRs. To this end, we generated peptide-presenting HLA-matched target cells by infecting target cells with SARS-CoV-2 GFP virus, by transducing target cells with a SARS-CoV-2 ORF or by pulsing target cells with peptide. Subsequently, we tested the lysing efficiency of TCR-engineered $CD8^+$ T cells for the different target cell lines.

In summary, with this work we aimed to gain in-depth knowledge of $CD8^+$ T cell immunity against SARS-CoV-2 in mild convalescent COVID-19 patients and to perform detailed characterizations of SARS-CoV-2-specific TCRs to provide a framework for the selection of TCRs for therapy.

3 Material and methods

3.1 Material

3.1.1 Antibodies

Table 1: List of antibodies

Human Antigen	Fluorophore	Clone	Supplier*
CD19	ECD	J3-119	Beckman Coulter
CD3	APC	UCHT1	Life Technologies
CD3	APC-Cyanine7	UCHT1	BioLegend
CD3	BV421	SK7	BD Biosciences
CD3	Pacific Blue	OKT3	BD Biosciences
CD3	PE	UCHT1	Beckman Coulter
CD3	PE-Cyanine7	UCHT1	Beckman Coulter
CD45	ECD	J33	Beckman Coulter
CD45	eF450	2D1	eBioscience
CD45	PB	PB986	DAKO/Agilent, Santa Clara,USA
CD45	PE-Cyanine7	2D1	eBioscience
CD45	PO	HI30	Exbio, Prague, Czech Republic
CD8	FITC	B9.11	Beckman Coulter
CD8	PE	3B5	eBioscience
CD8α	APC	RPA-T8	BioLegend
CD8α	APC-eFluor 780	OKT8	eBioscience
CD8α	eFlour 450	OKT8	eBioscience
CD8α	PE	OKT8	eBioscience

CD8α	PE-Cyanine7	OKT8	eBioscience
HLA-A2	FITC	BB7.2	BD Biosciences
HLA-A3	APC	REA950	Miltenyi
HLA-B7	PE	BB7.1	BioLegend
HLA-B8	APC-Vio770	REA145	Miltenyi
HLA-ABC	Pacific Blue	W6/32	BioLegend
hTCR	FITC	FITC IP26	BioLegend
IFN-γ	FITC	25723.11	BD Biosciences
IFN-γ catch	FITC	25723.11	Miltenyi
IL-2	APC	5.344.111	BD Biosciences
TNFα	PE-Cyanine7	MAb11	eBioscience
murine TRBC	APC	H57-597	BioLegend
murine TRBC	APCFire750	H57-597	BioLegend
*Strep*Tavidin	APC		eBioscience

* BD Biosciences, Franklin Lakes, USA; Beckman Coulter, Brea, USA; BioLegend, San Diego, USA; eBioscience now Thermo Fisher Scientific, Ulm, Germany; Life Technologies now Thermo Fisher Scientific, Ulm, Germany; Miltenyi, Bergisch Gladbach, Germany

3.1.2 Biological samples

Table 2: List of biological samples

Biological sample	**Origin**	**Institute**
PBMCs	Asymptomatic seropositive and seronegative donors	Klinikum Rechts der Isar, Munich, Germany
PBMCs	Convalescent mild COVID-19 donors	Helios Clinic West, Munich, Germany; German Heart Center Munich, Germany; University Medicine Mannheim, Germany

PBMCs	Healthy volunteers	Institut for Medical Microbiology, Immunology, and Hygiene, Technical University Munich, Germany
PBMCs	Prepandemic donors	Institute for Transfusion Medicine, Dresden, Germany

3.1.3 Cell lines and bacteria

Table 3: List of cell lines and bacteria

Organism	**Purpose**	**Manufacturer**
A549-ACE2-H2B-RFP, competent A549 cells	Target cells	Kind gift from Pichlmair lab
competent HLA-A*03:01 A549 cells	Target cells	in-house
competent HLA-A*03:01 A549-Nsp2-GFP cells	Target cells	in-house
competent HLA-A*03:01 A549-Gaussia-GFP cells	Target cells	in-house
Jurkat-TPR	Effector cells	in-house
K562-HLA-A*01:01	Target cells	in-house
K562-HLA-A*02:01	Target cells	in-house
K562-HLA-A*03:01	Target cells	in-house
K562-HLA-A*11:01	Target cells	in-house
K562-HLA-B*01:01	Target cells	in-house
K562-HLA-B*35:01	Target cells	in-house
RD114	Retroviral packaging	in-house
E. coli Stbl3	Plasmid amplification	Thermo Fisher Scientific Waltham, USA

3.1.4 Chemicals and reagents

Table 4: List of chemicals and reagents

Compound	Supplier
1-Ethyl-3-methylimidazolium Dicyanamid, 98 %	Thermo Fisher Scientific, Ulm, Germany
2-Propanol	Roth, Karlsruhe, Germany
6x loading dye	Thermo Fisher Scientific, Ulm, Germany
aCD3/aCD28 Expamer	Juno Therapeutics/BMS, Munich, Germany
β-Mercaptoethanol	Roth, Karlsruhe, Germany
Agarose	Roth, Karlsruhe, Germany
Agencourt CleanSeq magnetic beads	Beckman Coulter, Brea, USA
Alt-R® Cas9 Electroporation Enhancer	IDT DNA, Coralville, USA
Alt-R™ HDR Enhancer v2	IDT DNA, Coralville, USA
Alt-R® S.p. HiFi Cas9 Nuclease V3	IDT DNA, Coralville, USA
Ampicillin	Roth, Karlsruhe, Germany
Biocoll Separating Solution	Merck Millipore, Darmstadt, Germany
Bovine Serum Albumin	Sigma, Taufkirchen, Germany
$CaCl_2$	Merck, Darmstadt, Germany
CRISPR/Cas9 tracrRNA	IDT DNA, Coralville, USA
DBCO-PEG4-Atto488/Biotin	Jena Bioscience, Jena, Germany
D-Biotin	Merck, Darmstadt, Germany
DMEM	Thermo Fisher Scientific, Ulm, Germany
DMSO	Merck, Darmstadt, Germany
dNTPs	Roche, Penzberg, Germany
DTT	Merck, Darmstadt, Germany
Dulbeccos Phosphate Buffered Saline	Merck, Darmstadt, Germany
Ethanol	Roth, Karlsruhe, Germany
Ethidium Monoazide	Molecular Probes, Leiden, Netherlands

Fetal Calf Serum	GE Healthcare, Chalfont St. Giles, UK
Gene ruler 1 kb DNA ladder	Thermo Fisher Scientific, Ulm, Germany
Gentamicin	Thermo Fisher Scientific, Ulm, Germany
Golgi-Plug	BD Biosciences, Franklin Lakes, USA
HCl	Roth, Karlsruhe, Germany
HEPES	Roth, Karlsruhe, Germany
Human serum	in-house production, xxx
Recombinant human Interleukin-2	Peprotech, Hamburg, Germany
Recombinant human Interleukin-7	Peprotech, Hamburg, Germany
Recombinant human Interleukin-15	Peprotech, Hamburg, Germany
Ionomycin	Merck, Darmstadt, Germany
LB agar & medium	in-house
L-Glutamine	Sigma, Taufkirchen, Germany
$MgCl_2$	Merck, Darmstadt, Germany
Natriumhydroxid, 98 %, reinst, pellets	Thermo Fisher Scientific, Ulm, Germany
Penicillin/Streptomycin	Thermo Fisher Scientific, Ulm, Germany
Phorbol myristate acetate	Merck, Darmstadt, Germany
Phytohaemagglutinin	Thermo Fisher Scientific, Ulm, Germany
Propidium Iodide	Merck, Darmstadt, Germany
Retronectin	Takara Bio, Shiga, Japan
Rotisafe Gel Stain	Roth, Karlsruhe, Germany
RPMI 1640 Gibco	Thermo Fisher Scientific, Ulm, Germany
Sodium Hypochlorite 5 % active chlorine	Thermo Fisher
Tris pH 8.5	in-house
Tris-HCl	Roth, Karlsruhe, Germany
Triton-X 100	Roth, Karlsruhe, Germany
Trypan blue	Roth, Karlsruhe, Germany
Trypsin-EDTA (0.25 %)	Thermo Fisher Scientific, Ulm, Germany
Tween® 20	Sigma, Taufkirchen, Germany

3.1.5 Consumables

Table 5: List of consumables

Item	Supplier
0.22 µm, 0.45 µm sterile filter	Kisker, Steinfurt, Germany
1.0 mL Sub-Q Spritzen	Kuhnle, Karlsruhe, Germany
1.0 mL, 1.5 mL 2.0 mL reagent tubes	Kuhnle, Karlsruhe, Germany
1.0 mL, 2.0 mL Cryo-vial	Th. Geyer, Renningen, Germany
1.5 mL LoBind-DNA reaction tube	Eppendorf, Hamburg, Germany
15 mL, 50 mL Falcon CELLSTAR®	Greiner Bio-One, Heidelberg, Germany
500 mL filtration system stericup (0.22 µm)	Kisker, Steinfurt, Germany
5 mL Polypropylene round-bottom tube	Greiner Corning, Durham, USA
5 mL Polystyrene round-bottom tube	Greiner Corning, Durham, USA
96-well V-plate	Kuhnle, Karlsruhe, Germany
C-Slide cell counting chamber slide	NanoEnTek, Seoul, South Korea
Culture flask 25 cm^2, 75 cm^2, 150 cm^2	Th. Geyer, Renningen, Germany
24-Well Plates, non-treated, Costar®	VWR, Radnor, USA
Cover plate	Greiner Bio-One, Heidelberg, Germany
E-Plate 96, E-Plate VIEW 96	OLS, Bremen, Germany
Parafilm	Merck, Darmstadt, Germany
PCR reaction tubes	Brand, Werthelm, Germany
Pipette filter tips (10 µL, 20 µL, 200 µL, 1 mL)	STARLAB, Hamburg, Germany
Serological pipettes (5 mL, 10 mL, 25 mL)	Greiner Bio-One, Heidelberg, Germany
Syringe (1 mL, 3 mL, 5 mL, 50 mL)	Braun, Melsungen, Germany
TipOne RPT Filter Pipette Tip (1 µL, 10 µL, 20 µL, 200 µL, 1 mL)	STARLAB, Hamburg, Germany
Tissue culture treated plates (6-, 12-, 24-, 48-, 96-Well)	Omnilab, Munich, Germany

3.1.6 Enzymes

Table 6: List of enzymes

Enzyme	Supplier
FastDigest EcoRI	Thermo Fisher Scientific, Waltham, USA
FastDigest NotI	Thermo Fisher Scientific, Waltham, USA
Herculase II	Stratagene, London, UK
T4 DNA ligase	Fermentas, St. Leon-Rot, Germany
Taq Polymerase	Thermo Fisher Scientific, Waltham, USA
Trypsin 0.25 %	SAFE Biosciences, Hampshire, UK

3.1.7 Equipment

Table 7: List of equipment

Equipment	Model	Supplier*
Automated Cell Counter	EVE™ PLUS	NanoEnTek, Seoul, South Korea
Balance	ACS/ ACJ 320-4M	Kern & Sohn, Balingen, GER
	EG 2200-2NM	Kern & Sohn, Balingen, GER
Bioanalyzer	2100 Bioanalyzer	Agilent, Santa Clara, USA
Centrifuges	Biofuge fresco	Heraeus, Hanau, GER
	Biofuge Stratos	Heraeus, Hanau, GER
	Multifuge 3 S-R	Heraeus, Hanau, GER
	Sorvall RC6+	Thermo scientific, Ulm, GER
	Varifuge 3.0RS	Heraeus, Hanau, GER
Electrophoresis chamber	PerfectBlue™ Gel System MiniL	Peqlab, Erlangen, GER
Electrophoresis power supply	EPS 600	Pharmacia Biotech, Uppsala, Sweden
FPLC	Äktapurifier™ Superdex 200 10/300 GL	GE Healthcare, Chalfont St. Giles, UK

Flow Cytometry analyzer	Cytoflex	Beckman Coulter, Brea, USA
	Cytoflex S	Beckman Coulter, Brea, USA
	MoFlo Astrios EQ	Beckman Coulter, Brea, USA
	BD FACSAria™ III Cell Sorter	BD Biosciences, Franklin Lakes, USA
Gel imaging system	MolecularImager® Gel Doc™ XR+	BioRad, München, GER
Heat block	Thermomixer compact	Eppendorf, Hamburg, GER
Ice maker	ZBE 30-10	Ziegra Eismaschinen, Isernhagen, GER
Incubator	HERAcell 240	Heraeus, Hanau, GER
Laminar flow hood	HERAsafe	Heraeus, Hanau, GER
Live-cell analyzer	Incucyte® S3 Live-Cell Analysis System	Satorius, Göttingen, GER
Magnet stand	DynaMag™-2	Thermo scientific, Ulm, GER
Microscope	Axiovert S100	Carl Zeiss, Jena, GER
Nanodrop device	ND-1000	Kisker, Steinfurt, GER
Sequencing device	NovaSeq 6000	Illumina, San Diego, USA
PCR Cycler	T3000 Thermocycler	Biometra, Göttingen, GER
pH-Meter	MultiCal pH 526	WTW, Weilheim, GER
RTCA analyzer	xCELLigence® RTCA MP	Agilent, Santa Clara, USA
	xCELLigence® RTCA eSight	Agilent, Santa Clara, USA
Thermocycler	SimpliAmp Thermocycler	Applied Biosystems, Darmstadt, GER
Transfection device	4D-Nucleofector™ Core Unit	Lonza, Basel, Switzerland
	4D-Nucleofector™ X-Unit	Lonza, Basel, Switzerland

	4D-Nucleofector™ Add-on	Lonza, Basel, Switzerland
Water bath	Type 1002	GFL, Burgwedel, GER
Cell Avidity Analyzer	Zmovi® Cell Avidity Analyzer	Lumicks, Amsterdam, Netherlands

Supplier*: GER Germany

3.1.8 Media and buffer

Table 8: List of media and buffer

Media and buffer	Composition
Antibiotics supplement (add 5 %)	20 mL Gentamicin
	200 mL Penicillin/Streptomycin
SC^+ (supplement complete with antibiotics)	1 mM β-Mercaptoethanol
	1 mg/mL Gentamicin
	23.83 g/L HEPES
	4.0 g/L L-Glutamine
	2,000 U/mL Penicillin-Streptomycin
SC^- (supplement complete without antibiotics)	1 mM β-Mercaptoethanol
	1 mg/mL Gentamicin
	23.83 g/L HEPES
	4.0 g/L L-Glutamine
Complete RPMI (cRPMI)	500 RPMI 1640
	25 mL SC^+
	50 mL FCS
Human serum RPMI (HS-RPMI)	35.71 mL RPMI 1640
	1.79 mL SC^+
	2.5 mL Human serum

RPMI SC^-	500 mL RPMI 1640
	25 mL SC^-
	50 mL FCS
Serum-free RPMI	500 mL RPMI 1640
	25 mL SC^+
Complete DMEM (cDMEM)	500 mL DMEM 1640
	25 mL SC^+
	50 mL FCS
FACS buffer	1x PBS
	0.5 % (w/v) BSA, pH 7.45
FACS-EDTA buffer	1x PBS
	0.5 % (w/v) BSA, pH 7.45
	2 mM EDTA
Freezing medium (FM)	90 % (v/v) FCS
	10 % (v/v) DMSO
Transfection buffer	100 mL H_2O
	0.27 M NaCl
	9.9 mM KCl
	3.5 mM Na_2HPO_4
	4.2 mM HEPES
LB-Ampicillin	1 L LB-medium
	100 mg/L Ampicillin

3.1.9 Molecular kits and standards

Table 9: List of molecular kits and standards

Kit/Standards	Supplier
Agencourt AMPure XP	Beckman Coulter, Brea, USA
BD Cytofix/Cytoperm	BD Biosciences, Franklin Lakes, USA
BigDye® Terminator v3.1 Cycle Sequencing RR-100	Applied Biosystems
Cell Trace™ Cell Proliferation Kit	Thermo Fisher Scientific, Ulm, Germany
Human IFN-γ Single-Color ELISPOT	Immunospot, Bonn, Germany
GeneRuler 1 kb DNA ladder	Thermo Fisher Scientific, Ulm, Germany
Herculase II Fusion Enzyme with dNTPs Combo	Agilent, Santa Clara, USA
High sensitivity DNA Kit	Agilent, Santa Clara, USA
P3 Primary Cell Nucleofector™ Kit	Lonza, Basel, Switzerland
SE Cell Line Nucleofector™ Kit	Lonza, Basel, Switzerland
Plasmid DNA MaxiPrep Kit	Thermo Fisher Scientific, Ulm, Germany
SV Miniprep DNA Purification System	Promega, Mannheim, Germany
Qubit™ dsDNA HS-Assay Kit	Thermo Fisher Scientific, Ulm, Germany
ReliaPrep DNA Cleanup and Concentration Kit	Promega, Mannheim, Germany

3.1.10 Oligonucleotides

Table 10: List of oligonucleotides

Name	Sequence	Supplier*
Alt-R® CRISPR/Cas9 crRNA TRAC antisense	AGAGTCTCTCAGCTGGTACA	IDT

Alt-R® CRISPR/Cas9 crRNA TRBC sense	GGAGAATGACGAGTGGACCC	IDT
Alt-R® CRISPR/Cas9 tracrRNA		IDT
HDR genomic fw primer	CTGCCTTTACTCTGCCAGAG	Merck
HDR genomic rv primer	CATCATTGACCAGAGCTCTG	Merck
Vector_ORF3a.FOR	CGACTACTAGCGTGCCTTTGGAGGGCAGAGGAA GTCTGCTAACATGC	Sigma
Vector_ORF3a.REV	AAACAAATCCATGGTGGCGGGCGGCCGCGGAT	Sigma
ORF3a.FOR	GTCGACGGATCCGCGGCCGCCCGCCACCATGGA TTTGTTTATGAGAATCT	Sigma
ORF3a.REV	AGCAGACTTCCTCTGCCCTCCAAAGGCACGCTA GTAGTCG	Sigma
Vector_Nsp2.FOR	CCTTCACACTCAAAGGCGGTGAGGGCAGAGGA AGT	Sigma
Vector_Nsp2.REV	AGTGTATGCCATGGTGGCGGGCGGCCGCGGAT	Sigma
Nsp2.FOR	GTCGACGGATCCGCGGCCGCCCGCCACCATGGC ATACACT	Sigma
Nsp2.REV	AGCAGACTTCCTCTGCCCTCACCGCCTTTGAGTG TGAAGG	Sigma
Vector_Gaussia.FOR	TCAAGGGGGCCGGTGGTGACGAGGGCAGAGGAA GTCTGCTAAC	Sigma
Vector_Gaussia.REV	AACTTTGACTCCCATGGTGGGCGGCCGCGGATCC	Sigma
Gaussia.FOR	GTCGACGGATCCGCGGCCGCCCGCCACCATGGGA GTCAAAGTTCTGTTTGC	Sigma
Gaussia.REV	AGCAGACTTCCTCTGCCCTCGTCACCACCGGCCC	Sigma

Supplier*: IDT DNA, Coralville, USA; Merck, Darmstadt, Germany; Sigma, Taufkirchen, Germany

3.1.11 Peptides

Table 11: List of peptides

Peptide	Sequence**	HLA type	IEDB	Supplier*
ORF1_AMD	**AMDEFIERY**	**HLA-A*01:01**	**-**	**P&E**
ORF1_DTD	**DTDFVNEFY**	**HLA-A*01:01**	**1311144**	**P&E**
ORF1_GTD	**GTDLEGNFY**	**HLA-A*01:01**	**1311156**	**P&E**
ORF1_LTN	**LTNIFGTVY**	**HLA-A*01:01**	**-**	**P&E**
ORF3a_FTS	**FTSDYYQLY**	**HLA-A*01:01**	**1309115**	**P&E**
S_CVA	CVADYSVLY**	HLA-A*01:01	7247	P&E
S_LTD	**LTDEMIAQY**	**HLA-A*01:01**	**1310623**	**P&E**
S_TSN	TSNQVAVLY	HLA-A*01:01	1087414	P&E
S_WTA	WTAGAAAYY	HLA-A*01:01	1327824	P&E
N_AQA	AQFAPSASA	HLA-A*02:01	3956	P&E
N_ILL	**ILLNKHIDA****	**HLA-A*02:01**	**27182**	**P&E**
N_LLL	**LLLDRLNQL****	**HLA-A*02:01**	**37473**	**P&E**
N_LQL	**LQLPQGTTL****	**HLA-A*02:01**	**38881**	**P&E**
ORF1_KLW	KLWAQCVQL**	HLA-A*02:01	32240	P&E
ORF3a_LLY	LLYDANYFL	HLA-A*02:01	1311180	P&E
S_ALN	**ALNTLVKQL****	**HLA-A*02:01**	**2801**	**P&E**
S_ELL	ELLHAPATV	HLA-A*02:01	1331642	P&E
S_FQF	FQFCNDPFL	HLA-A*02:01	1392157	P&E
S_HLM	HLMSFPQSA	HLA-A*02:01	1318059	P&E
S_KIA	**KIADYNYKL**	**HLA-A*02:01**	**1319519**	**P&E**
S_KVG	**KVGGNYNYL**	**HLA-A*02:01**	**-**	**P&E**
S_SII	SIIAYTMSL	HLA-A*02:01	1309137	P&E
S_TLD	TLDSKTQSL	HLA-A*02:01	1075075	P&E
S_VLN	**VLNDILSRL****	**HLA-A*02:01**	**69657**	**P&E**
S_VVF	**VVFLHVTYV****	**HLA-A*02:01**	**71663**	**P&E**
S_YLQ	YLQPRTFLL	HLA-A*02:01	1309147	P&E
N_KTF	KTFPPTEPKK**	HLA-A*03:01	33668	P&E
ORF1_ASM	**ASMPTTIAK**	**HLA-A*03:01**	**1310291**	**P&E**
ORF1_KLF	**KLFDRYFKY**	**HLA-A*03:01**	**1312859**	**P&E**
ORF1_KTI	KTIQPRVEK	HLA-A*03:01	1311176	P&E
ORF1_VTN	**VTNNTFTLK**	**HLA-A*03:01**	**1311232**	**P&E**
S_GVY	GVYFASTEK	HLA-A*03:01	1312627	P&E

S_KCY	KCYGVSPTK	HLA-A*03:01	1311170	P&E
S_QIY	QIYKTPPIK	HLA-A*03:01	1313344	P&E
S_RLF	**RLFRKSNLK**	**HLA-A*03:01**	**1075031**	**P&E**
S_VTY	VTYVPAQEK	HLA-A*03:01	1310928	P&E
M_ATS	ATSRTLSYYK	HLA-A*11:01	5150	P&E
M_LSY	**LSYFIASFR**	**HLA-A*11:01**	**1321267**	**P&E**
N_ATE	ATEGALNTPK**	HLA-A*11:01	4936	P&E
N_KTF	KTFPPTEPKK	HLA-A*11:01	33668	P&E
N_KTF	KTFPPTEPK	HLA-A*11:01	33667	P&E
ORF1_ASM	**ASMPTTIAK**	**HLA-A*11:01**	**1310291**	**P&E**
ORF1_KLF	**KLFDRYFKY**	**HLA-A*11:01**	**1312859**	**P&E**
ORF1_STF	**STFNVPMEK**	**HLA-A*11:01**	**1311591**	**P&E**
ORF1_TTI	**TTIKPVTYK**	**HLA-A*11:01**	**1313808**	**P&E**
ORF1_VTN	**VTNNTFTLK**	**HLA-A*11:01**	**1311232**	**P&E**
S_NSA	NSASFSTFK	HLA-A*11:01	1313244	P&E
S_RLF	RLFRKSNLK	HLA-A*11:01	1075031	P&E
S_TLK	TLKSFTVEK	HLA-A*11:01	1313756	P&E
M_SYF	**SYFIASFRL**	**HLA-A*24:02**	**1313718**	**P&E**
N_DYK	DYKHWPQIAQF	HLA-A*24:02	1310340	P&E
N_LSP	**LSPRWYFYY****	**HLA-A*24:02**	**39576**	**P&E**
ORF1_NYM	**NYMPYFFTL**	**HLA-A*24:02**	**1310703**	**P&E**
ORF1_VYI	VYIGDPAQL**	HLA-A*24:02	72048	P&E
ORF1_WSW	**WSMATYYLF**	**HLA-A*24:02**	**1313970**	**P&E**
ORF1_YFM	**YFMRFRRAF**	**HLA-A*24:02**	**1334348**	**P&E**
ORF3a_VYF	VYFLQSINF	HLA-A*24:02	1310934	P&E
S_GYQ	**GYQPYRVVVL****	**HLA-A*24:02**	**23436**	**P&E**
S_KWP	KWPWYIWLGF	HLA-A*24:02	1311572	P&E
S_NYN	NYNYLYRLF	HLA-A*24:02	1313269	P&E
S_PYR	**PYRVVVLSF****	**HLA-A*24:02**	**50166**	**P&E**
S_QYI	QYIKWPWYI	HLA-A*24:02	1310756	P&E
S_VYS	**VYSTGSNVF**	**HLA-A*24:02**	**1313944**	**P&E**
S_YFP	YFPLQSYGF	HLA-A*24:02	1075121	P&E
S_YYH	YYHKNNKSW	HLA-A*24:02	1328953	P&E
N_KPR	KPRQKRTAT	HLA-B*07:02	1311570	P&E
N_SPR	SPRWYFYYL**	HLA-B*07:02	60242	P&E
ORF1_KPN	**KPNELSRVL**	**HLA-B*07:02**	**1319902**	**P&E**

ORF1_KPV	**KPVETSNSF**	**HLA-B*07:02**	**-**	**P&E**
ORF1_RPD	RPDTRYVL	HLA-B*07:02	1311209	P&E
ORF1_VPM	**VPMEKLKTL**	**HLA-B*07:02**	**1310914**	**P&E**
S_FPQ	FPQSAPHGV	HLA-B*07:02	1316853	P&E
S_MIA	MIAQYTSAL	HLA-B*07:02	1313153	P&E
S_SPR	SPRRARSVA	HLA-B*07:02	1311590	P&E
ORF1_DLK	DLKGKYVQI	HLA-B*08:01	1310332	P&E
ORF1_FVK	**FVKHKHAFL**	**HLA-B*08:01**	**1310425**	**P&E**
ORF1_SLS	**SLSHRFYRL**	**HLA-B*08:01**	**-**	**P&E**
ORF1_YLK	**YLKLRSDVL**	**HLA-B*08:01**	**-**	**P&E**
S_EPV	EPVLKGVKL	HLA-B*08:01	1310371	P&E
S_FNA	FNATRFASV	HLA-B*08:01	-	P&E
S_INI	INITRFQTL	HLA-B*08:01	1318821	P&E
S_LIT	LITGRLQSL	HLA-B*08:01	36724	P&E
N_AQF	AQFAPSASA**	HLA-B*15:01	3956	P&E
ORF1_LVQ	LVQMAPISAM	HLA-B*15:01	1311576	P&E
ORF1_FAV	**FAVDAAKAY**	**HLA-B*35:01**	**1331939**	**P&E**
ORF1_HSI	**HSIGFDYVY**	**HLA-B*35:01**	**-**	**P&E**
ORF1_LVA	**LVAEWFLAY**	**HLA-B*35:01**	**1321432**	**P&E**
ORF1_NVL	**NVLEGSVAY**	**HLA-B*35:01**	**-**	**P&E**
ORF1_VPF	**VPFWITIAY**	**HLA-B*35:01**	**1326965**	**P&E**
S_LPF	LPFNDGVYF	HLA-B*35:01	1321049	P&E
S_QPT	QPTESIVRF	HLA-B*35:01	1323461	P&E
S_FAM	FAMQMAYRF	HLA-B*3501	1316310	P&E
S_IPF	IPFAMQMAY	HLA-B*3501	1318829	P&E
S_LGA	LGAENSVAY	HLA-B*3501	1320443	P&E
ORF1_GEA	GEAANFCAL	HLA-B*40:01	1311563	P&E
ORF1_GEV	GEVITFDNL	HLA-B*40:01	1311565	P&E
M_SEL	SELVIGAVIL	HLA-B*40:10	1075044	P&E
N_MEL	MEVTPSGTWL**	HLA-B*40:10	190494	P&E
S_YEQ	YEQYIKWPW	HLA-B*44:03	1311601	P&E
N_MEW	MEVTPSGTW**	HLA-B*44:10	190494	P&E
ORF1_SEF	SEFSSLPSY**	HLA-B*44:10	57432	P&E
M_NRF	NRFLYIIKL	HLA-C*07:02	1310684	P&E
N_QRN	QRNAPRITF	HLA-C*07:02	1309136	P&E
S_EYV	EYVSQPFLM	HLA-C*07:02	1316287	P&E

S_FRK	FRKSNLKPF	HLA-C*07:02	-	P&E
S_VRF	VRFPNITNL	HLA-C*07:02	70718	P&E

Sequence**: 100 % homology with SARS-CoV-1;

Supplier*: P&E, Peptides and Elephants, Potsdam, Germany;

Bold-printed peptides were part of the initial 9-mer peptide pool.

3.1.12 Sequencing antibodies

Table 12: List of sequencing antibodies

Antibody	Clone	Supplier
Total Seq-C antibody	0251	Biolegend, San Diego, USA
Total Seq-C antibody	0252	Biolegend, San Diego, USA
Total Seq-C antibody	0253	Biolegend, San Diego, USA
Total Seq-C antibody	0254	Biolegend, San Diego, USA
Total Seq-C antibody	0255	Biolegend, San Diego, USA
Total Seq-C antibody	0256	Biolegend, San Diego, USA

3.1.13 SARS-CoV-2-specific TCR sequences

Table 13: List of SARS-CoV-2-specific TCR sequences

TCR	Epitope	TRAV	TRAJ	TRA_1_cdr3	TRBV	TRBJ	TRB_1_cdr3
13	**ORF1_VTN**	**TRAV13-1**	**TRAJ47**	**CAAFGNKLVF**	**TRBV16**	**TRBJ1-5**	**CASSHSNSNQPQHF**
28	**ORF1_VTN**	**TRAV12-1**	**TRAJ31**	**CVVRNNNARLMF**	**TRBV9**	**TRBJ2-1**	**CASSVDGSSYNEQFF**
32	**ORF1_VTN**	**TRAV12-2**	**TRAJ9**	**CAPLGGRRGFKTIF**	**TRBV7-8**	**TRBJ2-1**	**CASSGGTSGSHNEQFF**
43	**ORF1_VTN**	**TRAV12-2**	**TRAJ17**	**CAVSGGRAAGNKLTF**	**TRBV7-9**	**TRBJ2-6**	**CASSAGSGANVLTF**
3398	**ORF3a_FTS**	**TRAV20**	**TRAJ35**	**CAVQAEGFGNVLHC**	**TRBV2**	**TRBJ2-2**	**CASSEPTSGELFF**
3399	**ORF3a_FTS**	**TRAV36 /DV7**	**TRAJ42**	**CAVETYGGSQGNLIF**	**TRBV13**	**TRBJ1-1**	**CASSAQGAGTEAFF**
3456	**ORF3a_FTS**	**TRAV38-2 /DV8**	**TRAJ38**	**CAYIYAGNNRKLIW**	**TRBV7-6**	**TRBJ2-1**	**CASSSDGGGFNEQFF**
5	ORF1_DTD	TRAV19	TRAJ47	CALSENGNKLVF	TRBV18	TRBJ1-1	CASSPGGGMNTEAFF
9	ORF1_DTD	TRAV19	TRAJ15	CALNQAGTALIF	TRBV18	TRBJ1-1	CASSRGGSMNTEAFF
21	ORF1_HSI	TRAV38-1	TRAJ13	CAPGGYQKVTF	TRBV27	TRBJ2-1	CASRAGMEQFF
38	ORF1_GTD	TRAV21	TRAJ6	CAVLSGGSYIPTF	TRBV6-6	TRBJ1-4	CASRDRGRIDEKLFF
58	ORF1_KLF	TRAV21	TRAJ44	CASESSKLTF	TRBV5-6	TRBJ2-5	CASGPGGGTQYF
62	ORF1_HSI	TRAV13-1	TRAJ32	CAASYGGATNKLIF	TRBV4-1	TRBJ2-3	CASSQVGGLFTDTQYF
65	ORF1_DTD	TRAV19	TRAJ47	CALSADGNKLVF	TRBV18	TRBJ1-2	CASSPGSGVTGYTF
66	ORF1_GTD	TRAV19	TRAJ37	CALPYSGNTGKLIF	TRBV7-7	TRBJ2-3	CASSLGLADPRGRTDTQYF
76	ORF1_DTD	TRAV19	TRAJ20	CALSEGDYKLSF	TRBV19	TRBJ2-3	CASSGGTDTQYF
85	ORF1_HSI	TRAV13-2	TRAJ12	CAENRDSSYKLIF	TRBV2	TRBJ2-2	CASSEAAGAVNTGELFF

455	ORF1_DTD	TRAV19	TRAJ29	CALTVPSGNTPLVF	TRBV10-3	TRBJ2-5	CAISTVRGMAYQETQYF
499	ORF1_ASM	TRAV12-1	TRAJ20	CVVNLNYKLSF	TRBV6-1	TRBJ2-1	CASSESGGENEQFF
523	ORF1_DTD	TRAV38-1	TRAJ48	CAFMNLISNFGNEKLTF	TRBV12-3	TRBJ2-3	CASSSQGTHPSDTDTQYF
560	ORF1_KLF	TRAV6	TRAJ33	CALNGMDSNYQLIW	TRBV28	TRBJ2-3	CASSPEAGALDTQYF
569	ORF1_STF	TRAV21	TRAJ9	CAGYTGGFKTIF	TRBV5-6	TRBJ2-7	CASTRWWAVREQYF
758	ORF1_DTD	TRAV19	TRAJ39	CALSENAGNMLTF	TRBV18	TRBJ1-1	CASSQGGGTEAFF
868	ORF1_DTD	TRAV19	TRAJ54	CALSEGSQKLVF	TRBV18	TRBJ2-1	CASSLAGGAGEQFF
1085	S_LTD	TRAV1-2	TRAJ34	CAVGTDKLIF	TRBV6-1	TRBJ1-2	CASSEQRGRDGYTF
1228	S_LTD	TRAV35	TRAJ22	CAGRLSGSARQLTF	TRBV4-1	TRBJ1-1	CASSQGGDDTEAFF
1862	ORF1_STF	TRAV21	TRAJ32	CAVYGGATNKLIF	TRBV5-4	TRBJ1-3	CASSLRSDLGNTIYF
1863	S_LTD	TRAV21	TRAJ58	CAVRFSKGTSGSRLTF	TRBV5-5	TRBJ2-3	CASSLLEPITDTQYF
1864	S_LTD	TRAV12-2	TRAJ52	CAVTNAGGTSYGKLTF	TRBV27	TRBJ2-3	CASSLSVHLDTQYF
1871	ORF1_STF	TRAV30	TRAJ22	CGTEAPHQSARQLTF	TRBV15	TRBJ1-6	CATRQSSYNSPLHF
1877	ORF1_FVK	TRAV10	TRAJ42	CVVSGGGSQGNLIF	TRBV6-6	TRBJ2-1	CASSYWVRVAGGTYNEQFF
1896	ORF1_VPF	TRAV41	TRAJ35	CATIGFGNVLHC	TRBV2	TRBJ1-2	CASKARDAYGYTF
1917	ORF1_VPF	TRAV13-1	TRAJ45	CAASLKSGGGADGLTF	TRBV20-1	TRBJ2-7	CSARPIVFTYEQYF
1951	ORF1_STF	TRAV17	TRAJ11	CATASSGYSTLTF	TRBV2	TRBJ2-5	CASKDSGTQETQYF
1968	S_LTD	TRAV1-1	TRAJ21	CAVGNFNKFYF	TRBV6-6	TRBJ2-7	CAASVGDSSSYEQYF
1996	ORF1_VPF	TRAV13-1	TRAJ47	CAARPMEYGNKLVF	TRBV11-2	TRBJ2-7	CASSALPLDRPPIEQYF
2056	ORF1_FVK	TRAV10	TRAJ42	CVVSGGGSQGNLIF	TRBV6-6	TRBJ2-5	CASTPVGGRETQYF

Bold-printed TCRs were part of the first scRNAseq experiment.

3.1.14 Vectors and viruses

Table 14: List of vectors and viruses

Backbone	**Insert**	**Antibiotica resistance**	**Viral system**	**Supplier**
pWPI	SARS-CoV-2-Nsp2	Puromycin	Lentivirus	Kind gift from Pichlmair lab
pWPI	humanized Gaussia luciferase (hGluc, Gaussia)	Puromycin	Lentivirus	Kind gift from Pichlmair lab
mp72	RNF43_A269fs-T2A-GFP		Retrovirus	Twist Bioscience, South San Francisco, USA
mp72	Nsp2-T2A-GFP		Retrovirus	in-house
mp72	Gaussia-T2A-GFP		Retrovirus	in-house
pMXs	HLA-A*03:01	Puromycin	Retrovirus	in-house
Virus				**Supplier**
SARS-CoV-2 GFP				in-house production (AG Pichlmair)

3.1.15 Software

Table 15: List of software

Software	Version	Supplier
Affinity Designer	1.10.5	Serif, Nottingham, UK
BioRender	2023	BioRender, Toronto, Canada
Cell Ranger	3.0.2/5.0.0	10X genomics, California, USA
CytExpert Software	2.4	Beckman Coulter, Brea, USA
FlowJo	10.8.1	Treestar, Ashland, USA
Graph Pad Prism	9.3.0	Graph Pad Software, La Jolla, USA
Hla-genotyper	0.4	
T cell epitope prediction tools		Immune epitope data base (IEDB)
Incucyte® S3 Software		Sartorius AG
matplotlib	3.1.3	
Microsoft Office		Microsoft, Redmond, USA
NETCTL	1.2	
NETHLA	4.0	
NetHLApan	4.1	
Netstab	1.0	
Oceon	1.4.1	Lumicks, Amsterdam, Netherlands
PickPocket	1.1	
RTCA xCelligence	2.0	ACEA Bioscience, San Diego, USA
Scanpy	1.4.3	
Scirpy	0.3	
scSplit	1.0	
seaborn	0.10.0	
SnapGene	6.0	GSL Biotech LLC, San Diego, USA
Souporcell	2.0	
uType software		Invitrogen/Thermo Fisher

3.2 Methodology

3.2.1 SARS-CoV-2 clinical samples

3.2.1.1 Study cohorts of SARS-CoV-2 patients

For the mild COVID-19 patient cohort, healthcare employees were included in the study when they experienced mild symptoms (cold, cough, and mild fever) and had a positive polymerase chain reaction (PCR) test on SARS-CoV-2 spike protein. Blood was collected at the Helios Clinic West Munich, German Heart Center Munich, and the University Medicine Mannheim. Participants donated 50 mL of blood at time points 4, 8, 12, and 24 weeks post COVID-19 infection. Critical data of participants: (female (f)/male (m)/unknown (u), 32/19/2; age ± SD, 40.5 ± 10.6 years). Asymptomatic participants were tested at the Klinikum Rechts der Isar, Munich for SARS-CoV-2-specific antibodies. Participants with a positive antigen test were included in the asymptomatic seropositive cohort (f/m/u, 18/10; age ± SD, 38.4 ± 13.5 years) and participants with a negative antigen test in the asymptomatic seronegative cohort (f/m/u, 23/14; age ± SD, 38.8 ± 13.6 years). Participants donated 10 mL of blood at two-time points between August and November 2020. Prepandemic samples of frozen PBMCs from healthy donors were collected between 2018 and 2019 at the Institute for Transfusion Medicine, Dresden (f/m/u, 12/10; age ± SD, 42.96 ± 12.9 years). All participants provided informed written consent. Approval for the study design and sample collection was obtained within the framework of the study 'Establishment and validation of epitope-specific SARS-CoV-2 blood-based testing methods' (EPI-SARS) by the ethics committee of the Technical University of Munich (reference number 182/20) and the Institutional Ethics Committee of the University Medicine Mannheim (reference number 2020-556N).

3.2.1.2 Serology

The analysis of anti-SARS-CoV-2 IgG antibodies was performed by the Diagnostic Department at the Institute for Medical Microbiology, Immunology, and Hygiene at the Technical University of Munich (TUM), Munich, Germany. Anti-SARS-CoV-2 IgG antibodies from mild COVID-19 and asymptomatic seropositive serum samples were measured at all time points. Antibody titers were determined using the iFlash SARS-CoV-2 (2019-nCoV) IgG antibody test (Shenzhen YHLO Biotech Co., Shenzhen, China) and the iFlash Immunoassay analyzer following the manufacturer's protocol. Briefly, serum samples were incubated with sample treatment solution and SARS-CoV-2 antigen-coated paramagnetic microparticles. After unbound material was washed from the solid phase, samples were incubated with acridinium-labeled anti-human IgG conjugate. Samples were washed, and the pre-Trigger and Trigger solutions were added to the reaction mix. As readout, the chemiluminescent reaction was measured with the iFlash optical system. The positive signal cutoff was calculated with SARS-CoV-2 IgG calibrators.

3.2.1.3 HLA genotyping

HLA genotyping was performed by collaborators at the Department of Clinical Chemistry, University Medicine Mannheim, Medical Faculty Mannheim of the University of Heidelberg, and by collaborators at the Laboratory of Immunogenetics and Molecular Diagnostics, Department of Transfusion Medicine, Cellular Therapeutics and Hemostaseology, LMU University Hospital, Munich.

For PCR amplification of complete HLA class I coding regions (HLA-A, -B and -C), 3 µL DNA product (10 - 50 ng/mL) were mixed with 3 µL forward and reverse primer mix (each

1.5 pmol/mL) and 5 µL LongAmp Tag 2x Master Mix. Amplification primers were located in the 5'- and 3'-untranslated regions of the HLA genes. PCR reaction was run on a SimpliAmp Thermocycler (94 °C for 7 min; 15 cycles: 94 °C for 1 min, 66 °C for 5 min; 30 cycles: 94 °C for 10 s, 65 °C for 50 s, 72 °C for 5 min; hold at 20 °C). Successful amplification was verified by loading 5 µL of PCR product on a 1 % agarose gel (130 V, 30 min).

For sanger sequencing, 5 µL 1:20 diluted amplification product were mixed with 5 µL Reaction Mix (composed of 0.5 µL BigDye® Terminator v3.1 Cycle Sequencing RR-100, 1.9 µL Q-solution and 2.6 µL water) and 5 µL of homemade sequencing primers (exon 1-7; 2.5 pmol/mL). PCR reaction was run on a 3130xl Genetic Analyzer (Applied Biosystems, Darmstadt, GER). Cycle sequencing assays were performed with a 100-fold approach by a Biomek NXP pipetting roboter (Beckman Coulter). PCR was run in a SimpliAmp Thermocycler (94 °C for 2 min, 30 cycles 94 °C for 10 s, 60 °C for 2 min, hold at 20 °C) and PCR products were purified using Agencourt CleanSeq magnetic beads in a Biomek NXP protocol following the manufacturer's instructions. After importing sequence raw data in the uType software, the sequences were analyzed for HLA type creation by aligning to the recent IMGT HLA allele database.

For asymptomatic seropositive and seronegative donors, the HLA type was determined via surface antibody staining.

3.2.1.4 Epitope prediction

The prediction tool NetMHC4.0 was used to predict the HLA class I binding strength to peptides of 8 - 11 amino acids in length of all ORFs from the Wuhan-Hu-1 reference sequence (NC_045512). The selection focused on the most prominent HLA types in the Caucasian population (HLA-A*01:01, HLA-A*02:01, HLA-A*03:01, HLA-A*11:01, HLA-A*24:02, HLA-B*07:02, HLA-B*08:01, HLA-B*35:01). All peptides with predicted binding strength < 50 nM were analyzed for immunogenicity, TAP transport, proteasomal cleavage, and processing using Netstab (V 1.0), NETCTL (V 1.2), PickPocket (V 1.1), and NetMHCpan (V 4.1). Peptides with the highest immunogenicity score were subsequently investigated for sequence homology to SARS-CoV-1, MERS, and common cold coronaviruses HCoV-OC43 (NC_006213), HCoV-HKU1 (NC_006577), HCoV-NL63 (NC_005831) and HCoV-229E (NC_002645). Peptides unique to SARS-CoV-2 and with the highest overall prediction score were ordered for synthesis for the in-house peptide pool. IEDB published SARS-CoV-2 epitopes and immunogenic epitopes homolog to SARS-CoV-1 (NC_004718) were added to the peptide pool.

3.2.2 Cell culture

3.2.2.1 Cell culture of primary T cells and cell lines

Suspension cell lines used in this thesis were the erythroleukemia cell line K562, used for antigen presentation, and the T cell leukemia cell line Jurkat triple parameter reporter (J-TPR), used for TCR characterization. Both suspension cell lines were cultivated in Roswell Park Memorial Institute medium (RPMI) complemented with 5 % SC^+ and 10 % fetal calf serum (FCS) (complete RPMI, cRPMI) at a density of $0.1 - 2 \times 10^6$ cells/mL. Cells were split every 2 - 4 days when a density of $1 - 2 \times 10^6$ cells/mL was reached (1:10 or 1:20).

Adherent cell lines used in this thesis were RD114, used for the production of retroviral particles, and the lung epithelial carcinoma cell line A549, used for functional assays. For the production of retroviral particles, RD114 cells were previously transfected with the pMP71 expression vector (containing the HLA heavy chain construct, gag/pol and amphotropic envelope). Both adherent cell lines were cultivated in Dulbecco's Modified Eagle medium (DMEM) complemented with 5 % SC^+ and 10 % FCS (complete DMEM, cDMEM). Cells were split when they

reached a confluency of 70 % - 90 %. For this, cells were first washed once with phosphate-buffered saline (PBS) without Ca^{2+}/Mg^{2+} to remove traces of serum. Following, trypsin was added to the cells, and the flask was placed in the incubator for 5 min to enable the detachment of the cells from the surface. Cells were washed off the plate with warm cDMEM to inactivate trypsin, and pelleted through centrifugation (1500 rpm, 5 min). Cells were washed once more with fresh cDMEM and centrifuged. After this, cells were counted and reseeded at an appropriate density in T75 flasks ($0.5 - 2 \times 10^6$ cells for RD114 cells and $0.1 - 0.5 \times 10^6$ cells for A549 cells).

All cells were cultivated at 37 °C, 5 % CO_2 in humidified incubators unless indicated otherwise. For freezing of cells, freezing medium (90 % FCS, 10 % dimethyl sulfoxide (DMSO)) was added to the cell pellets, and the cell suspensions were placed in cryovial tubes in Mr. Frosty containers to ensure optimal cooling speed of 1 °C/min to -80 °C. Cells were left at -80 °C or moved to -172 °C liquid nitrogen tanks for long-term storage. Cells were thawed by placing cryovial tubes into a 37 °C water bath until a small piece of ice remained. The cell suspension was then added to 10 mL of warm medium, washed once, and placed in the incubator at an appropriate density.

3.2.2.2 Isolation of PBMCs from whole blood

Biocoll gradient was performed according to the manufacturer's protocol (Merck Millipore). Briefly, whole blood was diluted 1:2 to 1:3 with PBS. Blood-PBS mixture was then carefully layered on 15 mL Biocoll solution and centrifuged for 15 min at 1000 x g at room temperature (RT) with break turned off. The PBMC layer was isolated into a 50 mL tube. The tube was then filled up with PBS, and PBMCs were washed twice by centrifugation. Cells were counted and put into culture for subsequent assays or frozen (see 3.2.2.1).

3.2.2.3 Activation of PBMCs and J-TPR cells for CRISPR

Freshly isolated PBMCs were seeded at a density of 1×10^6 cells/mL in cRPMI supplemented with 300 U/mL IL-2, 5 ng/mL interleucin-7 (IL-7), 5 ng/mL interleucin-15 (IL-15) and 1.5 µL/1×10^6 cells CD3/CD28 expamer [165]. PBMCs were stimulated in the incubator (37 °C, 5 % CO_2) for two days. For exponential growth conditions, Jurkat TPR cells were split two to three days before the CRISPR experiment to a concentration of 0.1×10^6/mL.

3.2.2.4 Antigen-specific T cell expansion and stimulation

Donor PBMCs were expanded with autologous peptide-pulsed PBMCs. For this, 20 % of PBMCs were pulsed with 10 µg/ml peptide at a concentration of 1×10^6 cells/mL for 2 h at RT in RPMI supplemented with 5 % SC^+ and 5 % human serum (HS) (HS-RPMI) under constant rotation on a shaker. Following pulsing, PBMCs were washed with fresh HS-RPMI three times and cocultured with the remaining 80 % of PBMCs at a final concentration of 1×10^6 cells/mL with addition of 50 U/mL IL-2. Fresh IL-2 (50 U/mL) was added every three to four days to the culture. Cells were expanded for twelve to 14 days before functional assays were performed. Following expansion, cells were restimulated with peptides to identify recently activated antigen-specific T cell populations in flow cytometry-based assays for cell sorting. For this, PBMCs were stimulated at a concentration of 1×10^6 cells/mL with 1 µg/mL peptide for 4 h at 37 °C, 5 % CO_2 in a humidified incubator.

3.2.2.5 Feeder cell expansion of TCR transgenic CD8 T cells

SARS-CoV-2-specific TCR-engineered $CD8^+$ T cells (see 3.2.5) were sorted for transgenic TCR expression on day five post CRISPR editing via mTRBC expression by flow cytometry (see

3.2.3.1). In brief, cells were sorted in 1 mL FCS in 15 mL Falcon tubes. After sorting, the tubes were filled up with HS-medium, inverted thoroughly, and centrifuged (1500 rpm, 5 min). The supernatant was removed, and the cells were put in culture in 200 µL HS-medium supplemented with 1 µg/mL phytohaemagglutinin (PHA) and 180 IU/mL IL-2 at a final concentration of 1×10^6 cells/mL. If less than 200,000 cells were sorted, the volume was filled up with irradiated feeder cells to reach 200,000 cells. For this, feeder cells from an allogeneic donor were irradiated with 35 Gy and adjusted to a concentration of 6×10^6 cells/mL to only add a small amount of extra volume. After seven days, 100 µL of medium were removed and 100 µL of fresh HS-RPMI + 1 µg/mL PHA + 180 IU/mL IL-2 were added. Cells were expanded by transferring the entire volume to the next bigger plate every two to three days with the addition of fresh medium supplemented with 1 µg/mL PHA and 180 IU/mL IL-2 (final concentration) as soon as the medium turned yellow, indicative of celluluar metabolism. As soon as the cells were transferred to a 6-well plate, only IL-2 was added to let the cells rest from PHA stimulation for one week before functional assays were performed.

3.2.3 Flow cytometry and cell sorting

3.2.3.1 Surface marker and intracellular cytokine staining

For surface staining, an appropriate volume of cells was taken out of the culture and centrifuged for 3 min, 1500 rpm, 4 °C in a 96-well V-plate. Cell pellets were resuspended in 200 µL cold FACS buffer, and one additional washing step was performed. After this, surface staining was performed for 20 min on ice, protected from light with respective antibody mixes. Up to 2×10^6 cells were stained in 50 µL. For live/dead discrimination, propidium iodide (PI) was added (1:100) to the cells and incubated for one additional minute. Cells were washed 2 x in FACS buffer, filtered through a 1 µm nylon mesh, and acquired at the Cytoflex or Cytoflex S flow cytometry analyzer. For intracellular cytokine staining, after an initial washing step in FACS buffer, cells were stained with EMA for live/dead discrimination (1:1000) for 15 min on ice in bright light. Following surface staining, cells were permeabilized with Cytofix/Cytoperm for 20 min on ice, protected from light. Cells were washed twice in 1 x Perm/Wash buffer and then stained with antibodies for intracellular markers for 30 – 45 min on ice, protected from light. After two more washing steps, cells were filtered through a 1 µm nylon mesh and acquired at the Cytoflex or Cytoflex S flow cytometry analyzer.

3.2.3.2 Fluorescent activated cell sorting

For fluorescent activated cell sorting (FACS), cells were stained for surface markers as described above (see 3.2.3.1) and resuspended at a maximum concentration of 20×10^6 cells/mL. Immediately before the sort, PI (1:100) was added to the cells, and cells were filtered to ensure the viability of all sorted cells and single-cell suspension, respectively. Cells were sorted at MoFlo Astrios EQ or BD FACSAria™ III Cell Sorter.

For sorting of antigen-specific $CD8^+$ T cells via the capturing of secreted IFN-γ on the cell surface, IFN-γ catch assays were performed following antigen-specific T cell expansion according to manufacturer's protocol (Miltenyi). All volumes refer to 1×10^6 cells/mL. PBMCs were stimulated as described in 3.2.2.4. Following stimulation, cells were washed with 1 mL cold FACS-EDTA buffer (PBS, 0.5 % (w/v) BSA, pH 7.45 + 2 mM EDTA) and centrifuged for 5 min, 1500 rpm, 4 °C. Cells were resuspended in 90 µL cold HS-RPMI and 10 µL IFN-γ catch reagent and incubated for 5 min on ice. As the expected number of IFN-γ secreting cells was < 5 %, 1 mL of warm HS-RPMI was added after the incubation. For IFN-γ capturing, cells were incubated for 45 min at 37 °C, 5 % CO_2 in a humidified incubator by inverting the tube every

5 min. The cells were then put on ice, washed with cold FACS-EDTA buffer (by filling up the tube), and centrifuged for 5 min, 1500 rpm, 4 °C. For surface staining, cells were resuspended in 90 µL antibody mix in FACS-EDTA buffer and 10 µL anti-IFN-γ FITC-conjugated detection antibody for 10 min on ice, protected from light. Following incubation, cells were washed with 2 mL cold FACS-EDTA buffer and centrifuged. IFN-γ expressing cells were acquired at a Cytoflex or Cytoflex S flow cytometry analyzer or sorted at the MoFlo Astrios EQ or BD FACSAria™ cell sorters.

3.2.3.3 Generation of pHLA Class I monomers and functionalized FLEXamers

All pHLA multimers were produced in-house as previously described [162,166]. Briefly, recombinantly expressed and purified *Strep*-tagged human HLA-A*01:01, HLA-A*02:01, HLA-A*03:01, HLA-A*11:01, HLA-B*08:01, and HLA-B*35:01 heavy chains and β2 microglobulin were denatured in urea before refolding into heterotrimeric pHLA complexes in the presence of respective excess peptide. Correctly folded pHLA monomers were purified by size exclusion chromatography on the fast protein liquid chromatography (FPLC) ÄKTApure, concentrated and stored at -80 °C or in liquid nitrogen [162, 167].

pHLA functionalization was performed via a tubulin tyrosine ligase (TTL) catalyzed ligation. The TTL reaction was performed in 25 µL - 100 µL reaction volume consisting of 20 µM FLEXamer, 5 µM TTL, and 1 mM 3-azido-L-tyrosine in TTL-reaction buffer (20 mM MES, 100 mM KCl, 10 mM $MgCl_2$, 2.5 mM ATP, and 5 mM reduced glutathione) at 25 °C for 3 h. Following buffer exchange to 20 mM Tris HCl and 50 mM NaCl (pH 8) by size-exclusion, azido-FLEXamers were stored at 4 °C or directly used for click functionalization. Azido-FLEXamers were click-functionalized by incubation of 20 µM azido-FLEXamer with either 400 µM DBCO-PEG4-Biotin or 400 µM DBCO-PEG4-Atto488 for 18 h at 16 °C. After buffer exchange to 20 mM Tris, 50 mM NaCl (pH 8), functionalized FLEXamers were stored at -80 °C [166].

3.2.3.4 pHLA multimer staining

For non-reversible multimer staining, 0.4 µg biotinylated pHLA were multimerized on 0.1 µg BV421-conjugated *Strep*Tavidin backbone in 50 µL for 30 min on ice, protected from light. Following multimerization, up to 5×10^6 cells were incubated with 50 µL BV421-conjugated *Strep*Tavidin for 45 min on ice, protected from light. Surface antibody staining was started after 25 min of *Strep*Tavidin incubation. After incubation, cells were washed 3 x in FACS buffer, filtered through a 1 µm nylon mesh, and acquired at the Cytoflex or Cytoflex S flow cytometry analyzer.

3.2.3.5 Measurement of TCR:pHLA dissociation rates (k_{off}-rate assays)

For reversible *Strep*Tamer staining, 1 µg Atto488-conjugated pHLA molecules were multimerized on 1 µL *Strep*Tactin APC-conjugated backbone for 30 min on ice, protected from light. Maximum cell numbers for multimerization and surface staining were the same as for non-reversible multimer staining. After *Strep*Tamer and antibody staining, up to 5×10^6 cells were resuspended in 200 µL FACS buffer. 2 mM D-biotin solution was freshly prepared and stored on ice until use, protected from light. Immediately before measurement, cells were filtered into polypropylene FACS tubes, and PI was added (1:100). Following PI incubation, 800 µL of FACS buffer were added, and cells were acquired at Cytoflex or Cytoflex S flow cytometry analyzer. After 30 sec, 1000 µL of 2 mM biotin solution were added. K_{off} rates were measured for 15 min at an acquisition speed of 133 µL/min.

3.2.4 Molecular biology techniques

3.2.4.1 Bacterial transformation and miniprep

For bacterial transformation, competent E. coli Stbl3 cells were taken out of a -80 °C freezer and thawed on ice. Once thawed, 1 µL of 10 µg/µL diluted plasmid DNA was added, and the plasmid-cell suspension was mixed by gentle pipetting and incubated for 30 min on ice. Following incubation, cells were heat shocked at 42 °C for 30 sec (1 min for volume > 50 µL), placed on ice for 2 min and plated on Amp LB agar plates. After overnight incubation at 37 °C, plates were stored at 4 °C. For Miniprep, clones were picked in 3 mL LB-Ampicllin medium and incubated shaking for 18 h at 37 °C. Miniprep was performed according to the manufacturer's protocol (Promega) and eluted in 30 µL - 50 µL H_2O.

3.2.4.2 Gibson assembly of SARS-CoV-2 and control ORFs

For the generation of endogenously processed and presented peptides, the pWPI_SARS-CoV-2-Nsp2 plasmid, and the pWPI_Gaussia plasmid were kindly gifted by the Pichlmair laboratory (3.1.14). By Gibson Assembly, the SARS-CoV-2 protein Nsp2 and the control protein Gaussia were cloned into the mp72 backbone. Transcriptional coupling of SARS-CoV-2 Nsp2 with green fluorescent protein (GFP) via a T2A linker ensured polycistronic expression and post-transcriptional separation of the two proteins. Despite the ectopic expression of the target protein, this system provides the expression of the entire ORF as well as natural peptide cleavage and epitope presentation on HLA class I complexes.

Backbone digestion by restriction enzymes

The mp72_RNF43_A269fs plasmid (2 µg) was cut with FastDigest restriction enzymes NotI (2 µL) and EcoRI (2 µL) at 37 °C for 15 min in the presence of Fast digest buffer (10x, 10 µL) in a total reaction volume of 50 µL after which the enzymes were thermally inactivated at 80 °C for 5 min. The resulting mp72 backbone and the RNF43_A269fs insert were separated on a 1 % agarose gel (45 min, 120 V), and the band containing the mp72 backbone (4564 bp) was cut for subsequent gel purification with the ReliaPrep DNA Cleanup and Concentration Kit. The backbone fragment concentration was measured by nanodrop.

Amplification of ORFs by PCR

The inserts used for Gibson Assembly were amplified by PCR from different plasmids with customized Gibson primers (table 16, P1 and P2). PCRs were run depending on the length of the amplified region (elongation time = t_el) and the annealing temperature (Tm) of the primers. Since the overlapping regions of eGFP were different for the final plasmids, eGFP DNA was PCR amplified in separate reactions (table 16, PCR #2, PCR #4).

Table 16: Setup of Gibson fragment amplification

Cloning	PCR #	Original plasmid	amplified region	P1	P2	amplicon length [bp]	T_amp	Tm	t_el
Nsp2-GFP	1	pWPI_SARS_CoV-2-Nsp2	nsp2 ORF	Nsp2.FOR	Nsp2.REV	2012	71	66	60
Nsp2-GFP	2	mp72_RNF43_A269fs	eGFP	Vector_Nsp2.FOR	Vector_Nsp2.REV	829	70	65	30
Gaussia-GFP	3	pWPI_Gaussia	hGluc	Gaussia.FOR	Gaussia.REV	650	71	66	30
Gaussia-GFP	4	mp72_RNF43_A269fs	eGFP	Vector_Gaussia.FOR	Vector_Gaussia.REV	829	70	65	30

P1 = Primer 1, P2 = Primer 2, Tm = melting temperature, T_amp = annealing temperature, t_el = elongation time

For the PCR reaction (table 17), the DNA template (30 ng) was mixed together with 1.25 µL primer 1 (P1, 10 µM), 1.25 µL primer 2 (P2, 10 µM), 0.5 µL dNTPs (25 mM each dNTP), 10 µL 5x Herculase II rct buffer, 0.5 µL Herculase II fusion DNA polymerase and ddH_20 to a final reaction volume of 50 µL.

Table 17: PCR cycling conditions of Gibson assembly

Step	Temperature	Duration	# of cycles
Denaturation	95 °C	2 min	1
Denaturation	95 °C	20 s	
Annealing	Primer Tm -5 °C [1)]	20 s	30
Elongation	72 °C	30 sec for $<$ 1 kb, 30 sec per kb for $>$ 1 kb [2)]	
Final Elongation	72 °C	3 min	1
Final hold	4 °C	∞	

1) Primer Tm for the different PCRs can be found in table 16.

2) Elongation time (t_el) for the respective PCR can be found in table 16.

Gibson assembly

For Gibson cloning, 100 ng of backbone were added to 3:1 excess of inserts (table 18). Gibson assembly was performed at 50 ° for 15 min with 0.02 – 0.5 pmols of fragments, and 10 µL of Gibson assembly master mix (2 x). The reaction was filled up to 20 µL with ddH_2O. Competent Stbl3 cells were transformed with 2 µL of Gibson assembly product, respectively (see 3.2.4.1).

Table 18: Molecular ratio calculation of Gibson assembly

Final plasmid	DNA fragments	Size [bp]	Required DNA mass [3:1]
Mp72_SARS-CoV-2-Nsp2_T2A_GFP	PCR 1	2012	132,3 ng
	PCR 2	829	54,49 ng
	backbone	4564	100 ng
Mp72_Gaussia_T2A_GFP	PCR 3	650	42,73 ng
	PCR 4	829	54,49 ng
	backbone	4564	100 ng

3.2.5 Genome engineering via CRISPR/Cas9

3.2.5.1 DNA template design

TCRs were assembled *in silico* according to the following structure: 5' homology arm, P2A linker, TCR beta chain with murine constant region, T2A linker, TCR alpha chain with murine constant region, bovine growth hormone polyadenylation signal (bGHpA), 3' homology arm. For enhanced surface expression, constant regions of both transgenic TCR chains contained an additional cysteine bridge [153]. Synthesized TCR constructs were provided by Twist Biosciences in a reexpression vector with ampicillin resistance.

3.2.5.2 Generation of dsDNA HDR template

Lyophilized plasmids containing transgenic TCR constructs for CRISPR/Cas9-mediated integration via HDR (2 µg) were reconstituted with 80 µL ddH_2O. The concentration was measured by Nanodrop, and plasmids were diluted to 10 ng/µL for bacterial transformation (see 3.2.4.1). The HDR template-containing plasmids were mixed together with the PCR master mix (table 19) and amplified by PCR (table 20).

Table 19: HDR PCR master mix

Reagent	**Final concentration**	**Amount (for 100 µL reaction)**
PCR grade water	n/a	65 µL
5x Herculase II Reaction Buffer	1x	20 µL
hTRAC HDR genomic forward primer (10 mM)	0.4 mM	4.0 µL
hTRAC HDR genomic reverse primer (10 mM)	0.4 mM	4.0 µL
dNTPs (10 mM)	0.5 mM	5.0 µL
Herculase II Fusion DNA Polymerase	1.0 %	1.0 µL
DNA (prediluted to 60 ng/µL)	600 ng/mL	1.0 µL
Total	**n/a**	**100 µL**

Table 20: PCR cycling conditions of HDR PCR

Steps	**Temperature**	**Time**	**Cycle**
Initial Denaturation	95 °C	3 min	1
Denaturation	95 °C	30 s	
Annealing	62 °C	30 s	34 cycles
Extension	72 °C	3 min	
Final extension	72 °C	3 min	1
Hold	4 °C	unlimited	

To confirm the purity of the amplified product, 2 µL of the PCR product were mixed with 6 x loading dye and ddH_2O to a final volume of 10 µL and run on a 1 % agarose gel (130 V, 45 min). Gene ruler 1 kb DNA ladder was run for size reference for HDR DNA template (∼ 2800 bp).

HDR constructs were purified with the Agencourt AMPure XP PCR purification system. In brief, beads were allowed to reach RT for 30 min and mixed thoroughly for 1 min by vortexing. PCR samples were transferred to a 1.5 mL LoBind-DNA reaction tube and Ampure XP beads were added in a 1:1 ratio. The reaction was mixed by pipetting and incubated for 5 min at RT. The tube was then placed on a magnetic stand for 3 – 5 min until the solution became clear. The supernatant was carefully removed by pipetting, after which tubes were removed from the magnetic stand. The beads were resuspended with 200 µL 70 % EtOH and tubes were placed back onto the magnetic stand for 3 - 5 min. The supernatant was removed, and one more washing step was repeated. The beads were dried for 3 min and resuspended in 22 µL 10 mM Tris buffer pH 8.5 to elute DNA from beads. The tubes were placed on the magnetic stand and incubated for 5 min. The supernatant was collected and the concentration of the HDR templates was measured by Nanodrop. Purified HDR templates were stored at -20 °C.

3.2.5.3 RNP production

In preparation for the production of Cas9 RNPs, hTRAC CRISPR RNA (crRNA), hTRBC crRNA and the trans-activating crRNA (tracrRNA) were diluted to 80 µM, while the electroporation enhancer was diluted to 400 µM with nuclease-free duplex buffer.

To generate assembled guide RNAs (gRNAs) (40 µM), equal amounts of crRNA hTRAC (stock: 80 µM) or crRNA hTRBC (stock: 80 µM) were annealed with tracrRNA (stock: 80 µM) at 95 °C for 5 min and let allowed to cool down to RT. gRNAs were stored on ice if not used immediately. 20 µM electroporation enhancer (stock: 400 µM) was added to TRAC or TRBC gRNAs, respectively. Cas9 (stock: 61 µM) was diluted to 6 µM or 20 µM with PBS for electroporation of 1×10^6 cells or $> 5 \times 10^6$ cells and stored on ice if not used immediately. Final RNPs were generated by adding equal volumes of Cas9 to gRNAs and incubation for 15 min at RT.

3.2.5.4 CRISPR/Cas9-mediated TCR KI

Activated cells (see 3.2.2.3) (up to 50 mL) were centrifuged, resuspended in 1 mM D-biotin solution (25 mL, 50 mL falcon tube) and incubated for 20 min at RT. Cells were then washed by filling up the tube with PBS and centrifuged (1500 rpm, 8 min). Two more washing steps were performed, one with 30 mL PBS and one with 30 mL cRPMI. Cells were then counted, split into different conditions and placed in the incubator at 37 °C, 5 % CO_2 until electroporation.

For electroporation, hTRAC RNPs, hTRBC RNPs (3 µL for 1×10^6, 1 µL for $> 5 \times 10^6$ cells) and HDR template (1 µg/1×10^6 cells) were incubated together for at least 30 sec at RT. In the meantime, cells were centrifuged and resuspended in appropriate volumes of P3 buffer (PBMCs) or SE buffer (J-TPR cells) (20 µL per 1×10^6) and added to assembled RNPs. Cells were then transferred either into 96-well nucleofection (1×10^6 cells) plates or nucleocuvette™ vessels ($> 5 \times 10^6$ cells) and electroporated with the program EH-100. PBMCs were transferred into prewarmed plates or flasks containing RPMI-SC$^-$ with addition of 180 IU/mL IL-2 at a concentration of 1×10^6 cells/mL. J-TPR cells (1×10^6 cells) were transferred into U-bottom plates with 0.5 µM HDR enhancer in a final volume of 175 µL cRPMI for 18 h overnight. After transfer into medium, cells were placed in the incubator (37 °C, 5 % CO_2). For PBMCs, antibiotics supplement (5 %) was added into culture 12 - 16 h post electroporation. For J-TPR cells, HDR enhancer was removed the following day by centrifugation, and cells were resuspended in fresh cRPMI.

3.2.6 Genome engineering via retroviral transduction

3.2.6.1 Transfection of RD114 cells via calcium precipitation

Depending on the time of seeding and cell batch proliferation, 0.8 - 1.2 x 10^6 RD114 cells were seeded per well in a 6-well plate to reach 30 – 50 % confluency on the next day. Transfection buffer was prepared earlier and stored in small aliquots at -20 °C. 3.31 M $CaCl_2$ solution was prepared immediately before transfection and filtered through 0.22 µm PVDF filters. All reaction steps described in the following refer to one well of a 6-well plate. The plasmid DNA-$CaCl_2$ solution was prepared by first adding 18 µg of plasmid DNA to ddH_2O (final volume: 150 µL), followed by 15 µL of $CaCl_2$ solution. 150 µL of transfection buffer were added to a polystyrene round-bottom tube. The plasmid DNA-$CaCl_2$ solution was then slowly added to the transfection buffer under vortexing. Following, the plasmid-transfection solution was incubated for 30 min at RT, vortexed once in between, and eventually added dropwise to RD114 cells. After 6 h, the medium was exchanged with 3 mL cRPMI. The retrovirus-containing supernatant was harvested after 48 h and filtered through 0.45 µm PVDF filters.

Table 21: Cell line generation via calcium precipitation

Plasmid	Target cell line
pMXs_HLA-A*01:01	A549-ACE2-H2B-RFP
pMXs_HLA-A*03:01	A549-ACE2-H2B-RFP
Mp72_SARS-CoV-2-Nsp2_T2A_GFP	A549-ACE2-H2B-RFP-HLA-A*03:01
Mp72_Gaussia_T2A_GFP	A549-ACE2-H2B-RFP-HLA-A*03:01

3.2.6.2 Transduction of cell lines with retroviral particles

The retronectin stock solution (1 µg/µL) was diluted 1:100 in PBS to reach a concentration of 0.01 µg/µL. Costar® non-treated 24-well plates were incubated with 400 µL/well retronectin overnight in the fridge or for 2 h at RT. After incubation, retronectin solution was removed, and wells were washed with 1 mL of PBS. Retrovirus was added to the plates and centrifuged for 1 h at 2,000 g, 32 °C. 1 x 10^5 target cells were added to retrovirus-containing wells and centrifuged for 30 min at 2,000 g, 32 °C after which the plates were placed in the incubator (37 °C, 5 % CO_2). After 24 h, the cells were washed once with 1 mL of PBS, detached by trypsinization (see 3.2.2) with 0.2 mL of trypsin, and transferred to a cell culture flask. After three days, GFP expression was checked by flow cytometry (see 3.2.3.1) and GFP^+ cells were sorted by FACS (see 3.2.3.2).

3.2.6.3 Selection for target gene expressing cells

For the A549-ACE2-H2B-RFP-HLA-A*03:01 (competent HLA-A*03:01 A549 cells) and cell line, the antibiotic selection was performed with 3 µg/mL puromycin for at least one week with the addition of fresh puromycin after every cell passage. For SARS-CoV-2-Nsp2_T2A_GFP and Gaussia_T2A_GFP transduced cell lines, the selection was performed by sorting via GFP^+ expression (see 3.2.3.2).

3.2.7 Functional assays

3.2.7.1 Antigen-specific activation of T cells and Jurkat cells

HLA-matched K562 cells were pulsed with a factor 10 peptide titration series from 10^{-4} M to 10^{-12} M of the respective peptide. For activation assays with PBMCs, K562 cells were peptide-pulsed for 4 h at 37 °C, 5 % CO_2 at a concentration of 3×10^6/mL. Following incubation, K562 cells were washed three times, and 50,000 K562 cells were coincubated at an effector to target ratio (E:T) of 1:1 with 50,000 mTRBC$^+$ TCR-transgenic CD8$^+$ T cells for 4 h. The readout of T cell activation was intracellular cytokine staining of IFN-γ, IL-2, and TNF-α. In the case of J-TPR cells, K562 cells were irradiated with 80 Gy before peptide-pulsing overnight at 37 °C, 5 % CO_2. On the next day, K562 cells were washed three times and coincubated at an E:T of 1:1 as described above with effector cells for 18 h. Readout of J-TPR TCR activation was achieved by coupling of T cell activation transcription factor (NFAT, NF-kB, and AP-1) response elements to fluorescent reporter molecules (GFP, CFP, mCherry, respectively) [168].

3.2.7.2 Cellular avidity measurements

The here-described protocol for cellular avidity measurements is according to the protocol provided by Lumicks (Oceon 1.4.1) and own protocol improvements. This protocol only summarizes individual steps and does not explain the details of chip handling. A dry 37 °C incubator was used for microfluid chip storage and incubation times. HLA-matched K562 cells were used as target cells and SARS-CoV-2-specific TCR-engineered J-TPR cells as effector cells. For optimal performance, all cell lines were split to 0.1×10^6 cells/mL three days before the experiment. Chips were activated with 400 µL of 1 M NaOH for 10 min at RT. For this, NaOH was pulled in the chip until only 10 µL NaOH were left in the reservoir. Chip activation was followed by two washing steps with 400 µL ddH_2O during which air was introduced. A third washing step was performed with 400 µL ddH_20 until 10 µL ddH_20 were left in the reservoir. For chip coating, a 5 mg/mL concanavalin A (ConA) working solution was prepared in PBS. Chips were subsequently coated with 100 µL ConA solution at 37 °C for 1 h or overnight. After chip coating, ConA was removed by flushing 200 µL warm PBS through the chamber twice with 10 µL of PBS remaining in the reservoir. PBS was exchanged to serum-free medium by flushing through 100 µL warm medium with 10 µL of medium remaining in the reservoir. After this, chips were ready for seeding and left in the 37 °C dry incubator with the lid screwed on to prevent evaporation.

Target cells were adjusted to a concentration of 60×10^6 cells/mL in serum-free medium, and 15 µL were used per chip for seeding. The remaining cell solution in the reservoir after seeding was removed, and the reservoir was washed three times with serum-free medium. Chips were incubated for 30 min in a 37 °C dry incubator, after which medium exchange was performed with 200 µL warm cRPMI. Chips were then incubated for 60 min. For on-chip peptide pulsing, 100 µL of 10^{-4} M peptide dilution were flushed into the chip with 10 µL of solution remaining in the reservoir and incubated for 30 min in a 37 °C dry incubator. After 30 min, 200 µL of cRPMI were flushed through twice with 10 µL remaining in the reservoir. Effector cells were stained with cell trace far red (CTFR) dye according to the manufacturer's instructions. CTFR dye was reconstituted in 20 µL DMSO, and required amounts were diluted 1/1000 with warm PBS. Exemplary, 1×10^6 effector cells were washed once with PBS in a 15 mL tube and resuspended with 1 mL diluted CTFR dye. Cells were incubated for 15 min (37 °C, 5 % CO_2) and resuspended once in between. Staining was then stopped by filling up the tube with warm cRPMI and centrifugation. Cells were resuspended at a concentration of 1×10^6 cells/mL and placed in the incubator (37 °C, 5 % CO_2) until measurement. On each chip, up to four measurements were performed. For this, 15 µL of effector cells were added to the reservoir and flushed onto the

target cells. The effector to target cell incubation was set to 5 min, after which a force ramp was applied from 0 pN to 1000 pN. Effector cells were then washed out, and target cells were ready for the next measurement. Data were analyzed with the Ocean software (V 1.4.1) and Prism (V 9.3.0).

3.2.7.3 Incucyte killing assay

A549 target cells were previously transduced with the viral entry protein ACE2 and with Histone2B-red fluorescent protein (RFP) for live cell imaging (A549-ACE2-H2B-RFP, competent A549 cells) by collaborators at the Pichlmair laboratory, Institute of Virology, TUM. Incucyte killing assays with viable SARS-CoV-2 virus were performed in collaboration with the Pichlmair laboratory under BSL-3 conditions.

Briefly, competent HLA-matched A549 target cells were detached by trypsinization, and 0.5×10^3 cells were seeded in cRPMI in 100 µL per well in a 96-well plate. 24 h post seeding, SARS-CoV-2-GFP virus (MOI 5) was added to the target cells in 100 µL cRPMI and the plate was placed in the Incucyte S3 instrument (37 °C, 5 % CO_2). Real-time images of non-infected (RFP channel) and infected cells (GFP channel) were captured every 3 h for 72 h. 24 h post infection, 100 µL of medium were removed and SARS-CoV-2 TCR-engineered $CD8^+$ T cells were added to the plate in an E:T titration from 0.1 to 10. T cells were added in 100 µL of fresh cRPMI with the addition of 100 IU/mL IL-2 (final concentration: 50 IU/mL). As controls, we used SARS-CoV-2 TCR-engineered $CD8^+$ T cells added on top of target cells without virus addition. Plates were placed back in the Incucyte S3 instrument, and the acquisition was continued for an additional 48 h. At the endpoint (72 h), the supernatant and T cells were removed by washing the wells carefully once with PBS. Fresh medium was added, and final pictures were acquired. Analysis was performed with the Incucyte® S3 software.

3.2.7.4 xCELLigence killing assay

HLA-matched competent A549 cells were detached by trypsinization, pulsed with 10^{-5} M of the respective peptide for 2 h at RT at a concentration of 3×10^6 cells/mL. Cells were then washed three times and 8×10^3 to 1×10^4 cells were seeded in 100 µL cRPMI. After detachment by trypsinization, competent HLA-A*03 A549-Nsp2-GFP or competent HLA-A*03 A549-Gaussia-GFP cells were seeded directly on the E-Plate 96 or E-Plate VIEW 96. Plates were placed in an xCELLigence RTCA MP or xCELLigence RTCA eSight instrument (37 °C, 5 % CO_2), and impedance measurement and image acquisition were performed every 15 min, 1 h, respectively, for 72 h. 24 h post target cell addition, 100 µL of medium were removed and SARS-CoV-2-specific TCR-engineered $CD8^+$ T cells were added to the plate in an E:T titration from 0.1 to 10 in 100 µL cRPMI + 100 IU/mL IL-2 (final concentration: 50 IU/mL IL-2). The plates were placed back in the xCELLigence instrument and impedance measurement (and image acquisition) was continued for an additional 48 h. As negative controls, we used SARS-CoV-2 TCR-engineered $CD8^+$ T cells added to competent A549 cells. As a positive control, 2 % Triton X was added to target cells. Analysis was performed with the RTCA xCELLigence (V 2.0).

3.2.8 Single-cell RNA sequencing and data analysis

3.2.8.1 Sample barcoding and preparation for 10x genomics

After a twelve to 14-day expansion of antigen-reactive cells and fresh restimulation with 1 µg/mL peptide for 2 h (see 3.2.2.4), followed by IFN-γ catch assay (see 3.2.3.2), samples were stained with hashtag antibodies for barcoding and subsequent pooling. Specifically, 2×10^6 cells were stained with 0.5 µg (1 µL) of each TotalSeq-C hashtag antibody in 50 µL FACS buffer and incubated for 30 min on ice. Subsequently, cells were washed 2 x with FACS buffer and stained for surface marker expression (see 3.2.3.1). Cells were sorted sequentially in the same well with the MoFlo Astrios EQ instruments. For the first single cell RNA sequencing experiment, 2„500 $CD8^+$ IFN-γ^+ cells and 10,000 $CD8^+$ IFN-γ^- cells were sorted for each donor. For the second single cell RNA sequencing experiment, only IFN-γ^+ cells were sorted. After sorting, cells were centrifuged, and the supernatant was removed carefully. Cells were resuspended in 37.2 µL mastermix and 37.8 µL ddH_2O and 70 µL of cell suspension were transferred to Chromium Next GEM Chip K.

3.2.8.2 10x genomics for single-cell RNA sequencing

Sample processing for 10x genomics was performed according to the manufacturer's protocol (Chromium next GEM Single Cell VDJ V1.1, Ref D). The quality control was performed with the high sensitivity DNA Kit on the Bioanalyzer 2100 instrument, and the quantification of libraries was performed with the Qubit dsDNA hs assay kit. All pipetting steps were performed with RPT filter tips in DNA LoBind tubes. For sequencing, libraries were pooled according to minimal required read counts (20,000 reads/cell for gene expression libraries, 5,000 reads/cell for TCR libraries). The HiSeq2500 instrument (28 + 91 bp) or the NovaSeq 6000 instrument (2 x 150 bp) were used for Illumina paired end sequencing for the first and second experiment, respectively. Annotations against the human genome (GRCh38, GRCh38-2020-A) and the corresponding VDJ reference (vdj_GRCh38_alts_ensembl-3.1.0, vdj_GRCh38_alts_ensembl-5.0.0) were performed with Cell Ranger (V 3.0.2, 10x genomics) and Cell Ranger (V 5.0.0, genomics) for the first and the second experiment, respectively.

3.2.8.3 Data pre-processing of single-cell RNA sequencing

Data pre-processing was performed according to Lueken & Theis, 2019 [169] and analysis with SCANPY [170]. Individual steps will be explained briefly in the following. Cells were excluded when the gene count was < 200 when genes were counted in less than three cells, and when mitochondrial genes were $> 20\,\%$. In addition, a cut-off was applied for the maximum number of counts (Exp 1: 50,000, Exp 2: 40,000) and the maximum number of genes (Exp 1: 7,000, Exp 2: 6,000). As the following steps, counts per cell were normalized and logarithmic values were computed. The variance was then scaled to the unit variance and zero mean. The number of counts, percentage of mitochondrial genes, and cell cycle score were regressed out, and highly variable genes were identified and filtered. Batch correction of individual donors was done with the batch-balanced k nearest neighbor (bbknn). Donor reallocation was done using scSplit [171] and HLA-genotyper/gene score for Y chromosome genes (`https://www.uniprot.org/docs/humchry.txt`) for the first experiment, and souporcell [172] together with barcoded antibodies for the second experiment. To allocate donors to clusters derived from scSplit demultiplexing, an HLA score was introduced considering all predictions and original genotypes.

3.2.8.4 Clonotype definition from single-cell RNA sequencing data

Clonotype analysis was performed using scirpy [173]. Cells with identical α and β chain CDR3 nucleotide sequences were defined as belonging to the same clonotype. TCRs were excluded when more than one TCR α or TCR β chain sequences were present.

3.2.8.5 Definition of gene signatures

The functionality signature was defined based on top genes correlating to experimentally determined EC_{50} values of re-expressed SARS-CoV-2-specific TCRs (r squared > 0.5, slope > 0.1). For the reactivity score, genes were first ranked per group using a t-test. Enriched genes were then selected based on TCRs that had a measurable EC_{50} value after re-expression (-log10(p-value) > 250). For the CD8 activation score, the published gene-ontology CD8 activation score GO: 0036037 was used.

3.2.9 Quantification and statistical analysis

Initial data analysis was performed using FlowJo (V 10.8.1), Oceon (V 1.4.1), Incucyte® S3 Software, RTCA xCELLigence (V 2.0). Statistical and correlation analyses were performed with GraphPad Prism (V 9.3.0) and stat.linregress method from the scipy (V 1.4.1) module. Data were displayed using GraphPad Prism (V 9.3.0), FlowJo (V 10.8.1), seaborn (V 0.10.0), and matplotlib (V 3.1.3) packages in Python. Significance was defined as *p-value < 0.05, **p-value < 0.01,***p-value < 0.001, ****p-value < 0.0001.

4 Results

4.1 Identification of SARS-CoV-2-specific T cells

4.1.1 Detection of SARS-CoV-2-specific T cells *ex vivo*

To study T cell responses against SARS-CoV-2, PBMCs from convalescent COVID-19 patients with a mild course of disease (mild COVID-19 patients) were used. To identify SARS-CoV-2-specific T cells *ex vivo*, PBMCs were stimulated with either the PepTivator S peptide pool or the in-house 9-mer peptide pool. The PepTivator S peptide pool consists of peptides of 15 amino acids in length (15-mers) covering predicted immunodominant domains of the SARS-CoV-2 spike (S) glycoprotein. Due to their length, peptides from the PepTivator S pool are predominantly presented on HLA class II complexes and are therefore expected to stimulate mainly $CD4^+$ T cells. Peptides from the in-house 9-mer peptide pool were selected based on their binding strength to HLA class I complexes and therefore expected to stimulate $CD8^+$ T cells. Other selection criteria included immunogenicity, TAP trafficking, proteasomal cleavage, and peptide processing (see 3.2.1.4). A total of 41 peptides were selected, twelve of which were homologous to SARS-CoV. The selected peptides were part of the open reading frames S, ORF1ab, N, M and E and were predicted to bind to nine highly prevalent HLA class I molecules (Table 11).

For *ex vivo* detection of SARS-CoV-2-specific T cells, we set the detection limit at 0.01 % IFN-γ^+ expressing T cells. After *ex vivo* stimulation, we detected IFN-γ^+ expressing $CD4^+$ / $CD8^-$ T cells to PepTivator S stimulation in 38 % of donors (eight responders, 13 non-responders) but IFN-γ^+ expressing $CD8^+$ T cells only in 19 % of donors (four responders, 17 non-responders) (Figure 5). This observation aligned with our expectation that the PepTivator S peptide pool predominantly stimulates $CD4^+$ T cells. After *ex vivo* stimulation with the in-house 9-mer peptide pool, the detection of INF-γ^+ $CD4^+$ and $CD8^+$ T cells was at the limit of detection with even lower frequencies than PepTivator S reactive T cells (Figure 5).

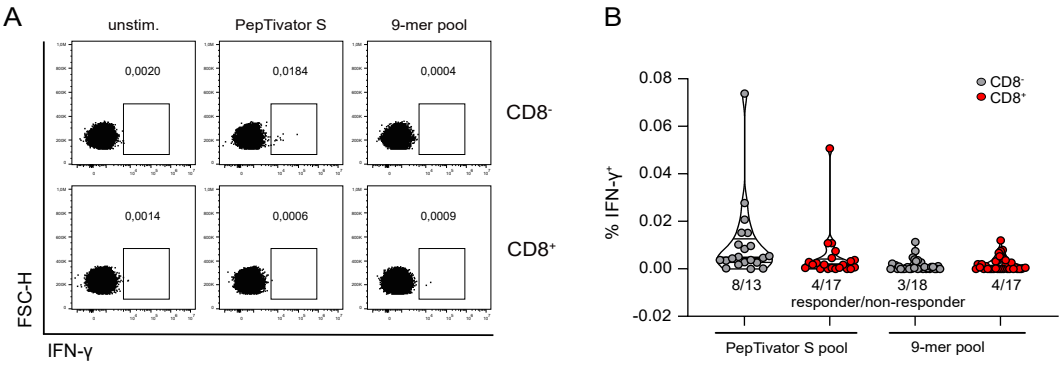

Figure 5: *Ex vivo* detection of SARS-CoV-2-specific T cells in mild COVID-19 patients.] (A) Representative flow cytometry plots and (B) quantification of IFN-γ expression of $CD8^+$ and $CD8^-/CD4^+$ T cells following *ex vivo* PepTivator S and 9-mer peptide pool stimulation. The figure was reprinted with permission from [84].

Because the 9-mer peptide pool contained fewer peptides than the PepTivator S peptide pool (estimated: 121 peptides), fewer activated antigen-specific T cells were expected. In addition, the frequency of $CD8^+$ T cells in the measured PBMCs was lower than that of $CD4^+$ T cells by a factor of 1/2 to 1/4. Limited initial sample material also affected the amount of SARS-CoV-2-specific T cells detected *ex vivo*. A combination of these factors most likely resulted in a low frequency of SARS-CoV-2-specific T cell responses after PepTivator S and 9-mer peptide pool stimulation. Importantly, positive responses were detected in very few individuals, with most remaining below the *ex vivo* detection limit. We can conclude that SARS-CoV-2-specific T cell responses for both peptide pools, PepTivator S and 9-mer, are at the limit of detectability.

4.1.2 Detection of SARS-CoV-2-specific CD8+ T cells after antigen-specific expansion

The frequency of $CD8^+$ T cells specific for the 9-mer peptide pool was very low *ex vivo* and also below the detection limit in most patients, making the analysis of SARS-CoV-2-specific $CD8^+$ T cells infeasible. To increase the sensitivity of detection of SARS-CoV-2-specific $CD8^+$ T cells, we adopted an *in vitro* expansion protocol originally developed for the expansion of SARS-CoV-specific T cells [174]. Specifically, SARS-CoV-2-specific $CD8^+$ T cells were selectively expanded with peptide-pulsed autologous APCs for twelve days in the presence of low levels of IL-2 (see 3.2.2.4). To assess the efficacy of this protocol, PBMCs from the same patient were stimulated with peptides and stained for intracellular cytokine expression before and after expansion. While SARS-CoV-2-specific $CD8^+$ T cells were below the detection limit before expansion, SARS-CoV-2-specific IFN-γ^+ $CD8^+$ T cells could be reliably detected after expansion in all patients tested. Furthermore, we detected low background levels of unstimulated cells and no significant increase in the frequency of SARS-CoV-2-specific $CD8^-$ T cells, demonstrating the specificity of this expansion assay (Figure 6).

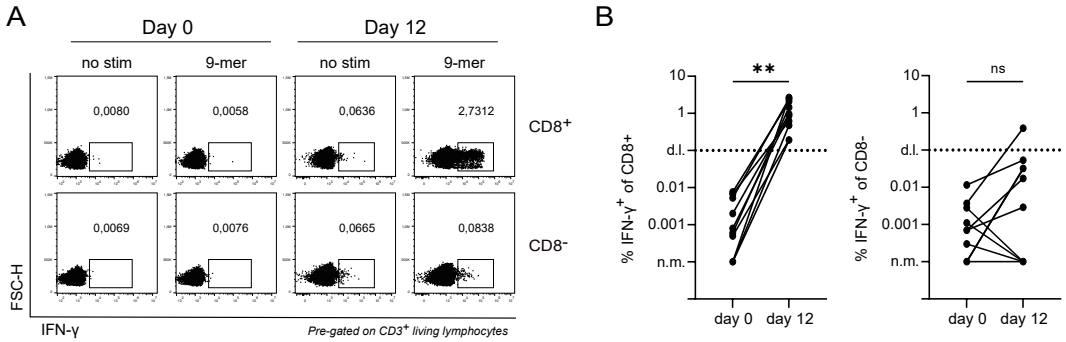

Figure 6: Expansion of SARS-CoV-2-specific $CD8^+$ T cells. For expansion of SARS-CoV-2-specific $CD8^+$ T cells, 20 % of PBMCs were pulsed with 10 µg/mL 9-mer peptide mix for 2 h at RT and then added to the remaining 80 % of PBMCs in culture at a concentration of 1×10^6 cells/mL in the presence of 50 U/mL IL-2. On day twelve of expansion, PBMCs were restimulated with 1 µg 9-mer peptide mix, and IFN-γ production was measured by intracellular cytokine staining. (A) Representative flow cytometry plots and (B) frequency of IFN-γ^+ expressing $CD8^+$ and $CD8^-$ T cells at day 0 and day 12 after expansion. (B) Day 0 and day 12-time points of each donor are connected by a black line. Paired-nonparametric Wilcoxon test was used to calculate the significance (**p-value < 0.01; ns, not significant). The figure was reprinted with permission from [84].

After establishing the *in vitro* expansion protocol with a selected number of donors (n = 10), we extended the analysis to PBMCs from all 44 patients in the mild COVID-19 patient cohort. We observed frequencies of SARS-CoV-2-specific $CD8^+$ T cells ranging from 0.1 % to more than 20 % of total $CD8^+$ T cells (Figure 7A). Regardless of the strength of the response after expansion, all donors with a frequency greater than 0.1 % IFN-γ^+ $CD8^+$ T cells after background subtraction were considered responders. In addition to mild COVID-19 patients, SARS-CoV-2-specific $CD8^+$ T cells from the asymptomatic seropositive and asymptomatic seronegative donor cohorts were also evaluated. Donors from both cohorts did not show typical symptoms SARS-CoV-2 infection, and previous exposure to the virus was detected by antigen testing. To investigate the potential cross-reactivity of 9-mer peptides, we also tested SARS-CoV-2-specific $CD8^+$ T cell responses in pre-pandemic donors.

Most patients in the mild COVID-19 and asymptomatic seropositive cohorts had detectable $CD8^+$ T cell responses after expansion. We found that the frequency of responders was very similar between symptomatic and asymptomatic seropositive donors (77 % and 78 %, respectively). Interestingly, the range of responses was also similar between the two cohorts, despite differences in the course of disease. The fact that the asymptomatic donor material was expanded fresh, whereas mild COVID-19 PBMCs were expanded frozen, did not result in differences in peptide response. Because the 9-mer peptide pool specifically expands $CD8^+$ T cells, $CD8^-$ T cells for the mild COVID-19 and asymptomatic seropositive cohorts showed mostly no detectable responses, even though they had a similar trend to $CD8^+$ T cells, but lower by a factor of 10 on the log scale. As expected, the asymptomatic seronegative and pre-pandemic donor cohorts showed lower $CD8^+$ T cell reactivity to the 9-mer peptide pool expansion with detectable responses in only 25 % and 32 % of the donors, respectively (Figure 7B). In addition, it was striking that the responses of pre-pandemic donors were much lower than those of asymptomatic seronegative donors, suggesting that some asymptomatic seronegative donors may have been exposed to the virus but tested antigen-negative. The observation that some pre-pandemic donors reacted to 9-mer SARS-CoV-2 peptides suggested the possibility of cross-reactivity with other viral epitopes to which the immune system had been exposed during previous infections.

We can conclude that we detected $CD8^+$ T cell responses to the 9-mer peptide pool after *in vitro* expansion in the majority of mild COVID-19 and asymptomatic seropositive donors, whereas the control groups, asymptomatic seronegative and pre-pandemic donors, showed only minor responses.

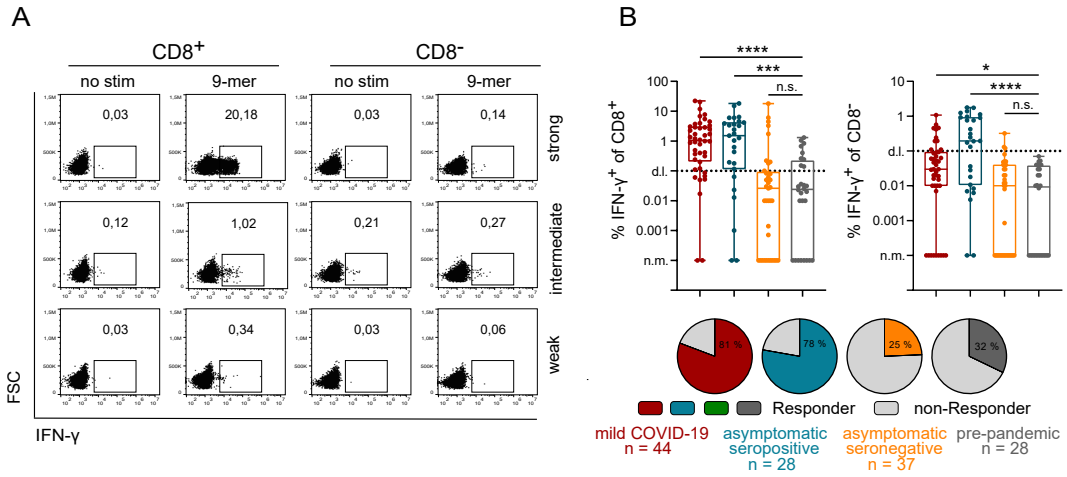

Figure 7: SARS-CoV-2-specific T cell responses of different patient cohorts after expansion. (A) Representative flow cytometry plots of IFN-γ^+ $CD8^+$ and $CD8^-$ T cells after expansion for no stimulation (no stim) control and 9-mer peptide stimulation for a strong, intermediate and weak responder. Cells were pregated based on lymphocytes, singlets, living, and $CD3^+$. (B) (Top) IFN-γ^+ responses of SARS-CoV-2 patient cohorts (mild COVID-19 and asymptomatic seropositive) and the control groups (asymptomatic seronegative and pre-pandemic) after expansion of $CD8^+$ (left) and $CD8^-$ T cells (right). Data are shown in a box and whiskers plot - min to max, all points shown. The box includes the 25th to the 75th percentile, and the middle line marks the median value. Statistical analyses were performed via one-way ANOVA with the Kruskal-Wallis test (*p-value < 0.05, ***p < 0.001, ****p < 0.0001). (Bottom) Pie charts of $CD8^+$ T cell responses of different patient cohorts. Responders are depicted in respective colors, and non-responders in light grey. The figure was reprinted with permission from [84].

4.1.3 HLA distribution of patient cohorts

The responsiveness of the different patient cohorts to the 9-mer peptide pool depends on the HLA types of the donors. To evaluate possible bias in the number of responders due to different HLA distributions in the different cohorts, we analyzed the HLA coverage per cohort. Overall, the HLA distribution of the patient cohorts (Figure 8B - E) showed comparable frequencies to the allele frequencies in the German population (Figure 8A), with HLA-A*02:01 being the dominant HLA type in all patient cohorts. Donors responding to the 9-mer peptide pool can therefore be considered as good representatives of responders in Germany. In mild COVID-19 patients and pre-pandemic donors, HLA typing revealed similar distributions for HLA-A*02:01, HLA-A*11:01, HLA-B*07:02 and HLA-B*35:01 (Figure 8B - C). We observed that the HLA types A*03:01 and C*07:02 were more prominent in mild COVID-19 patients, whereas the HLA types A*01:01 and B*08:01 were more prominent in pre-pandemic donors. In asymptomatic donors, the HLA types could only be determined by flow cytometry staining, and therefore only the frequencies of HLA-A*02, HLA-A*03, HLA-B*07 and HLA-B*08 were obtained (Figure 8D - E). The frequencies were roughly comparable to mild COVID-19 patients with slightly lower frequencies of HLA-B*07 and higher frequencies of HLA-B*08. Since the responsiveness to the peptide pool of mild COVID-19 and asymptomatic seropositive donors was very similar, we expected the HLA distribution of the other HLA types to be similar. Due to sample limitations,

asymptomatic donors could not be analyzed further. Considering a similar HLA distribution between the patient cohorts, we can therefore conclude that the differences observed between the patient cohorts in the frequencies of IFN-γ^+ CD8$^+$ T cells after 9-mer peptide pool stimulation were real.

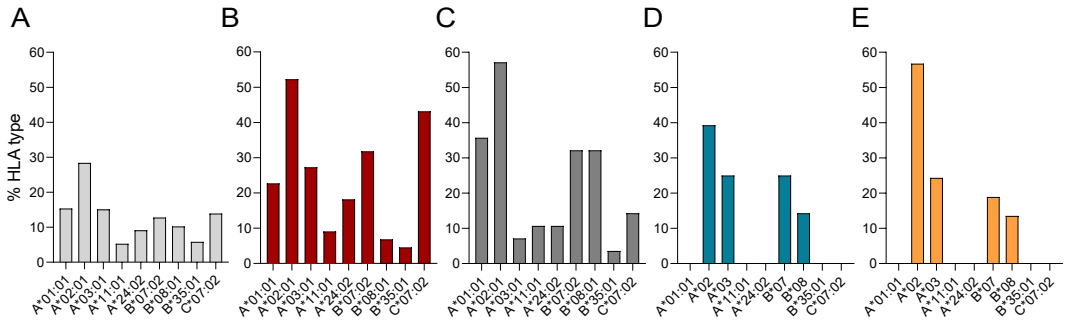

Figure 8: HLA distribution of patients cohorts. (A) Bar graph of population allele frequencies in Germany [175] - Germany DKMS - German donors (n=3456066), (B) mild COVID-19 donors, (C) pre-pandemic donors, (D) asymptomatic seropositive and (E) asymptomatic seronegative donors. Parts of the figure were reprinted with permission from [84].

4.1.4 Persistence of SARS-CoV-2-specific CD8+ T cell responses

PBMCs from mild COVID-19 and asymptomatic seropositive donors were collected at different time points after the first PCR positive or antigen-positive test, respectively. This allowed us not only to measure the simultaneous occurrence of IgG and T cell responses but also to monitor the persistence of cellular and humoral immune responses over time. At the first follow-up visit, IgG levels (AU/mL) were above the detection limit of 10 AU/mL in most mild COVID-19 patients and in all asymptomatic seropositive donors. In comparison, SARS-CoV-2-specific CD8$^+$ T cell responses (IFN-γ^+) could be measured in 34 of 44 (77 %) mild COVID-19 patients and 21 of 27 (78 %) asymptomatic seropositive donors. Importantly, the majority of donors had both, detectable IgG levels and CD8$^+$ T cell responses, suggesting successful establishment of humoral and cellular immunity after mild symptomatic and asymptomatic SARS-CoV-2 infection (Figure 9A).

By measuring IgG levels over a period of 259 days in mild COVID-19 donors and 205 days in asymptomatic seropositive donors, we found that SARS-CoV-2 antibody levels declined rapidly over time in both cohorts (Figure 9B). Although IgG levels were measured over different time periods for both cohorts, and although the recruitment of asymptomatic seropositive donors (days after enrollment) did not match the recruitment of mild COVID-19 patients (days after PCR test), the same trend was observed. The persistence of peptide-specific CD8$^+$ T cells could be measured stably for all time points, in contrast to antibody levels, and no trend towards a decrease in responses was observed in mild COVID-19 patients or asymptomatic seropositive donors (Figure 9C).

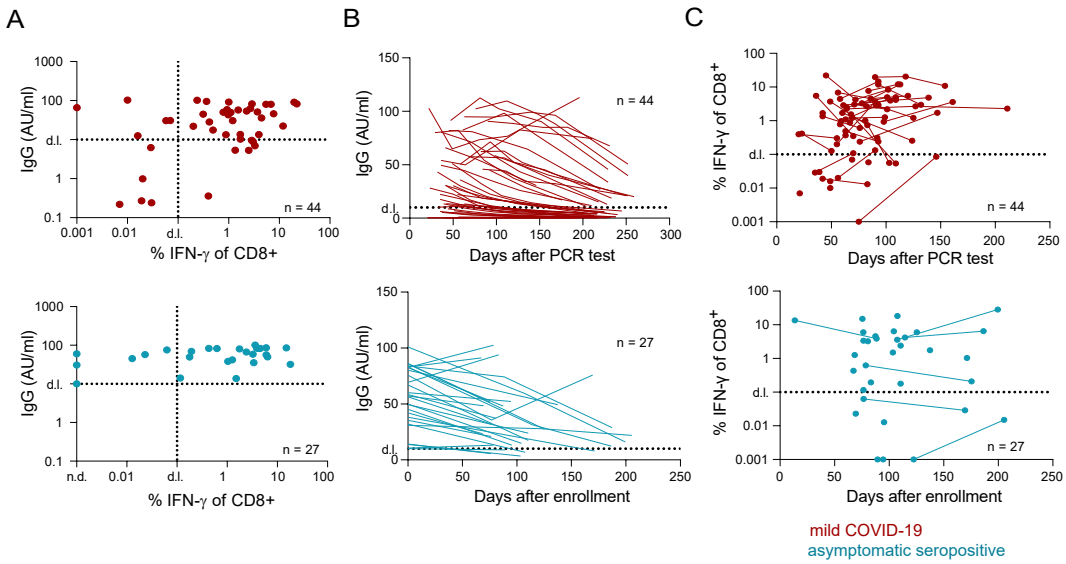

Figure 9: Cellular versus humoral persistence of SARS-CoV-2-specific responses. SARS-CoV-2-specific $CD8^+$ T cells and IgG levels were measured in mild COVID-19 (red) and asymptomatic seropositive (blue) donors. (A) Correlation of IgG levels (AU/mL) and INF-γ^+ $CD8^+$ T cells at the first follow-up visit (62.4 ± 20.4 days after PCR-confirmed infection and 102.6 ± 24.5 days after study enrollment, respectively). IgG levels (B) and INF-γ^+ $CD8^+$ T cell responses (C) at all sample collection time points as days after PCR test or days after enrollment, respectively. Data of the same donor are connected by a line. The figure was reprinted with permission from [84].

Additional sample material was collected from a selected number of mild COVID-19 patients who had no re-infection within one year of the initial PCR positive test. Importantly, even twelve months after infection, $CD8^+$ T cell responses were detected in most donors, whereas IgG levels were mostly undetectable (Figure 10A). For 37 donors of the mild COVID-19 patient cohort, an additional time point was collected two years after the initial SARS-CoV-2 PCR-confirmed infection. After two years, 20 donors had only one SARS-CoV-2 infection, and 17 donors had more than one infection. Of the donors with one infection, 16 donors (80 %) were responders to the 9-mer peptide pool in 2020, and twelve donors were still responders (60 %) in 2022 (Figure 10B - C). By dividing the 20 donors into responders (green plot in the middle) and non-responders at the first time point (grey plot on the right), we were able to follow the changes in responses over time (Figure 10C). Of the 17 responders, five donors with one infection lost responsiveness to the 9-mer pool. In contrast, only one non-responder with one infection had a 'de novo' response from 2020 to 2022, just above the detection limit (grey plot on the right). Although five of the original 17 responders lost responsiveness to the peptide pool over two years (29 %), most donors continued to respond to SARS-CoV-2 9-mer peptides after expansion, further supporting the claim made in Figure 9 with suggested memory formation and long-term $CD8^+$ T cell immunity after infection with SARS-CoV-2. Of the 17 donors with more than one infection, eleven donors responded to SARS-CoV-2 peptides in 2020 (64 %) and 14 donors in 2022 (82 %) (Figure 10B, D). The improved $CD8^+$ T cell response for these donors was likely enhanced by reinfection, suggesting that reinfection is helpful in maintaining high levels of SARS-CoV-2-specific $CD8^+$ T cells. To track T cell responses over time, we again divided donors into responders and non-responders (Figure 10D, green and grey plots, respectively). We found that

out of eleven responders with more than one infection in 2020, only one donor showed waning CD8$^+$ T cell responses to the peptide pool. Interestingly, four of the six non-responders in 2020 had a 'de novo' T cell response after reinfection. This suggests that multiple infections help to maintain detectable CD8$^+$ T cell responses and even stimulate 'de novo' CD8$^+$ T cell responses. In summary, we found that while SARS-CoV-2-specific antibody levels of mild COVID-19 donors declined quickly, CD8$^+$ T cell responses were stably detected over time, in many patients even two years after initial SARS-CoV-2 infection.

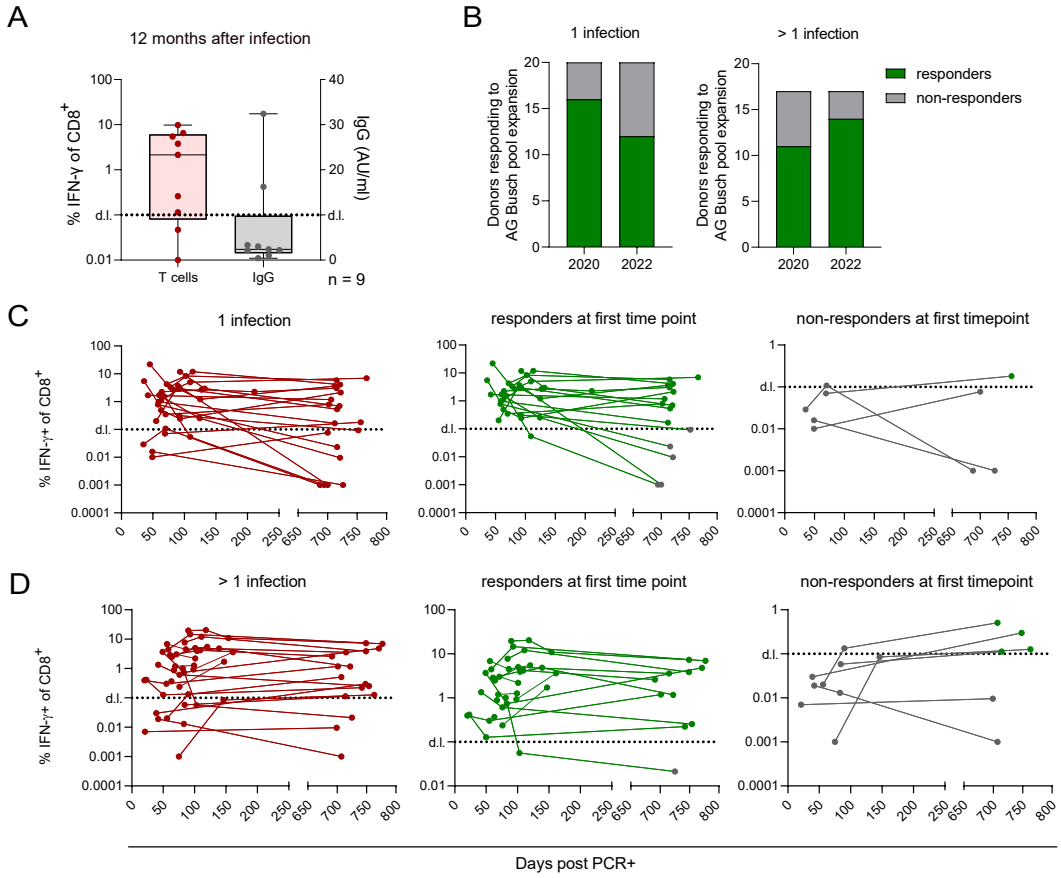

Figure 10: Detection of SARS-CoV-2-specific CD8$^+$ T cells up to two years after infection. (A) INF-γ^+ CD8$^+$ T cell responses and IgG levels twelve months after infection. Data are illustrated in a box and whiskers plot - min to max, all points are shown. The box includes the 25th to the 75th percentiles, and the middle line marks the median. IFN-γ values are oriented at the left and IgG values at the right y-axis. (B - D) Only donors are shown for which a two-year follow-up time point was collected. (B) Quantification of responders and non-responders for 2020 and 2022 time points for donors with one and more than one infection. (C-D) Time course of IFN-γ^+ levels of CD8$^+$ T cell responses of donors with one (C) and more than one infection (D). The first six sample collections and the two-year follow-up time point are separated by a break in the x-axis. Donors that switched from responder to non-resonder and vice versa are marked by a clored dot in the respective other color in 2022. Parts of the figure were reprinted with permission from [84].

4.1.5 Identification of immunodominant SARS-CoV-2 epitopes

For in-depth characterization of SARS-CoV-2 T cell immunity, the identification of single immunodominant epitopes is essential. To identify immunogenic and immunodominant epitopes, PBMCs from all mild COVID-19 donors were expanded with all 41 peptides of the 'original' 9-mer peptide pool. Due to limited sample material and to achieve higher throughput in testing potential immunogenic responses, we divided the peptides into four subpools for restimulation to first identify reactive subpools (data not shown). In a second experiment, we then expanded mild COVID-19 donor PBMCs with peptides from the reactive subpool(s) only and restimulated PBMCs with single peptides in separate conditions. In total, we identified 19 immunogenic epitopes of which eleven epitopes were immunodominant (immunodominance defined as $\geq 50\,\%$ of responders), and five had an immunodominance of $\geq 70\,\%$ (A1/ORF3_FTS, A3/ORF1_KLF, A3/ORF1_VTN, A3/ORF1_ASM, A1/ORF1_DTD) (Figure 11A - B) (Table 22). In addition, we detected multiple epitope responses per donor, suggesting that an immune response is generated against multiple viral proteins simultaneously. Furthermore, the absolute magnitude of the response for the same epitope differed between donors (Figure 11A). For example, for the A1/ORF3a_FTS epitope, the responses of ten HLA-matched donors ranged from 1.08 % to 14.87 % of INF-γ^+ CD8$^+$ T cells, with a mean of 4.0 % and a standard deviation (STD) of 4.2. Another exemplary epitope with a wide range of responses was A2/S_KIA with a range from 0.38 % to 1.97 % of INF-γ^+ CD8$^+$ T cells in five donors (mean: 0.70, STD: 0.58).

In addition to donor-dependent differences, we also observed that some epitopes induced higher frequencies of INF-γ^+ CD8$^+$ T cells than others, suggesting higher precursor frequency or fitness of the cells during expansion (Figure 11C). Specifically, we detected epitopes with high (A1/ORF3_FTS: 4.69 %, B8/ORF1_FVK: 1.88 %), intermediate (A2/S_VVF: 0.54 %, A1/ORF1_DTD: 0.50 %), and low (A2/S_ALN: 0.2 %, A24/N_LSP: 0.12 %) mean IFN-γ^+ CD8$^+$ T cell responses. Although no direct correlation was found between the degree of immunodominance and IFN-γ^+ frequency of CD8$^+$ T cells, a trend was observed in which epitopes with high immunodominance also had high mean IFN-γ^+ signals. Representative is the A1/ORF3a_FTS epitope with an immunodominance of 100 % of HLA-matched donors and a high mean IFN-γ signal of 4.68 % (Figure 11B, C).

Responses of pre-pandemic donors to 9-mer peptides were detected only against a few epitopes (A1/ORF3_FTS, A1/ORF1_DTD, A2/N_LLL, B35/ORF1_VPF) and were significantly lower in magnitude. For all potential 'cross-reactive' epitopes, we found reactivity in only one HLA-matched pre-pandemic donor each. Furthermore, the responses were much lower than in donors with SARS-CoV-2 infection. For epitopes with high immunodominance, A1/ORF3a_FTS and A1/ORF1_DTD, this corresponded to 100 % vs 17 % and 70 % vs 17 % of mild COVID-19 donors versus pre-pandemic donors, respectively. For epitope A2/N_LLL, which had a low immunogenicity of only 8.6 %, one responding pre-pandemic donor resulted in a higher frequency of 14.2 %. While the B35/ORF1_VPF epitope had a reported immunogenicity of 50 %, it is important to note that only two HLA-B*35:01 donors were measured. We suspect that the pre-pandemic HLA-B*35:01 donor who responded to B35/ORF1_VPF with an immunogenicity of 100 % as well as the 50 % response rate of the mild COVID-19 donors were most likely the result of data bias (Figure 11A, D).

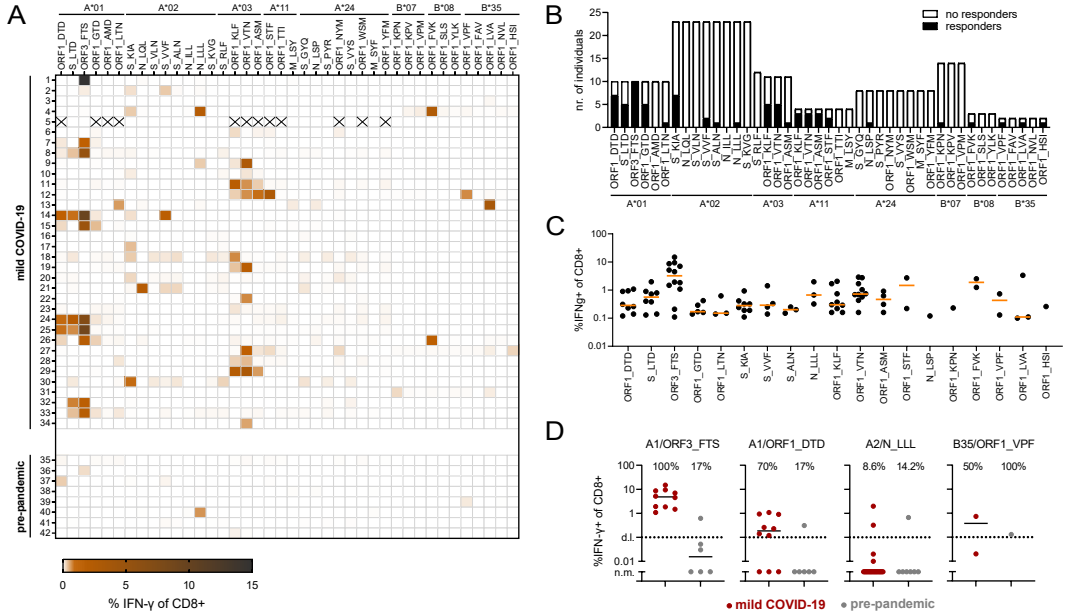

Figure 11: Identification of immunodominant SARS-CoV-2 epitopes of the 'original' peptide pool. (A) Heatmap of IFN-γ^+ CD8$^+$ T cells of mild COVID-19 and pre-pandemic donors for all epitopes of the 'original' 9-mer peptide pool. Peptides are organized according to HLA type. (B) Bar graph of immunodominance of epitopes for HLA-matched individuals. (C) Magnitude of responses per epitope for positive responses only. An orange line marks the mean. (D) Responses of selected epitopes of mild COVID-19 and pre-pandemic donors. A black line marks the mean. Parts of the figure were reprinted with permission from [84].

Table 22: Response frequency of peptides from the 'original' peptide pool

Peptide	HLA type	Responder/ non-responder (response frequency)	Peptide	HLA type	Responder/ non-responder (response frequency)
ORF1_AMD	HLA-A*01:01	0/10 (0 %)	ORF1_TTI	HLA-A*11:01	0/4 (0 %)
ORF1_DTD	HLA-A*01:01	7/3 (70 %)	ORF1_VTN	HLA-A*11:01	3/1 (75 %)
ORF1_GTD	HLA-A*01:01	5/5 (50 %)	S_RLF	HLA-A*03:01	0/12 (0 %)
ORF1_LTN	HLA-A*01:01	1/9 (10 %)	M_SYF	HLA-A*24:02	0/8 (0 %)
ORF3_FTS	HLA-A*01:01	10/0 (100 %)	N_LSP	HLA-A*24:02	1/7 (13 %)
S_LTD	HLA-A*01:01	5/5 (50 %)	ORF1_NYM	HLA-A*24:02	0/8 (0 %)
N_ILL	HLA-A*02:01	0/23 (0 %)	ORF1_WSW	HLA-A*24:02	0/8 (0 %)
N_LLL	HLA-A*02:01	1/22 (4.3 %)	ORF1_YFM	HLA-A*24:02	0/8 (0 %)

N_LQL	HLA-A*02:01	0/23 (0 %)	S_GYQ	HLA-A*24:02	0/8 (0 %)
S_ALN	HLA-A*02:01	1/22 (4.3 %)	S_PYR	HLA-A*24:02	0/8 (0 %)
S_KIA	HLA-A*02:01	7/16 (30 %)	S_VYS	HLA-A*24:02	0/8 (0 %)
S_KVG	HLA-A*02:01	0/23 (0 %)	ORF1_KPN	HLA-B*07:02	1/13 (7.1 %)
S_VLN	HLA-A*02:01	0/23 (0 %)	ORF1_KPV	HLA-B*07:02	0/14 (0 %)
S_VVF	HLA-A*02:01	2/21 (8.6 %)	ORF1_VPM	HLA-B*07:02	0/14 (0 %)
ORF1_ASM	HLA-A*03:01	1/10 (9.1 %)	ORF1_FVK	HLA-B*08:01	1/2 (33 %)
ORF1_KLF	HLA-A*03:01	5/6 (45 %)	ORF1_SLS	HLA-B*08:01	0/3 (0 %)
ORF1_VTN	HLA-A*03:01	5/6 (45 %)	ORF1_YLK	HLA-B*08:01	0/3 (0 %)
S_RLF	HLA-A*03:01	0/12 (0 %)	ORF1_FAV	HLA-B*35:01	0/2 (0 %)
M_LSY	HLA-A*11:01	0/4 (0 %)	ORF1_HSI	HLA-B*35:01	1/1 (50 %)
ORF1_ASM	HLA-A*11:01	3/1 (75 %)	ORF1_LVA	HLA-B*35:01	1/1 (50 %)
ORF1_KLF	HLA-A*11:01	3/1 (75 %)	ORF1_NVL	HLA-B*35:01	0/2 (0 %)
ORF1_STF	HLA-A*11:01	2/2 (50 %)	ORF1_VPF	HLA-B*35:01	1/1 (50 %)

The ‘original’ 41 peptide 9-mer pool contained epitopes against the most common HLA class I molecules in the Caucasian population. While coverage of 100 % was achieved for the HLA types HLA-A*01:01, HLA-A*11:01 and HLA-B*35:01, coverage for some of the other HLA types was considerably lower with 63 %, 40 %, 33 % for HLA-A*03:01, HLA-A*02:01, HLA-B*08:01, respectively, and much lower for HLA-A*24:01 and HLA-B*07:02 with less than 15 % (Figure 12A). To achieve better response rates for some of these HLA types, but also to include more HLA types for better coverage of the Caucasian population, we developed an ‘extended’ peptide pool with 62 additional peptides predicted to bind to the HLA types from the ‘original’ peptide pool and also to new HLA-types (HLA-B*15:01, HLA-B*40:01 and HLA-B*44:03). 37 of the 62 peptides were part of the spike protein and 25 peptides were part of other ORFs (Table 11). The S_RLF epitope from the ‘original’ peptide pool was included again to be measured at a different time point as it showed good prediction not only for HLA-A*03:01 but also for HLA-A*11:01. In the ‘original’ peptide pool it showed no reactivity in HLA-A*03:01 positive donors. The selection of peptides for the ‘extended’ peptide pool was based on HLA class I epitope prediction tools similar to the ‘original’ peptide pool (see 3.2.1.4) and on published epitopes from literature. With the ‘extended’ peptide pool, the response rate of HLA-A*02:01, HLA-A*24:01 and HLA-B*07:02 was improved to 70 %, 75 % and 71 %, respectively. In addition, coverage of 100 % was achieved for HLA-B*40:01 and new response rates of 71 %, 57 % and 5 % were achieved for HLA-B*15:01, HLA-B*44:03 and HLA-C*07:02, respectively (Figure 12B).

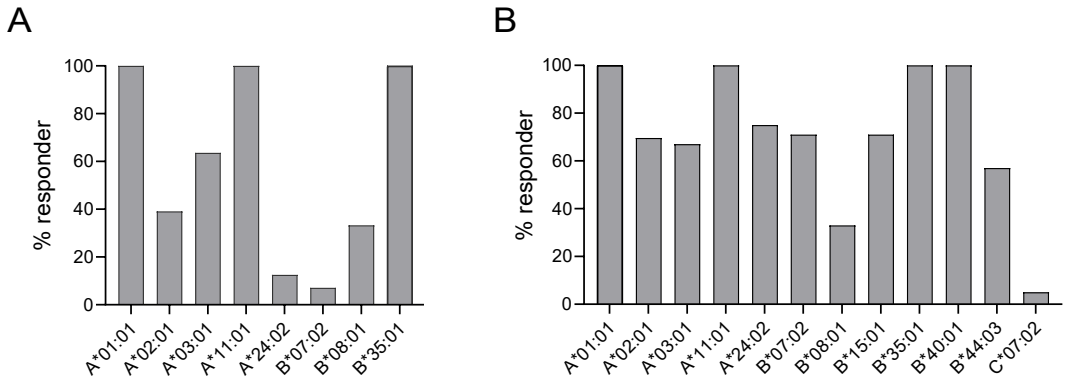

Figure 12: HLA type of mild COVID-19 responders to SARS-CoV-2-specific epitopes. HLA class I types of responders to (A) 'original' and (B) 'extended' SARS-CoV-2-specific 9-mer peptide pool. Responses for each HLA type are the sum of individual peptide responses. The figure was reprinted with permission from [84].

To identify peptides of the 'extended' peptide pool, we proceeded from the subpool peptide deconvolution strategy used above (see 4.1.5) to direct expansion of mild COVID-19 PBMCs with HLA-matched peptides, followed by restimulation with single peptides. This had the advantage of allowing more conditions to be tested at the same time and increasing the speed of peptide identification. Because sample material was limited and we wanted to preserve some donor material for future experiments, not all HLA-matched donors of common HLA alleles were tested. For example, only eight of ten donors (80 %) were tested for HLA-A*01:01, only twelve of 23 donors (52 %) were tested for HLA-A*02:01 and only nine of eleven donors (82 %) were tested for HLA-A*03:01. This could lead to under- or over-representation of some peptide responses. However, since the main goal was to increase HLA coverage and identify immunogenic epitopes, this bottleneck was accepted.

Overall, we detected responses in 33 out of 44 mild COVID-19 patients (75 %) after expansion with peptides from the 'extended' peptide pool. Importantly, however, we were able to expand six donors in whom we had previously detected no responses after expansion, resulting in an overall responsiveness of mild COVID-19 donors to both peptide pools of 91 % (Figure 13A) (Table 23). Multiple epitope reactivities per donor were also observed for peptides from the 'extended' peptide pool. In addition, we again found differences in magnitude between donors for the same epitope. For example, responses to the B7/N_SPR epitope were detected in eleven donors and ranged from 0.15 % to 18.8 % of IFN-γ^+ CD8$^+$ T cells (mean: 3.85 % STD: 5.29 %) (Figure 13A). Epitopes from the 'extended' pool show very high immunogenicity with 18 newly identified immunogenic epitopes, eight of which showed an immunodominance of $\geq$ 70 % (B7/N_SPR, B35/S_LPF, B40/M_SEL, B44/N_MEV, A2/S_YLQ, A2/ORF1_KLW, A11/N_ATE, A3/N_KTF). In addition, the epitope A11/S_RLF showed responses in 50 % of HLA-matched donors (Figure 13B).

When comparing the IFN-γ frequencies after expansion, also for peptides of the 'extended' pool, different mean IFN-γ^+ CD8$^+$ T cells frequencies were observed with a trend towards the co-occurrence of high immunodominance and high frequencies of IFN-γ^+ CD8$^+$ T cells. Representative epitopes were B7/N_SPR and B40/M_SEL, both with immunodominance of 100 % and mean IFN-γ signals of 6.70 % and 4.24 %, respectively. In contrast, peptides with low immunodominance, such as A3/N_KTF (22 %) and B44/ORF1_SEF (22 %), had comparatively low mean IFN-γ frequencies of 0.16 % and 0.25 %, respectively (Figure 13C). Outliers from this trend could generally be attributed to epitopes to which few donors responded (N_QRN,

immunodominance: 7.7 %, IFN-γ: 5.5 % or A24/ORF1_VYI immunodominance: 25 %, IFN-γ: 0.6 %). To understand the polyfunctionality of a T cell response, we added the number of individual peptide responses per donor from the 'original' and the 'extended' peptide pools. We found that most donors show immunogenicity against four epitopes at the same time, followed by two, three and seven epitopes (Figure 13D). Of course, this number depends on the HLA background of the patient cohort and is likely to increase as more immunodominant epitopes for the respective HLA types of the patients are added.

In summary, we identified SARS-CoV-2 epitopes with high immunodominance in mild COVID-19 donors. Furthermore, we observed multiple epitope responses per donor and differences in magnitude for the same epitope in different donors with a trend towards correlation of immunodominance and IFN-γ levels. In addition, we detected little cross-reactivity with pre-pandemic samples for the 9-mer epitopes from the first peptide pool, confirming the specificity of the selected epitopes for SARS-CoV-2.

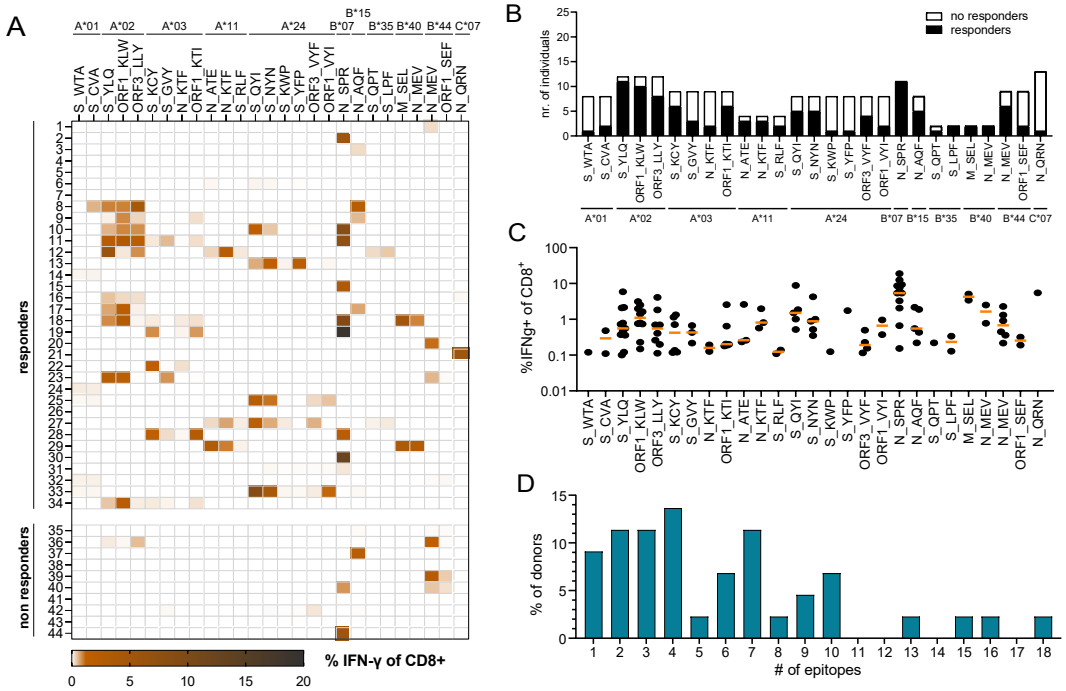

Figure 13: Identification of immunodominant SARS-CoV-2 epitopes of the 'extended' peptide pool. (A) Heatmap of IFN-γ^+ $CD8^+$ T cells of mild COVID-19 and pre-pandemic donors for all epitopes of the 'extended' 9-mer peptide pool. Peptides are organized according to HLA type. (B - C) Only peptides with an immune response against at least one donor are shown. (B) Bar graph of immunodominance of epitopes for HLA-matched individuals. (C) Magnitude of responses per epitope only for positive responses. An orange line marks the mean. (D) Quantification of the number of epitopes each donor responds against. Parts of the figure were reprinted with permission from [84].

Table 23: Response frequency of peptides from the 'extended' peptide pool

Peptide	HLA type	Responder/ non-responder (response %)	Peptide	HLA type	Responder/ non-responder (response %)
S_CVA	HLA-A*01:01	2/6 (25 %)	S_YYH	HLA-A*24:02	0/8 (0 %)
S_TSN	HLA-A*01:01	0/8 (0 %)	N_KPR	HLA-B*07:02	0/11 (0 %)
S_WTA	HLA-A*01:01	1/7 (13 %)	N_SPR	HLA-B*07:02	11/0 (100 %)
N_AQA	HLA-A*02:01	0/12 (0 %)	ORF1_RPD	HLA-B*07:02	0/11 (0 %)
ORF1_KLW	HLA-A*02:01	10/2 (83 %)	S_FPQ	HLA-B*07:02	0/11 (0 %)
ORF3_LLY	HLA-A*02:01	8/4 (67 %)	S_MIA	HLA-B*07:02	0/11 (0 %)
S_ELL	HLA-A*02:01	0/12 (0 %)	S_SPR	HLA-B*07:02	0/11 (0 %)
S_FQF	HLA-A*02:01	0/12 (0 %)	ORF1_DLK	HLA-B*08:01	0/3 (0 %)
S_HLM	HLA-A*02:01	0/12 (0 %)	S_EPV	HLA-B*08:01	0/3 (0 %)
S_SII	HLA-A*02:01	0/12 (0 %)	S_FNA	HLA-B*08:01	0/3 (0 %)
S_TLD	HLA-A*02:01	0/12 (0 %)	S_INI	HLA-B*08:01	0/3 (0 %)
S_YLQ	HLA-A*02:01	11/1 (92 %)	S_LIT	HLA-B*08:01	0/3 (0 %)
N_KTF	HLA-A*03:01	2/7 (22 %)	N_AQF	HLA-B*15:01	5/3 (63 %)
ORF1_KTI	HLA-A*03:01	6/3 (67 %)	ORF1_LVQ	HLA-B*15:01	0/8 (0 %)
S_GVY	HLA-A*03:01	3/6 (33 %)	S_LPF	HLA-B*35:01	2/0 (100 %)
S_KCY	HLA-A*03:01	6/3 (67 %)	S_QPT	HLA-B*35:01	1/1 (50 %)
S_QIY	HLA-A*03:01	0/9 (0 %)	S_FAM	HLA-B*35:01	0/2 (0 %)
S_VTY	HLA-A*03:01	0/9 (0 %)	S_IPF	HLA-B*35:01	0/2 (0 %)
M_ATS	HLA-A*11:01	0/4 (0 %)	S_LGA	HLA-B*35:01	0/2 (0 %)
N_ATE	HLA-A*11:01	3/1 (75 %)	ORF1_GEA	HLA-B*40:01	0/2 (0 %)
N_KTF	HLA-A*11:01	3/1 (75 %)	ORF1_GEV	HLA-B*40:01	0/2 (0 %)
N_KTF	HLA-A*11:01	0/4 (0 %)	M_SEL	HLA-B*40:10	2/0 (100 %)
S_NSA	HLA-A*11:01	0/4 (0 %)	N_MEL	HLA-B*40:10	2/0 (100 %)
S_RLF	HLA-A*11:01	2/2 (50 %)	S_YEQ	HLA-B*44:03	0/9 (0 %)
S_TLK	HLA-A*11:01	0/4 (0 %)	N_MEW	HLA-B*44:10	6/3 (67 %)
N_DYK	HLA-A*24:02	0/8 (0 %)	ORF1_SEF	HLA-B*44:10	2/7 (22 %)
ORF1_VYI	HLA-A*24:02	2/6 (25 %)	M_NRF	HLA-C*07:02	0/13 (0 %)
ORF3_VYF	HLA-A*24:02	4/4 (50 %)	N_QRN	HLA-C*07:02	1/12 (7.7 %)
S_KWP	HLA-A*24:02	1/7 (13 %)	S_EYV	HLA-C*07:02	0/13 (0 %)
S_NYN	HLA-A*24:02	5/3 (63 %)	S_FRK	HLA-C*07:02	0/13 (0 %)
S_QYI	HLA-A*24:02	5/3 (63 %)	S_VRF	HLA-C*07:02	0/13 (0 %)
S_YFP	HLA-A*24:02	1/7 (13 %)			

To conclude this chapter, we found that SARS-CoV-2-specific T cell responses were below the detection limit for most mild COVID-19 donors for the PepTivator S and SARS-CoV-2 9-mer peptide pools. To better detect low-frequency SARS-CoV-2-specific responses, we developed an expansion protocol to selectively expand SARS-CoV-2-specific $CD8^+$ T cells without expanding $CD4^+$ T cells. Subsequently, we were able to detect $CD8^+$ T cell responses to the 9-mer peptide pool for 77 % and 78 % of mild COVID-19 and asymptomatic seropositive donors. The control groups, asymptomatic seronegative and pre-pandemic donors had low responses after expansion. Analysis of donor HLA types revealed that the patient cohorts had similar HLA distributions, suggesting that the responses to the 9-mer peptide pool were real and not biased by HLA distribution. We then examined the persistence of SARS-CoV-2-specific responses and found that although SARS-CoV-2 antibody levels were readily detectable at the first time point, they quickly dropped below the detection limit. In contrast, $CD8^+$ T cell responses were stably detected over time and persisted in most individuals for up to two years after initial SARS-CoV-2 infection, suggesting long-term development of T cell immunity. Reinfection stabilized these responses and further stimulated 'de novo' $CD8^+$ T cell responses. We then deconvoluted the peptide pool and identified SARS-CoV-2 epitopes with high immunodominance. To achieve better response rates for some of the HLA types and to include more HLA types, we also developed an 'extended' peptide pool in which we again demonstrated highly immunodominant peptides. We also observed that each donor reacted to multiple epitopes simultaneously and discovered a range in $CD8^+$ T cell IFN-γ frequencies in different donors for the same epitope. By comparing immunodominance with IFN-γ frequencies, we identified a trend of correlation between high immunodominance and IFN-γ levels. Finally, we tested peptides from the 'original' pool in pre-pandemic donors and found overall low responses in a few epitopes, confirming the specificity of selected epitopes for SARS-CoV-2.

4.2 Identification and functional characterization of SARS-CoV-2-specific TCRs

4.2.1 Identification of TCRs specific for SARS-CoV-2 epitopes A3/ORF1_VTN and A1/ORF3a_FTS

Following the identification of immunodominant SARS-CoV-2-specific epitopes in subsection 4.1, we were intrigued to further investigate $CD8^+$ T cell immunity in mild COVID-19 patients by analyzing TCRs that recognize these SARS-CoV-2-specific epitopes. For the identification of SARS-CoV-2-specific TCRs by single cell RNA sequencing (scRNAseq) two epitopes with high immunodominance were selected as a proof of concept, the HLA-A*01:01-restricted epitope A1/ORF3a_FTS (100 %) and the HLA-A*03:01-restricted epitope A3/ORF1_VTN (75 %). For each epitope, two HLA-matched donors were selected (donors 22 and 34 for A3/ORF1_VTN; donors 32 and 33 for A1/ORF3a_FTS) and expanded for twelve days. As before, for expansion, 20 % of the PBMCs were pulsed with 10 µg/mL of the total 'original' peptide pool for 2 h at RT before being added to the remaining 80 % of the PBMCs in culture (see 3.2.2.4). To induce a selective activation phenotype of $CD8^+$ T cells specific for the epitopes A3/ORF1_VTN and A1/ORF3a_FTS, PBMCs from the four donors were freshly restimulated with the respective epitope of interest prior cell sorting. In this way, TCRs specific for A1/ORF3a_FTS and A3/ORF1_VTN could be identified based on the T cell activation marker IFN-γ after fresh peptide stimulation. The IFN-γ catch assay was used to isolate peptide reactive T cells. This assay allowed IFN-γ molecules produced after fresh restimulation to be captured on the cell surface of activated T cells (see 3.2.2.4). Subsequent staining of surface-presenting IFN-γ with anti-IFN-γ antibodies conjugated to fluorochromes allowed us to sort recently activated cells by flow cytometry.

In addition to 2,500 IFN-γ^+ cells, we sorted 10,000 IFN-γ^- cells per sample. With this, we wanted to distinguish recently activated $CD8^+$ T cells by an activated phenotype from $CD8^+$ T cells that were not recently activated. Previously, we have shown that most donors respond to more than one SARS-CoV-2 epitope (see 4.1.5). By expanding PBMCs from all four donors with the entire peptide pool, we also expanded $CD8^+$ T cells specific for other SARS-CoV-2 epitopes. We anticipated that in addition to identifying A3/ORF1_VTN and A1/ORF3a_FTS-specific $CD8^+$ T cells by recent activation, we could also identify TCRs specific for other epitopes based on clonotype size. Following cell sorting, we pooled cells from all four donors and identified TCR sequences from the sorted cells by scRNAseq and data analysis (see 3.2.8) (Figure 14A).

To organize individual cells based on transcriptomic similarities and identify clusters of similarity, we used the widely used and popular Leiden algorithm, an iterative algorithm that connects communities based on similarity and leads to optimal local assignment [176]. Leiden clustering revealed eight clusters of similarity (cluster 0 - cluster 7) (Figure 14B). The clusters with the largest clonotype sizes were cluster 0, followed by cluster 1 and cluster 5. Based on the clonotype size, we expected expanded SARS-CoV-2-specific $CD8^+$ T cell clonotypes in these three clusters. Since the IFN-γ expression of recently activated cells was used as a selection marker for cell sorting of A1/ORF3a_FTS and A3/ORF1_VTN-specific $CD8^+$ T cells, cluster 1, the cluster with the highest IFN-γ expression, was expected to contain A1/ORF3a_FTS and A3/ORF1_VTN-specific $CD8^+$ T cells. In addition, cluster 1 was characterized by high expression of the cytolytic marker granzyme B (GZMB), the activation markers XCL1 and CD69, and the proliferation markers IL-2 and CRTAM (Figure 14B), all genes associated with T cell activation. In this line of thinking, we assumed that TCRs responding to some of the other SARS-CoV-2 epitopes would be found in clusters 0 and 5.

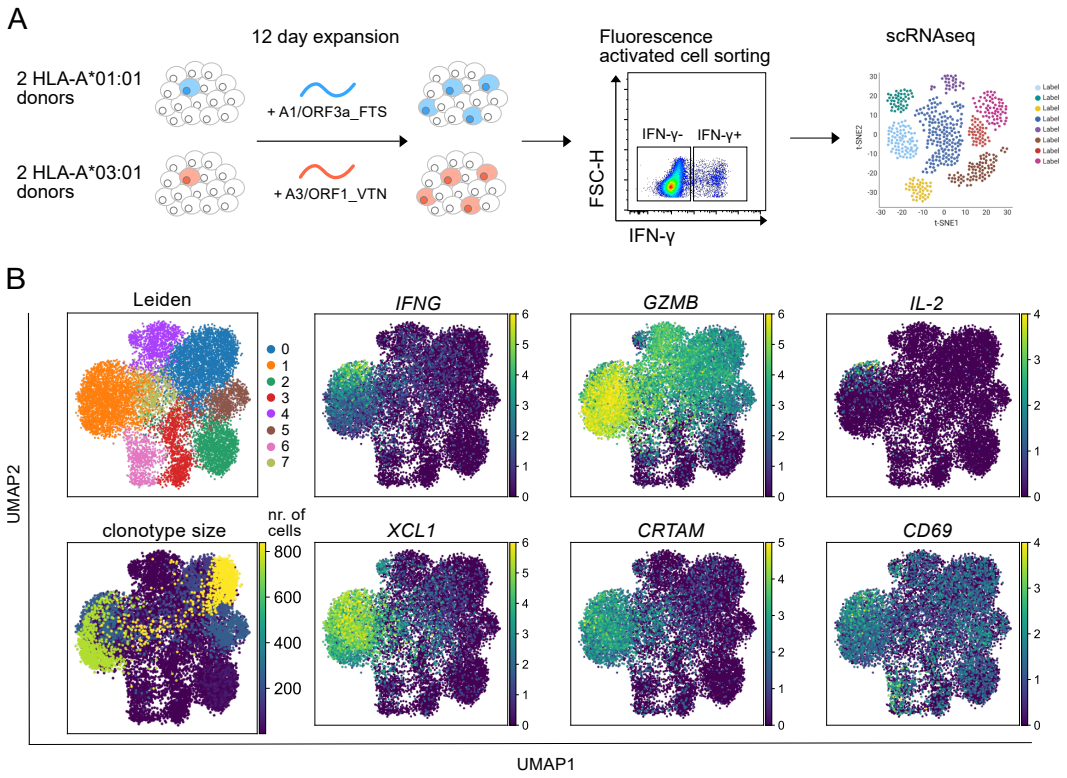

Figure 14: scRNAseq and identification of TCRs specific for the A3/ORF1_VTN and A1/ORF3_FTS epitopes. (A) Schematic of the workflow for TCR isolation. (B) UMAP clusters of Leiden clustering, clonotype size and gene expression of IFNG, GZMB, IL-2, XCL1, CRTAM and CD69. Parts of the figure were reprinted or adapted with permission from [84].

CD8$^+$ T cell repertoires specific for the A3/ORF1_VTN epitope were highly polyclonal. In particular, for donor 34, the IFNG$^+$ cluster was characterized by larger clonotype sizes compared to the IFNG$^-$ cluster (Figure 15A). Similarly, the clonotypes identified from donors 32 and 33 specific for epitope A1/ORF3a_FTS were highly polyclonal with a higher frequency of large clones for both donors in the IFNG$^+$ cluster compared to the IFNG$^-$ cluster (Figure 15B). Larger clonotype sizes in the IFNG$^+$ cluster were indicative of successful antigen-specific expansion of A3/ORF1_VTN and A1/ORF3a_FTS-specific CD8$^+$ T cells. Expanded clonotypes in the IFNG$^-$ cluster most likely belong to TCRs specific for other SARS-CoV-2 epitopes. Cells belonging to the IFNG$^+$ cluster were enriched for A3/ORF1_VTN and A1/ORF3a_FTS-responsive CD8$^+$ T cells. In contrast, cells specific for other epitopes were randomly selected into the 10,000 sorted IFNG$^-$ cells and were not specifically enriched. Therefore, we expected cells in the IFNG$^+$ cluster to have larger clonotypes on average. For functional TCR characterizations, clonotypes were selected from the top ten expanded clonotypes belonging to either the putative SARS-CoV-2-specific cluster 1 (IFNG$^+$) or the negative clusters 0 and 5 as controls (IFNG$^-$). For the A3/ORF1_VTN epitope, clonotypes part of the IFNG$^+$ cluster 1 (donor 22: 28, 32, donor 34: 13, 43) and clonotypes part of the IFNG$^-$ clusters 0 and 5 (donor 22: 18, 40, donor 34: 82) were selected (Figure 15C). Similarly, for the A1/ORF3a_FTS epitope, clonotypes from the IFNG$^+$ cluster 1 (donor 32: 3456, donor 33: 3398), as well as clonotypes from the IFNG$^-$ clusters 0 and 5 (donor 32: 3399, donor 33: 3409), were selected (Figure 15D).

We can conclude that expansion of mild COVID-19 PBMCs with the SARS-CoV-2 epitopes A1/ORF3a_FTS and A3/ORF1_VTN, followed by fresh restimulation and isolation of recently activated CD8$^+$ T cells, allowed us to identify polyclonal CD8$^+$ T cell populations with putative epitope-specific clones in the IFNG$^+$ transcriptional clusters and not in the IFNG$^-$ clusters.

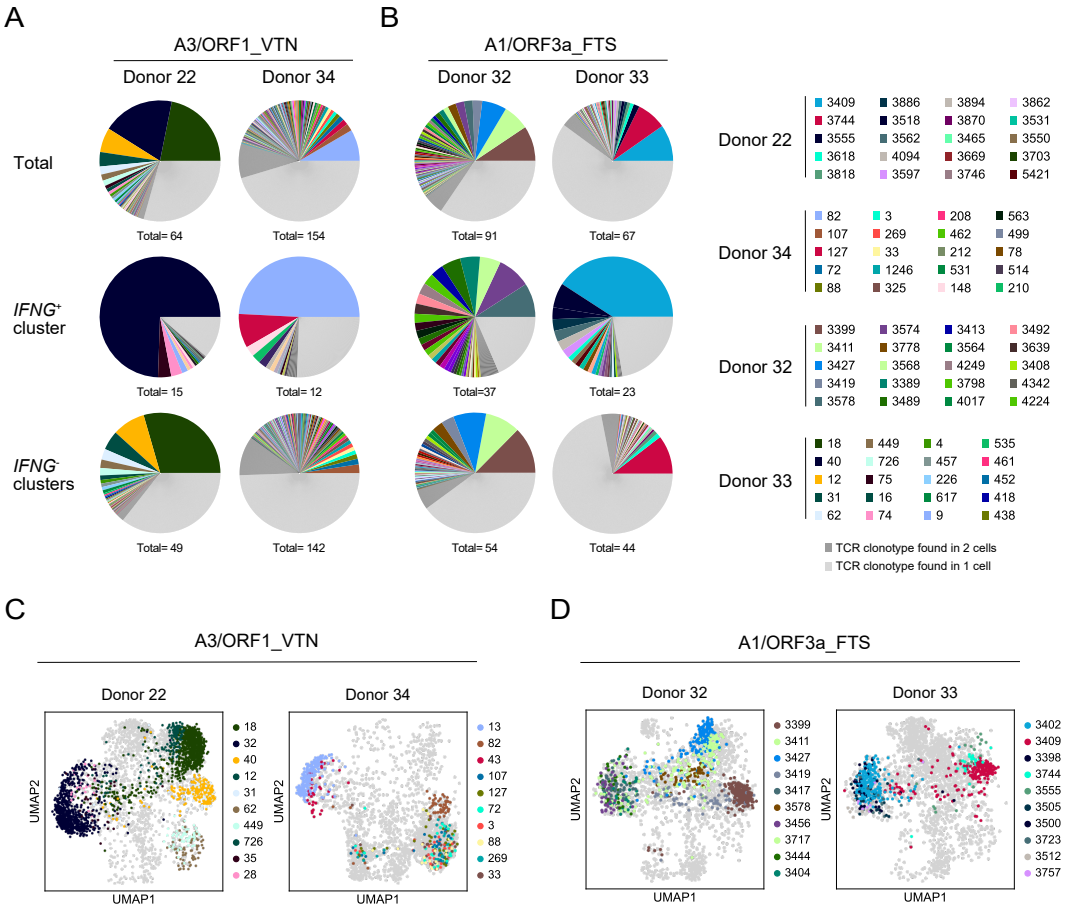

Figure 15: Clonotype classification of TCRs specific for A3/ORF1_VTN and A1/ORF3a_FTS epitopes. (A - B) Clonotype distribution of TCRs specific for A3/ORF1_VTN (A) and A1/ORF3a_FTS (B) epitopes for all four donors, shown for total clusters (top), IFNG$^+$ clusters (middle) and IFNG$^-$ clusters (bottom). Data are shown as parts of whole. (C - D) Top ten expanded clonotypes for A3/ORF1_VTN (C) and A1/ORF3a_FTS (D) epitopes, shown separately per donor in Leiden clustering. The figure was reprinted with permission from [84].

4.2.2 TCR re-expression via CRISPR/Cas9-mediated OTR in primary T cells

For the functional characterization of SARS-CoV-2-specific TCRs, CRISPR/Cas9-mediated OTR was performed to replace the endogenous TCR of healthy donor CD8$^+$ T cells with a transgenic SARS-CoV-2-specific TCR integrated into the endogenous TRAC locus (see 3.2.5). The transgenic TCRs were designed to have murine constant chains to distinguish them from the

endogenous TCRs of unedited cells. By default, the murine TCR beta constant chain (mTRBC) was stained with fluorochrome-conjugated antibodies for detection by flow cytometry. Successful CRISPR/Cas9-mediated OTR could thus be detected by KO of the endogenous TCR (measured by hTCR-FITC) and KI of the transgenic TCR (measured by mTRBC-APC). All putative SARS-CoV-2-specific TCRs were successfully re-expressed. As controls, we used cells edited only for the KO of the endogenous TCR, where only assembled RNPs were added but no HDR template for KI and unedited (mock) cells. Endogenous TCR KO of the selected TCRs was achieved with an overall high efficiency of 94.8 % - 99.1 % (mean ± STD) (96.8 % ± 1.38) and transgenic TCR KI with efficiencies of 8.3 % - 14.9 % (11.8 ± 2.78) for putative A3/ORF1_VTN and A1/ORF3a_FTS-specific TCRs and TCRs from the IFNG$^-$ clusters in CD8$^+$ T cells (Figure 16).

In conclusion, we have successfully re-expressed putative SARS-CoV-2-specific TCRs in healthy donor PBMCs by CRISPR/Cas9-mediated OTR through KO of the endogenous TCR and KI of the transgenic TCR at the TCR alpha locus.

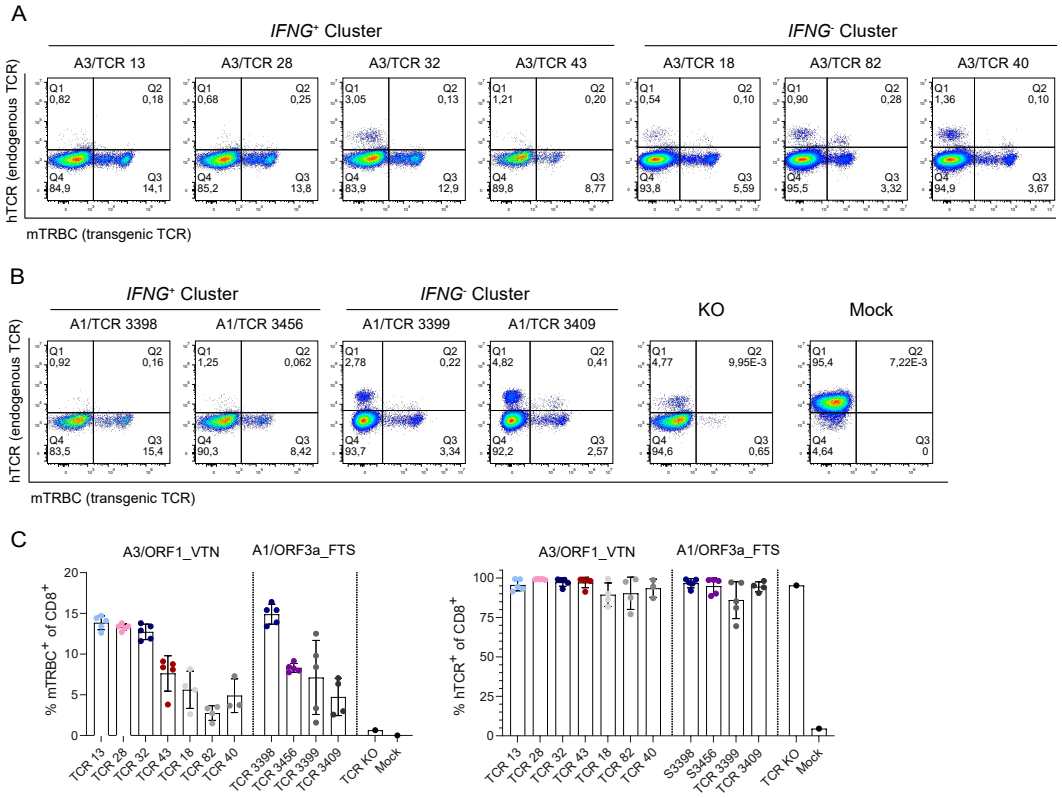

Figure 16: Generation of TCR-engineered SARS-CoV-2-specific CD8$^+$ T cells. (A-B) Representative flow cytometry plots showing the KO of endogenous TCRs (hTCR$^-$) and the KI of transgenic SARS-CoV-2-specific TCRs (mTRBC$^+$). CRISPR/Cas9-mediated OTR of TCRs specific for the A3/ORF1_VTN epitope (A) and the A1/ORF3a_FTS epitope (B) are shown for TCRs from the IFNG$^+$ and the IFNG$^-$ clusters, respectively, as well as KO control and mock (B). One of four technical replicates is shown. (C) Quantification of KO and KI efficiencies for all TCR-transgenic T cells. One to five experimental replicates are shown with the mean as a bar graph ± SD. Cells were pre-gated on lymphocytes, singlets, living, CD8$^+$.

4.2.3 pHLA multimer staining of TCR-engineered T cells specific for A3/ORF1_VTN and A1/ORF3a_FTS epitopes

Following the successful KI of SARS-CoV-2-specific TCRs into $CD8^+$ T cells via OTR, we assessed the peptide binding specificity of the TCRs to their respective pHLA multimer. pHLA multimer staining of A3/ORF1_VTN-specific TCRs revealed that TCR 13, TCR 28 and TCR 43 had high binding specificity as shown by diagonal double positive staining for the A3/ORF1_VTN pHLA multimer and anti-mTRBC antibody. In contrast, only a small proportion of TCR 32 $mTRBC^+$ $CD8^+$ T cells also responded to the A3/ORF1_VTN multimer, suggesting that TCR 32 may be of lower affinity. A3/ORF1_VTN pHLA multimer staining of TCRs from the $IFNG^-$ cluster (TCR 18, TCR 40, TCR 82) was negative, confirming the specificity of A3/ORF1_VTN-specific TCRs. In addition, TCRs from the $IFNG^+$ cluster showed no multimer binding to an irrelevant multimer (HLA-A*03:01 multimer loaded with SARS-CoV-2-specific epitope: A3/ORF1_KLF), suggesting specificity for the relevant multimer. Surprisingly, however, we found that TCR 40 was reactive to the irrelevant A3/ORF1_KLF epitope. This demonstrated that we could indeed identify TCRs specific for other SARS-CoV-2 epitopes of the 9-mer pool from the $IFNG^-$ cluster (Figure 17A). TCR 3398 and TCR 3456 both had a strong multimer staining to A1/ORF3a_FTS pHLA, shown by $multimer^+$ $mTRBC^+$ populations. TCRs from the $IFNG^-$ cluster (TCR 3399, TCR 3409) were unreactive to the A1/ORF3a_FTS pHLA multimer, suggesting specific multimer recognition of TCRs from the $IFNG^+$ cluster. TCR 3398 and TCR 3456, as well as TCR 3399, and TCR 3409 did not react to an irrelevant HLA-A*01 multimer (CMV epitope: pp50(245-253)) (Figure 17B).

Overall, we were able to show that all TCRs from the $IFNG^+$ cluster, but none from the $IFNG^-$ clusters, were specific for their respective pHLA multimers (A3/ORF1_VTN, A1/ORF3a_FTS).

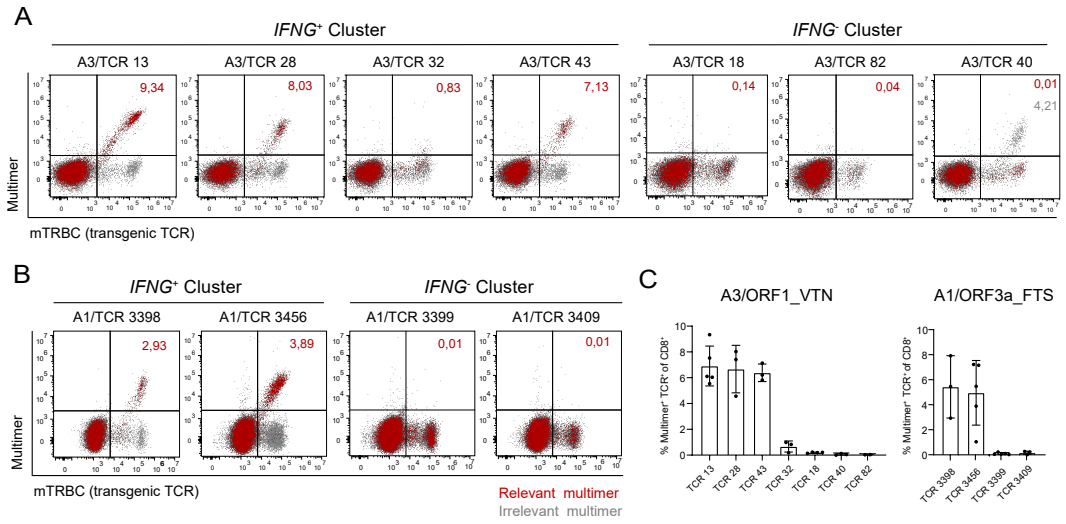

Figure 17: Multimer staining of TCRs specific for A3/ORF1_VTN and A1/ORF3a_FTS epitopes. Representative flow cytometry plots showing A3/ORF1_VTN (A) and A1/ORF3a_FTS (B) pHLA multimer staining of TCR-engineered $CD8^+$ T cells. Binding to the corresponding (red) and irrelevant (grey) pHLA multimer is shown. Cells were pregated on lymphocytes, singlets, living, $CD8^+$. (C) Quantification of $multimer^+$ frequencies. Three to five experimental replicates and mean ± SD are shown. The figure was reprinted with permission from [84]).

4.2.4 Structural avidity measurement of A3/ORF1_VTN and A1/ORF3a_FTS-specific TCRs

A3/ORF1_VTN and A1/ORF3a_FTS pHLA multimer staining of re-expressed TCRs showed strong staining for most SARS-CoV-2-specific TCRs. Evaluation of the pHLA:TCR complex by multimer staining is a good method to assess binding specificity. Our next step in defining specific TCRs was by evaluating the binding strength to the corresponding epitope. This can be done by TCR-ligand k_{off} rate measurements [163]. K_{off} rates assess the structural avidity by measuring the dissociation of monomeric pHLA molecules (k_{off} rate) from surface-expressed TCR molecules. Importantly, T cell populations with slower k_{off} rates also showed protective capacity in two murine infection models [163]. We therefore assumed that k_{off} rate measurements could be helpful in guiding the selection of SARS-CoV-2-specific TCRs. For k_{off} rate measurements, *Strep*-tagged pHLA molecules were multimerized on a *Strep*Tacin-APC backbone. The resulting *Strep*Tamer complex was then disrupted by the addition of D-biotin, which binds to *Strep*-tag binding sites on *Strep*Tacin with higher affinity than the pHLA *Strep*-tag. Imminent dissociation of *Strep*Tactin-APC was subsequently tracked by a decrease in the APC signal. The dissociation kinetics of the resulting monomeric pHLA molecules from the TCR depended on the binding strength of the TCR to the pHLA and were tracked via the fluorochrome Atto488 conjugated to the pHLA molecules (see 3.2.3.5) [163]. For better comparability between SARS-CoV-2-specific TCRs, TCRs specific for the same epitope were color-coded with anti-CD45 antibodies conjugated to different fluorochromes and then subsequently pooled for measurement in the same reaction. In this way, *Strep*Tactin dissociation started at the same time for each TCR:*Strep*Tamer complex after the addition of D-biotin.

For A3/ORF1_VTN-specific TCRs, TCR:pHLA k_{off} rates could be determined for three out of four TCRs with the slowest k_{off} rate for TCR 13 (half-life; 631 s), followed by TCR 43 (253 s) and TCR 28 (95 s). While the determined half-life of TCR 13 was variable between experiments, it was still higher on average compared to TCR 43 and TCR 28. This trend was also observed in multimer stainings, where TCR 13 showed stronger pHLA staining than TCR 43 and TCR 28. For TCR 32, no k_{off} rates could be determined because the dissociation was too fast to be measured (Figure 18A, C). For TCR 32, we could see *Strep*Tamer staining, but to a lesser extent than for the other A3/ORF1_VTN-specific TCRs as indicated by the lower initial mean fluorescence intensity (MFI). Nevertheless, we could still observe the loss of the backbone fluorescence intensity after D-biotin addition, indicating a technically successful *Strep*Tamer staining (Figure 18A). Overall, a k_{off} rate measurement for TCR 32 was consistent with a very weak A3/ORF1_VTN multimer staining, indicating low specificity of the TCR (see 4.2.3). For A1/ORF3a_FTS-specific TCRs, k_{off} rates could be determined for both TCRs with a mean half-life of 148 s for TCR 3456 and 32 s for TCR 3398 (Figure 18B, D). The quality of the *Strep*Tamer staining for TCR 3398 was not as high as for TCR 3456, as seen by a lower initial MFI (Figure 18B). This together with a slower half-life of TCR 3456, supports a stronger binding of TCR 3456 to the A1/ORF3a_FTS epitope. This trend was also observed in A1/ORF3a_FTS multimer stainings, where the multimer$^+$ mTRBC$^+$ staining for TCR 3456 was more robust compared to TCR 3398 (see 4.2.3).

We can conclude that k_{off} rate measurements of A3/ORF1_VTN as well as A1/ORF3a_FTS-specific TCRs showed significant differences between pHLA half-lives, which furthermore were in line with multimer staining intensities.

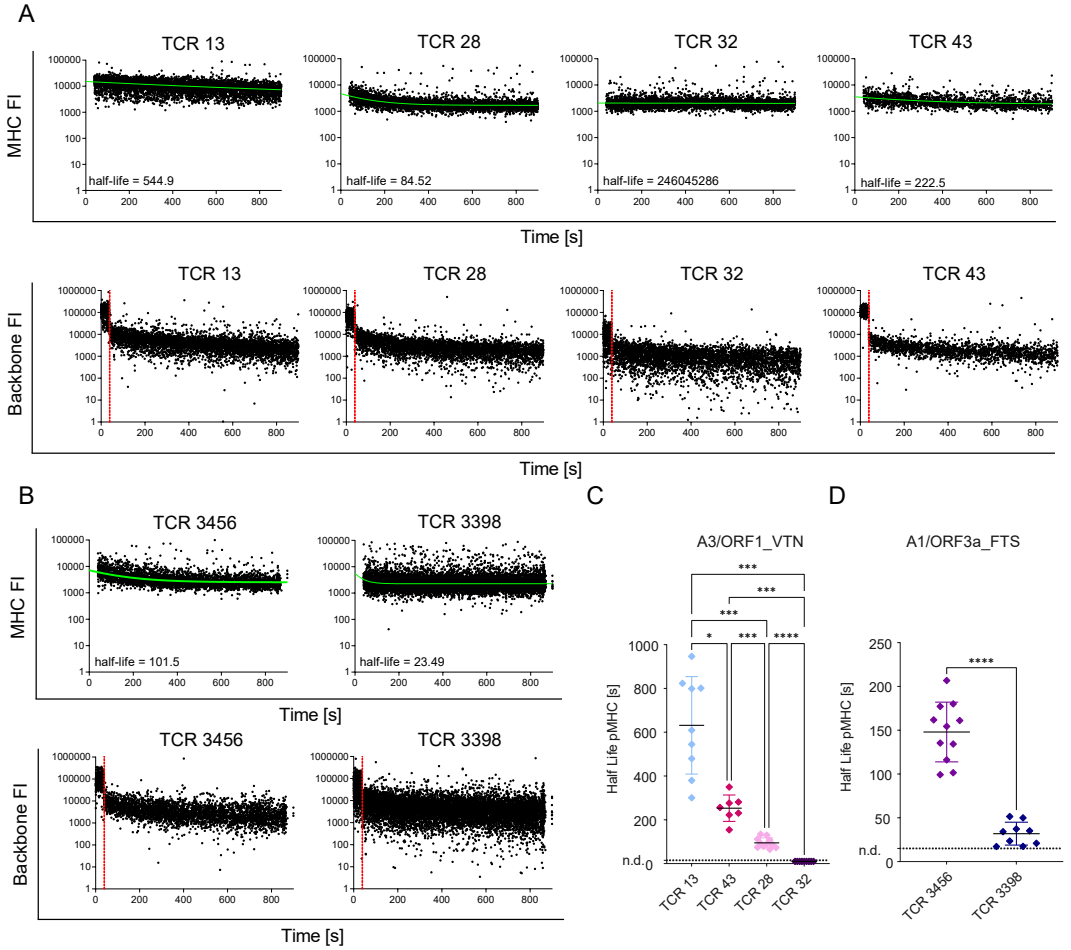

Figure 18: K_{off} rate measurements of A3/ORF1_VTN and A1/ORF3a_FTS-specific TCRs. (A-B) Representative pHLA-Atto488 and *Strep*Tactin-APC backbone dissociation over time for TCRs specific for A3/ORF1_VTN (A) and A1/ORF3a_FTS (B) epitopes. (A) For half-life calculation, nonlinear regression with binding kinetics: dissociation - one phase exponential decay was applied (green line). (B) Red dotted line indicates onset of dissociation by addition of D-biotin. (C-D) Quantification of the pHLA-Atto488 half-life of TCRs specific for A3/ORF1_VTN (C) and A1/ORF3a_FTS (D). Eight to twelve technical replicates are shown. The mean value is indicated by a black line. Half-life $\leq$ 10 s was determined to be not detectable (n.d.). FI = fluorescence intensity, *p-value $<$ 0.05, ***p-value $<$ 0.001, ****p-value $<$ 0.0001.

4.2.5 Peptide sensitivity measurement of A3/ORF1_VTN and A1/ORF3a_FTS specific TCRs

To evaluate the specificity of TCRs, one can also measure T cell activation signaling after antigen stimulation by quantifying intracellular cytokine secretion (functional avidity). Specifically, we determine the half-maximum effective concentration (-log$EC_{(50)}$, EC_{50}), by testing the sensitivity of TCR-transgenic $CD8^+$ T cells through titration of the corresponding epitope to saturation.

This was done by pulsing HLA-matched K562 cells with 10^{-4} M to 10^{-12} M of the respective peptide and subsequent cocultivation at an E:T ratio of 1:1 with TCR-transgenic CD8$^+$ T cells (see 3.2.7.1). Peptide-specific activation was measured by quantifying CD8$^+$ T cells expressing the proinflammatory cytokine IFN-γ. For epitope A3/ORF1_VTN, IFN-γ EC_{50} values of TCR 13 and TCR 28 were highest, followed by TCR 43 and finally TCR 32 with the lowest value. Interestingly, TCR 13 and TCR 28 had almost the same IFN-γ EC_{50} value with -7.58 and -7.56, respectively (Figure 19A (left), B) (Table 24), despite different k_{off} rates. TCR 43 followed with an IFN-γ EC_{50} value of -6.41. In contrast, k_{off} rate measurements suggested higher functionality for TCR 43 than for TCR 28. For the epitope A1/ORF3a_FTS, TCR 3398 and TCR 3456 both had a high IFN-γ EC_{50} value with -7.53 and -7.82, respectively (Figure 19A (right), B) (Table 24). This data is in line with k_{off} rate measurements which also support the higher specificity of TCR 3456. However, we did see no correlation of k_{off} rate measurements and IFN-γ EC_{50} values for TCRs specific for the A3/ORF1_VTN and A1/ORF3a_FTS epitopes (Figure 19C).

Overall, we can conclude that TCRs specific for the A3/ORF1_VTN and A1/ORF3a_FTS epitopes were highly specific and especially A3/ORF1_VTN-specific TCRs showed a wide range in IFN-γ EC_{50} values.

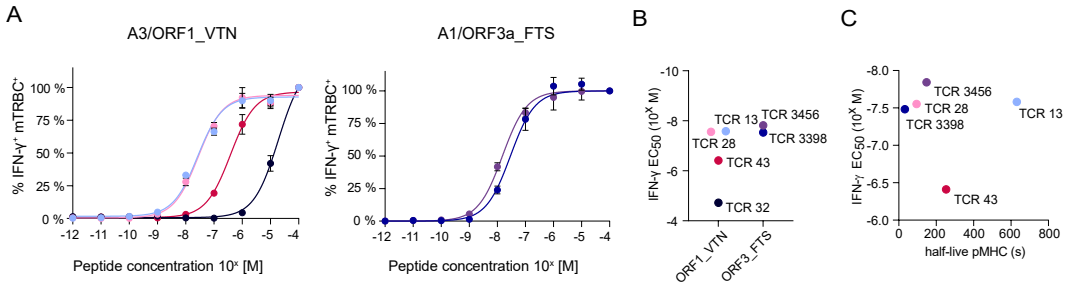

Figure 19: EC_{50} assays of TCRs specific for the A3/ORF1_VTN and A1/ORF3a_FTS epitopes. (A) Normalized EC_{50} assays from 10^{-4} M to 10^{-12} M. HLA-matched K562 cells were peptide-pulsed for 2 h prio to the addition of 50,000 TCR-transgenic CD8$^+$ T cells (E:T ratio = 1:1). Readout was by intracellular IFN-γ antibody staining. The mean of two experimental replicates ± SD is shown. (B) Summary of IFN-γ EC_{50} values. (C) Correlation plot of IFN-γ EC_{50} and pHLA half-lives. Parts of the figure were reprinted with permission from [84].

Table 24: IFN-γ EC_{50} values

Epitope	HLA type	TCR	IFN-γ EC_{50}
ORF1_VTN	HLA-A*03:01	13	-7.58
ORF1_VTN	HLA-A*03:01	28	-7.55
ORF1_VTN	HLA-A*03:01	32	-4.72
ORF1_VTN	HLA-A*03:01	43	-6.41
ORF3_FTS	HLA-A*01:01	3456	-7.84
ORF3_FTS	HLA-A*01:01	3398	-7.48

4.2.6 Implementation of gene scores for the prediction of TCR specificity

Having characterized SARS-CoV-2-specific TCRs at the functional level, we next wanted to investigate whether experimentally determined TCR specificity could be correlated with parental cell gene expression phenotypes after recent antigen stimulation measured during scRNAseq. We envisioned that this could help to understand if TCR specificity is embedded in transcriptional data and whether this information can be used to predict TCR specificity. To this end, we correlated experimentally determined IFN-γ EC_{50} values of SARS-CoV-2 TCRs with various parameters and gene scores to find the best fit. TCRs that were not specific for the investigated epitopes were assigned an IFN-γ EC_{50} value of 0 (Figure 20A).

We first correlated IFN-γ EC_{50} values to a published gene-ontology $CD8^+$ T cell activation score (GO:0036037), for which we assumed a good correlation of specific TCRs due to recent activation of T cells just prior to the scRNAseq experiment. While the correlation resulted in a good linear regression fit for all TCRs, for specific TCRs, only a r^2 of 0.60 was obtained. Note that the fit for all TCRs is distorted by the set IFN-γ EC_{50} value of 0. Therefore, results of correlations with all TCRs should also be considered independent of the IFN-γ EC_{50} value. Since the $CD8^+$ T cell activation score did not correlate well with our data for specific TCRs, we defined gene scores that would better fit our data set. The first score we defined is called the functionality score because it is based on genes that correlate with the ranking of IFN-γ EC_{50} values. As expected, since the training data set was used to define this score, we could see a good correlation for both, all TCRs and specific TCRs only (r^2: 0.96). Importantly, non-specific TCRs all had a functionality score lower than zero, while specific TCRs correlated according to their IFN-γ EC_{50} values. We also defined a reactivity score consisting of genes that had the most significant differential expression between specific and non-specific TCRs, i.e. TCRs with a measurable IFN-γ EC_{50} value and TCRs without an IFN-γ EC_{50} value. While the reactivity score showed a strong correlation with all TCRs, with non-specific TCRs having a negative reactivity score and specific TCRs having a score between one and two, only a weak correlation was found when considering only specific TCRs.

For scRNAseq of SARS-CoV-2-specific TCRs, T cells were isolated based on their INF-γ expression by a method called INF-γ catch (see 4.2.1). Our subsequent analysis was, therefore to understand if IFNG gene expression could also be correlate with TCR specificity. Again, a good correlation of IFN-γ EC_{50} values with all TCRs was found, but only a weak correlation of only specific TCRs was observed. As the next possible correlating parameter, we examined the clonotype size. Since clonal expansion is a hallmark of a functional immune response and T cells recognizing a specific epitope of the virus undergo extensive proliferation, we hypothesized that the clonotype size might correlate with TCR specificity. All identified SARS-CoV-2-specific TCRs were clonally expanded. Correlation of clonotype size with IFN-γ EC_{50} values showed surprisingly only a negative correlation for all TCRs as well as for specific TCRs. Considering all TCRs, no strong correlation was expected as the scRNAseq data set also contained TCRs specific for other epitopes. For specific TCRs, TCR 32 seemed to be the main driver of the negative correlation, as the clonotype was highly expanded but had a low IFN-γ EC_{50} value (Figure 20A). Next, we tried to see if a combination of scores could discriminate specific and non-specific TCRs even better. By correlating the two most promising scores, the functionality score and the $CD8^+$ T cell activation score, the TCR clonotype distribution could be observed according to the scores. Importantly, a combination of these scores resulted in a good two-dimensional separation of specific (A3/ORF1_VTN: TCR 13, TCR 28, TCR 43) (A1/ORF3a_FTS; TCR 3456, TCR 3398), low specific (A3/ORF1_VTN: TCR 32) and non-specific (A3/ORF1_VTN: TCR 18, TCR 40, TCR 82) (A3/ORF1_VTN: TCR 3399, TCR 3409) TCRs for all four donors (Figure 20B). We can conclude that by designing gene scores that fit to our EC_{50} values, we were able to discriminate between specific and non-specific TCRs.

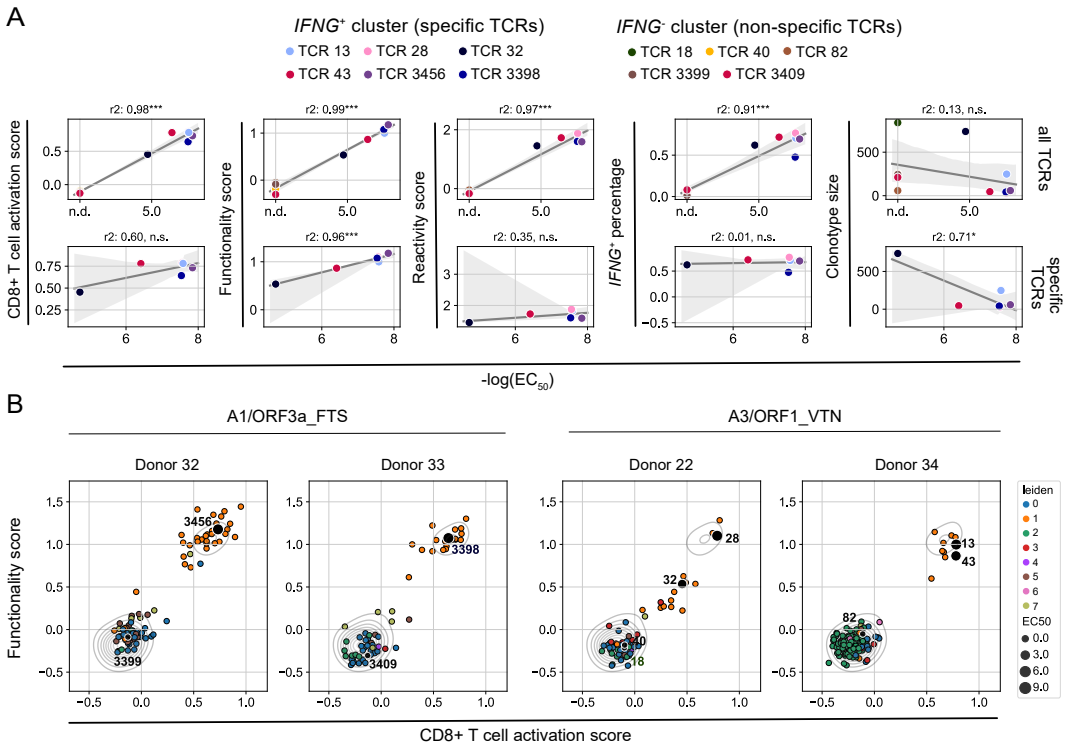

Figure 20: Definition of gene scores for the assignment of TCR functionality. (A) Linear regression analysis of experimentally determined IFN-γ EC_{50} values and gene expression scores for signatures of $CD8^+$ T cell activation, functionality, reactivity, $IFNG^+$ percentage, and clonotype size for all TCRs (top) and functional TCRs only (bottom). Wald test with t-distribution of test statistic was used for two-sided p-value hypothesis test (null hypothesis; slope is zero) (n.s. not significant, *p-value < 0.05, ***p-value < 0.001). The grey area represents the 95 % confidence interval. (B) Correlations of functionality score with $CD8^+$ T cell activation score are shown separately for TCRs from the same donor. TCRs are colored according to the Leiden cluster, the size of the dots corresponds to IFN-γ EC_{50} values. Contour plots show the kernel density estimation of all donors. The figure was reprinted with permission from [84].

4.2.7 Identification of TCRs against ten more immunodominant SARS-CoV-2 epitopes

To identify SARS-CoV-2-specific TCRs against more epitopes and also to test previously defined gene scores of recent activation, PBMCs from ten donors showing reactivity against a total of nine SARS-CoV-2 epitopes were expanded for twelve days in the presence of only their respective SARS-CoV-2 epitope and low levels of IL-2. Donors were then restimulated with their respective epitope for 4 h, followed by IFN-γ catch staining. If a donor responded to two epitopes, PBMCs of that donor were expanded in the presence of both epitopes and later split for separate restimulation. Prior to cell sorting, donors were additionally stained with hashtag antibodies. This allowed the pooling of sample material from many different donors in the same sequencing lane. In contrast to the first scRNAseq experiment, here only IFN-γ^+ $CD8^+$ T cells were sorted. This

allowed cells from multiple donors and conditions to be sorted in the same experiment. After sorting of IFN-γ^+ cells, scRNAseq and TCR identification were performed (Figure 21A).

Leiden cluster analysis revealed eight clusters of similarity. Since no negative control cells were included in this sort and theoretically only IFN-γ expressing cells were sorted, high expression of CD8$^+$ T cell activation markers was expected for several clusters. IFN-γ expression was detectable in multiple Leiden clusters, with the highest expression in clusters 0, 1 and 2. The pro-inflammatory cytokine IL-2 and the activation marker CD69 showed increased expression in clusters 1 and 2, whereas the T cell activation markers VSIR and XCL1 were highest expressed in clusters 0, 1 and 2. LAG3 seemed to be expressed at similar levels in all clusters, and CRTAM also showed the highest expression in cluster 6.

In summary, although there was some heterogeneity among the T cell activation markers, SARS-CoV-2-specific T cells appeared to be contained in clusters 0, 1 and 2. In contrast, clusters 3, 4, and 6 most likely contained irrelevant TCRs (Figure 21B).

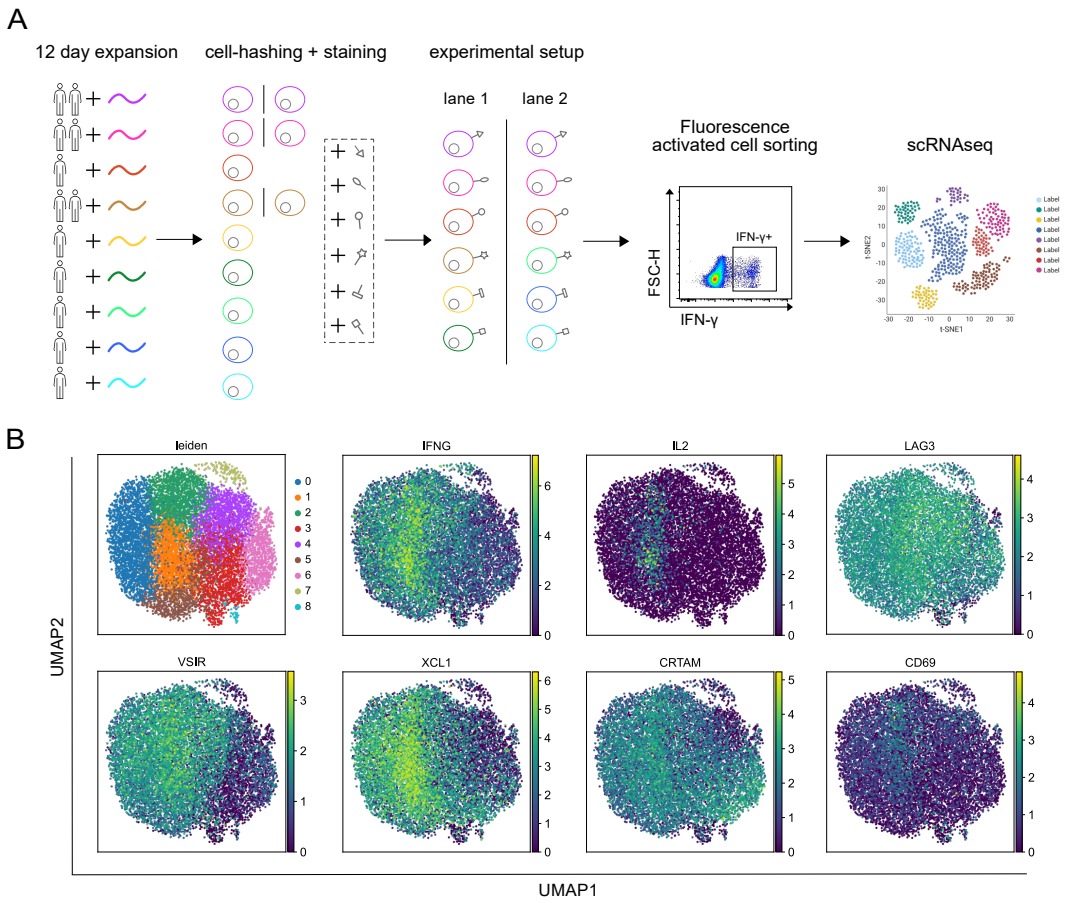

Figure 21: scRNAseq and identification of TCRs specific for nine SARS-CoV-2 epitopes. (A) Schematic of the workflow for TCR isolation. Only IFN-γ^+ cells were sorted (between 167 and 8,000 cells depending on the source material) and sequenced via 10x genomics. (B) UMAP clusters of Leiden clustering and gene expression of IFNG, IL2, LAG3, VSIR, XCL1, CRTAM, and CD69. The figure was modified and reprinted with permission from [84].

By applying the previously defined gene scores of recent activation to the new data set, we observed that the published CD8$^+$ T cell activation score, as well as the empirically determined functionality and reactivity scores, were higher in the Leiden clusters that overall showed the strongest gene expression of T cell activation markers (cluster 1, cluster 2) (Figure 22A). Next, we plotted the TCRs identified in the second scRNAseq experiment with the functionality and reactivity gene scores. In addition, we superimposed the functionally characterized TCRs from the first scRNAseq experiment on the functionality and reactivity score landscape of the second scRNAseq experiment. This allowed us to infer from the relative positions of the already characterized TCRs what the functionality landscape of the new TCR set might look like. We observed that TCRs from the new data set were distributed across the functionality landscape overlapping predominantly with characterized functional TCRs but also with characterized non-functional TCRs. We can therefore assume that the TCRs from the second scRNAseq experiment contain many high specificity TCRs and also some low specificity TCRs (Figure 22B).

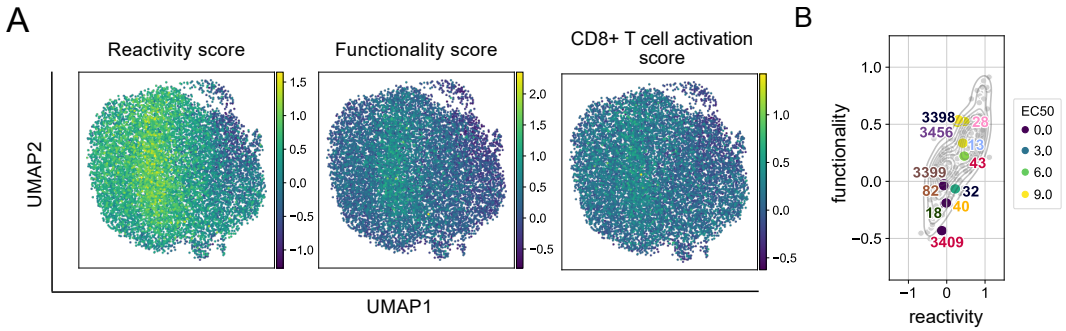

Figure 22: Correlation of signatures of recent activation with new TCRs. (A) Gene expression of reactivity score, functionality score, and CD8$^+$ T cell score of TCRs specific for nine SARS-CoV-2 epitopes. Data are shown in UMAP dimensions. (B) Correlation of functionality score and reactivity score for all TCRs specific for nine SARS-CoV-2 epitopes (in grey). Overlaid are TCRs from the previous scRNAseq experiment, highlighted in color according to their EC_{50} value. The figure was reprinted with permission from [84].

While some clonotypes were quite large in cell number, the overall TCR repertoire was highly polyclonal across epitopes and donors. Due to the combination of many samples, only a few clonotypes were obtained for some TCRs, limiting downstream repertoire analysis (Figure 23A). Overall, clonotypes were distributed across the functionality and reactivity score landscape according to their relative expression of score-defining genes. For some donor - epitope combinations, TCRs with putative high, medium and low specificity were identified (donor 24 - A1/ORF1_DTD, donor 24 - A2/S_LTD, donor 14 - A2/S_KIA). For other donor/epitope combinations, we found mainly TCRs with predicted high specificity (donor 25 - A1/ORF1_DTD, donor 25 - A1/ORF1_LTD, donor 29 - A11/ORF1_AMS, donor 29 - A11/ORF1_KLF, donor 27 - B35/ORF1_HSI). For donor 26 - A1/ORF1_GTD, even two discrete clusters could be identified, one with high specificity and one with low or no predicted specificity. Overall, there was a trend towards high scores for both, reactivity and functionality score, which also correlated to some extent with higher IFNG expression (Figure 23B).

In summary, we identified expanded CD8$^+$ T cell clonotypes and TCRs specific for ten additional immunodominant epitopes. The identified TCR repertoires were polyclonal and TCRs clustered according to their predicted specificity in the previously defined gene score landscape.

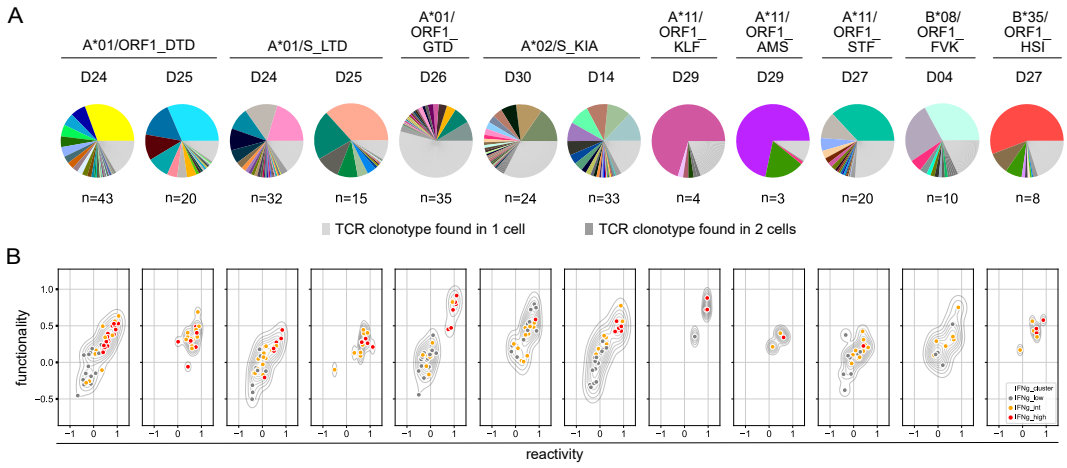

Figure 23: Clonotype classification of TCRs specific for nine SARS-CoV-2 epitopes. (A) Clonotype distribution of TCRs from eight donors specific for nine SARS-CoV-2 epitopes. One donor was previously excluded from further analysis due to insufficient cell numbers. Data are shown as parts of whole. (B) Correlation of functionality score and reactivity score for all clonotypes, shown separately for each donor – epitope combination. TCRs are color-coded according to their IFN-γ expression as low, intermediate or high as grey, yellow or red, respectively. The figure was reprinted with permission from [84].

In conclusion, in chapter 4.2 we successfully isolated SARS-CoV-2-specific CD8$^+$ T cells and identified SARS-CoV-2-specific TCRs from mild COVID-19 patients. Specifically, we expanded A3/ORF1_VTN and A1/ORF3a_FTS-specific CD8$^+$ T cells *in vitro*, followed by fresh restimulation with the corresponding epitope to induce signatures of recent activation. We then used the expression of the pro-inflammatory cytokine IFN-γ to isolate recently activated CD8$^+$ T cells by sorting and subsequently identified TCRs by performing scRNAseq. We identified transcription clusters with detectable or absent IFNG expression and speculated to find epitope-specific TCRs in the IFNG$^+$ cluster. Using CRISPR/Cas9-mediated OTR, we re-expressed TCRs in healthy donor PBMCs and were able to demonstrate epitope specificity, binding specificity, and functionality of TCRs from the IFNG$^+$ cluster by performing multimer staining, k_{off} rate measurements, and IFN-γ EC_{50} assays. For the A3/ORF1_VTN epitope, we additionally observed differences between highly specific TCRs and a less specific TCR as seen by lower multimer staining, slower half-life and lower IFN-γ EC_{50} values. Compared to TCRs identified from the IFNG$^+$ cluster, TCRs from the IFNG$^-$ cluster were non-specific for the A3/ORF1_VTN and A1/ORF3a_FTS epitopes, suggesting potential correlations between transcriptional signatures and TCR functionality. By correlating experimentally determined IFN-γ EC_{50} values of specific and non-specific TCRs with differential gene expression, we subsequently designed gene signatures that correspond to TCR specificity. Finally, by performing a second TCR isolation experiment with ten additional epitopes, we applied these gene signatures to the new data set of TCRs and suggested their specificity according to their relative position in the gene score landscape compared to previously characterized TCRs.

4.3 Functional characterization of a second set of SARS-CoV-2-specific TCRs in J-TPR cells

4.3.1 Use of the J-TPR system for high-throughput TCR characterization

The functional characterization of TCRs in primary CD8$^+$ T cells is quite tedious, since after CRISPR/Cas9-mediated OTR and confirmation of transgenic TCR KI, T cells are only fit for experiments for a few weeks. After that, the TCRs have to be reintegrated into a new batch of PBMCs. The often required purity sorting of TCR-transgenic T cells, together with the time required for expansion (three to four weeks), can greatly affect the overall functionality of the T cells. For the high-throughput characterization of SARS-CoV-2-specific TCRs, we therefore used the J-TPR cell line. J-TPR cells, which are derived from Jurkat E6.1 cells (ATCC: TIB-152), have been modified so that response elements for the T cell activation transcription factors NFAT, NF-kB, and AP-1 drive the expression of the fluorescent proteins CFP, eGFP, and mCherry, respectively [168]. Activation of TCRs can therefore be measured by the emission spectra of these proteins. Compared to the use of PBMCs for functional screening, J-TPR cells offer several advantages. The reporter system allows easy readout of TCR activation by flow cytometry. In addition, the use of a cell line allows for better comparability due to no donor-to-donor variability and also for unlimited culturing, which is ultimately more time and cost efficient, making high-throughput assays more feasible.

To first determine whether TCR functionality in J-TPR cells is comparable to peptide sensitivity measurements of primary CD8$^+$ T cells, we reintroduced TCRs from the first scRNAseq experiment into J-TPR cells. Similar to the re-expression of TCRs in primary CD8$^+$ T cells, TCR-α and TCR-β chains were *in silico* assembled into a HDR construct, amplified by PCR as a HDR template and re-expressed in J-TPR cells using CRISPR/Cas9-mediated OTR (see 4.2.2). We then performed peptide sensitivity assays with the A3/ORF1_VTN and A1/ORF3a_FTS epitopes. NFAT EC_{50} values ranged from -4.4 M (TCR 32) to -5.7 M (TCR 13) for the A3/ORF1_VTN epitope and from -6.07 M (TCR 3398) to -6.12 M (TCR 3456) for the A1/ORF3a_FTS epitope (Figure 24) (Table 26).

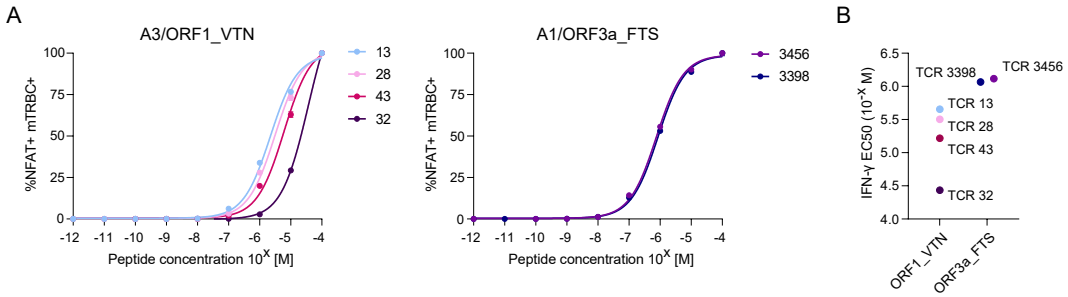

Figure 24: NFAT EC_{50} values of TCRs specific for A3/ORF1_VTN and A1/ORF3a_FTS epitopes. (A) Normalized IFN-γ EC_{50} curves from 10^{-12} M to 10^{-4} M and (B) quantification of TCR-engineered J-TPR cells specific for A3/ORF1_VTN and A1/ORF3a_FTS. The mean of two technical replicates ± SD is shown.

We next compared NFAT EC_{50} values with IFN-γ EC_{50} values (Figure 19) and found that the ranking of EC_{50} values remained the same for all A3/ORF1_VTN and A1/ORF3a_FTS-specific TCRs. However, we also noticed that the range of IFN-γ EC_{50} values observed in primary

$CD8^+$ T cells was narrower for NFAT EC_{50} values measured in J-TPR cells. In addition, NFAT EC_{50} values of A3/ORF1_VTN and A1/ORF3a_FTS-specific TCRs were lower than IFN-γ EC_{50} values (Figure 24B). When attempting to measure k_{off} rates of J-TPR cells (not shown), we found that J-TPR cells had lower surface TCR expression, resulting in unsuccessful k_{off} rate measurements. Lower surface TCR expression would also explain the reduced peptide sensitivity resulting in lower NFAT EC_{50} values. In conclusion, NFAT EC_{50} measurements in J-TPR cells were comparable to IFN-γ EC_{50} measurements in primary $CD8^+$ T cells, confirming that J-TPR cells are suitable for high-throughput characterization of TCRs.

4.3.2 Re-expression of SARS-CoV-2 TCRs in J-TPR cells

To validate previously defined gene signatures and to determine the quality of additional pHLA SARS-CoV-2 epitope repertoires, we intended to re-express and functionally characterize TCRs with different HLA restrictions identified in the second scRNAseq experiment. After evaluating TCRs for their functionality and reactivity scores, TCRs were selected for re-expression based on their relative position as either predicted specific (defined as positive values for both scores) or predicted non-specific (defined as a negative value for at least one of the scores) (Figure 25) (Table 25).

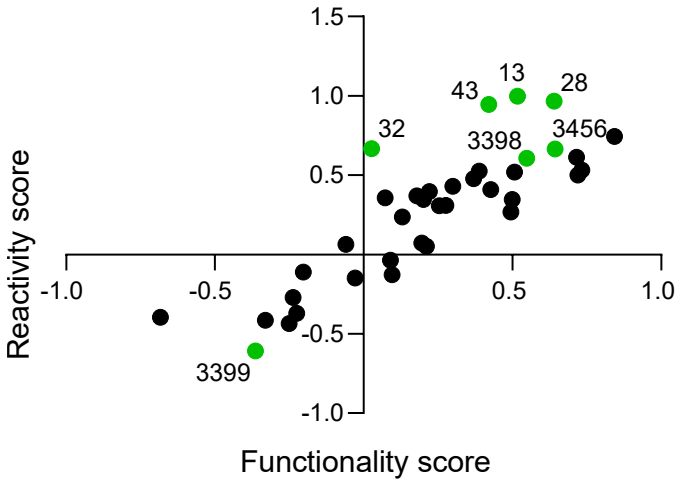

Figure 25: Functionality and reactivity scores for SARS-CoV-2-specific TCRs. Functionality and reactivity scores of TCRs from the first (green) and second (black) scRNAseq experiment.

In total, 37 TCRs specific for nine SARS-CoV-2 epitopes were selected for re-expression. To facilitate detection of cells with transgenic TCRs by flow cytometry, TCRs from the second scRNAseq experiment were also designed to contain murine constant chains. Following CRISPR/Cas9-mediated OTR, SARS-CoV-2-specific J-TPR cell lines could therefore be sorted for expression of the transgenic TCR by staining of the murine constant region (mTRBC) (Figure 26).

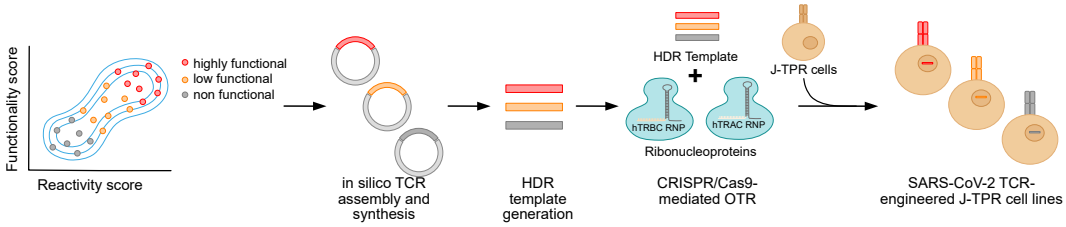

Figure 26: Workflow of the generation of SARS-CoV-2-specific TCR-engineered J-TPR cell lines. Schematic illustration of TCR selection based on gene score values, *in silico* assembly, HDR template generation and integration into J-TPR cells via CRISPR/Cas9-mediated OTR. The figure was reprinted with permission from [177].

SARS-CoV-2 TCR-engineered J-TPR cell lines were generated for all selected TCRs via CRISPR/Cas9-mediated OTR (see 3.2.5). Successful KO of endogenous TCR and KI of transgenic TCR were assessed by flow cytometry using hTCR and mTRBC staining, similar to primary $CD8^+$ T cells. KO efficiencies ranged from 99.3 % to 97.3 % and KI efficiencies from 0.1 % to 11.7 % (Figure 27A - B). TCR-engineered J-TPR cells ($mTRBC^+$) were then sorted for purity and expanded. Sorted J-TPR cells showed long-term expression of the transgenic TCR with no significant decrease in receptor expression, making them suitable for downstream functional characterization (Figure 27C).

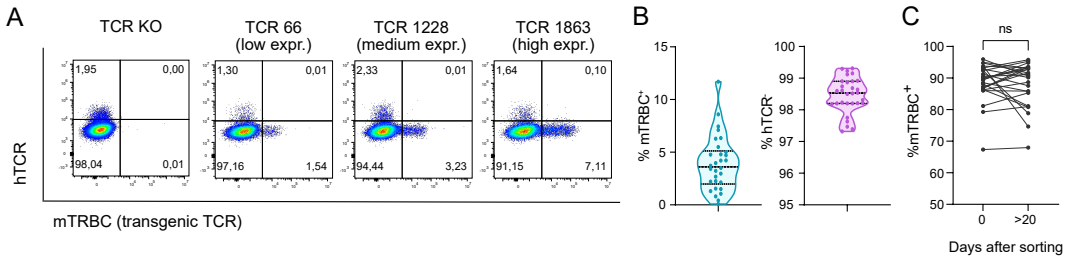

Figure 27: Generation of TCR-engineered SARS-CoV-2-specific J-TPR cell lines. (A) Flow cytometry plots showing endogenous TCR KO (hTCR) and transgenic TCR KI (mTRBC) representative of a TCR with high, medium and low KI efficiency. Cells were gated on J-TPR cells, singlets, living. (B) Quantification of KO/KI for all SARS-CoV-2-specific J-TPR cell lines shown as violin plots. The mean is shown as a broad dashed line and the quartiles as narrow dashed lines. (C) Tracking of transgenic TCR expression over time. Data points from the same TCR are connected by a black line. Paired t-test was used to calculate significance (ns = not significant). The figure was reprinted with permission from [177].

In summary, we selected 37 TCRs from the second scRNAseq experiment to confirm the gene scores and to identify epitope-specific TCRs, which we subsequently re-expressed in J-TPR cells via CRISPR/Cas9-mediated OTR.

4.3.3 pHLA multimer staining of TCR-engineered J-TPR cells

To evaluate the binding of SARS-CoV-2-specific TCRs to their respective epitopes, multimer staining was performed for all TCR-engineered J-TPR cell lines (Figure 28). We observed a range of multimer staining from 99 % for TCR 499 to 25 % for TCR 1864. TCR 76 showed

no correlation between pHLA multimer and mTRBC staining, and was therefore considered multimer negative. Based on this observation, TCRs with reactivities of $\leq 5\,\%$ were considered multimer negative.

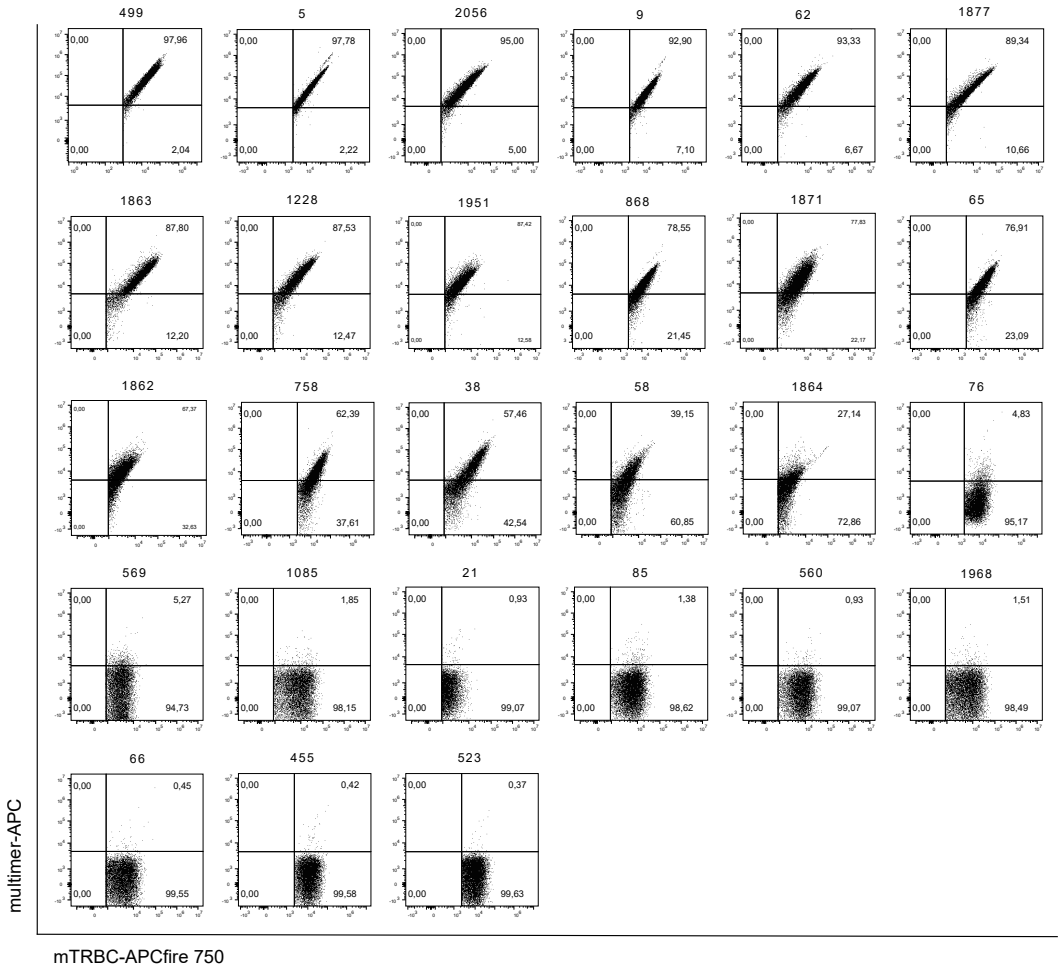

Figure 28: Multimer staining of SARS-CoV-2-specific TCR-engineered J-TPR cell lines. Multimer staining is shown in decreasing multimer$^+$ mTRBC$^+$ frequencies from left to right and top to bottom. To quantify the multimer$^+$ rate of mTRBC$^+$ cells, cells were gated on J-TPR cells, singlets, living and mTRBC$^+$ expression. The figure was reprinted with permission from [177].

Interestingly, a range of multimer positivity was also observed over the same epitope (e.g., A1/ORF1_DTD, A11/ORF1_STF) (Figure 29). For A1/ORF1_DTD, five TCRs with positive multimer staining (TCR 5, TCR 9, TCR 868, TCR 65, TCR 758; ordered by decreasing multimer$^+$ frequency) and two TCRs with negative multimer staining (TCR 455, and TCR 523) were measured. For A11/ORF1_STF, three TCRs with positive multimer staining (TCR 1951, TCR 1871, and TCR 1862; ordered by decreasing multimer$^+$ frequency) and one TCR with negative multimer staining (TCR 569) were measured. The three TCRs putatively specific for the B35/ORF1_VPF epitope (TCR 1896, TCR 1917, and TCR 1996) did not show positive multimer staining. Based on their reactivity and functionality scores, we would have expected TCR 1896

to be reactive to the B35/ORF1_VPF epitope and the other two TCRs to be negative (Table 25). In addition, TCRs specific for the A2/S_KIA epitope (TCR 10, TCR 34, TCR 54, TCR 63, TCR 87, TCR 250, TCR 478) did not show a positive multimer response.

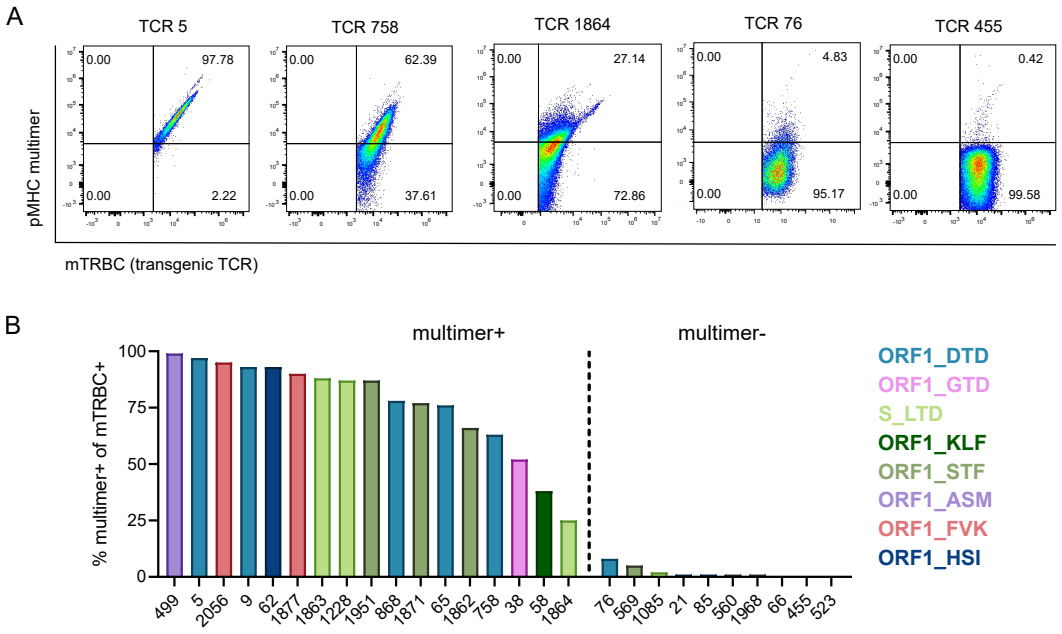

Figure 29: Quantification of pHLA multimer staining of SARS-CoV-2-specific TCR-engineered J-TPR cells. (A) Flow cytometry plots showing representative multimer$^+$ mTRBC$^+$ populations with high (TCR 5), medium (TCR 758), low (TCR 1864) and no pHLA multimer staining (TCR 76, TCR 455). Cells were gated on J-TPR cells, singlets, living and mTRBC$^+$ expression. (B) Quantification of multimer$^+$ mTRBC$^+$ populations of all SARS-CoV-2-specific TCR-engineered J-TPR cell lines. Bar graphs of TCRs responding to the same epitope are shown in the same color. The figure was reprinted with permission from [177].

As a next step, we wanted to understand if the gene scores defined from the first scRNAseq experiment could be used to predict the TCR specificity of the second scRNAseq experiment. For this, the multimer staining frequencies of SARS-CoV-2-specific TCRs from the second scRNAseq experiment were overlaid with the gene scores from the first scRNAseq experiment. For most TCRs, the multimer staining showed a nice association with the gene scores, with multimer$^+$ TCRs also having positive functionality and reactivity scores. TCRs with no multimer staining tended to be low for both scores (Figure 30A). Of the eight predicted non-specific TCRs based on their gene scores, six were confirmed and two TCRs reacted with SARS-CoV-2 multimers. The two false negative TCRs, TCR 1862 and TCR 1951, were both specific for the A11/ORF1_STF epitope and were well above the detection limit with values of 66 % and 87 % multimer$^+$ J-TPR cells. Of the 19 predicted specific TCRs, we could confirm the prediction of 15 TCRs with positive multimer staining. For four TCRs the predicted specificity could not be confirmed (TCR 21, TCR 76, TCR 65, TCR 560). TCR 76 was selected as the first TCR with negative multimer staining. Contrary to the prediction, TCR 85 and TCR 560 had a very high value for both the functionality score and the reactivity score (Figure 30B and C). Finally, we calculated the sensitivity and specificity of our gene scores. The sensitivity is the true positive rate, and

here describes the probability of detecting true multimer$^+$ TCRs within the set of predicted positive TCRs (true positive TCRs are divided by the sum of true positive and false negative TCRs (15 TCRs / (15 TCRs + 2 TCRs) = 0.88)). The specificity is the true negative rate and describes the probability of detecting true multimer$^-$ TCRs (true negative TCRs are divided by the sum of true negative and false positive TCRs (6 TCRs / (6 TCRs + 4 TCRs) = 0.60)). Overall, this resulted in a sensitivity of 88 % and a specificity of 60 %. We excluded from this analysis TCRs that were predicted to be specific for the B35/ORF1_VPF epitope due to the non-functioning multimer, as later confirmed by a positive EC_{50} value of TCR 1896 (see 4.3.4). We also excluded TCRs predicted to be specific for the A2/S_KIA epitope since their lack of specificity and functionality is most likely due to errors in sample sorting or processing, and their inclusion would have drastically affected the specificity calculations.

In summary, we can conclude that the gene signatures defined from the first scRNAseq experiment did indeed predict the specificity of putative SARS-CoV-2-specific TCRs from the second scRNAseq experiment. Furthermore, we found that the characterized TCRs exhibit heterogeneity in the quality of epitope recognition.

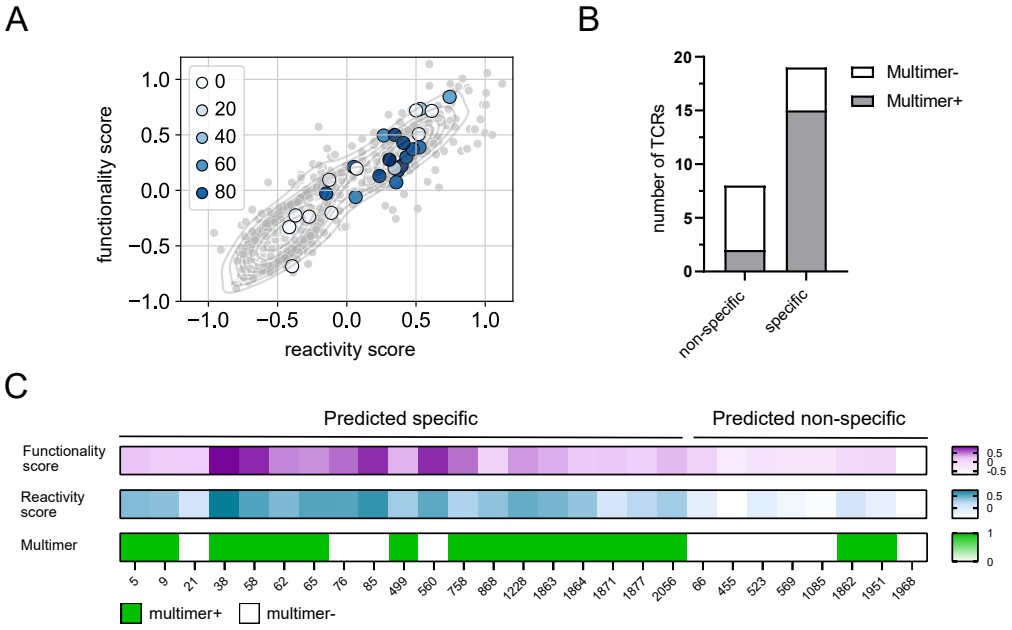

Figure 30: Correlation of multimer staining with the prediction of gene scores. (A) Gene scores superimposed on the multimer staining of selected TCRs, color-coded according to the intensity of the multimer staining. (B) Assignment of the number of multimer$^+$ and multimer$^-$ TCRs according to the prediction of specific and non-specific. (C) Plots of gene scores and multimer staining per TCR. Gene scores are shown as a continuous color code and multimer staining as positive (green) or negative (white). The figure was adapted with permission from [177].

4.3.4 Peptide sensitivity measurements of TCR-engineered J-TPR cells

To measure peptide sensitivity, activation of TCR-engineered J-TPR cells was assessed after co-culture with peptide-pulsed HLA-matched K562 cells. Log scale peptide titration from 10^{-12} M to 10^{-4} M resulted in a gradual increase in NFAT response element activation as measured by the

reporter molecule GFP (Figure 31A). Overall, we observed different levels of NFAT-GFP activation for different TCR-engineered J-TPR cell lines at the same peptide-pulsing concentration. For example, TCR 5 showed strong NFAT expression at 10^{-7} M while TCR 758 showed similar activation only one log scale higher at 10^{-6} M (Figure 31B). Since activation level correlates with peptide sensitivity, TCR activation with less peptide presented on target cells correlates with higher sensitivity and potency of a TCR.

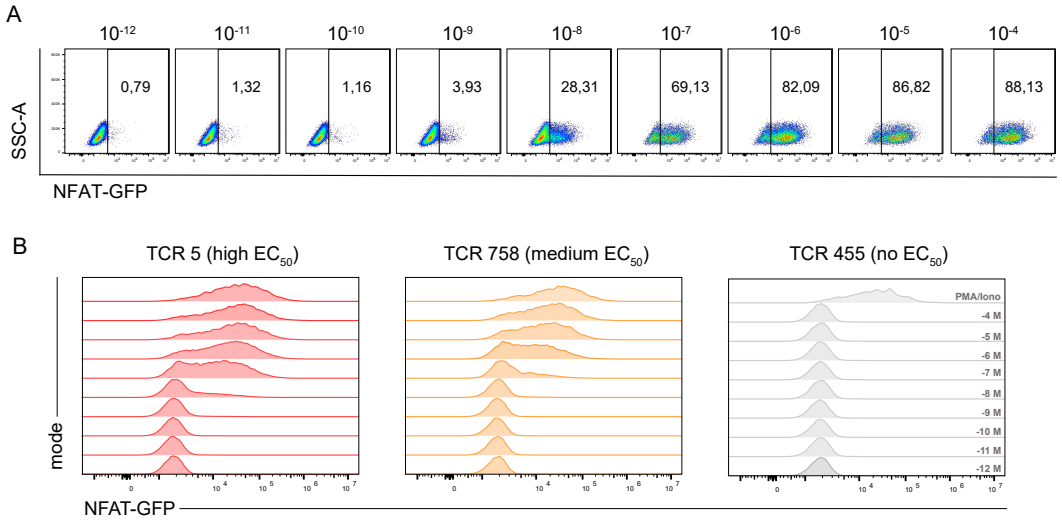

Figure 31: NFAT-GFP signal of J-TPR cells following coincubation with peptide-pulsed K562 cells. (A) Representative flow cytometry plots of NFAT-GFP signal from TCR-engineered J-TPR cells after 18 h coincubation with peptide-pulsed K562 cells according to peptide titration from 10^{-12} M to 10^{-4} M. Cells were gated on J-TPR cells, singlets, and living. (B) NFAT-GFP MFI after corresponding peptide titration of a TCR with high (TCR 5), medium (TCR 758) and no (TCR 455) IFN-γ EC_{50} value. Parts of the figure were reprinted with permission from [177].

Calculation of EC_{50} values resulted in a range of NFAT EC_{50} from -7.7 M (TCR 499) to -3.2 M (TCR 2056) for 19 SARS-CoV-2 epitope-specific TCRs (Table 26). Of the 30 TCRs, 19 were specific and eleven TCRs had no measurable NFAT EC_{50} value (Figure 32A). The multimer staining for B35/ORF1_VPF-specific TCRs (TCR 1896, TCR 1917, and TCR 1996) was negative (see 4.3.3). Interestingly, TCR 1896, which was also predicted to be specific according to the gene score classifications (Table 25), had a measurable IFN-γ EC_{50} value, suggesting that the B35/ORF1_VPF pHLA multimer was indeed not functional. For the A1/ORF1_DTD, A11/ORF1_STF and A2/S_LTD epitopes, we identified several functional TCRs. To better understand the measured differences in functionality, for follow-up studies, we focused on TCRs specific for the A1/ORF1_DTD and A11/ORF1_STF epitopes. For A1/ORF1_DTD-specific TCRs, we observed a range of NFAT EC_{50} values from -6.4 M (TCR 76) to -7.6 M (TCR 5). The A11/ORF1_STF epitope-specific TCRs were also highly functional with a smaller range of NFAT EC_{50} values from -6.8 M (TCR 1862) to -6.9 M (TCR 1871) (Figure 32C).

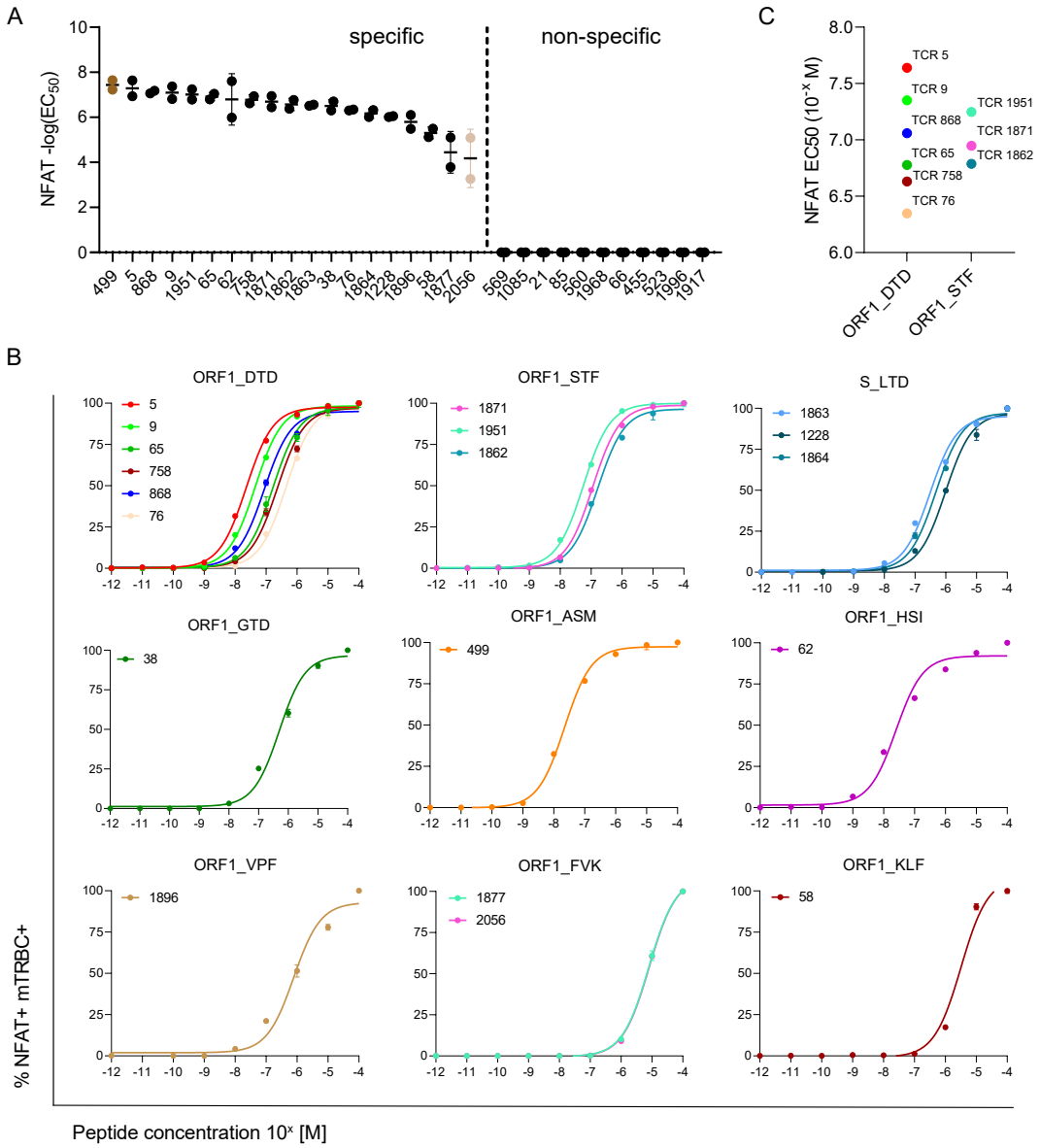

Figure 32: NFAT EC_{50} values of TCRs specific for SARS-CoV-2 epitopes. (A) Quantification of NFAT EC_{50} values of all SARS-CoV-2-specific TCR-engineered J-TPR cell lines. Experimentally determined specific and non-specific TCRs are separated by a dotted line. The highest and lowest functional TCR are colored in dark and light brown, respectively. Two experimental replicates and the mean are shown. (B) Normalized NFAT-GFP curves from 10^{-12} M to 10^{-4} M of TCR-engineered J-TPR cells responding to nine epitopes. TCRs against the same epitope are shown in the same graph. (C) NFAT EC_{50} quantification of TCRs specific for A1/ORF1_DTD and A11/ORF1_STF. EC_{50} = half maximal effective concentration. The figure was adapted with permission from [177].

The experimentally determined NFAT EC_{50} values showed a good correlation with the gene scores, as most TCRs with a high value in both scores also had high NFAT EC_{50} values (Figure 33A). However, we did not observe a strong correlation of EC_{50} levels with gene scores. Of the 20 predicted specific TCRs, 17 were confirmed specific and three showed no specificity, resulting in a sensitivity of 89 %. Of ten predicted non-specific TCRs, eight were confirmed non-specific and two had a measurable NFAT EC_{50} value, resulting in a specificity of 73 % (Figure 33B). The two TCRs falsely predicted to be non-specific (TCR 1862, TCR 1951), had a measurable NFAT EC_{50} value and also reliable multimer staining, confirming that the TCRs were indeed specific. The three TCRs for which specificity could not be confirmed (TCR 21, TCR 65, TCR 560) also had negative multimer staining. TCR 76 was predicted to be functional, but was classified by us as non-specific due to a low frequency of multimer$^+$ TCR-engineered T cells. An NFAT EC_{50} value of -6.3 M finally confirmed the specificity of TCR 76. TCRs specific for the B35/ORF1_VPF epitope (TCR 1896, TCR 1917, TCR 1996) had a measurable NFAT EC_{50} value despite a previously measured negative multimer staining, suggesting a possible technical limitation with the B35/ORF1_VPF multimer (Figure 33C).

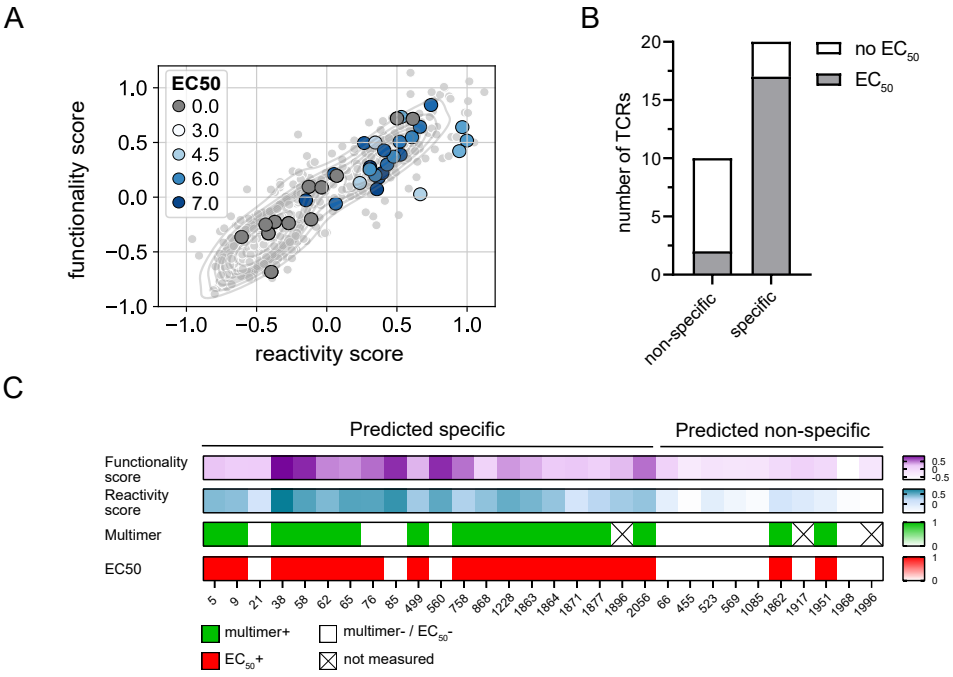

Figure 33: Correlation of NFAT EC_{50} values with prediction of gene scores. (A) Overlay of functionality and reactivity scores for all TCRs with NFAT EC_{50} values. TCRs are color-coded according to their NFAT EC_{50} values in five intensity levels from grey to white to blue. (B) Allocation of the number of TCRs with or without a measurable NFAT EC_{50} value according to the prediction of specific and non-specific. (C) Plots of gene scores, multimer and NFAT EC_{50} values for each TCR. Gene scores are shown as a continuous color code, and multimer staining and NFAT EC_{50} values are shown as positive (green and red, respectively) or negative (white). TCRs for which no multimer staining could be measured are marked with an X. The figure was adapted with permission from [177].

All EC_{50} value calculations were based on analysis of the T cell activation transcription factor NFAT. A linear correlation for the expression of NFAT and NFκB was previously shown for CMV-specific TCRs [178]. To investigate whether NFκB also has a linear correlation with NFAT for SARS-CoV-2-specific TCRs, NFκB EC_{50} values were calculated for the investigated set of SARS-CoV-2-specific TCRs. The NFκB EC_{50} values ranged from -4.7 M (TCR 2056) to -7.4 M (TCR 499). The separation of the measured specific and non-specific TCRs was the same as for the NFAT EC_{50} values (Figure 34A). For linear correlation analysis, a simple linear regression was applied and yielded a strong correlation for the two transcription factors with $R^2 = 0.9988$ (Figure 34B).

In conclusion, we found that while gene signatures showed good prediction of specific and non-specific TCRs, no strong correlation was observed with the level of NFAT EC_{50} values. NFAT EC_{50} values also had a range of heterogeneity and a linear correlation with NFkB EC_{50} values.

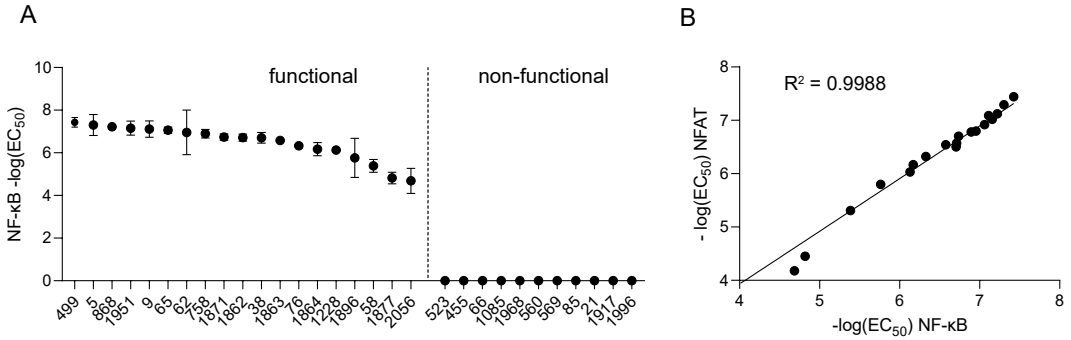

Figure 34: NFκB EC_{50} values of TCRs specific for SARS-CoV-2 epitopes. (A) Quantification of NFκB EC_{50} values of all SARS-CoV-2-specific TCR-engineered J-TPR cell lines. Experimentally determined specific and non-specific TCRs are separated by a dashed line. Two experimental replicates and the mean are shown. (B) Correlation of NFAT and NFκB EC_{50} mean values. R^2 of the linear correlation is shown. EC_{50} = half maximal effective concentration. The figure was reprinted with permission from [177].

4.3.5 Improvement of the predictive capacity of the gene sores

The 'original' functionality and reactivity gene scores were defined based on $CD8^+$ T cell IFN-γ EC_{50} values of a few TCRs specific for the two SARS-CoV-2 epitopes A1/ORF3a_FTS and A3/ORF1_VTN. We observed that the gene scores did not correlate very well with the measured NFAT EC_{50} values (Figure 33A), and hypothesized that the gene signatures might not work equally well for the new dataset, especially since the training set consisted of a limited selection of TCRs. To investigate the reason for the misalignment of the gene scores with the NFAT EC_{50} values, we calculated both scRNAseq experiments together and plotted the correlation of the NFAT EC_{50} values of all TCRs separately for the reactivity and functionality scores. For comparison, NFAT EC_{50} values of TCRs from the first scRNAseq experiment were also included. With few exceptions, predicting TCR specificity for the new set of TCRs based on the 'original' reactivity score worked well. For the 'original' functionality score, however, TCR functionality prediction worked rather poorly, with no clear correlation of the score with experimentally determined NFAT EC_{50} values (Figure 35A). We hypothesized that this could be due to one of two reasons. Either the addition of more TCRs from the second scRNAseq experiment resulted in a more accurate gene score, or different confounding experimental conditions cause differences

in gene regulation. By including the NFAT EC_{50} values of the 30 additional TCRs specific for nine SARS-CoV-2 epitopes from the second scRNAseq experiment, a 'refined' gene score was calculated with the assumption that it would provide a more accurate representation of the entire data set. Interestingly, all genes comprising the 'refined' reactivity score were part of the 'original' score, highlighting the potential relevance of this gene list for predicting whether or not a SARS-CoV-2 TCR would be specific after short-term *in vitro* reactivation. To no surprise, genes defining the 'refined' functionality score were not part of the 'original' score (Figure 35B). To further investigate this observation, we analyzed the shifts of normalized gene scores from 'original' to 'refined' values. The normalized reactivity score of all TCRs remained comparable from 'original' to 'refined', as indicated by many straight lines. For the normalized functionality score, however, we observed large shifts from the 'original' to the 'refined' score for most TCRs, mostly upward (Figure 35C). Importantly, the experimentally measured NFAT EC_{50} values from the first and second experiments showed a nice positive correlation with the 'refined' functionality gene score (Figure 35D). More details on the scRNAseq analysis, as well as 'original' and 'refined' gene score calculations, can be found in [177]. In summary, we found that adding 30 more TCRs from the second scRNAseq experiment to redefine the gene scores improved the predictive power of both scores.

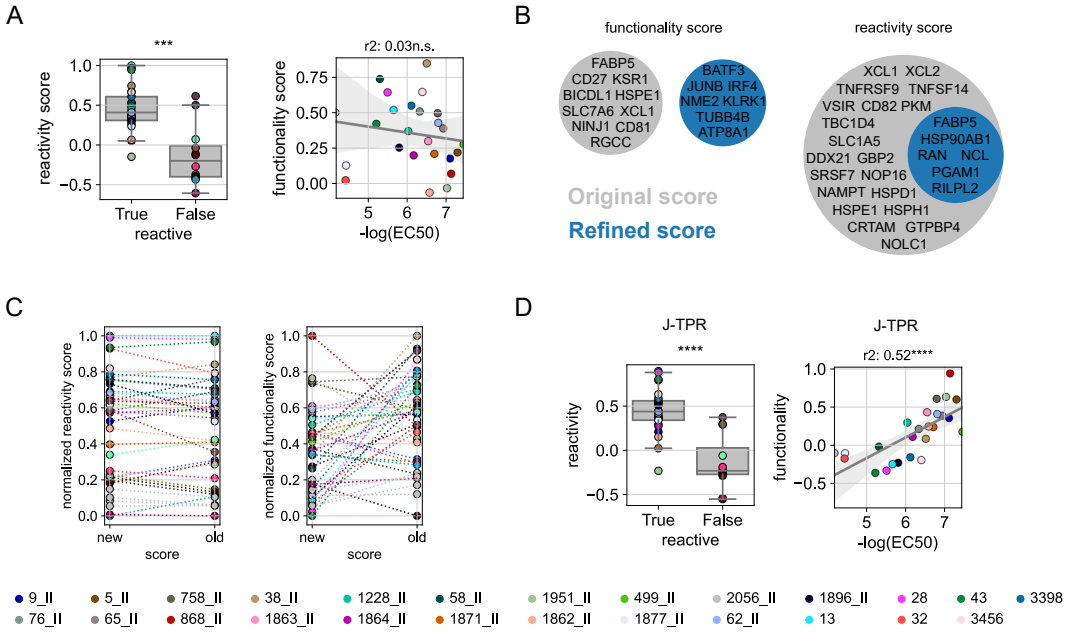

Figure 35: Improvement of gene scores for better prediction of TCR specificity. (A) 'Original' reactivity and functionality scores defined by TCRs from the first scRNAseq experiment. Shown are TCRs from both scRNAseq experiments. For the reactivity score, TCRs with a measurable NFAT EC_{50} value (defined as True) and TCRs with no measurable NFAT EC_{50} value (defined as False) are shown. For the functionality score, actual NFAT EC_{50} values are shown. (B) Gene lists of the original and refined scores. (C) Normalized 'original' and 'refined' gene scores. The same TCRs for both values are connected by a dotted line. (D) 'Refined' reactivity and functionality score defined by all TCRs from both scRNAseq experiments. Scores were defined as in (A) (***$p < 0.001$, ****$p < 0.0001$). The figure was reprinted with permission from [177].

4.3.6 Cellular avidity measurements of TCRs specific for A1/ORF1_DTD and A11/ORF1_STF

Functional data measured *in vitro* often do not correlate well with actual *in vivo* functionality. Recently, a few studies have been published suggesting that cellular avidity can accurately predict cellular responses *in vivo* and outcomes during immunotherapy [179, 180]. Unlike cellular affinity, which measures singular pHLA - TCR interactions, cellular avidity considers the entire immunological synapse. We measured the cellular avidity of SARS-CoV-2-specific TCRs in a novel instrument called z-movi (Lumicks, Amsterdam, Netherlands). Here, target cells are bound to a glass surface, after which effector cells are flushed into the microfluidic channel. Target and effector cells are then allowed to form immunological synapses for 5 min. By applying an acoustic force ramp from 0 pN to 1000 pN, effector cells detach from target cells depending on their cellular avidity. Cellular avidity was measured for TCR-engineered J-TPR cells specific for the A1/ORF1_DTD and A11/ORF1_STF epitopes. As a control, TCR 455, which was isolated for the A1/ORF1_DTD epitope but has not shown epitope specificity or functionality in previous assays, was used. Measurable differences between bound J-TPR cells and the control TCR, TCR 455, were observed for all TCRs. Some TCRs remained bound to target cells even at higher forces (A1/ORF1_DTD: TCR 5, TCR 9; A11/ORF1_STF: TCR 1871, TCR 1951), indicating high cellular avidity. Other TCRs had a rather fast reduction of bound J-TPR cells (A1/ORF1_DTD: TCR 76, A11/ORF1_STF: TCR 1862), indicating low cellular avidity (Figure 36A).

As a rule of thumb, cellular avidity was quantified at the beginning of the plateau where the change of the control TCR over 100 pN is less than 2 %. Among the A1/ORF1_DTD-specific TCRs, TCR 5 and TCR 9 had the strongest cellular avidity, followed by TCR 65, TCR 758 and TCR 76. Among the A11/ORF1_STF-specific TCRs, TCR 1871 had the strongest avidity, followed by TCR 1951 and TCR 1862 (Figure 36B). We next correlated all cellular avidity values at their respective 2 % plateau value with NFAT EC_{50} values, but could only observe a low correlation (Figure 36C, top). Since we noticed that the trends of TCRs from both epitopes went in different directions, we correlated only A1/ORF1_DTD TCRs and detected a significant correlation with an R^2 value of 0.94 (Figure 36C, bottom). A11/ORF1_STF TCRs alone did not show a strong correlation, and we suspected that this might be because the two values, cellular avidity and NFAT EC_{50}, were too similar (not shown).

In summary, we measured the cellular avidity of TCRs specific for the A1/ORF1_DTD and A11/ORF1_STF epitopes and found a range of cellular avidity that also correlated well with the level of NFAT EC_{50} for the A1/ORF1_DTD epitope.

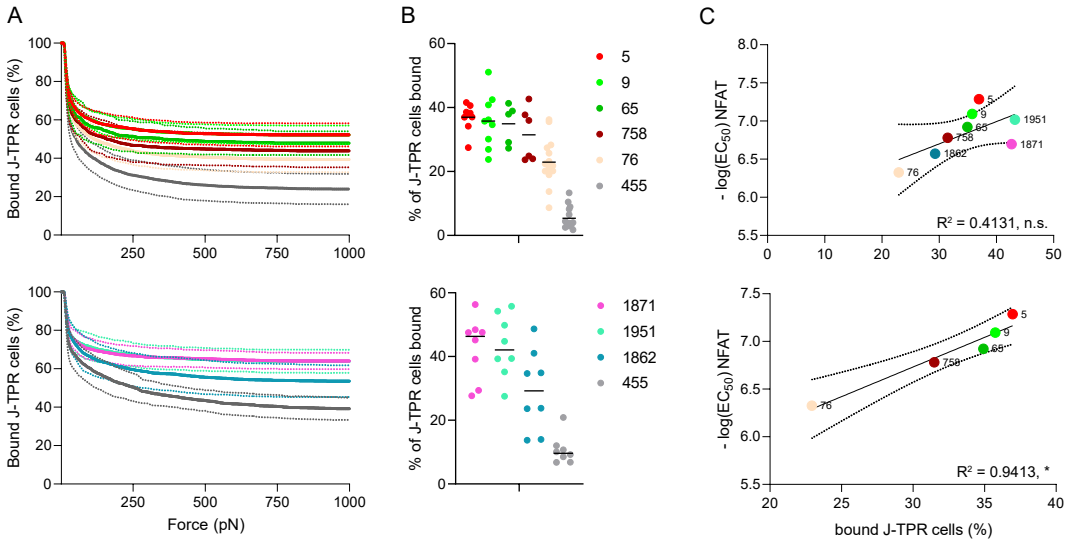

Figure 36: Cellular avidity measurements of TCR-engineered J-TPR cell lines. (A-B) TCRs specific for A1/ORF1_DTD (top) and A11/ORF1_STF (bottom) are shown. (A) Percentage of bound J-TPR cells over a force ramp from 0 pN to 1000 pN. Mean of five to 15 technical replicates and ± SD are shown. (B) Normalized J-TPR cells bound at Δ 100 pN < 2 %. Normalization to TCR 455 was performed separately for each chip. The mean is shown as a black line. (C) Simple linear regression analysis with 95 % confidence interval of NFAT EC_{50} value with bound J-TPR cells at 2 % value from (B) for all TCRs (top) and A1/ORF1_DTD TCRs only (bottom) (n.s. not significant, *p-value < 0.05).

To conclude this section, we showed comparable functionality of TCRs in J-TPR cells previously characterized in primary $CD8^+$ T cells. While TCRs specific for the A3/ORF1_VTN and A1/ORF3a_FTS epitopes had higher NFAT EC_{50} values and while the range, especially for A3/ORF1_VTN-specific TCRs, was more narrow compared to IFN-γ EC_{50} values, the NFAT EC_{50} ranking remained the same as for primary $CD8^+$ T cells. Thus, we evaluated the J-TPR cell line as suitable for high-throughput measurement of SARS-CoV-2-specific TCRs. Next, we classified TCRs from the second scRNAseq experiment as predicted specific and non-specific based on defined gene signatures. To expand the repertoire of functional TCRs and to test the predictive ability of the gene scores, we re-expressed 37 TCRs in J-TPR cells. We confirmed that the previously defined gene signatures predicted the multimer specificity of the re-expressed TCRs. Multimer staining of re-expressed TCRs in J-TPR cells was also heterogeneous across epitopes and even for the same epitope. This finding supports the development of a polyfunctional TCR repertoire after mild COVID-19 infection. Experimentally determined peptide sensitivity values (NFAT EC_{50}) also showed a good correlation with gene scores. We furthermore found a linear correlation of NFAT EC_{50} values with NFκB EC_{50} values as published in the literature [178]. However, we did not find a strong correlation between the level of EC_{50} values and gene signatures. By calculating new gene scores that include the entire data set of TCRs, we defined a 'refined' gene signature that correlated better with our data set. Nevertheless, we envision that the 'refined' gene signature may be useful for predicting TCRs in other settings. Finally, we were able to show that cellular avidity measurements of A1/ORF1_DTD-specific TCRs correlated with NFAT EC_{50} values.

4.4 Killing assays of SARS-CoV-2-specific TCR-transgenic CD8+ T cells

In chapter 4.1, we showed that CD8+ T cell immune responses against SARS-CoV-2 were readily detectable in most mild COVID-19 patients after an *in vitro* expansion step. We further demonstrated that CD8+ T cell immune responses were long-lasting and that reinfection can boost CD8+ T cell immunity against SARS-CoV-2. We continued to identify CD8+ T cell immunodominant SARS-CoV-2-specific epitopes responsible for the observed immune responses and found that most donors had immune responses against multiple SARS-CoV-2-specific epitopes. In chapters 4.2 and 4.3, we then identified TCRs recognizing these epitopes to better understand the underlying mechanism of SARS-CoV-2-specific CD8+ T cell immunity. For functional TCR characterizations, we re-expressed these TCRs in healthy donor PBMCs or J-TPR cells using CRISPR/Cas9-mediated OTR and showed that SARS-CoV-2-specific TCRs were highly specific and functional for their respective epitope. In an *in vivo* infection scenario, antigen-specific CD8+ T cells, after recognizing their respective epitope, continue to eliminate virus-infected target cells. For a complete functional characterization of TCRs, it is therefore essential to demonstrate antigen-specific lysis of infected or epitope-presenting target cells.

4.4.1 Killing potential of TCR-engineered CD8+ T cells specific for A3/ORF1_VTN and A1/ORF3a_FTS

4.4.1.1 Near-physiological killing assay using replicating SARS-CoV-2-GFP virus

Antigen-specific killing assays can be used to assess the cytotoxic capacity of TCRs *in vitro*. To measure target cell killing in the context of SARS-CoV-2 infection, we developed an *in vitro* killing assay in which we infected competent A549 target cells with SARS-CoV-2 virus. Competent A549 cells are derived from the lung epithelial carcinoma cell line A549, which was transduced with the viral entry receptor ACE2 and H2B-RFP for live cell tracking. We additionally modified competent A549 cells with HLA molecules to ensure that our epitope of interest was presented on the surface. Thus, *in vitro* SARS-CoV-2 infection of competent A549 cells is mediated via the ACE2 receptor, after which viral replication as well as presentation of viral proteins on HLA molecules occurs similar to *in vivo* infections. For replicating virus killing assays, competent A549-HLA-A*01 or -A*03 cells were infected with a GFP-modified SARS-CoV-2 WT virus (SARS-CoV-2-GFP). The fluorescent protein GFP is encoded in the viral genome and produced as a protein upon infection. Infection can therefore be easily tracked by measuring GFP+ expression in target cells. After the addition of SARS-CoV-2-specific TCR-engineered CD8+ T cells, the killing of infected target cells can be measured by a decrease in GFP+ signal. A selection of TCR-engineered CD8+ T cells specific for the A3/ORF1_VTN and A1/ORF3a_FTS epitopes were generated and added to infected HLA-matched competent A549 target cells 24 h after infection. Image acquisition was continued for another 48 h, followed by endpoint analysis (Figure 37A).

For TCR 13 and TCR 28-engineered CD8+ T cells, an E:T dependent decrease in virus growth (GFP+ signal) was observed over the 72 h time course. Similarly, the number of infected target cells (RFP+ GFP+ signal) showed a titration-dependent effect over time. Following the addition of TCR 32-engineered CD8+ T cells, a reduction in virus growth and infected targets was only observed at high E:T ratios. This is consistent with previously measured functionality data where TCR 32 was shown to be specific for the A3/ORF1_VTN epitope but of low functionality. Significantly, no unspecific killing of uninfected target cells (RFP+ signal) was observed for all TCRs and all E:T ratios (Figure 37B). Quantification of viral spread and survival of infected

target cells at the endpoint showed the same trend as during live acquisition. Endpoint quantification also showed E:T dependent killing for TCR 13 and TCR 28, and killing at the high E:T ratio of 30:1 for TCR 32 (Figure 37C).

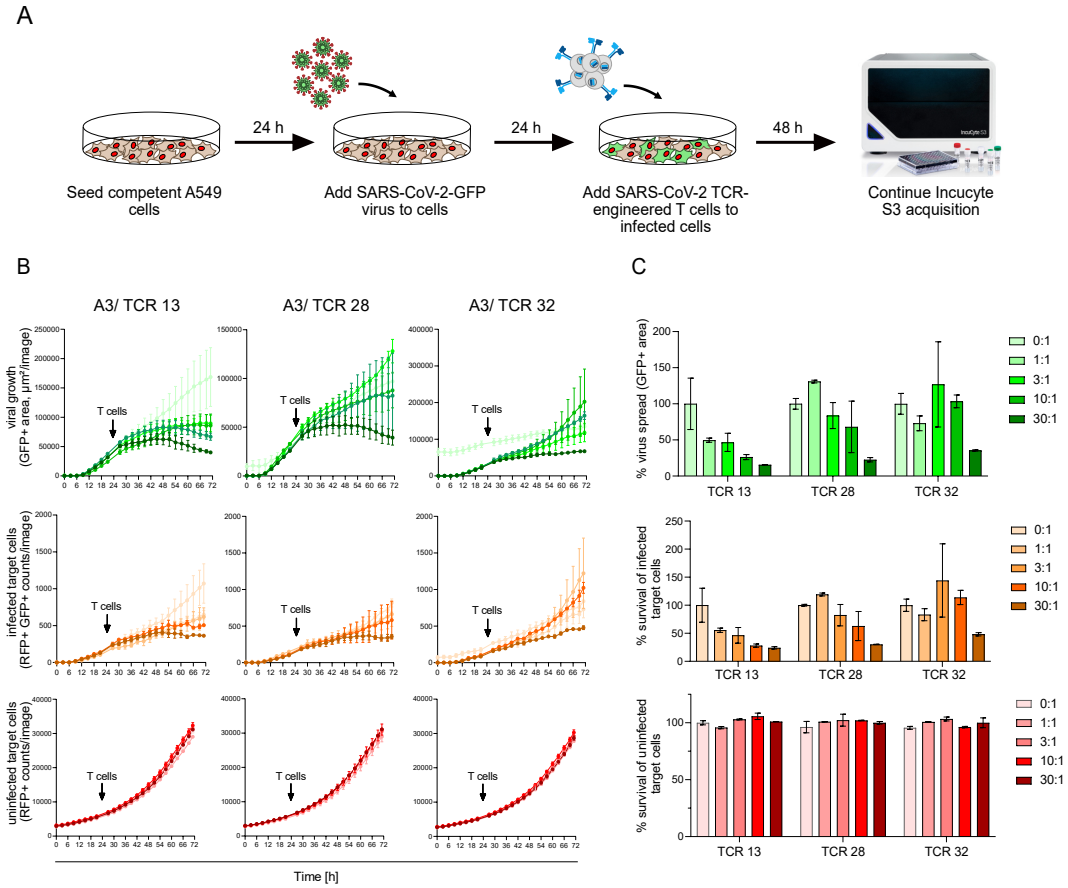

Figure 37: Incucyte killing assay with epitope A3/ORF1_VTN-specific TCR-engineered CD8$^+$ T cells. (A) Schematic of Incucyte killing assay. Competent A549 cells were infected with SARS-CoV-2-GFP virus 24 h after seeding. 24 h post infection, SARS-CoV-2-specific TCR-transgenic CD8$^+$ T cells were added and the acquisition was continued for another 48 h. (B – C) Competent A549-HLA-A*03 cells were infected with SARS-CoV-2-GFP virus. 24 h post infection, epitope A3/ORF1_VTN-specific TCR-transgenic CD8$^+$ T cells were added at E:T ratios of 1:1, 3:1, 10:1, 30:1. Medium was added for the 0:1 condition. (B) Live tracking and (C) 72 h endpoint analysis of virus growth, infected and uninfected target cells. Shown is the mean of two technical replicates ± SD. T cell addition is marked at the 24 h time point. Data were normalized to the 0:1 condition to 100 %. Parts of the figure were reprinted with permission from [84].

In previous characterizations, we showed that TCR 3456, derived from the scRNAseq IFNG$^+$ cluster, is highly functional against the A1/ORF3a_FTS epitope. In contrast, TCR 3399 from the scRNAseq IFNG$^-$ cluster was not expected to result in specific target cell killing. Viral growth was greatly reduced after the addition of TCR 3456-engineered CD8$^+$ T cells for all E:T ratios,

but especially for the 10:1 and 30:1 ratios. Consistent with this, the number of infected target cells decreased after T cell addition for both E:T ratios. No cytotoxicity was observed for the negative control TCR, TCR 3399 and no unspecific killing of uninfected target cells was observed for both TCRs and all E:T titrations in A1/ORF3a_FTS-dependent killing assays (Figure 38A). An E:T dependent reduction in viral spread and survival of infected target cells was detected at the 72 h endpoint quantification for TCR 3456 but not for TCR 3399 (Figure 38B).

In conclusion, we demonstrated that TCR-engineered CD8$^+$ T cells, which showed to be functional for the A3/ORF1_VTN and A1/ORF3a_FTS epitopes, kill SARS-CoV-2-GFP virus-infected target cells in an E:T dependent manner. In addition, the low-functional TCR, TCR 32, showed killing only at high E:T ratios, and no unspecific killing of uninfected target cells was observed.

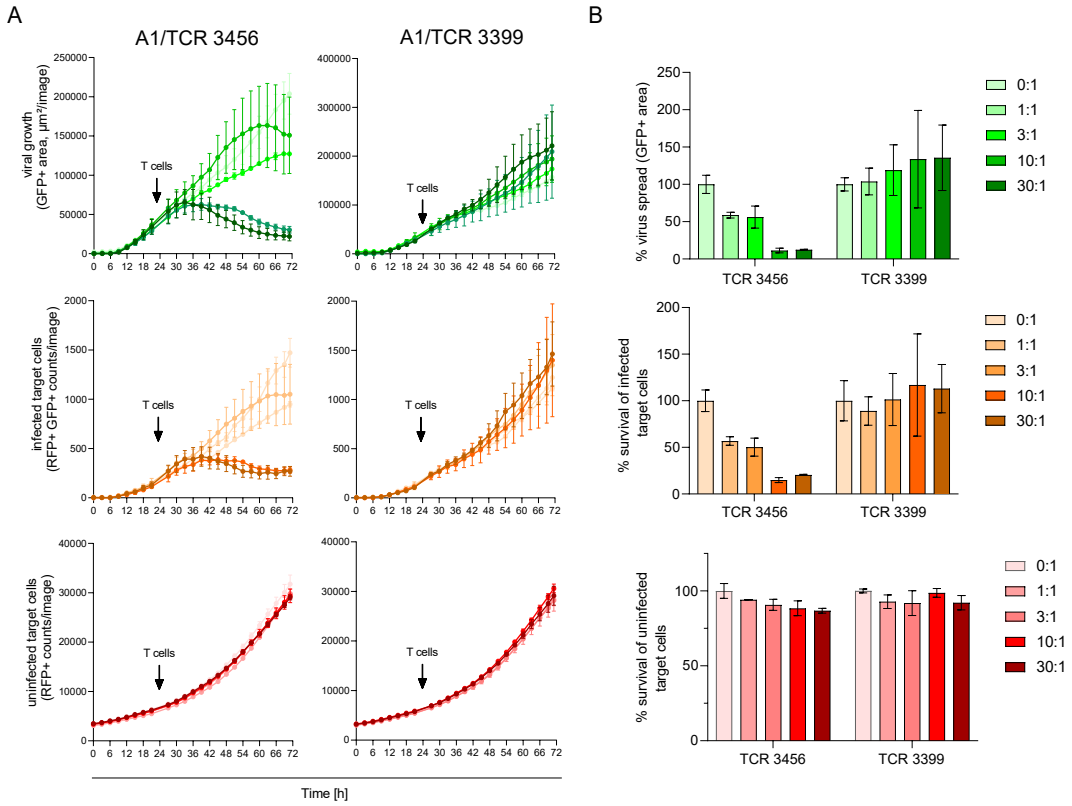

Figure 38: Incucyte killing assay with epitope A1/ORF3a_FTS-specific TCR-engineered CD8$^+$ T cells. (A – B) Competent A549-HLA-A*01 cells were infected with SARS-CoV-2-GFP virus. 24 h post infection, epitope A1/ORF3a_FTS-specific TCR-transgenic CD8$^+$ T cells were added at E:T ratios of 1:1, 3:1, 10:1, 30:1. Medium was added for the 0:1 condition. (A) Live tracking and (B) 72 h endpoint analysis of virus growth, infected and uninfected target cells. The mean of two technical replicates ± SD is shown. T cell addition is marked at the 24 h time point. Data were normalized to the 0:1 condition to 100 %. Parts of the figure were reprinted with permission from [84].

4.4.1.2 Near-physiological killing assay using SARS-CoV-2 ORF-transduced target cells

While the SARS-CoV-2 killing assay described above had the clear advantage of being close to an *in vivo* infection setting, it had several disadvantages. Viral infections required strict BSL3 work, which was only feasible at low-throughput. In addition, the low level of target cell infections resulted in highly variable data and thus the need for more experimental replicates. Furthermore, the production of the virus and the measurement of the MOI for each virus batch was very time consuming. As a result, we developed an alternative killing assay for which we generated A549 target cell lines transduced with a SARS-CoV-2 or control protein. This would ensure close to physiological epitope presentation while avoiding the technical limitations of working with viable viruses. We chose the SARS-CoV-2 protein Nsp2 for transduction because it carries the SARS-CoV-2 epitope A3/ORF1_VTN. Since the epitope is HLA-A*03 restricted, we further selected competent A549-HLA-A*03 cells to generate competent A549-HLA-A*03-Nsp2 cells. TCR-engineered $CD8^+$ T cells specific for the A3/ORF1_VTN epitope could thus be used for killing assays with competent A549-HLA-A*03-Nsp2 cells. As a control protein, we chose the humanized Gaussia luciferase protein (hGLuc, Gaussia).

Detailed steps of Gibson cloning are described in 3.2.4.2. Briefly, the mp72_RNF43_A269fs plasmid (Figure 39A) was digested with restriction enzymes (EcoRI and NotI). The resulting backbone was Gibson cloned together with the amplified eGFP fragment and either the SARS-CoV-2-Nsp2 insert from the pWPI_SARS-CoV-2-Nsp2 plasmid (Figure 39B) or the hGluc insert from the pWPI_Gaussia plasmid (Figure 39C). The final plasmids mp72_SARS-CoV-2_Nsp2_T2A_GFP (SARS-CoV-2-Nsp2 plasmid) (Figure 39D) and mp72_Gaussia_T2A_GFP (Gaussia plasmid) (Figure 39D) were used for retroviral transfection of competent A549-HLA-A*03 cells. Cells with successful transfection expressed GFP and Nsp2 (or GFP and the control protein Gaussia) as separate proteins due to polycistronic expression and post-transcriptional splicing. Competent A549-HLA-A*03-Nsp2 and competent A549-HLA-A*03-Gaussia cell lines were then sorted for GFP^+ expression and cocultured with $CD8^+$ T cells expressing relevant TCRs to evaluate cytotoxicity potential.

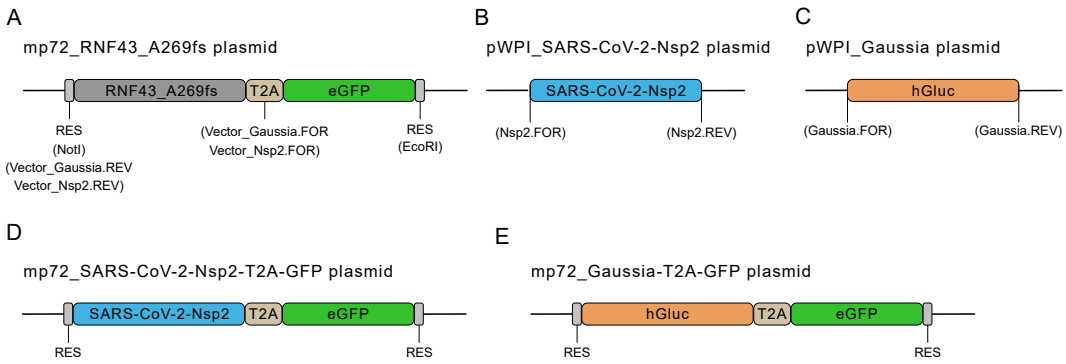

Figure 39: Recombination sites for Nsp2-T2A-GFP and Gaussia-T2A-GFP Gibson cloning. Section of plasmid maps with relevant restriction sites and binding sites of primers are marked. (A) Backbone plasmid pMP72 RNF43_A269fs. Section of plasmid maps of the target proteins (B) Nsp2 and (C) Gaussia used for Gibson assembly. Plasmids generated by Gibson cloning: (D) SARS-CoV-2-Nsp2 plasmid (mp72_SARS-Cov-2-Nsp2_T2A_GFP) and (E) Gaussia control plasmid (mp72_Gaussia_T2A_GFP). RES = restriction enzyme site.

For cytotoxicity measurements, the xCELLigence RTCA eSight instrument was used for cellular impedance measurements and image acquisition. Cellular impedance was measured by applying an electrical potential across the well using gold microelectrodes fused to the bottom of each well. This was used to measure target cell attachment and subsequent detachment. Specifically, competent A549-HLA-A*03-Nsp2 and competent A549-HLA-A*03-Gaussia target cell lines were seeded onto 96-well RTCA eSight plates and 24 h later TCR-engineered CD8$^+$ T cells were added. Impedance measurements and image analysis were then continued for another 48 h (Figure 40A). Due to the expression of H2B-RFP in the nucleus of A549 target cells, the amount of attached target cells can be tracked over time by quantifying the RFP signal in addition to the impedance measurement. Target cell killing was then quantified by total integrated intensity (TII), which takes into account the total amount of RFP signal by multiplying the fluorescence intensity by the fluorescent area (RRI x μm^2). Thus, target cell killing could be measured as a decrease in RFP TII after the addition of antigen-specific CD8$^+$ T cells, similar to impedance values.

TCR 13-, TCR 28-, and TCR 43-engineered CD8$^+$ T cells showed fast killing of competent A549-HLA-A*03-Nsp2 cells at an E:T ratio of 5:1. Compared to these TCRs, the killing ability of TCR 32-engineered CD8$^+$ T cells was limited (Figure 40B, green lines), consistent with previous functionality and killing data of TCR 32. This confirmed that the A3/ORF1_VTN epitope was processed and presented at sufficient levels on competent A549-HLA-A*03-Nsp2 cells and that the observed killing was comparable to the virus-infection model. As a control for endogenous expression of the peptide from the ORF system, we used competent-A549-HLA-A*03 cells pulsed with the A3/ORF1_VTN epitope. For TCR 13-, TCR 28-, and TCR 43-engineered CD8$^+$ T cells, complete lysis of competent A549-HLA-A*03 target cells pulsed with 10^{-5} M A3/ORF1_VTN peptide was observed (Figure 40B, orange lines). We hypothesized that epitope density on the target cell surface determines the speed at which target cells are recognized by TCR-engineered T cells. Since the killing of peptide-pulsed target cells was slightly faster than that of endogenously presented target cells, we would suggest that the epitope density on the surface of competent A549-HLA-A*03-Nsp2 cells was slightly less than 10^{-5} M. It is important to note that a peptide concentration of 10^{-5} M is quite high and that lower epitope densities would be expected in an *in vivo* setting. Also, in the peptide-pulsed condition, TCR 32-engineered CD8$^+$ T cells did not lyse all target cells according to virus-infected and endogenously presented target cell killing assays. In contrast to on-target effects, addition of TCR-engineered CD8$^+$ T cells to competent A549-HLA-A*03-Gaussia cells did not result in specific killing (Figure 40 B, blue lines). Also the addition of medium to competent Nsp2-A549 cells, competent A549-HLA-A*03-Gaussia cells, or competent A549 cells (pulsed and unpulsed) did not result in specific target cell lysis. For the positive control condition, TritonX, immediate target cell lysis was observed, visible as the fastest decrease in cellular impedance. The TII curves of all conditions showed the same trend as the cellular impedance curves (Figure 40C).

To better compare the killing curves between the different conditions, we calculated the area under the curve (AUC) (Figure 41A) for all TCR-engineered CD8$^+$ T cells and found low AUC values for the 'experimental conditions' ORF1_VTN pulsed and Nsp2-transduced for TCR 13, TCR 28, and TCR 43 and a higher AUC value for TCR 32, in line with the above observations. As expected, the Gaussia-transduced conditions, as well as the medium and unpulsed controls, had higher AUC values. To further quantify the observed differences, we normalized the killing of ORF1_VTN, Nsp2-transduced, and Gaussia-transduced to the unpulsed condition for ORF1_VTN. Triton X was used as a positive control with 100 % killing and medium unpulsed as a negative control with 0 % killing. The frequency of killed target cells was very high for the ORF1_VTN peptide-pulsed and Nsp2-transduced conditions for TCR 13, TCR 28, and TCR 43, while it was lower for the corresponding conditions for TCR 32. (Figure 41B).

In conclusion, we found that A3/ORF1_VTN-specific TCR-engineered CD8$^+$ T cells kill Nsp2-transduced target cell lines in an E:T dependent manner. Consistent with replicating virus killing assays, CD8$^+$ T cells engineered with highly-functional TCRs (TCR 13, TCR 28, TCR 43) kill Nsp2-transduced target cells with high efficiency, whereas the low-functional TCR, TCR 32, showed limited killing capacity. No specific cell lysis was observed for the control condition.

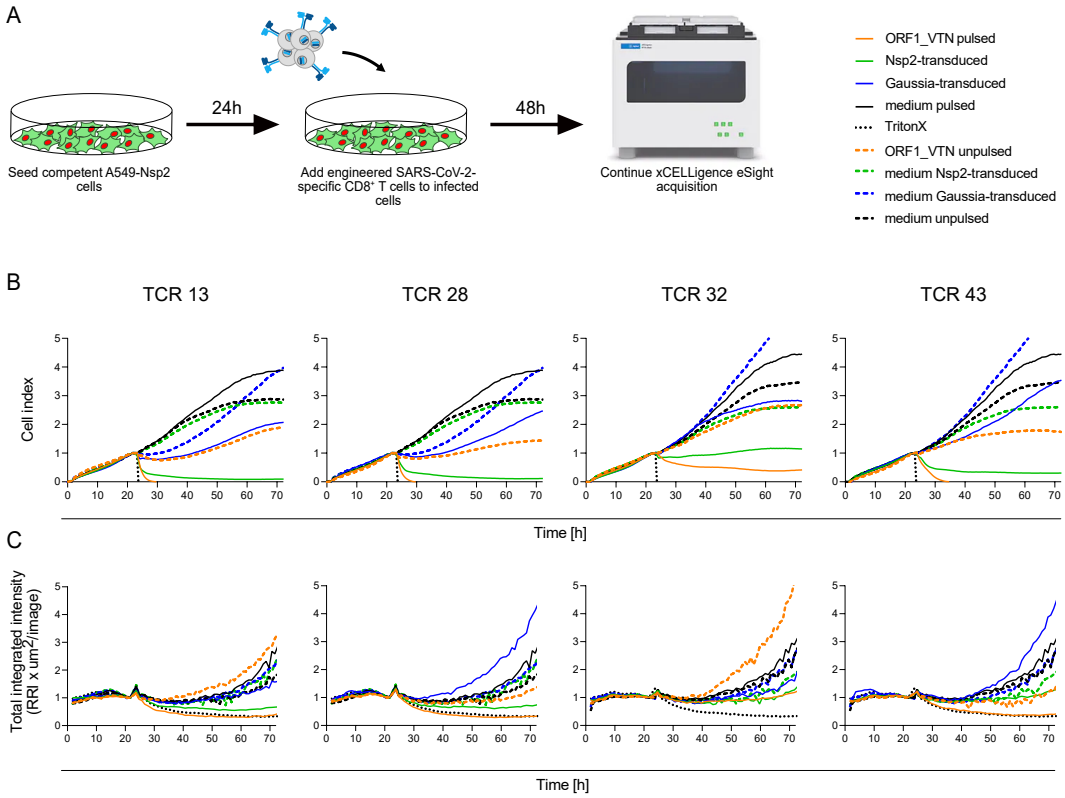

Figure 40: xCELLigence killing assay with competent A549-HLA-A*03-Nsp2 cells and A3/ORF1_VTN-specific TCR-engineered CD8$^+$ T cells. (A) Schematic workflow of the xCELLigence killing assay. Competent A549-HLA-A*03-Nsp2 target cells were seeded on 96-well RTCA eSight plates and incubated for 24 h before TCR-engineered CD8$^+$ T cells were added at an E:T ratio of 5:1. Acquisition was continued for another 48 h. (B) Cellular impedance and (C) normalized total integrated intensity (TII) (bottom) for TCR 13, TCR 28, TCR 32, and TCR 43-engineered CD8$^+$ T cells are shown. Competent A549-HLA-A*03 cells pulsed with A3/ORF1_VTN, competent A549-HLA-A*03-Nsp2 or competent A549-HLA-A*03-Gaussia cells were used as target cells. Either TCR-engineered T cells or medium was added. All data were normalized to the time point of T cell addition. An E:T ratio of 5:1 was used for all conditions. Parts of the figure were reprinted with permission from [155].

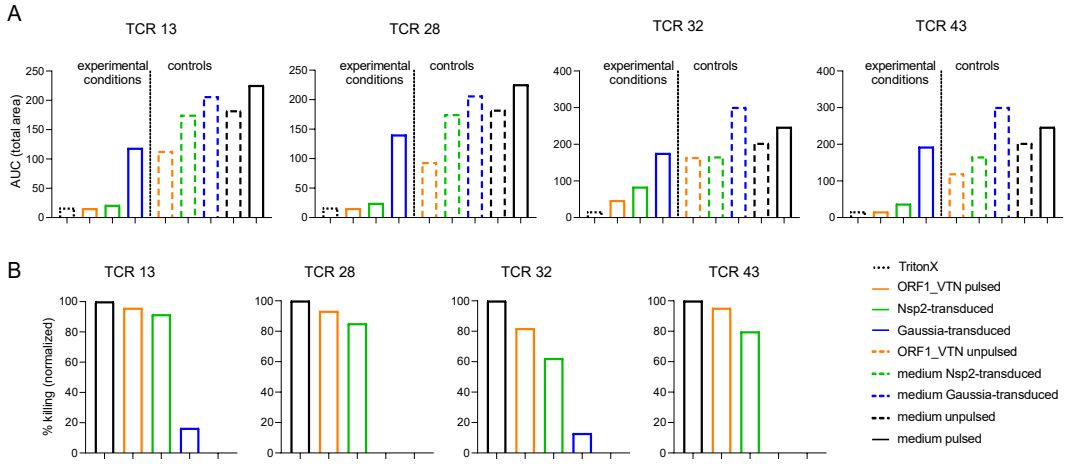

Figure 41: AUC quantification of xCELLigence killing assay with competent A549-HLA-A*03-Nsp2 cells. (A) AUC (total area) quantification of A3/ORF1_VTN-specific killing of TCR-engineered CD8+ T cells (TCR 13, TCR 28, TCR 32, TCR 43) over a 72 h time course. (B) Normalized AUC killing curves. Medium AUC was defined as 0 % killing and Triton X as 100 % killing. TCRs were normalized to the unpulsed A3/ORF1_VTN AUC condition. AUC = area under the curve.

4.4.2 Killing potential of TCR-engineered CD8+ T cells specific for A1/ORF1_VTN and A11/ORF1_STF

In functional TCR assays, such as J-TPR peptide sensitivity assays (see 4.3.4) or cellular avidity assays (see 4.3.6), TCRs specific for the A1/ORF1_VTN and A11/ORF1_STF epitopes showed a high degree of specificity. We were next interested to determine whether TCR-engineered CD8+ T cells were also cytotoxic. In the previous subchapter 4.4.1.2, we showed that transduction of transgenic antigens was comparable to that of epitope-pulsed target cells. In addition, the pulsing of peptides allows us to vary the level of antigen density compared to antigen-transduced target cells. Thus, next to determining the cytotoxic capacity of TCRs, we were also interested in understanding how the level of antigen density affects target cell killing. Therefore, competent HLA-A*01 or HLA-A*11 A549 target cells were pulsed with A1/ORF1_VTN or A11/ORF1_STF epitopes at a density of 10^{-5} M and 10^{-5} M, respectively. Peptide-pulsed target cells were seeded on 96-well RTCA eSight plates, and OTR-engineered CD8+ T cells were added 24 h later.

At 10^{-5} M antigen density, good killing of competent A549-HLA-A*03 target cells was observed for A1/ORF1_DTD-specific CD8+ T cells at an E:T ratio of 5:1. This was expected, as all of the TCRs investigated were also shown to be functional in previous assays (see Figure 32). In comparison, for the 10^{-7} M peptide-pulsed target cell curve separation, the target cell lysis was reduced and the killing curves were more spread out, highlighting differences in the killing capacity of TCRs with lower antigen density (Figure 42A). At 10^{-7} M antigen density, the first drop in cellular impedance began for some TCRs immediately after CD8+ T cell addition (TCR 5, TCR 65, TCR 758), while for other TCRs it started later (TCR 868, TCR 9) compared to the 10^{-5} M condition. The addition of TCR-engineered CD8+ T cells to unpulsed cells also dampened cell growth to some extent compared to the medium only condition. This was probably due to the addition of five times the amount of T cells to the target cells. However, a clear separation of specific killing was seen for all conditions, suggesting that no unspecific killing occurred. The

addition of medium to pulsed or unpulsed cells showed the highest impedance signal increase and the TritonX conditions demonstrated imminent lysis of all cells.

Also, CD8$^+$ T cells engineered with functional TCRs (TCR 1862, TCR 1871, TCR 1951) specific for the A11/ORF1_STF epitope lysed peptide-pulsed target cells very efficiently at an E:T ratio of 5:1. The functionality of A11/ORF1_STF-specific TCRs was also demonstrated in previous assays (see Figure 32). In comparison, TCR 569, which was previously shown to be unspecific, did not show any specific killing. As expected, the killing potential of A11/ORF1_STF-specific CD8$^+$ T cells was reduced at a lower antigen density (10^{-7} M), although it remained highly efficient (Figure 42B).

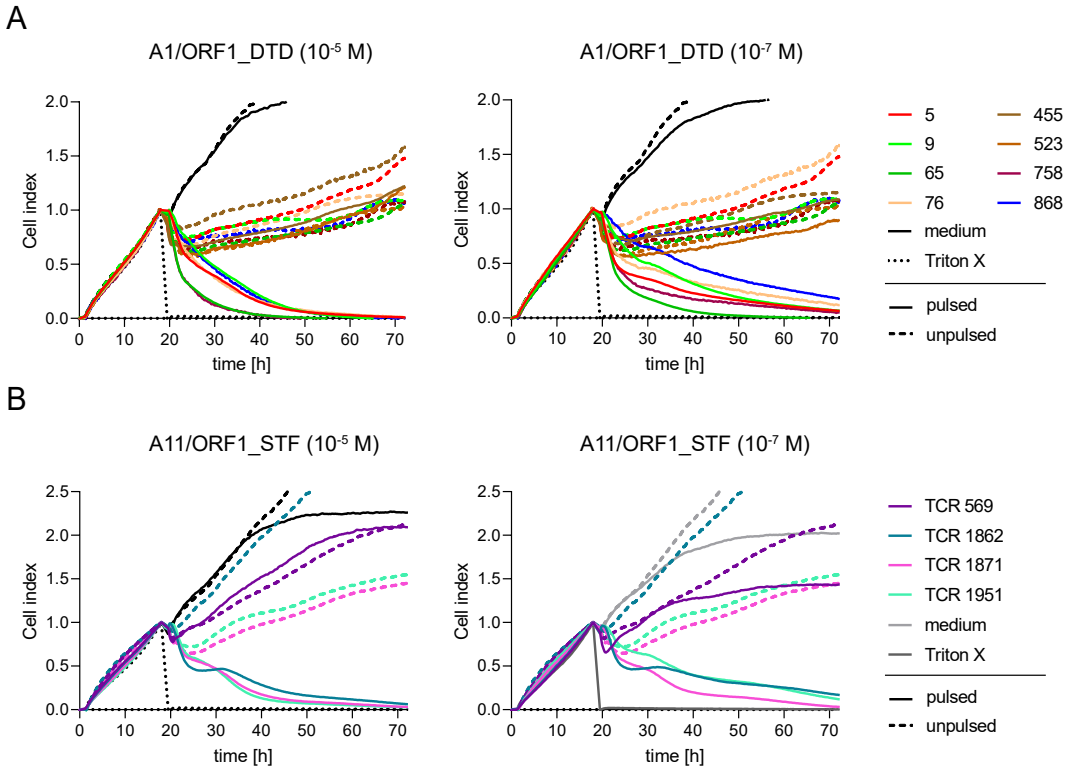

Figure 42: xCELLigence killing assay with epitope A1/ORF1_DTD or A11/ORF1_STF TCR-engineered CD8$^+$ T cells. (A – B) Target cells were pulsed with either 10^{-5} M (left) or 10^{-7} M (right) of peptide and TCR-engineered CD8$^+$ T cells were added after 19 h (solid line). As a control, engineered T cells were added to unpulsed target cells (dotted line). An E:T ratio of 5:1 was used for all conditions. (A) Cellular impedance measurements of competent A549-HLA-A*01 target cells pulsed with the A1/ORF1_DTD epitope and co-cultured with TCR-engineered CD8$^+$ T cells. (B) Cellular impedance measurements of competent A549-HLA-A*11 target cells pulsed with the A11/ORF1_STF epitope and co-cultured with TCR-engineered CD8$^+$ T cells.

For better comparability between TCRs and to qualitatively assess the killing potential of different TCRs, the AUC was calculated. The AUC was either normalized to the respective unpulsed target cell condition (Figure 43A, C) or to a non-functional TCR (TCR 455 for A1/ORF1_DTD and TCR 569 for A11/ORF1_STF) (Figure 43B, D). When comparing the AUC rankings be-

tween 10^{-5} M and 10^{-7} M pulsed target cells for A1/ORF1_DTD and A11/ORF1_STF, it was noticeable that the differences between TCRs became larger with less peptide present on the target cells. While the unpulsed control normalization also takes into account the addition of CD8+ T cells to unpulsed target cells, the normalization with the unfunctional TCR focuses only on the peptide-pulsed killing curves.

For the 10^{-5} M A1/ORF1_DTD normalizations, the ranking remained the same for all TCRs except the last two TCRs (TCR 868 and TCR 9) with TCR 758 and TCR 65 showing the largest killing. For the 10^{-7} M A1/ORF1_DTD normalizations, the frequency of killing showed a greater change in ranking but TCR 65 remained in first place, followed by TCR 5 or TCR 756 (Figure 43A - B). For the 10^{-5} M A11/ORF1_STF normalization, the differences between TCRs were larger for the unpulsed normalization, whereas for the TCR 569 normalization, the differences between TCRs became quite small. For 10^{-7} M A11/ORF1_STF, the addition of TCR 1871-engineered CD8+ T cells eliminated all target cells (Figure 42B, right). Figure 43D normalization is in line with this and showed the best killing percentage.

In conclusion, TCR-engineered CD8+ T cells killed target cells pulsed with 10^{-5} M A1/ORF1_DTD or A11/ORF1_STF peptides with high efficiency. Pulsing with 10^{-7} M peptides resulted in reduced target cell killing but better separation of conditions.

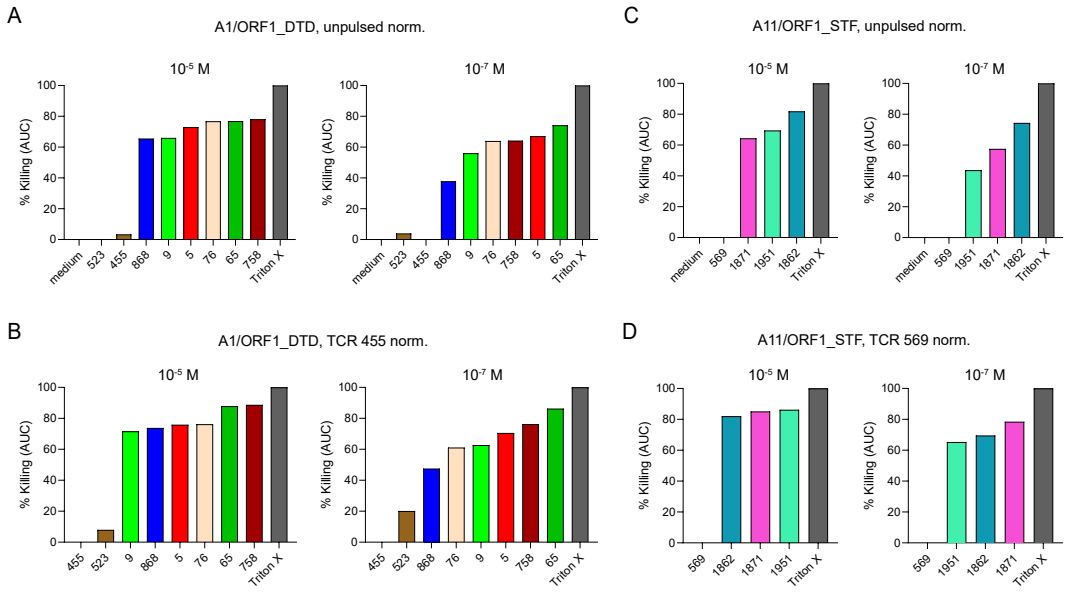

Figure 43: Quantification of killing assays with A1/ORF1_DTD or A11/ORF1_STF pulsed competent A549 target cells. AUC of TCR-engineered CD8+ T cell killing of 10^{-5} M (left) and 10^{-7} M (right) peptide pulsing. A1/ORF1_DTD pulsed competent A549-HLA-A*01 target cells (A - B) and A11/ORF1_STF pulsed competent A549-HLA-A*11 target cells (C - D). (A and C) Medium AUC was defined as 0 % killing and Triton X as 100 % killing. TCRs were normalized to their respective unpulsed condition AUC. (B and D) TCR 455 AUC or TCR 569 were defined as 0 % killing and Triton X as 100 % killing. TCRs were normalized to TCR 455 or TCR 569 AUC. Parts of the figure were reprinted with permission from [177].

To conclude this chapter, we can summarize that SARS-CoV-2-specific TCR-engineered CD8$^+$ T cells showed high cytotoxicity against target cells in all killing assays. Based on the infection of target cells, the replicating SARS-CoV-2 virus killing assay can be considered the closest to a physiological environment. While we observed good killing for A3/ORF1_VTN and A1/ORF3a_FTS-specific CD8$^+$ T cells engineered with highly specific TCRs, we also found that CD8$^+$ T cells engineered with a low-specific or non-specific TCR showed reduced or no target cell killing, respectively. In addition, we did not observe unspecific killing of uninfected cells, demonstrating the on-target specificity of SARS-CoV-2-specific TCR-engineered CD8$^+$ T cells. Nevertheless, infection of target cells with replicating SARS-CoV-2 virus had several drawbacks that made high-throughput experiments difficult. As an alternative, we developed a near-physiological killing assay in which target cells were transduced with a SARS-CoV-2 ORF. By transducing target cells with the SARS-CoV-2 protein Nsp2, we ensured natural antigen processing and presentation of the A3/ORF1_VTN epitope. We observed good killing for CD8$^+$ T cells engineered with the previously characterized highly specific TCRs and limited killing for CD8$^+$ T cells engineered with the previously characterized low-specific TCR TCR 32. These observations were also in line with the virus replication killing assay. Furthermore, we showed that peptide-pulsed target cells exhibited comparable lysis after addition of TCR-engineered T cells. To better understand the dependence on antigen density and to investigate the cytotoxic potential of more TCRs, we peptide-pulsed target cells with different molarities of the A1/ORF1_VTN and A11/ORF1_STF epitopes. This allowed us to show that A1/ORF1_VTN and A11/ORF1_STF-specific TCR-engineered CD8$^+$ T cells were highly cytotoxic; on the other hand, we found that lower antigen density resulted in reduced killing efficiency but also in broader distribution of otherwise functionally similar TCRs.

Having analyzed TCRs specific for different SARS-CoV-2 epitopes, we would now like to make some final assessments about the functionality of SARS-CoV-2-specific TCRs by comparing their functionality in different assays. In summary, we identified epitope-specific TCRs by performing scRNAseq of SARS-CoV-2 epitope-expanded and recent activated CD8$^+$ T cells. We then characterized the TCRs by re-expression in either healthy donor PBMCs or J-TPR cell lines.

To determine the binding specificity of a TCR to its respective epitope, we first performed multimer stainings. From the first scRNAseq experiment, we investigated TCRs specific for the A1/ORF3a_FTS and A3/ORF1_VTN epitopes by re-expressing them in healthy donor PBMCs. We found that TCRs predicted to be specific based on gene expression signatures (IFNG$^+$ cluster) also had positive multimer stainings. While TCR 13, TCR 28 and TCR 43, which are specific for the A3/ORF1_VTN epitope, showed strong multimer staining, we observed that TCR 32 demonstrated a rather weak signal. For the A1/ORF3a_FTS epitope, both TCRs from the IFNG$^+$ cluster, TCR 3456 and TCR 3398, showed positive multimer stainings. In contrast, TCRs from the IFNG$^-$ cluster did not show positive multimer stainings, suggesting a correlation between transcriptional data and epitope specificity. Following the second scRNAseq experiment, we re-expressed TCRs in J-TPR cells and found that TCR multimer staining correlated with functionality prediction of previously defined gene scores. To compare differences between assays, we focused on the A1/ORF1_DTD and A11/ORF1_STF epitopes, with the following ranking for multimer staining: TCR 5 > TCR 9 > TCR 868 > TCR 65 > TCR 758 > TCR 76 and TCR 1951 > TCR 1871 > TCR 1862, respectively. In summary, we found that SARS-CoV-2-specific TCRs were specific for their respective epitopes.

In a next step, we measured TCR:pHLA k_{off} rates for A1/ORF3a_FTS and A3/ORF1_VTN-specific TCRs and found high half-lives for TCR 13, followed by TCR 43 and TCR 28. Consistent with previously observed weak multimer staining, TCR 32 had no measurable k_{off} rate. As previously observed by multimer staining, also in k_{off} rate measurements, TCR 3456 had a

higher half-life than TCR 3398. K_{off} rate measurements can be summarized by a similar trend as multimer stainings, while absolute values did not show a strong correlation.

To determine the peptide sensitivity, we measured IFN-γ EC_{50} values of A3/ORF1_VTN-specific TCRs and found that TCR 13 and TCR 28 had a very high and similar EC_{50} value, followed by TCR 43 and finally TCR 32 with a low IFN-γ EC_{50} value. This was in contrast to k_{off} rate measurements where TCR 43 had a higher half-life than TCR 28. NFAT EC_{50} values of J-TPR cells from A1/ORF3a_FTS and A3/ORF1_VTN-specific TCRs had the same ranking as IFN-γ EC_{50} values despite lower EC_{50} values and a narrower distribution range. Measurements of A1/ORF3a_FTS-specific TCRs reveals that TCR 3456 had a slightly higher IFN-γ EC_{50} value than TCR 3398, in line with multimer staining and k_{off} rate measurements. NFAT EC_{50} values of A1/ORF3a_FTS-specific TCRs mirrored the previously observed trend with lower and closer EC_{50} values. Notably, the ranking remained the same as for IFN-γ EC_{50} values. NFAT EC_{50} values of TCRs from the second scRNAseq experiment showed high functionality and good alignment with the specificity prediction. We observed a range in NFAT EC_{50} values across epitopes, but also for the same epitope. For TCRs specific for the A1/ORF1_DTD and A11/ORF1_STF epitopes, we observed the same ranking as for multimer stainings. We can conclude that EC_{50} values showed that SARS-CoV-2-specific TCRs had high functionalities, were transferable from primary T cells to J-TPR cells, and had the same ranking as multimer stainings.

For TCRs specific for the A1/ORF1_DTD and A11/ORF1_STF epitopes, we additionally measured the cellular avidity in TCR-engineered J-TPR cell lines in the following order: TCR 5 > TCR 9 > TCR 65 > TCR 758 > TCR 76 and TCR 1871 > TCR 1951 > TCR 1862, respectively. The ranking of TCRs specific for the A1/ORF1_DTD epitope was the same as for the NFAT EC_{50} values and slightly different for the A11/ORF1_STF-specific TCRs. Accordingly, we can conclude that the cellular avidity measurements are roughly consistent with the sequence of previous measurements.

For A3/ORF1_VTN and A1/ORF3a_FTS-specific TCRs, we also performed live virus killing assays with TCR-transgenic CD8$^+$ T cells and could show good killing of highly functional TCRs (TCR 13, TCR 28) and poor killing of the low functional TCR, TCR 32. In addition, TCR 3456 showed good killing and TCR 3399 from the IFNG$^-$ cluster showed no unspecific killing. Furthermore, we transduced cell lines with Nsp2, the protein in which the epitope A3/ORF1_VTN is incorporated, and observed comparable killing to the replicating virus killing assay, i.e. good killing for highly functional TCRs (TCR 13, TCR 28, TCR 43) and poor target cell lysis for the low-functional TCR, TCR 32. Finally, we also measured the cytotoxicity of A1/ORF1_DTD and A11/ORF1_STF-specific CD8$^+$ T cells and found that all TCRs were highly cytotoxic with the following ranking: TCR 65 and TCR 758 > TCR 76 > TCR 5 > TCR 9, TCR 868. Although this ranking is derived from only one measurement, it was surprising that TCR 76 performed quite well. A11/ORF1_STF specific CD8$^+$ T cells were also highly cytotoxic, but the killing order changed depending on the normalization. The fitness of the cells after sorting and expansion could be a confounding factor to qualitatively assess the killing potential of different TCR-engineered CD8$^+$ T cells. In addition, we observed that lower antigen density helped to spread out differences between similar TCRs. In conclusion, SARS-CoV-2-specific TCRs were highly cytotoxic, but differences in target cell killing should be carefully evaluated.

In summary, we were able to confirm the overall functionality of SARS-CoV-2-specific TCRs, although minor differences in the ranking of TCR functionality were observed between some of the assays (multimer staining, k_{off} rates, EC_{50} assays, cellular avidity measurements, and killing assays).

5 Discussion

5.1 Persistence and protectivity of SARS-CoV-2-specific CD8$^+$ T cells

SARS-CoV-2 antibody levels of mild convalescent COVID-19 patients were well above the detection limit several weeks after infection. We and others have found that SARS-CoV-2 antibody levels declined quite rapidly after this initial peak. This was to be expected in acute infections and has been confirmed elsewhere [73, 74]. In contrast, we detected SARS-CoV-2-specific CD8$^+$ T cells even two years after infection. While several studies have reported SARS-CoV-2-specific CD8$^+$ T cells up to one year after infection [181, 182], to our knowledge, this study provides the longest follow-up after infection. It is known from other acute viral infections that memory formation of the adaptive immune system by vaccination can provide long-term protection. For yellow fever and hepatitis A, vaccination has been shown to provide long-lasting immunity for more than ten years [183, 184]. The demonstration of long-lasting immune responses, together with the polyclonality and functionality of the TCR repertoires specific for SARS-CoV-2, suggests that long-lasting protective immunity may develop.

However, with the emergence of the Omicron strain, real-world data indicated relatively high rates of reinfection [185]. A recent meta-analysis of 65 studies found that protection against reinfection and symptomatic disease was high for the ancestral strain and early SARS-CoV-2 variants but low for the Omicron variant [87]. Since antibodies, not T cells, are important for preventing infection, the increase in reinfections with Omicron is most likely due to SARS-CoV-2-specific neutralizing antibodies that have lost their effectiveness against Omicron [186]. T cells, on the other hand, are important for attenuating the course of the disease. Indeed, it has been shown, that prior infection or vaccination leads to a milder disease course [87, 186]. This is most likely mediated by SARS-CoV-2-specific CD8$^+$ T cells targeting conserved epitopes, which are not strongly affected by the high mutation rate of the virus [187]. In fact, most of the immunodominant epitopes identified in this work are not mutated in the Omicron variant. SARS-CoV-2-specific TCRs for these epitopes were found to be highly effective and will most likely protect against severe COVID-19 in Omicron-infected individuals.

Protection against severe disease can also be conferred by cross-reactive immune responses with other viruses. For some epitopes, we detected CD8$^+$ T cell responses in pre-pandemic donors with low immunogenicity. Although we did not find similarities of these epitopes with CCCs, they could have induced cross-reactive memory T cells from previous infections with other viruses. Further complicating the understanding of cross-reactivity is that cross-reactive T cells can be either beneficial or detrimental [188]. Beneficial cross-reactive CD8$^+$ T cells are primed to high homology epitopes from a prior infection and cross-react with high avidity against a secondary infection, whereas detrimental cross-reactive CD8$^+$ T cells are primed to low homology epitopes, resulting in low avidity SARS-CoV-2 epitope binding [188]. However, as these T cells dominate the secondary infection, the low avidity of these T cells leads to the production of proinflammatory cytokines without induction of cytolysis and ultimately to immunopathology and reduced viral clearance [188].

5.2 Potential biases of experimental design on epitope identification

Overall, we detected $CD8^+$ T cell responses in 34 of 44 mild convalescent COVID-19 patients (77 %). This is consistent with reports in literature ranging from 70 % to 88.5 % [89, 189–191]. One explanation for why the response frequency was not 100 % could be that some epitopes from the peptide pools were not immunogenic for some donors, who would react to other epitopes instead. It is also possible that SARS-CoV-2-specific memory T cells from some donors did not proliferate with our expansion protocol or that some donors did not establish T cell memory. In addition, we observed that one donor typically recognized more than one SARS-CoV-2 epitope (Figure 13 D), with most donors recognizing four epitopes (13.6 %, six donors). Others have also reported recognition of multiple epitopes in convalescent COVID-19 donors [83,192]. In line with our data, a study with a comparable number of epitopes and donors identified an average of five immunogenic epitopes per donor from 89 peptides restricted to a total of eleven HLA types and derived from seven SARS-CoV-2 ORFs [192]. The recognition of multiple epitopes suggests the formation of a multilayered T cell response that may be associated with improved virus recognition and protection against mutation.

Peptides from the first in-house 9-mer peptide pool were selected based on their predicted binding to the most common HLA class I molecules. Of the 41 peptides, we found 29 immunogenic peptides (70.7 %), and, of these, eleven immunodominant peptides ($\geq$ 50 % responders). For the design of the second peptide pool, in addition to *in silico* binding predictions, we also included peptides previously reported in literature to elicit $CD8^+$ T cell-specific immune responses [86, 189, 190, 193–195]. From these 62 peptides, we found 27 immunogenic peptides (43.5 %), of which 18 were also immunodominant. While the selection of the first pool yielded a better rate of immunogenic peptides (70.7 % vs 43.5 %), the second pool yielded a higher rate of immunodominant peptides (11 vs. 18). This is likely due to the inclusion of previously published epitopes for the second pool. Of the 62 peptides in the second pool, 35 peptides were selected based on literature and 27 based on binding prediction. From the literature selection, 20 epitopes were found to be immunogenic (57.1 %), whereas from the binding prediction only seven epitopes (25.9 %) were recognized by convalescent donor $CD8^+$ T cells. While our method of epitope selection led to the identification of some immunogenic and immunodominant epitopes, the pre-selection of epitopes from literature certainly increased the chances of finding immunodominant peptides. The better binding prediction for peptides from the first pool (70.7 %) compared to the second pool (25.9 %) may be explained by the fact that at the time we selected peptides for the second pool, most of the highly immunogenic peptides had already been identified by other research groups. Many peptides that we identified as potential candidates in the binding predictions for the second pool, had already been published in literature and were therefore assigned to the 'literature' category. Peptides that we additionally identified from the binding predictions, might be less immunogenic. Thus, we preselected immunogenic peptides in the 'literature' category that may have arbitrarily influenced the binding prediction subpool. Finally, why some of the published epitopes could not be confirmed in our hands is difficult to understand and may be due to different assay sensitivities and different donor materials.

The SARS-CoV-2 genome consists of ten ORFs [196]. We selected potential immunogenic epitopes from ORF1ab, ORF2 (S), ORF3a, ORF5 (M), and ORF9 (N) and identified epitopes from all the ORFs studied to induce immune responses in mild convalescent individuals. The largest of these ORFs is ORF1ab (21,290 bp), followed by S (3,822 bp), N (908 bp), ORF3a (828 bp) and M (669 bp) [197]. Because we expected the S protein to have the highest immunogenicity, we selected disproportionately more epitopes of the S protein (46 epitopes) compared to ORF1ab (34 epitopes), N (15 epitopes), M (five epitopes) and ORF3a (three epitopes). If we had

selected epitopes proportional to genomic size, we would have selected 80 epitopes for ORF1ab, 14 epitopes for S and three for the other ORFs. Immune responses were detected against 54 % of ORF1 epitopes, 63 % of N epitopes but only 34 % of S epitopes. Although the bias due to differences in HLA types was not analyzed in detail, it was striking that the S protein elicited fewer immune responses than other ORFs. This was also observed in other studies where most of the 9-mer immunodominant epitopes were found in ORF1, ORF3, or N [83,189,193]. In addition, immune responses against the other ORFs (ORF4, ORF6 – ORF 8, ORF10) could also be detected [86,190,193]. Taken together, while the S protein appears to be less immunogenic than other ORFs, all SARS-CoV-2 ORFs are immunogenic and capable of eliciting immune responses against the virus.

We have identified immunogenic epitopes for twelve HLA types with response rates (% responders) ranging from 100 % for HLA-A*01:01, HLA-A*11:01, HLA-B*35:01, HLA-B*40:01 to 5 % for HLA-C*07:02. The response rate is the number of HLA-matched donors that elicit a $CD8^+$ T cell response to any of the HLA-matched epitopes. For most HLA types, we were able to increase the response rate by adding more peptides from the second peptide pool. Importantly, while for rare HLA types all donors were tested for the identification of immunogenic peptides from the second pool, for common HLA-types (HLA-A*01:01, HLA-A*24:02, HLA-A*03:01, HLA-B*07:02) only a subset of HLA-matched donors was selected due to limited sample material. For HLA-A*01:01, all ten HLA-matched donors were previous responders and eight were tested in the second pool. Therefore, there was no donor selection bias in the second pool for HLA-A*01:01. For HLA-A*02:01, eleven of 23 HLA-matched donors were tested; of the twelve donors not tested, five were previous responders and seven were non-responders. No major bias was observed for HLA-A*02:01. For HLA-A*03, nine of twelve HLA-matched donors were tested. Of the three donors not tested, all were previous non-responders. Therefore, the response frequency of HLA-A*03:01 peptides is likely to be overestimated. For HLA-B*07:02, eleven of 14 HLA-matched donors were tested. All three not tested donors were previous non-responders. However, of the eleven donors tested for HLA-B*07:02, only one donor was a previous responder. Therefore, we would argue that no major donor selection bias was observed for HLA-B*07:02. To combine the response rates from both peptide pools, the response rate was calculated by considering all HLA-matched donors. However, this also resulted in a presumed over- or underrepresentation of the response rate for these HLA types. For example, the overall response rate for HLA-A*02:01 was 70 %. However, the HLA-A*02:01 epitope A2/S_YLQ had a response rate of 92 %, meaning that eleven of twelve donors tested responded to the peptide. In total, there were 23 HLA-A*02:01 donors in the patient cohort, eleven of whom were not tested for A2/S_YLQ and were therefore considered non-responders. Of the eleven donors not tested for A2/S_YLQ, five were previous responders and seven were non-responders. Due to its high immunodominance, A2/S_YLQ may also induce an immune response in some of the other non-responders, thus increasing the overall HLA-A*02:01 response rate.

In summary, we found $CD8^+$ T cell responses at levels comparable to those reported in the literature. In addition, we evaluated the hit rates of immunogenic peptides and found that we selected a high number of immunodominant peptides by binding prediction and confirmed many immunodominant epitopes published in the literature. We identified a disproportionate selection of epitopes compared to the size of the ORFs and found that the S protein elicited fewer immune responses than other ORFs. We also found a potential bias due to over- or underrepresentation of the immunogenicity of peptides in the second pool.

5.3 Identification of SARS-CoV-2-specific immunodominant epitopes

For HLA-A*02:01, in addition to A2/S_YLQ (YLQPRTFLL) (92 %), we found A2/ORF1_KLW (KLWAQCVQL) (83 %) and A2/ORF3_LLY (LLYDANYFL) (67 %) to be highly immunodominant. These observations were confirmed in literature with 77.8 % for A2/S_YLQ, 88.9 % for A2/ORF1_KLW and 88.9 % for A2/ORF3_LLY [193]. Three epitopes of more rare HLA types also had an immunodominance of 100 % in our cohort, namely HLA-B*35:01-LPFNDGVYF (B35/S_LPF), HLA-B*40:10-SELVIGAVIL (B40/M_SEL) and HLA-B*40:10-MEVTPSGTWL (B40/N_MEV). However, due to the low prevalence of these HLA types in our patient cohort, each epitope could only be measured in two donors. B40/M_SEL was identified in the literature with an immunodominance of 50 % in six of twelve donors [86]. These data suggest that our immunodominance may be biased by the limited number of donors. B40/N_MEV, which was included in the peptide pool based on ELISpot data, and B35/S_LPF, which was included based on multimer staining after vaccination, were not analyzed for immunodominance in the original papers [190, 195].

Some other epitopes of common HLA types stood out with an immunodominance of 100 %, the HLA-A*01:01-restricted epitope FTSDYYQLY (A1/ORF3a_FTS) and the HLA-B*07:02-restricted epitope SPRWYFYYL (B7/N_SPR). Ferretti et al. found an immunodominance of 100 % for A1/ORF3a_FTS and 80 % for B7/N_SPR [193]. B7/N_SPR has also been identified as one of the most immunodominant epitopes in many other studies [83,85,189,191,193]. B7/N_SPR is highly conserved among betacoronaviruses, and cross-reactivity with the same epitope was observed in SARS-CoV and CCCs (HCoVOC43 and HKU1) [193]. While SARS-CoV shares the same epitope with SARS-CoV-2, the CCCs HCoVOC43 and HKU1 have a sequence similarity to B7/N_SPR of 89 % (position: S1L) [188]. The pre-existing immunity with CCCs may be the reason for the high immunodominance for B7/N_SPR. Cross-reactive epitopes of CCCs to A1/ORF3a_FTS have not yet been identified. However, it is possible that A1/ORF3a_FTS is cross-reactive with other common viruses. Another epitope with potential cross-reactivity is A2/ORF1_KLW, for which we found 83 % immunodominance. A2/ORF1_KLW shares the same epitope with SARS-CoV and sequence similarity with HCoVOC43 and HKU1 epitopes of 55 %. While there is evidence that $CD8^+$ cross-reactivity is beneficial for COVID-19 disease progression [188], we did not detect cross-reactivity for most immunogenic epitopes when analyzing pre-pandemic donors, supporting the formation of new memory T cells during an infection with SARS-CoV-2.

Some epitopes such as B7/N_SPR elicited on average higher frequencies of reactive $CD8^+$ T cells compared to other epitopes (Figure 11 C, Figure 13 C). Although some factors might influence the success of T cell expansion, such as different cell starting numbers or the freeze/thaw process, it might also be influenced by different precursor frequencies prior to expansion. Our hypothesis was supported by experiments by Nguyen et al. where they measured SARS-CoV-2-specific T cells in COVID-19 convalescent patients *ex vivo* and could show differences in precursor frequencies among different epitopes. On average, the *ex vivo* frequencies of SARS-CoV-2-specific memory $CD8^+$ T cells were in the range of 1×10^{-5} to 5×10^{-5}. In comparison, *ex vivo* frequencies of influenza or EBV memory $CD8^+$ T cells are typically 2 to 10-times higher [198]. The B7/N_SPR epitope is considered to be the most dominant $CD8^+$ T cell epitope known to date [189, 190, 193, 198] and had remarkably high precursor frequencies (6.9×10^{-4}), similar in magnitude to an established influenza epitope [189, 190, 193, 198]. Interestingly, high precursor frequencies for the B7/N_SPR epitope were also measured in pre-pandemic donors (4.6×10^{-5}), which were also higher than antigen-specific naïve T cell populations [193,198]. While B7/N_SPR-reactive T cells from COVID-19 donors were predominantly located in the central memory com-

partment (61 %), B7/N_SPR-reactive T cells from pre-pandemic donors had a predominantly naïve phenotype. This suggests that B7/N_SPR-specific T cells are selected from a naïve precursor pool rather than from a pre-existing memory population. Nguyen et al. observed a highly diverse TCR$\alpha\beta$ repertoire for B7/N_SPR with variable usage of TRAV, TRBV, TRAJ, and TRBJ gene segments and no common motifs for CDR3α and CDR3β. They further argued that a diverse TCR$\alpha\beta$ repertoire and high recombination probability could indicate a high degree of TCR$\alpha\beta$ plasticity to recognize the B7/N_SPR epitope. This in turn could lead to the formation of a large and diverse naïve TCR$\alpha\beta$ repertoire and consequently to a high precursor frequency of B7/N_SPR-specific $CD8^+$ T cells [198]. Whether this is a general observation for high precursor frequency clonotypes remains to be shown.

In conclusion, we identified highly immunodominant epitopes and found that some immunodominant epitopes share sequence homology with SARS-CoV and CCCs. In addition, we found an atypically high precursor frequency for the B7/N_SPR epitope, which is likely due to a large naïve precursor pool and may account for the strong immune responses observed in all HLA-matched donors. While cross-reactive $CD8^+$ T cells are mostly considered beneficial for infection with SARS-CoV-2, most of the immunodominant epitopes from our pools were unique to SARS-CoV-2 and capable of eliciting 'de novo' $CD8^+$ T cell responses.

5.4 Impact of SARS-CoV-2 variant mutations on T cell functionality

Initial vaccine development focused on the S protein to induce humoral and cellular immunity. Neutralizing antibodies produced by B cells rapidly block viral entry, while T cells specific for the S protein recognize and eliminate SARS-CoV-2-infected cells. Due to the selective pressure of antibodies on the S protein, SARS-CoV-2 variants have shown to mutate sufficiently to evade antibody immunity and therapeutic mAbs [82,132]. Following this logic, we assumed that ORFs other than the S protein would mutate less. This was confirmed by a study of 454 HLA class I $CD8^+$ T cell epitopes identified by activation-induced marker (AIM) assays [187]. Overall, 94.9 % of the $CD8^+$ T cell epitopes were conserved in Omicron. Specifically, 98.3 % (294/299) of the epitopes from other ORFs, but only 88.4 % (137/155) of the epitopes from the S protein were conserved. $CD4^+$ T cell epitopes identified in the same AIM assays were conserved to 94.7 % (178/188) and to 80.4 % (74/92) when derived from non-spike and spike ORFs. The authors further analyzed 122 $CD8^+$ T cell epitopes identified by multimer staining and found a similar trend with 98.1 % (102/104) of the epitopes outside the S protein being conserved but only 88.9 % (16/18) of the epitopes from the S protein. Finally, by analyzing only the immunodominant epitopes identified from the meta-analysis of 18 studies, they showed that all 19 immunodominant epitopes were conserved in Omicron [187].

By performing intracellular cytokine assays with ancestral and Omicron S peptide pools, Choi et al. were able to further experimentally validate that PBMCs from convalescent COVID-19 donors had reduced activity for Omicron epitopes compared to the ancestral epitopes of 76.7 % and 88 % of $CD8^+$ and $CD4^+$ T cells, respectively. In vaccinated donors, reactivities decreased to 89.4 % and 83.9 % of $CD8^+$ and $CD4^+$ T cells, respectively [187]. Of the immunogenic epitopes identified from our peptide pools, only two epitopes with an immunogenicity of 30 % were mutated in Omicron (A3/S_GVY and A2/S_KIA) (the amino acid sequence of Omicron was obtained from GISAID). The mutation of A3/S_GVY (GVYFASTEK) resulted in an amino acid exchange (position: T7I) with preserved predicted binding level. Mutation of A2/S_KIA (KIADYNYKL) resulted in an amino acid exchange (position: K1N) with predicted lower binding specificity.

In summary, ORFs other than S mutate less and therefore generate more conserved CD8$^+$ T cell responses. For the future design of vaccines, to induce robust CD8$^+$ T cell immunity, ORFs other than S protein should also be included.

5.5 Identification and isolation of SARS-CoV-2-specific CD8$^+$ T cells

We detected SARS-CoV-2-specific CD8$^+$ T cells at very low frequencies *ex vivo*. This observation was also confirmed by others [189, 198, 199]. To facilitate detection, given the limited amount of starting material, we expanded SARS-CoV-2-specific CD8$^+$ T cells by adapting a protocol for the expansion of SARS-CoV-specific CD8$^+$ T cells [174]. The *in vitro* expansion step, while critical in this project, carries a bias to selecting mainly high-avidity T cell clones, as they theoretically expand faster and stronger to antigen stimulation. This has the limitation that low-avidity T cell clones may be underrepresented, a bias that should be considered when analyzing epitope-specific repertoires. On the contrary, our expansion protocol could be useful to identify highly functional TCRs for therapy, since good expansion and high avidity are crucial factors for a T cell product. To preserve the original phenotype of SARS-CoV-2-specific T cells and to detect low-avidity clones, direct *ex vivo* pHLA multimer staining can be performed [83, 200, 201]. However, the simultaneous detection of CD8$^+$ T cells specific for different SARS-CoV-2 epitopes *ex vivo* by barcoded multimers may also be associated with lower sensitivity, as shown in a study by Saini et al. in which only 122 immunogenic epitopes were identified from the 3141 HLA class I epitopes tested, resulting in a hit rate of 3.9 % [83].

Others have used tetramer-associated magnetic enrichment (TAME), just tetramer staining, activation-induced markers (AIM), or anti-CD107a to isolate SARS-CoV-2-specific CD8$^+$ T cells [199, 202–204]. Tetramers have been used to isolate SARS-CoV-2-specific CD8$^+$ T cells *ex vivo* [199], or after expansion [203]. Although the tetramer technology is characterized by high specificity, some reactive T cells may be lost upon activation due to TCR downregulation. In addition, only the pHLA-TCR binding and not T cell activation is considered, which likely results in the isolation of TCRs with low avidity. Furthermore, the generation of multimers is time consuming and not always successful. Ford et al. used the AIM markers CD69 and CD137 to isolate SARS-CoV-2-specific T cells *ex vivo* [204]. Activation markers capture most antigen-reactive T cells, but staining may be associated with higher background signals. Shimizu et al. used CD107a as a marker to detect degranulating cells and found that 80 % of IFN-γ secreting cells also express CD107a [202], resulting in a partial loss of the repertoire. IFN-γ is a reliable marker for the detection of antigen reactive CD8$^+$ T cells [205]. Given the clean staining and high selectivity of IFN-γ, we therefore used a method called IFN-γ catch to isolate antigen-specific CD8$^+$ T cells. Here, secreted IFN-γ is captured on the surface of cytokine-producing cells by bispecific anti-CD45 anti-IFN-γ antibodies and fluorochrome-conjugated anti-INFγ capture antibodies. However, the sensitivity of this assay may be limited because not all IFN-γ expressing cells secrete IFN-γ in sufficient amounts to be detected by flow cytometry and not all activated cells secrete IFN-γ.

In conclusion, although each method has its limitations, isolation of SARS-CoV-2-specific TCRs could be successfully performed by all methods. In our hands, detection of SARS-CoV-2-specific CD8$^+$ T cells with IFN-γ resulted in a good signal-to-noise ratio with little background staining from unspecific or unstimulated cells. In addition, fresh restimulation prior to cell sorting allowed us to isolate recently activated cells with the IFN-γ catch assay while detecting transcriptomic activation signatures.

5.6 The landscape of SARS-CoV-2-specific TCR repertoires

SARS-CoV-2-specific TCRs were isolated from twelve donors and were specific for a total of eleven epitopes. For all donors and epitope specificities, we observed diverse TCR repertoires and high clonotype expansions. For functional characterization, TCRs were subsequently re-expressed in healthy donor PBMCs using CRISPR/Cas9-mediated OTR. OTR is the process by which the transgenic TCR is integrated into the TCRα locus. At the same time, the concomitant KO of the TCRβ locus prevents mispairing between the transgenic and endogenous TCR. Due to natural receptor regulation, integration of transgenic TCRs by OTR is expected to generate engineered T cells that closely resemble physiological T cells with more homogeneous surface expression [149].

We characterized SARS-CoV-2-specific TCRs by measuring epitope specificity (pHLA multimer), structural avidity (k_{off} rate), functional avidity (EC_{50} and killing assays) and cellular avidity. Most of the SARS-CoV-2-specific TCRs were highly potent and showed functionality in all assays. In one case, for TCR 76, we found reactivity for one assay (EC_{50}) but no reactivity for another assay (pHLA multimer staining). When comparing highly functional TCRs for the same epitope, we mostly observed the same ranking, but sometimes a slightly different ranking between assays. Remarkably, the ranking of A1/ORF1_DTD-specific TCRs between multimer staining, EC_{50} values and cellular avidity was the same (Figure 29, Figure 32, Figure 36), while the TCR ranking for killing assays was slightly different (Figure 42, Figure 43). For A11/ORF1_STF-specific TCRs, multimer staining and EC_{50} values had the same ranking, but for cellular avidity values, the ranking of TCR 1951 and TCR 1871 was reversed (Figure 29, Figure 32, Figure 36). For killing assays, the order was the same to EC_{50} values when normalized to the same control (Figure 42, Figure 43). In contrast, differences between TCRs with a wide range of functionality could be reliably detected in different assays. For example, the ORF1_VTN-specific TCRs, TCR 13 and TCR 32, where TCR 13 was highly functional and TCR 32 was low functional in all assays (Figure 17, Figure 18, Figure 19, Figure 37). While the ORF1_VTN-specific TCR 28 had a higher EC_{50} value than TCR 43, it had a shorter half-life as measured by k_{off} rates. From previous studies, we know that k_{off} rates do not correlate very well with *in vitro* functionality. Consistent with EC_{50} values, TCR 28 showed slightly better killing than TCR 43 as measured by AUC (total area) in Nsp2-transduced cell lines (Figure 41).

To generate TCR-engineered $CD8^+$ T cells, healthy donor T cells were OTR-engineered with transgenic TCRs, cell sorted, and expanded for three weeks. While killing was observed for all functional TCRs, the duration of expansion as well as the potential exhaustion of T cells might have affected the cytotoxic capacity of each TCR-engineered T cell product differently. Nevertheless, this work attempted to calculate an absolute ranking, but it did not perfectly reflect other evaluations of TCR functionality. For the generation of ACT T cell products, shorter *in vitro* culture was shown to result in reduced differentiation, improved effector functions, and ultimately improved anti-tumor activity [206]. In future experiments, shorter cultivation of TCR-engineered $CD8^+$ T cells could also lead to more robust killing data.

5.7 Gene scores for the identification of SARS-CoV-2-specific TCRs

From the first scRNAseq experiment, we selected TCRs for re-expression based on their UMAP clustering, relative clone size, and differential gene expression of selected markers known to be upregulated in activated T cells such as INFG, GZMB, XCL1, etc.. Using this data set, we wanted to see if we could make predictions about specific and non-specific TCRs and also about

the degree of functionality. Therefore, we determined EC_{50} values in TCR-engineered T cells and correlated them with parameters extracted from the transcriptomic data of the parental T cells, such as a public $CD8^+$ T cell activation score, IFNG expression, and clonotype size. Surprisingly, we found only weak ($CD8^+$ T cell activation score, IFNG expression) or negative (clonotype size) correlations between these parameters and the experimentally determined EC_{50} values. The IFNG expression of functional TCRs did not correlate with EC_{50} values, as all TCRs with measurable functionality appeared to have comparable IFNG levels. Thus, IFNG can be used to identify functional epitope-specific TCRs but is not a good correlator to predict the degree of TCR functionality. Clonotype size correlated negatively with TCR functionality, with TCR 32 likely biasing the analysis because it was highly expanded but had the lowest EC_{50} value. This result surprised us since we expected that T cells expressing highly functional TCRs would respond faster and expand more upon stimulation than T cells with low-functional TCRs. Although we found that the majority of expanded clones expressed functional TCRs, this did not follow a linear correlation. Consistent with our observation, the presence of a large circulating clone with low functionality has recently been shown by others in cancer patients [207].

Therefore, to find better predictors of TCR functionality, we empirically defined gene scores that correlated with our data. On the one hand, we defined a reactivity score that included the most differentially expressed genes between epitope-specific and non-specific TCRs; on the other hand, we defined a functionality score that also included genes that best correlated with IFN-γ EC_{50}. These scores performed well in the first scRNAseq experiment but not similarly when applied to the second data set. While the reactivity score efficiently predicted specific and non-specific TCRs, the functionality score only weakly correlated with the NFAT EC_{50} evaluated in J-TPR cells of the new set of TCRs. For the reactivity score, the gene signatures in the two experiments largely overlapped. The genes included in the first experiment were canonical markers of T cell activation such as XCL1/2, CRTAM and the TNF family, which can explain the reliable performance across different settings [208,209]. The genes of the second experiment were mainly included in the gene list of the first experiment and some 'new' genes are still involved in T cell functions (e.g. FABP5, PGAM, RILPL2) [210–212]. In conclusion, the reactivity signature could reliably identify truly antigen-specific T cells. The gene signatures of the functionality score varied between experiments, suggesting that this score may be experimentally dependent. Nevertheless, re-expression of a limited number of TCRs in both data sets was sufficient to generate experiment-specific gene signatures that correlated with TCR functionality and can therefore be used to accurately infer the functionality of all other TCRs in the data set. In addition, we hypothesize that the experimental setup prior to TCR identification influenced both scores. After antigen-specific expansion, PBMCs were restimulated with a high amount of peptide (10^{-6} M), which most likely resulted in activation of all T cells responding to the peptide (both low and high functional). This experimental design is therefore more suitable for defining the reactivity score. For the functionality score, which takes into account the EC_{50} value, this may not be true to the same extent, because activated TCRs may show similar expression of activation genes regardless of their EC_{50} value due to the high peptide dose used.

Some TCRs did not respond to SARS-CoV-2 epitopes, even though they were isolated with specific peptide stimulation (TCR 21, TCR 455, TCR 560, TCR 1996). By applying gene scores, most of these non-specific TCRs could be distinguished from truly functional TCRs. However, some TCRs remained false positive (TCR 21, TCR 85, TCR560) or false negative (TCR 1862 and TCR 1951), i.e. they were predicted to be functional but lacked reactivity or vice versa. We suspected that this might be because the functionality and reactivity gene scores were defined based on only a few TCRs from the first scRNAseq experiment. In fact, by refining the gene scores, both TCRs, TCR 1862 and TCR 1951, which were defined as non-specific based on their previous negative functionality score, were found to be specific with the new scores.

5.8 Comparing killing assays for TCR cytotoxicity measurements

The chromium (^{51}Cr) release assay is the gold standard for measuring cytolytic T cell killing. Because the use of ^{51}Cr has several disadvantages, such as the use of radioactive material, environmental safety concerns, and high costs due to the short half-life of the isotope, other assays have been developed in recent years. The luciferase assay is based on the principle that the firefly luciferase gene is expressed in healthy target cells and that luciferase is released when target cells die. By measuring the residual luminescence of the target cells, viable and dead cells can be accurately quantified [213]. Another assay that indirectly measures target cell killing by T cells is the CD107a degranulation assay. Here, membrane expression of CD107a, a marker of immune cell activation and cytotoxic degranulation, can be quantified and correlated with the cytolytic function of T cells [214].

To measure the cytotoxicity of TCR-engineered CD8$^+$ T cells, we chose imaging and impedance-based assays. The Incucyte allows live cell tracking and quantification of target cells. High resolution imaging was critical for the SARS-CoV-2 virus killing assay because the infectivity of the SARS-CoV-2 virus was low and infected cells could be specifically quantified. For the transgenic-antigen killing assay, we used the xCELLigence RTCA eSight instrument to measure target cell impedance and its decrease during killing. Measuring the decrease in impedance or the detachment of the target cell from the well surface is a well-established method for monitoring target cell killing. The image resolution of the xCELLigence instrument, while not as good as that of the Incucyte, is still sufficient to quantify target cell killing, but would likely not be able to detect infection.

A clear advantage of the virus-infection model is that target cells are infected with SARS-CoV-2 by receptor-mediated entry. This ensures natural protein processing and peptide presentation on HLA class I molecules. However, in our hands, low infection rates also led to high variability between experiments. Due to viable viral infection, these assays had to be performed under BSL-3 conditions, which allowed only low-throughput experiments. We therefore developed an alternative killing assay in which the target cell line was transduced with a protein (Nsp2) containing the epitope of interest (ORF1_VTN). Target cell killing showed the same trend as in the virus-infection model, but was more homogeneous overall, likely due to antigen expression by all target cells. In addition, these assays could be performed under BSL-2 conditions. Furthermore, after transduction of a specific ORF, many TCR-transgenic CD8$^+$ T cells can be measured. Compared to the virus-infection model, the expression level of the transgenic antigen is not physiological, so the result may differ from a real infection in terms of quantitative cytotoxicity. If epitopes from other ORFs are to be examined, this ORF must be transduced separately due to the size limitation of retroviruses. Pulsing target cells with peptides is certainly the simplest and most high-throughput killing assay, as any desired epitope specific for the HLA type of the target cells can be added. However, it is also considered to be the least physiological assay because it neglects whether the epitope is actually presented on HLA class I complexes under physiological conditions. Importantly, for CD8$^+$ T cells carrying ORF1_VTN TCRs of different functionality, all three assays showed comparable killing, even though only a small proportion of target cells in the virus-infected system were actually infected.

In summary, the virus-infection assay is superior in terms of near-physiological peptide processing and presentation, but the other two assays are more suitable for the study of many TCRs.

6 Conclusion

In this work, we have shown that patients with mild COVID-19 infection, as well as asymptomatic seropositive patients, develop reliable $CD8^+$ T cell immune responses to SARS-CoV-2 infection. Furthermore, $CD8^+$ T cell immune responses were long-lasting, whereas antibody levels declined rapidly, suggesting long-term T cell immunity and possible correlates of protection, at least from severe COVID-19. In addition, we showed that the investigated SARS-CoV-2 epitopes, identified using *in silico* prediction tools and from the literature, are highly immunodominant and provide an important tool for studying SARS-CoV-2-specific responses. Since most mild convalescent COVID-19 donors also responded to multiple epitopes, a low probability of T cell immune escape is expected with the emergence of new variants.

We identified SARS-CoV-2-reactive TCRs from mild convalescent COVID-19 patients. For this, we selectively expanded $CD8^+$ T cells with SARS-CoV-2 peptides and freshly restimulated cells to induce activation signatures. Consequently, we were able to identify SARS-CoV-2-specific $CD8^+$ T cells and corresponding TCRs by sorting IFN-γ-expressing T cells and by performing scRNAseq, respectively. In all donors, TCR repertoires were highly polyclonal, indicating a multilayered immune response. We further systematically investigated SARS-CoV-2-specific TCRs by integrating them into healthy donor PBMCs via CRISPR/Cas9-mediated OTR. Because functional TCR characterization in primary T cells is tedious, we further developed a platform for high-throughput characterization of TCRs by integrating SARS-CoV-2-specific TCRs into J-TPR cell lines using the same cell engineering technology. We have extensively characterized SARS-CoV-2-specific TCRs and demonstrated that they are highly functional. By using the functional avidity (EC_{50}) of TCRs together with transcriptomic data from parental cells, we developed gene scores capable of identifying truly epitope-specific TCRs and that to some extent predicted their degree of functionality. Overall, we showed that the identified TCR repertoires specific for SARS-CoV-2 epitopes are highly functional. We anticipate that the gene scores developed here will be useful for predicting TCR functionality in other settings as well.

In conclusion, we have shown that both symptomatic and asymptomatic COVID-19 donors have detectable immune responses against SARS-CoV-2, and that $CD8^+$ T cell immune responses are long-lasting, polyclonal, and highly functional. In addition, we provided tools for the characterization of TCRs that may be useful for the development of TCRs for therapy.

7 Appendix

Table 25: Gene score classifiers of SARS-COV-2 TCRs

TCR	Epitope	Functionality score	Reactivity score	Functionality prediction
13	**ORF1_VTN**	0,5172	0,9984	**positive**
28	**ORF1_VTN**	0,6403	0,9658	**positive**
32	**ORF1_VTN**	0,0266	0,6663	**positive**
43	**ORF1_VTN**	0,4208	0,9448	**positive**
3456	**ORF3_FTS**	0,6430	0,6643	**positive**
3398	**ORF3_FTS**	0,5478	0,6073	**positive**
3399	**ORF3_FTS**	-0,3637	-0,6070	**negative**
5	ORF1_DTD	0,2208	0,3960	positive
9	ORF1_DTD	0,1785	0,3697	positive
21	ORF1_HSI	0,1956	0,0714	positive
38	ORF1_GTD	0,8425	0,7431	positive
58	ORF1_KLF	0,7336	0,5312	positive
62	ORF1_HSI	0,4275	0,4085	positive
65	ORF1_DTD	0,3884	0,5252	positive
66	ORF1_GTD	0,0951	-0,1273	negative
76	ORF1_DTD	0,5068	0,5201	positive
85	ORF1_HSI	0,7159	0,6136	positive
455	ORF1_DTD	-0,3305	-0,4155	negative
499	ORF1_ASM	0,2767	0,3085	positive
523	ORF1_DTD	-0,2027	-0,1113	negative
560	ORF1_KLF	0,7203	0,5008	positive
569	ORF1_STF	-0,2372	-0,2716	negative
758	ORF1_DTD	0,4946	0,2668	positive
868	ORF1_DTD	0,0722	0,3576	positive
1085	S_LTD	-0,2254	-0,3706	negative
1228	S_LTD	0,3698	0,4769	positive

1862	ORF1_STF	-0,0595	0,0643	negative
1863	S_LTD	0,2990	0,4302	positive
1864	S_LTD	0,2007	0,3457	positive
1871	ORF1_STF	0,2111	0,0504	positive
1877	ORF1_FVK	0,1296	0,2356	positive
1896	ORF1_VPF	0,2545	0,3065	positive
1917	ORF1_VPF	0,0894	-0,0368	negative
1951	ORF1_STF	-0,0284	-0,1487	negative
1968	S_LTD	-0,6832	-0,3951	negative
1996	ORF1_VPF	-0,2511	-0,4349	negative
2056	ORF1_FVK	0,4993	0,3463	positive

Bold printed TCRs were part of the first scRNAseq experiment.

Table 26: NFAT EC_{50} values

Epitope	**Sequence**	**TCR**	**NFAT EC_{50}**
ORF1_ASM	ASMPTTIAK	499	-7.440
ORF1_DTD	DTDFVNEFY	5	-7.286
ORF1_DTD	DTDFVNEFY	868	-7.122
ORF1_DTD	DTDFVNEFY	9	-7.093
ORF1_STF	STFNVPMEK	1951	-7.017
ORF1_DTD	DTDFVNEFY	65	-6.922
ORF1_HSI	HSIGFDYVY	62	-6.795
ORF1_DTD	DTDFVNEFY	758	-6.780
ORF1_STF	STFNVPMEK	1871	-6.696
ORF1_STF	STFNVPMEK	1862	-6.572
S_LTD	LTDEMIAQY	1863	-6.537
ORF1_GTD	GTDLEGNFY	38	-6.502
ORF3_FTS	**FTSDYYQLY**	**3456**	**-6.346**
ORF1_DTD	DTDFVNEFY	76	-6.325
S_LTD	LTDEMIAQY	1864	-6.168
ORF3_FTS	**FTSDYYQLY**	**3398**	**-6.066**
S_LTD	LTDEMIAQY	1228	-6.033
ORF1_VPF	VPFWITIAY	1896	-5.799

ORF1_VTN	**VTNNTFTLK**	**13**	**-5.656**
ORF1_VTN	**VTNNTFTLK**	**28**	**-5.503**
ORF1_KLF	KLFDRYFKY	58	-5.308
ORF1_VTN	**VTNNTFTLK**	**43**	**-5.217**
ORF1_FVK	FVKHKHAFL	1877	-4.446
ORF1_VTN	**VTNNTFTLK**	**32**	**-4.435**
ORF1_FVK	FVKHKHAFL	2056	-4.175
ORF1_DTD	DTDFVNEFY	455	0
ORF1_DTD	DTDFVNEFY	523	0
ORF1_GTD	GTDLEGNFY	66	0
ORF1_HSI	HSIGFDYVY	21	0
ORF1_HSI	HSIGFDYVY	85	0
ORF1_KLF	KLFDRYFKY	560	0
ORF1_STF	STFNVPMEK	569	0
ORF1_VPF	VPFWITIAY	1917	0
ORF1_VPF	VPFWITIAY	1996	0
S_LTD	LTDEMIAQY	1085	0
S_LTD	LTDEMIAQY	1968	0
ORF3_FTS	**FTSDYYQLY**	**3399**	**0**

Bold printed peptides were part of first scRNAseq experiment.

References

[1] P. A. Roche and K. Furuta. The ins and outs of MHC class II-mediated antigen processing and presentation. *Nature Reviews Immunology*, 15(4):203–216, feb 2015. doi:10.1038/nri3818.

[2] S. C. Meuer, D. A. Cooper, J. C. Hodgdon, R. E. Hussey, K. A. Fitzgerald, S. F. Schlossman, and E. L. Reinherz. Identification of the receptor for antigen and major histocompatibility complex on human inducer t lymphocytes. *Science*, 222(4629):1239–1242, dec 1983. doi:10.1126/science.6606228.

[3] J. S. Danska, A. M. Livingstone, V. Paragas, T. Ishihara, and C. G. Fathman. The presumptive cdr3 regions of both t cell receptor alpha and beta chains determine t cell specificity for myoglobin peptides. *Journal of Experimental Medicine*, 172(1):27–33, jul 1990. doi:10.1084/jem.172.1.27.

[4] Q. Qi, Y. Liu, Y. Cheng, J. Glanville, D. Zhang, J.-Y. Lee, R. A. Olshen, C. M. Weyand, S. D. Boyd, and J. J. Goronzy. Diversity and clonal selection in the human t-cell repertoire. *Proceedings of the National Academy of Sciences*, 111(36):13139–13144, aug 2014. doi:10.1073/pnas.1409155111.

[5] E. Rosati, C. M. Dowds, E. Liaskou, E. K. K. Henriksen, T. H. Karlsen, and A. Franke. Overview of methodologies for t-cell receptor repertoire analysis. *BMC Biotechnology*, 17(1), jul 2017. doi:10.1186/s12896-017-0379-9.

[6] B. Arden. Conserved motifs in t-cell receptor CDR1 and CDR2: implications for ligand and CD8 co-receptor binding. *Current Opinion in Immunology*, 10(1):74–81, feb 1998. doi:10.1016/s0952-7915(98)80035-6.

[7] K. C. Garcia, M. Degano, R. L. Stanfield, A. Brunmark, M. R. Jackson, P. A. Peterson, L. Teyton, and I. A. Wilson. An alphabeta t cell receptor structure at 2.5 a and its orientation in the tcr-mhc complex. 274(5285):209–219, oct 1996. doi:10.1126/science.274.5285.209.

[8] D. N. Garboczi, P. Ghosh, U. Utz, Q. R. Fan, W. E. Biddison, and D. C. Wiley. Structure of the complex between human t-cell receptor, viral peptide and HLA-a2. *Nature*, 384(6605):134–141, nov 1996. doi:10.1038/384134a0.

[9] L. Klein, B. Kyewski, P. M. Allen, and K. A. Hogquist. Positive and negative selection of the t cell repertoire: what thymocytes see (and don't see). *Nature Reviews Immunology*, 14(6):377–391, may 2014. doi:10.1038/nri3667.

[10] R. M. ZINKERNAGEL and P. C. DOHERTY. Restriction of in vitro t cell-mediated cytotoxicity in lymphocytic choriomeningitis within a syngeneic or semiallogeneic system. *Nature*, 248(5450):701–702, apr 1974. doi:10.1038/248701a0.

[11] S. Sommer. The importance of immune gene variability (MHC) in evolutionary ecology and conservation. *Frontiers in Zoology*, 2(1), oct 2005. doi:10.1186/1742-9994-2-16.

[12] T. Shiina, K. Hosomichi, H. Inoko, and J. K. Kulski. The HLA genomic loci map: expression, interaction, diversity and disease. *Journal of Human Genetics*, 54(1):15–39, jan 2009. doi:10.1038/jhg.2008.5.

[13] K. Falk, O. Rötzschke, S. Stevanović, G. Jung, and H.-G. Rammensee. Allele-specific motifs revealed by sequencing of self-peptides eluted from MHC molecules. *Nature*, 351(6324):290–296, may 1991. doi:10.1038/351290a0.

[14] R. M. Chicz, R. G. Urban, W. S. Lane, J. C. Gorga, L. J. Stern, D. A. A. Vignali, and J. L. Strominger. Predominant naturally processed peptides bound to HLA-DR1 are derived from MHC-related molecules and are heterogeneous in size. *Nature*, 358(6389):764–768, aug 1992. doi:10.1038/358764a0.

[15] M. Matsumura, D. H. Fremont, P. A. Peterson, and lan A. Wilson. Emerging principles for the recognition of peptide antigens by MHC class i molecules. *Science*, 257(5072):927–934, aug 1992. doi:10.1126/science.1323878.

[16] A. J. Godkin, K. J. Smith, A. Willis, M. V. Tejada-Simon, J. Zhang, T. Elliott, and A. V. S. Hill. Naturally processed HLA class II peptides reveal highly conserved immunogenic flanking region sequence preferences that reflect antigen processing rather than peptide-MHC interactions. *The Journal of Immunology*, 166(11):6720–6727, jun 2001. doi:10.4049/jimmunol.166.11.6720.

[17] M. L. Dustin. The immunological synapse. *Cancer Immunology Research*, 2(11):1023–1033, nov 2014. doi:10.1158/2326-6066.cir-14-0161.

[18] G. F. Gao, J. Tormo, U. C. Gerth, J. R. Wyer, A. J. McMichael, D. I. Stuart, J. I. Bell, E. Y. Jones, and B. K. Jakobsen. Crystal structure of the complex between human cd8αα and hla-a2. *Nature*, 387(6633):630–634, jun 1997. doi:10.1038/42523.

[19] Y. Yin, X. X. Wang, and R. A. Mariuzza. Crystal structure of a complete ternary complex of t-cell receptor, peptide–MHC, and CD4. *Proceedings of the National Academy of Sciences*, 109(14):5405–5410, mar 2012. doi:10.1073/pnas.1118801109.

[20] S. E. Kerry, J. Buslepp, L. A. Cramer, R. Maile, L. L. Hensley, A. I. Nielsen, P. Kavathas, B. J. Vilen, E. J. Collins, and J. A. Frelinger. Interplay between TCR affinity and necessity of coreceptor ligation: High-affinity peptide-MHC/TCR interaction overcomes lack of CD8 engagement. *The Journal of Immunology*, 171(9):4493–4503, nov 2003. doi:10.4049/jimmunol.171.9.4493.

[21] A. H. Courtney, W.-L. Lo, and A. Weiss. TCR signaling: Mechanisms of initiation and propagation. *Trends in Biochemical Sciences*, 43(2):108–123, feb 2018. doi:10.1016/j.tibs.2017.11.008.

[22] H. W. Virgin, E. J. Wherry, and R. Ahmed. Redefining chronic viral infection. *Cell*, 138(1):30–50, jul 2009. doi:10.1016/j.cell.2009.06.036.

[23] M. H. Heim and R. Thimme. Innate and adaptive immune responses in HCV infections. *Journal of Hepatology*, 61(1):S14–S25, nov 2014. doi:10.1016/j.jhep.2014.06.035.

[24] K. R. Rai, P. Shrestha, B. Yang, Y. Chen, S. Liu, M. Maarouf, and J.-L. Chen. Acute infection of viral pathogens and their innate immune escape. *Frontiers in Microbiology*, 12, jun 2021. doi:10.3389/fmicb.2021.672026.

[25] A. L. Bon, N. Etchart, C. Rossmann, M. Ashton, S. Hou, D. Gewert, P. Borrow, and D. F. Tough. Cross-priming of cd8+ t cells stimulated by virus-induced type i interferon. *Nature Immunology*, 4(10):1009–1015, sep 2003. doi:10.1038/ni978.

[26] E. J. Wherry and R. Ahmed. Memory CD8 t-cell differentiation during viral infection. *Journal of Virology*, 78(11):5535–5545, jun 2004. doi:10.1128/jvi.78.11.5535-5545.2004.

[27] M. J. Bevan. Helping the cd8+ t-cell response. *Nature Reviews Immunology*, 4(8):595–602, aug 2004. doi:10.1038/nri1413.

[28] A. Hamann, K. Klugewitz, F. Austrup, and D. Jablonski-Westrich. Activation induces rapid and profound alterations in the trafficking of t cells. *European Journal of Immunology*, 30(11):3207–3218, nov 2000. doi:10.1002/1521-4141(200011)30:11<3207::aid-immu3207>3.0.co;2-l.

[29] S. M. Kaech, S. Hemby, E. Kersh, and R. Ahmed. Molecular and functional profiling of memory CD8 t cell differentiation. *Cell*, 111(6):837–851, dec 2002. doi:10.1016/s0092-8674(02)01139-x.

[30] D. S. Hui, E. I. Azhar, T. A. Madani, F. Ntoumi, R. Kock, O. Dar, G. Ippolito, T. D. Mchugh, Z. A. Memish, C. Drosten, A. Zumla, and E. Petersen. The continuing 2019-nCoV epidemic threat of novel coronaviruses to global health — the latest 2019 novel coronavirus outbreak in wuhan, china. *International Journal of Infectious Diseases*, 91:264–266, feb 2020. doi:10.1016/j.ijid.2020.01.009.

[31] A. E. Gorbalenya, S. C. Baker, R. S. Baric, R. J. de Groot, C. Drosten, A. A. Gulyaeva, B. L. Haagmans, C. Lauber, A. M. Leontovich, B. W. Neuman, D. Penzar, S. Perlman, L. L. M. Poon, D. V. Samborskiy, I. A. Sidorov, I. Sola, and J. Ziebuhr. The species severe acute respiratory syndrome-related coronavirus: classifying 2019-nCoV and naming it SARS-CoV-2. *Nature Microbiology*, 5(4):536–544, mar 2020. doi:10.1038/s41564-020-0695-z.

[32] A. Hosseini, V. Hashemi, N. Shomali, F. Asghari, T. Gharibi, M. Akbari, S. Gholizadeh, and A. Jafari. Innate and adaptive immune responses against coronavirus. *Biomedicine & Pharmacotherapy*, 132:110859, dec 2020. doi:10.1016/j.biopha.2020.110859.

[33] P. V'kovski, A. Kratzel, S. Steiner, H. Stalder, and V. Thiel. Coronavirus biology and replication: implications for SARS-CoV-2. *Nature Reviews Microbiology*, 19(3):155–170, oct 2020. doi:10.1038/s41579-020-00468-6.

[34] J. F.-W. Chan, K.-H. Kok, Z. Zhu, H. Chu, K. K.-W. To, S. Yuan, and K.-Y. Yuen. Genomic characterization of the 2019 novel human-pathogenic coronavirus isolated from a patient with atypical pneumonia after visiting wuhan. *Emerging Microbes & Infections*, 9(1):221–236, jan 2020. doi:10.1080/22221751.2020.1719902.

[35] S. Lytras, J. Hughes, D. Martin, P. Swanepoel, A. de Klerk, R. Lourens, S. L. K. Pond, W. Xia, X. Jiang, and D. L. Robertson. Exploring the natural origins of SARS-CoV-2 in the light of recombination. *Genome Biology and Evolution*, 14(2), feb 2022. doi:10.1093/gbe/evac018.

[36] T. G. Ksiazek, D. Erdman, C. S. Goldsmith, S. R. Zaki, T. Peret, S. Emery, S. Tong, C. Urbani, J. A. Comer, W. Lim, P. E. Rollin, S. F. Dowell, A.-E. Ling, C. D. Humphrey, W.-J. Shieh, J. Guarner, C. D. Paddock, P. Rota, B. Fields, J. DeRisi, J.-Y. Yang, N. Cox, J. M. Hughes, J. W. LeDuc, W. J. Bellini, and L. J. A. and. A novel coronavirus associated with severe acute respiratory syndrome. *New England Journal of Medicine*, 348(20):1953–1966, may 2003. doi:10.1056/nejmoa030781.

[37] A. Pormohammad, S. Ghorbani, A. Khatami, R. Farzi, B. Baradaran, D. L. Turner, R. J. Turner, N. C. Bahr, and J.-P. Idrovo. Comparison of confirmed covid-19 with sars and mers cases - clinical characteristics, laboratory findings, radiographic signs and outcomes: A systematic review and meta-analysis. *Reviews in Medical Virology*, 30(4), jun 2020. doi:10.1002/rmv.2112.

[38] L. F. Wang and B. T. Eaton. Bats, civets and the emergence of SARS. In *Current Topics in Microbiology and Immunology*, pages 325–344. Springer Berlin Heidelberg, 2007. doi:10.1007/978-3-540-70962-6_13.

[39] E. I. Azhar, S. A. El-Kafrawy, S. A. Farraj, A. M. Hassan, M. S. Al-Saeed, A. M. Hashem, and T. A. Madani. Evidence for camel-to-human transmission of MERS coronavirus. *New England Journal of Medicine*, 370(26):2499–2505, jun 2014. doi:10.1056/nejmoa1401505.

[40] A. Zumla, D. S. Hui, and S. Perlman. Middle east respiratory syndrome. *The Lancet*, 386(9997):995–1007, sep 2015. doi:10.1016/s0140-6736(15)60454-8.

[41] World Health Organisation. Middle east respiratory syndrome coronavirus (mers-cov). https://www.who.int/health-topics/middle-east-respiratory-syndrome-coronavirus-mers#tab=tab_1. Accessed: 2023-04-13.

[42] E. Mathieu, H. Ritchie, L. Rodés-Guirao, C. Appel, C. Giattino, J. Hasell, B. Macdonald, S. Dattani, D. Beltekian, E. Ortiz-Ospina, and M. Roser. Coronavirus pandemic (covid-19). *Our World in Data*, 2020. Accessed: 2023-04-18.

[43] World Health Organisation. Coronavirus disease (covid-19) pandemic. https://www.who.int/emergencies/diseases/novel-coronavirus-2019, 2021. Accessed: 2023-04-13.

[44] R. A. Weiss and A. R. McLean. What have we learnt from SARS? In *SARS*, pages 112–116. Oxford University Press, mar 2005. doi:10.1093/acprof:oso/9780198568193.003.0015.

[45] K. Koelle, M. A. Martin, R. Antia, B. Lopman, and N. E. Dean. The changing epidemiology of SARS-CoV-2. *Science*, 375(6585):1116–1121, mar 2022. doi:10.1126/science.abm4915.

[46] D. Wrapp, N. Wang, K. S. Corbett, J. A. Goldsmith, C.-L. Hsieh, O. Abiona, B. S. Graham, and J. S. McLellan. Cryo-EM structure of the 2019-nCoV spike in the prefusion conformation. *Science*, 367(6483):1260–1263, mar 2020. doi:10.1126/science.abb2507.

[47] C. Elias, A. Sekri, P. Leblanc, M. Cucherat, and P. Vanhems. The incubation period of COVID-19: A meta-analysis. *International Journal of Infectious Diseases*, 104:708–710, mar 2021. doi:10.1016/j.ijid.2021.01.069.

[48] M. Varia, S. Wilson, S. Sarwal, A. McGeer, E. Gournis, E. Galanis, B. Henry, and T. H. O. I. Team. Investigation of a nosocomial outbreak of severe acute respiratory syndrome (sars) in toronto, canada. *CMAJ*, 169(4):285–292, August 2003.

[49] V. Virlogeux, V. J. Fang, M. Park, J. T. Wu, and B. J. Cowling. Comparison of incubation period distribution of human infections with MERS-CoV in south korea and saudi arabia. *Scientific Reports*, 6(1), oct 2016. doi:10.1038/srep35839.

[50] K. M. Coerdt and A. Khachemoune. Corona viruses: reaching far beyond the common cold. *African Health Sciences*, 21(1):207–13, apr 2021. doi:10.4314/ahs.v21i1.27.

[51] E. de Wit, A. L. Rasmussen, D. Falzarano, T. Bushmaker, F. Feldmann, D. L. Brining, E. R. Fischer, C. Martellaro, A. Okumura, J. Chang, D. Scott, A. G. Benecke, M. G. Katze, H. Feldmann, and V. J. Munster. Middle east respiratory syndrome coronavirus (MERS-CoV) causes transient lower respiratory tract infection in rhesus macaques. *Proceedings of the National Academy of Sciences*, 110(41):16598–16603, sep 2013. doi:10.1073/pnas.1310744110.

[52] N. Petrovsky. SARS coronavirus infections of the lower respiratory tract and their prevention. In *The Microbiology of Respiratory System Infections*, pages 45–53. Elsevier, 2016. doi:10.1016/b978-0-12-804543-5.00003-8.

[53] K. Nakagawara, S. Chubachi, H. Namkoong, H. Tanaka, H. Lee, S. Azekawa, S. Otake, T. Fukushima, A. Morita, M. Watase, K. Sakurai, T. Kusumoto, T. Asakura, K. Masaki, H. Kamata, M. Ishii, N. Hasegawa, N. Harada, T. Ueda, S. Ueda, T. Ishiguro, K. Arimura, F. Saito, T. Yoshiyama, Y. Nakano, Y. Mutoh, Y. Suzuki, R. Edahiro, K. Murakami, Y. Sato, Y. Okada, R. Koike, Y. Kitagawa, K. Tokunaga, A. Kimura, S. Imoto, S. Miyano, S. Ogawa, T. Kanai, and K. Fukunaga. Impact of upper and lower respiratory symptoms on COVID-19 outcomes: a multicenter retrospective cohort study. *Respiratory Research*, 23(1), nov 2022. doi:10.1186/s12931-022-02222-3.

[54] P. V. Markov, M. Ghafari, M. Beer, K. Lythgoe, P. Simmonds, N. I. Stilianakis, and A. Katzourakis. The evolution of SARS-CoV-2. *Nature Reviews Microbiology*, 21(6):361–379, apr 2023. doi:10.1038/s41579-023-00878-2.

[55] R. J. Mason. Pathogenesis of COVID-19 from a cell biology perspective. *European Respiratory Journal*, 55(4):2000607, apr 2020. doi:10.1183/13993003.00607-2020.

[56] M. Z. Tay, C. M. Poh, L. Rénia, P. A. MacAry, and L. F. P. Ng. The trinity of COVID-19: immunity, inflammation and intervention. *Nature Reviews Immunology*, 20(6):363–374, apr 2020. doi:10.1038/s41577-020-0311-8.

[57] Z. Wu and J. M. McGoogan. Characteristics of and important lessons from the coronavirus disease 2019 (COVID-19) outbreak in china. *JAMA*, 323(13):1239, apr 2020. doi:10.1001/jama.2020.2648.

[58] Z. Qian, E. A. Travanty, L. Oko, K. Edeen, A. Berglund, J. Wang, Y. Ito, K. V. Holmes, and R. J. Mason. Innate immune response of human alveolar type II cells infected with severe acute respiratory syndrome–coronavirus. *American Journal of Respiratory Cell and Molecular Biology*, 48(6):742–748, jun 2013. doi:10.1165/rcmb.2012-0339oc.

[59] G. Xu, F. Qi, H. Wang, Y. Liu, X. Wang, R. Zou, J. Yuan, X. Liao, Y. Liu, S. Zhang, and Z. Zhang. The transient IFN response and the delay of adaptive immunity feature the severity of COVID-19. *Frontiers in Immunology*, 12, jan 2022. doi:10.3389/fimmu.2021.816745.

[60] Y. Nazerian, M. Ghasemi, Y. Yassaghi, A. Nazerian, and S. M. Hashemi. Role of SARS-CoV-2-induced cytokine storm in multi-organ failure: Molecular pathways and potential therapeutic options. *International Immunopharmacology*, 113:109428, dec 2022. doi:10.1016/j.intimp.2022.109428.

[61] Z. Xu, L. Shi, Y. Wang, J. Zhang, L. Huang, C. Zhang, S. Liu, P. Zhao, H. Liu, L. Zhu, Y. Tai, C. Bai, T. Gao, J. Song, P. Xia, J. Dong, J. Zhao, and F.-S. Wang. Pathological findings of COVID-19 associated with acute respiratory distress syndrome. *The Lancet Respiratory Medicine*, 8(4):420–422, apr 2020. doi:10.1016/s2213-2600(20)30076-x.

[62] L. Bergamaschi, F. Mescia, L. Turner, A. L. Hanson, P. Kotagiri, B. J. Dunmore, H. Ruffieux, A. D. Sa, O. Huhn, M. D. Morgan, P. P. Gerber, M. R. Wills, S. Baker, F. J. Calero-Nieto, R. Doffinger, G. Dougan, A. Elmer, I. G. Goodfellow, R. K. Gupta, M. Hosmillo, K. Hunter, N. Kingston, P. J. Lehner, N. J. Matheson, J. K. Nicholson, A. M. Petrunkina, S. Richardson, C. Saunders, J. E. Thaventhiran, E. J. Toonen, M. P. Weekes, B. Göttgens, M. Toshner, C. Hess, J. R. Bradley, P. A. Lyons, and K. G. Smith. Longitudinal analysis reveals that delayed bystander cd8+ t cell activation and early immune pathology distinguish severe COVID-19 from mild disease. *Immunity*, 54(6):1257–1275.e8, jun 2021. doi:10.1016/j.immuni.2021.05.010.

[63] C. Lucas, P. Wong, J. Klein, T. B. R. Castro, J. Silva, M. Sundaram, M. K. Ellingson, T. Mao, J. E. Oh, B. Israelow, T. Takahashi, M. Tokuyama, P. Lu, A. Venkataraman, A. Park, S. Mohanty, H. Wang, A. L. Wyllie, C. B. F. Vogels, R. Earnest, S. Lapidus, I. M. Ott, A. J. Moore, M. C. Muenker, J. B. Fournier, M. Campbell, C. D. Odio, A. Casanovas-Massana, A. Obaid, A. Lu-Culligan, A. Nelson, A. Brito, A. Nunez, A. Martin, A. Watkins, B. Geng, C. Kalinich, C. Harden, C. Todeasa, C. Jensen, D. Kim, D. McDonald, D. Shepard, E. Courchaine, E. B. White, E. Song, E. Silva, E. Kudo, G. DeIuliis, H. Rahming, H.-J. Park, I. Matos, J. Nouws, J. Valdez, J. Fauver, J. Lim, K.-A. Rose, K. Anastasio, K. Brower, L. Glick, L. Sharma, L. Sewanan, L. Knaggs, M. Minasyan, M. Batsu, M. Petrone, M. Kuang, M. Nakahata, M. Campbell, M. Linehan, M. H. Askenase, M. Simonov, M. Smolgovsky, N. Sonnert, N. Naushad, P. Vijayakumar, R. Martinello, R. Datta, R. Handoko, S. Bermejo, S. Prophet, S. Bickerton, S. Velazquez, T. Alpert, T. Rice, W. Khoury-Hanold, X. Peng, Y. Yang, Y. Cao, Y. Strong, R. Herbst, A. C. Shaw, R. Medzhitov, W. L. Schulz, N. D. Grubaugh, C. D. Cruz, S. Farhadian, A. I. Ko, S. B. Omer, and A. I. and. Longitudinal analyses reveal immunological misfiring in severe COVID-19. *Nature*, 584(7821):463–469, jul 2020. doi:10.1038/s41586-020-2588-y.

[64] T.-D. Kanneganti. Intracellular innate immune receptors: Life inside the cell. *Immunological Reviews*, 297(1):5–12, aug 2020. doi:10.1111/imr.12912.

[65] D. Blanco-Melo, B. E. Nilsson-Payant, W.-C. Liu, S. Uhl, D. Hoagland, R. Møller, T. X. Jordan, K. Oishi, M. Panis, D. Sachs, T. T. Wang, R. E. Schwartz, J. K. Lim, R. A. Albrecht, and B. R. tenOever. Imbalanced host response to SARS-CoV-2 drives development of COVID-19. *Cell*, 181(5):1036–1045.e9, may 2020. doi:10.1016/j.cell.2020.04.026.

[66] J. M. Burke, L. A. S. Clair, R. Perera, and R. Parker. SARS-CoV-2 infection triggers widespread host mRNA decay leading to an mRNA export block. *RNA*, 27(11):1318–1329, jul 2021. doi:10.1261/rna.078923.121.

[67] M. S. Diamond and T.-D. Kanneganti. Innate immunity: the first line of defense against SARS-CoV-2. *Nature Immunology*, 23(2):165–176, feb 2022. doi:10.1038/s41590-021-01091-0.

[68] Y. Konno, I. Kimura, K. Uriu, M. Fukushi, T. Irie, Y. Koyanagi, D. Sauter, R. J. Gifford, S. Nakagawa, and K. Sato. SARS-CoV-2 ORF3b is a potent interferon antagonist whose activity is increased by a naturally occurring elongation variant. *Cell Reports*, 32(12):108185, sep 2020. doi:10.1016/j.celrep.2020.108185.

[69] J.-Y. Li, C.-H. Liao, Q. Wang, Y.-J. Tan, R. Luo, Y. Qiu, and X.-Y. Ge. The ORF6, ORF8 and nucleocapsid proteins of SARS-CoV-2 inhibit type i interferon signaling pathway. *Virus Research*, 286:198074, sep 2020. doi:10.1016/j.virusres.2020.198074.

[70] P. Moss. The t cell immune response against SARS-CoV-2. *Nature Immunology*, 23(2):186–193, feb 2022. doi:10.1038/s41590-021-01122-w.

[71] L. Piccoli, Y.-J. Park, M. A. Tortorici, N. Czudnochowski, A. C. Walls, M. Beltramello, C. Silacci-Fregni, D. Pinto, L. E. Rosen, J. E. Bowen, O. J. Acton, S. Jaconi, B. Guarino, A. Minola, F. Zatta, N. Sprugasci, J. Bassi, A. Peter, A. D. Marco, J. C. Nix, F. Mele, S. Jovic, B. F. Rodriguez, S. V. Gupta, F. Jin, G. Piumatti, G. L. Presti, A. F. Pellanda, M. Biggiogero, M. Tarkowski, M. S. Pizzuto, E. Cameroni, C. Havenar-Daughton, M. Smithey, D. Hong, V. Lepori, E. Albanese, A. Ceschi, E. Bernasconi, L. Elzi, P. Ferrari, C. Garzoni, A. Riva, G. Snell, F. Sallusto, K. Fink, H. W. Virgin, A. Lanzavecchia, D. Corti, and D. Veesler. Mapping neutralizing and immunodominant sites on the SARS-CoV-2 spike receptor-binding domain by structure-guided high-resolution serology. *Cell*, 183(4):1024–1042.e21, nov 2020. doi:10.1016/j.cell.2020.09.037.

[72] M. S. Suthar, M. G. Zimmerman, R. C. Kauffman, G. Mantus, S. L. Linderman, W. H. Hudson, A. Vanderheiden, L. Nyhoff, C. W. Davis, O. Adekunle, M. Affer, M. Sherman, S. Reynolds, H. P. Verkerke, D. N. Alter, J. Guarner, J. Bryksin, M. C. Horwath, C. M. Arthur, N. Saakadze, G. H. Smith, S. Edupuganti, E. M. Scherer, K. Hellmeister, A. Cheng, J. A. Morales, A. S. Neish, S. R. Stowell, F. Frank, E. Ortlund, E. J. Anderson, V. D. Menachery, N. Rouphael, A. K. Mehta, D. S. Stephens, R. Ahmed, J. D. Roback, and J. Wrammert. Rapid generation of neutralizing antibody responses in COVID-19 patients. *Cell Reports Medicine*, 1(3):100040, jun 2020. doi:10.1016/j.xcrm.2020.100040.

[73] J. Seow, C. Graham, B. Merrick, S. Acors, S. Pickering, K. J. A. Steel, O. Hemmings, A. O'Byrne, N. Kouphou, R. P. Galao, G. Betancor, H. D. Wilson, A. W. Signell, H. Winstone, C. Kerridge, I. Huettner, J. M. Jimenez-Guardeño, M. J. Lista, N. Temperton, L. B. Snell, K. Bisnauthsing, A. Moore, A. Green, L. Martinez, B. Stokes, J. Honey, A. Izquierdo-Barras, G. Arbane, A. Patel, M. K. I. Tan, L. O'Connell, G. O'Hara, E. MacMahon, S. Douthwaite, G. Nebbia, R. Batra, R. Martinez-Nunez, M. Shankar-Hari, J. D. Edgeworth, S. J. D. Neil, M. H. Malim, and K. J. Doores. Longitudinal observation and decline of neutralizing antibody responses in the three months following SARS-CoV-2 infection in humans. *Nature Microbiology*, 5(12):1598–1607, oct 2020. doi:10.1038/s41564-020-00813-8.

[74] F. Muecksch, H. Wise, B. Batchelor, M. Squires, E. Semple, C. Richardson, J. McGuire, S. Clearly, E. Furrie, N. Greig, G. Hay, K. Templeton, J. C. C. Lorenzi, T. Hatziioannou, S. Jenks, and P. D. Bieniasz. Longitudinal serological analysis and neutralizing antibody levels in coronavirus disease 2019 convalescent patients. *The Journal of Infectious Diseases*, 223(3):389–398, nov 2020. doi:10.1093/infdis/jiaa659.

[75] B. Isho, K. T. Abe, M. Zuo, A. J. Jamal, B. Rathod, J. H. Wang, Z. Li, G. Chao, O. L. Rojas, Y. M. Bang, A. Pu, N. Christie-Holmes, C. Gervais, D. Ceccarelli, P. Samavarchi-Tehrani, F. Guvenc, P. Budylowski, A. Li, A. Paterson, F. Y. Yue, L. M. Marin, L. Caldwell, J. L. Wrana, K. Colwill, F. Sicheri, S. Mubareka, S. D. Gray-Owen, S. J. Drews, W. L. Siqueira, M. Barrios-Rodiles, M. Ostrowski, J. M. Rini, Y. Durocher, A. J. McGeer, J. L. Gommerman, and A.-C. Gingras. Persistence of serum and saliva antibody responses to SARS-CoV-2 spike antigens in COVID-19 patients. *Science Immunology*, 5(52), oct 2020. doi:10.1126/sciimmunol.abe5511.

[76] C. Lucas, J. Klein, M. E. Sundaram, F. Liu, P. Wong, J. Silva, T. Mao, J. E. Oh, S. Mohanty, J. Huang, M. Tokuyama, P. Lu, A. Venkataraman, A. Park, B. Israelow, C. B. F. Vogels, M. C. Muenker, C.-H. Chang, A. Casanovas-Massana, A. J. Moore, J. Zell, J. B. Fournier, A. Obaid, A. J. Robertson, A. Lu-Culligan, A. Zhao, A. Nelson, A. Brito, A. Nunez, A. Martin, A. E. Watkins, B. Geng, C. J. Chun, C. C. Kalinich, C. A. Harden, C. Todeasa, C. Jensen, C. E. Dorgay, D. Kim, D. McDonald, D. Shepard,

E. Courchaine, E. B. White, E. Song, E. Silva, E. Kudo, G. DeIuliis, H. Rahming, H.-J. Park, I. Matos, I. Ott, J. Nouws, J. Valdez, J. Fauver, J. Lim, K.-A. Rose, K. Anastasio, K. Brower, L. Glick, L. Sharma, L. Sewanan, L. Knaggs, M. Minasyan, M. Batsu, M. Petrone, M. Kuang, M. Nakahata, M. Linehan, M. H. Askenase, M. Simonov, M. Smolgovsky, N. C. Balkcom, N. Sonnert, N. Naushad, P. Vijayakumar, R. Martinello, R. Datta, R. Handoko, S. Bermejo, S. Prophet, S. Bickerton, S. Velazquez, T. Alpert, T. Rice, W. Khoury-Hanold, X. Peng, Y. Yang, Y. Cao, Y. Strong, Z. Lin, A. L. Wyllie, M. Campbell, A. I. Lee, H. J. Chun, N. D. Grubaugh, W. L. Schulz, S. Farhadian, C. D. Cruz, A. M. Ring, A. C. Shaw, A. V. Wisnewski, I. Yildirim, A. I. Ko, S. B. Omer, and A. I. and. Delayed production of neutralizing antibodies correlates with fatal COVID-19. *Nature Medicine*, 27(7):1178–1186, may 2021. doi:10.1038/s41591-021-01355-0.

[77] B. Diao, C. Wang, Y. Tan, X. Chen, Y. Liu, L. Ning, L. Chen, M. Li, Y. Liu, G. Wang, Z. Yuan, Z. Feng, Y. Zhang, Y. Wu, and Y. Chen. Reduction and functional exhaustion of t cells in patients with coronavirus disease 2019 (COVID-19). *Frontiers in Immunology*, 11, may 2020. doi:10.3389/fimmu.2020.00827.

[78] Y. Zhou, B. Fu, X. Zheng, D. Wang, C. Zhao, Y. Qi, R. Sun, Z. Tian, X. Xu, and H. Wei. Pathogenic t-cells and inflammatory monocytes incite inflammatory storms in severe COVID-19 patients. *National Science Review*, 7(6):998–1002, mar 2020. doi:10.1093/nsr/nwaa041.

[79] D. Martonik, A. Parfieniuk-Kowerda, M. Rogalska, and R. Flisiak. The role of th17 response in COVID-19. *Cells*, 10(6):1550, jun 2021. doi:10.3390/cells10061550.

[80] L. Min and Q. Sun. Antibodies and vaccines target RBD of SARS-CoV-2. *Frontiers in Molecular Biosciences*, 8, apr 2021. doi:10.3389/fmolb.2021.671633.

[81] Z. Zhao, J. Zhou, M. Tian, M. Huang, S. Liu, Y. Xie, P. Han, C. Bai, P. Han, A. Zheng, L. Fu, Y. Gao, Q. Peng, Y. Li, Y. Chai, Z. Zhang, X. Zhao, H. Song, J. Qi, Q. Wang, P. Wang, and G. F. Gao. Omicron SARS-CoV-2 mutations stabilize spike up-RBD conformation and lead to a non-RBM-binding monoclonal antibody escape. *Nature Communications*, 13(1), aug 2022. doi:10.1038/s41467-022-32665-7.

[82] Y. Cao, J. Wang, F. Jian, T. Xiao, W. Song, A. Yisimayi, W. Huang, Q. Li, P. Wang, R. An, J. Wang, Y. Wang, X. Niu, S. Yang, H. Liang, H. Sun, T. Li, Y. Yu, Q. Cui, S. Liu, X. Yang, S. Du, Z. Zhang, X. Hao, F. Shao, R. Jin, X. Wang, J. Xiao, Y. Wang, and X. S. Xie. Omicron escapes the majority of existing SARS-CoV-2 neutralizing antibodies. *Nature*, 602(7898):657–663, dec 2021. doi:10.1038/s41586-021-04385-3.

[83] S. K. Saini, D. S. Hersby, T. Tamhane, H. R. Povlsen, S. P. A. Hernandez, M. Nielsen, A. O. Gang, and S. R. Hadrup. Sars-cov-2 genome-wide t cell epitope mapping reveals immunodominance and substantial cd8+ t cell activation in covid-19 patients. *Science Immunology*, 6(58), apr 2021. doi:10.1126/sciimmunol.abf7550.

[84] K. I. Wagner, L. M. Mateyka, S. Jarosch, V. Grass, S. Weber, K. Schober, M. Hammel, T. Burrell, B. Kalali, H. Poppert, H. Beyer, S. Schambeck, S. Holdenrieder, A. Strötges-Achatz, V. Haselmann, M. Neumaier, J. Erber, A. Priller, S. Yazici, H. Roggendorf, M. Odendahl, T. Tonn, A. Dick, K. Witter, H. Mijočević, U. Protzer, P. A. Knolle, A. Pichlmair, C. S. Crowell, M. Gerhard, E. D'Ippolito, and D. H. Busch. Recruitment of highly cytotoxic cd8+ t cell receptors in mild SARS-CoV-2 infection. *Cell Reports*, 38(2):110214, jan 2022. doi:10.1016/j.celrep.2021.110214.

[85] A. Tarke, J. Sidney, C. K. Kidd, J. M. Dan, S. I. Ramirez, E. D. Yu, J. Mateus, R. da Silva Antunes, E. Moore, P. Rubiro, N. Methot, E. Phillips, S. Mallal, A. Frazier, S. A. Rawlings, J. A. Greenbaum, B. Peters, D. M. Smith, S. Crotty, D. Weiskopf, A. Grifoni, and A. Sette. Comprehensive analysis of t cell immunodominance and immunoprevalence of SARS-CoV-2 epitopes in COVID-19 cases. *Cell Reports Medicine*, 2(2):100204, feb 2021. doi:10.1016/j.xcrm.2021.100204.

[86] A. Nelde, T. Bilich, J. S. Heitmann, Y. Maringer, H. R. Salih, M. Roerden, M. Lübke, J. Bauer, J. Rieth, M. Wacker, A. Peter, S. Hörber, B. Traenkle, P. D. Kaiser, U. Rothbauer, M. Becker, D. Junker, G. Krause, M. Strengert, N. Schneiderhan-Marra, M. F. Templin, T. O. Joos, D. J. Kowalewski, V. Stos-Zweifel, M. Fehr, A. Rabsteyn, V. Mirakaj, J. Karbach, E. Jäger, M. Graf, L.-C. Gruber, D. Rachfalski, B. Preuß, I. Hagelstein, M. Märklin, T. Bakchoul, C. Gouttefangeas, O. Kohlbacher, R. Klein, S. Stevanović, H.-G. Rammensee, and J. S. Walz. SARS-CoV-2-derived peptides define heterologous and COVID-19-induced t cell recognition. *Nature Immunology*, 22(1):74–85, sep 2020. doi:10.1038/s41590-020-00808-x.

[87] C. Stein, H. Nassereldine, R. J. D. Sorensen, J. O. Amlag, C. Bisignano, S. Byrne, E. Castro, K. Coberly, J. K. Collins, J. Dalos, F. Daoud, A. Deen, E. Gakidou, J. R. Giles, E. N. Hulland, B. M. Huntley, K. E. Kinzel, R. Lozano, A. H. Mokdad, T. Pham, D. M. Pigott, R. C. R. Jr., T. Vos, S. I. Hay, C. J. L. Murray, and S. S. Lim. Past SARS-CoV-2 infection protection against re-infection: a systematic review and meta-analysis. *The Lancet*, 401(10379):833–842, mar 2023. doi:10.1016/s0140-6736(22)02465-5.

[88] J. Zhao, J. Zhao, A. K. Mangalam, R. Channappanavar, C. Fett, D. K. Meyerholz, S. Agnihothram, R. S. Baric, C. S. David, and S. Perlman. Airway memory cd4+ t cells mediate protective immunity against emerging respiratory coronaviruses. *Immunity*, 44(6):1379–1391, jun 2016. doi:10.1016/j.immuni.2016.05.006.

[89] A. Grifoni, D. Weiskopf, S. I. Ramirez, J. Mateus, J. M. Dan, C. R. Moderbacher, S. A. Rawlings, A. Sutherland, L. Premkumar, R. S. Jadi, D. Marrama, A. M. de Silva, A. Frazier, A. F. Carlin, J. A. Greenbaum, B. Peters, F. Krammer, D. M. Smith, S. Crotty, and A. Sette. Targets of t cell responses to SARS-CoV-2 coronavirus in humans with COVID-19 disease and unexposed individuals. *Cell*, 181(7):1489–1501.e15, jun 2020. doi:10.1016/j.cell.2020.05.015.

[90] J. Braun, L. Loyal, M. Frentsch, D. Wendisch, P. Georg, F. Kurth, S. Hippenstiel, M. Dingeldey, B. Kruse, F. Fauchere, E. Baysal, M. Mangold, L. Henze, R. Lauster, M. A. Mall, K. Beyer, J. Röhmel, S. Voigt, J. Schmitz, S. Miltenyi, I. Demuth, M. A. Müller, A. Hocke, M. Witzenrath, N. Suttorp, F. Kern, U. Reimer, H. Wenschuh, C. Drosten, V. M. Corman, C. Giesecke-Thiel, L. E. Sander, and A. Thiel. SARS-CoV-2-reactive t cells in healthy donors and patients with COVID-19. *Nature*, 587(7833):270–274, jul 2020. doi:10.1038/s41586-020-2598-9.

[91] G. Saletti, T. Gerlach, J. M. Jansen, A. Molle, H. Elbahesh, M. Ludlow, W. Li, B.-J. Bosch, A. D. M. E. Osterhaus, and G. F. Rimmelzwaan. Older adults lack SARS CoV-2 cross-reactive t lymphocytes directed to human coronaviruses OC43 and NL63. *Scientific Reports*, 10(1), dec 2020. doi:10.1038/s41598-020-78506-9.

[92] R. Kundu, J. S. Narean, L. Wang, J. Fenn, T. Pillay, N. D. Fernandez, E. Conibear, A. Koycheva, M. Davies, M. Tolosa-Wright, S. Hakki, R. Varro, E. McDermott, S. Hammett, J. Cutajar, R. S. Thwaites, E. Parker, C. Rosadas, M. McClure, R. Tedder, G. P. Taylor, J. Dunning, and A. Lalvani. Cross-reactive memory t cells associate with protection

against SARS-CoV-2 infection in COVID-19 contacts. *Nature Communications*, 13(1), jan 2022. doi:10.1038/s41467-021-27674-x.

[93] R. Channappanavar, C. Fett, J. Zhao, D. K. Meyerholz, and S. Perlman. Virus-specific memory cd8 t cells provide substantial protection from lethal severe acute respiratory syndrome coronavirus infection. *Journal of Virology*, 88(19):11034–11044, oct 2014. doi:10.1128/jvi.01505-14.

[94] N. L. Bert, A. T. Tan, K. Kunasegaran, C. Y. L. Tham, M. Hafezi, A. Chia, M. H. Y. Chng, M. Lin, N. Tan, M. Linster, W. N. Chia, M. I.-C. Chen, L.-F. Wang, E. E. Ooi, S. Kalimuddin, P. A. Tambyah, J. G.-H. Low, Y.-J. Tan, and A. Bertoletti. SARS-CoV-2-specific t cell immunity in cases of COVID-19 and SARS, and uninfected controls. *Nature*, 584(7821):457–462, jul 2020. doi:10.1038/s41586-020-2550-z.

[95] Paul-Ehrlich-Institut. European commission grants marketing authorisation for biontech/pfizer's covid-19 vaccine for the european union. https://www.pei.de/EN/newsroom/hp-news/2020/201221-marketing-authorisation-covid-19-vaccine-european-commission.html, 2020. Accessed: 2023-04-12.

[96] U. Sahin, K. Karikó, and Özlem Türeci. mRNA-based therapeutics — developing a new class of drugs. *Nature Reviews Drug Discovery*, 13(10):759–780, sep 2014. doi:10.1038/nrd4278.

[97] T. Schlake, A. Thess, M. Fotin-Mleczek, and K.-J. Kallen. Developing mRNA-vaccine technologies. *RNA Biology*, 9(11):1319–1330, nov 2012. doi:10.4161/rna.22269.

[98] European Medicines Agency. Ema recommends covid-19 vaccine moderna for authorisation in the eu. https://www.ema.europa.eu/en/news/ema-recommends-covid-19-vaccine-moderna-authorisation-eu. Accessed: 2023-04-12.

[99] F. P. Polack, S. J. Thomas, N. Kitchin, J. Absalon, A. Gurtman, S. Lockhart, J. L. Perez, G. P. Marc, E. D. Moreira, C. Zerbini, R. Bailey, K. A. Swanson, S. Roychoudhury, K. Koury, P. Li, W. V. Kalina, D. Cooper, R. W. Frenck, L. L. Hammitt, Özlem Türeci, H. Nell, A. Schaefer, S. Ünal, D. B. Tresnan, S. Mather, P. R. Dormitzer, U. Şahin, K. U. Jansen, and W. C. Gruber. Safety and efficacy of the BNT162b2 mRNA covid-19 vaccine. *New England Journal of Medicine*, 383(27):2603–2615, dec 2020. doi:10.1056/nejmoa2034577.

[100] L. R. Baden, H. M. E. Sahly, B. Essink, K. Kotloff, S. Frey, R. Novak, D. Diemert, S. A. Spector, N. Rouphael, C. B. Creech, J. McGettigan, S. Khetan, N. Segall, J. Solis, A. Brosz, C. Fierro, H. Schwartz, K. Neuzil, L. Corey, P. Gilbert, H. Janes, D. Follmann, M. Marovich, J. Mascola, L. Polakowski, J. Ledgerwood, B. S. Graham, H. Bennett, R. Pajon, C. Knightly, B. Leav, W. Deng, H. Zhou, S. Han, M. Ivarsson, J. Miller, and T. Zaks. Efficacy and safety of the mRNA-1273 SARS-CoV-2 vaccine. *New England Journal of Medicine*, 384(5):403–416, feb 2021. doi:10.1056/nejmoa2035389.

[101] M. W. Tenforde, W. H. Self, M. Gaglani, A. A. Ginde, D. J. Douin, H. K. Talbot, J. D. Casey, N. M. Mohr, A. Zepeski, T. McNeal, S. Ghamande, K. W. Gibbs, D. C. Files, D. N. Hager, A. Shehu, M. E. Prekker, A. E. Frosch, M. N. Gong, A. Mohamed, N. J. Johnson, V. Srinivasan, J. S. Steingrub, I. D. Peltan, S. M. Brown, E. T. Martin, A. S. Monto, A. Khan, C. L. Hough, L. W. Busse, A. Duggal, J. G. Wilson, N. Qadir, S. Y. Chang, C. Mallow, C. Rivas, H. M. Babcock, J. H. Kwon, M. C. Exline, M. Botros, A. S.

Lauring, N. I. Shapiro, N. Halasa, J. D. Chappell, C. G. Grijalva, T. W. Rice, I. D. Jones, W. B. Stubblefield, A. Baughman, K. N. Womack, J. P. Rhoads, C. J. Lindsell, K. W. Hart, Y. Zhu, K. Adams, D. Surie, M. L. McMorrow, and M. M. P. and. Effectiveness of mRNA vaccination in preventing COVID-19–associated invasive mechanical ventilation and death — united states, march 2021–january 2022. *MMWR. Morbidity and Mortality Weekly Report*, 71(12):459–465, mar 2022. doi:10.15585/mmwr.mm7112e1.

[102] M. A. Kennedy and R. J. Parks. Adenovirus virion stability and the viral genome: Size matters. *Molecular Therapy*, 17(10):1664–1666, oct 2009. doi:10.1038/mt.2009.202.

[103] A. N. Lukashev and A. A. Zamyatnin. Viral vectors for gene therapy: Current state and clinical perspectives. *Biochemistry (Moscow)*, 81(7):700–708, jul 2016. doi:10.1134/s0006297916070063.

[104] S. A. Mendonça, R. Lorincz, P. Boucher, and D. T. Curiel. Adenoviral vector vaccine platforms in the SARS-CoV-2 pandemic. *npj Vaccines*, 6(1), aug 2021. doi:10.1038/s41541-021-00356-x.

[105] Z. C. Hartman, D. M. Appledorn, and A. Amalfitano. Adenovirus vector induced innate immune responses: Impact upon efficacy and toxicity in gene therapy and vaccine applications. *Virus Research*, 132(1-2):1–14, mar 2008. doi:10.1016/j.virusres.2007.10.005.

[106] Europäische Kommission. Europäische kommission erteilt dritte zulassung für sicheren und wirksamen impfstoff gegen covid-19. https://ec.europa.eu/commission/presscorner/detail/de/ip_21_306, 2021. Accessed: 2023-04-12.

[107] European Medicnes Agency. Jcovden (previously covid-19 vaccine janssen). https://www.ema.europa.eu/en/medicines/human/EPAR/jcovden-previously-covid-19-vaccine-janssen, 2023. Accessed: 2023-04-12.

[108] M. Voysey, S. A. C. Clemens, S. A. Madhi, L. Y. Weckx, P. M. Folegatti, P. K. Aley, B. Angus, V. L. Baillie, S. L. Barnabas, Q. E. Bhorat, S. Bibi, C. Briner, P. Cicconi, E. A. Clutterbuck, A. M. Collins, C. L. Cutland, T. C. Darton, K. Dheda, C. Dold, C. J. A. Duncan, K. R. W. Emary, K. J. Ewer, A. Flaxman, L. Fairlie, S. N. Faust, S. Feng, D. M. Ferreira, A. Finn, E. Galiza, A. L. Goodman, C. M. Green, C. A. Green, M. Greenland, C. Hill, H. C. Hill, I. Hirsch, A. Izu, D. Jenkin, C. C. D. Joe, S. Kerridge, A. Koen, G. Kwatra, R. Lazarus, V. Libri, P. J. Lillie, N. G. Marchevsky, R. P. Marshall, A. V. A. Mendes, E. P. Milan, A. M. Minassian, A. McGregor, Y. F. Mujadidi, A. Nana, S. D. Padayachee, D. J. Phillips, A. Pittella, E. Plested, K. M. Pollock, M. N. Ramasamy, A. J. Ritchie, H. Robinson, A. V. Schwarzbold, A. Smith, R. Song, M. D. Snape, E. Sprinz, R. K. Sutherland, E. C. Thomson, M. E. Török, M. Toshner, D. P. J. Turner, J. Vekemans, T. L. Villafana, T. White, C. J. Williams, A. D. Douglas, A. V. S. Hill, T. Lambe, S. C. Gilbert, A. J. Pollard, M. Aban, K. W. Abeyskera, J. Aboagye, M. Adam, K. Adams, J. P. Adamson, G. Adewatan, S. Adlou, K. Ahmed, Y. Akhalwaya, S. Akhalwaya, A. Alcock, A. Ali, E. R. Allen, L. Allen, F. B. Alvernaz, F. S. Amorim, C. S. Andrade, F. Andritsou, R. Anslow, E. H. Arbe-Barnes, M. P. Ariaans, B. Arns, L. Arruda, L. Assad, P. D. A. Azi, L. D. A. Azi, G. Babbage, C. Bailey, K. F. Baker, M. Baker, N. Baker, P. Baker, I. Baleanu, D. Bandeira, A. Bara, M. A. Barbosa, D. Barker, G. D. Barlow, E. Barnes, A. S. Barr, J. R. Barrett, J. Barrett, K. Barrett, L. Bates, A. Batten, K. Beadon, E. Beales, R. Beckley, S. Belij-Rammerstorfer, J. Bell, D. Bellamy, S. Belton, A. Berg, L. Bermejo, E. Berrie, L. Berry, D. Berzenyi, A. Beveridge, K. R. Bewley, I. Bharaj, S. Bhikha, A. E. Bhorat, Z. E. Bhorat, E. M. Bijker, S. Birch, G. Birch, K. Birchall, A. Bird, O. Bird, K. Bisnauthsing, M. Bittaye,

L. Blackwell, R. Blacow, H. Bletchly, C. L. Blundell, S. R. Blundell, P. Bodalia, E. Bolam, E. Boland, D. Bormans, N. Borthwick, F. Bowring, A. Boyd, P. Bradley, T. Brenner, A. Bridges-Webb, P. Brown, C. Brown, C. Brown-O'Sullivan, S. Bruce, E. Brunt, W. Budd, Y. A. Bulbulia, M. Bull, J. Burbage, A. Burn, K. R. Buttigieg, N. Byard, I. C. Puig, A. Calvert, S. Camara, M. Cao, F. Cappuccini, R. Cardona, J. R. Cardoso, M. Carr, M. W. Carroll, A. Carson-Stevens, Y. de M. Carvalho, H. R. Casey, P. Cashen, T. R. Castro, L. C. Castro, K. Cathie, A. Cavey, J. Cerbino-Neto, L. F. F. Cezar, J. Chadwick, C. Chanice, D. Chapman, S. Charlton, K. S. Cheliotis, I. Chelysheva, O. Chester, E. Chiplin, S. Chita, J.-S. Cho, L. Cifuentes, E. Clark, M. Clark, R. Colin-Jones, S. L. Collins, H. Colton, C. P. Conlon, S. Connarty, N. Coombes, C. Cooper, R. Cooper, L. Cornelissen, T. Corrah, C. A. Cosgrove, F. B. Costa, T. Cox, W. E. Crocker, S. Crosbie, D. Cullen, D. R. Cunha, C. J. Cunningham, F. C. Cuthbertson, D. M. da Costa, S. N. F. D. Guarda, L. P. da Silva, A. C. da Silva Moraes, B. E. Damratoski, Z. Danos, M. T. Dantas, M. S. Datoo, C. Datta, M. Davids, S. L. Davies, K. Davies, H. Davies, S. Davies, J. Davies, E. J. Davis, J. Davis, J. A. de Carvalho, J. D. Jager, S. de Jesus Jnr, L. M. D. O. Kalid, D. Dearlove, T. Demissie, A. Desai, S. D. Marco, C. D. Maso, T. Dinesh, C. Docksey, T. Dong, F. R. Donnellan, T. G. D. Santos, T. G. D. Santos, E. P. D. Santos, N. Douglas, C. Downing, J. Drake, R. Drake-Brockman, R. Drury, J. D. Plessis, S. J. Dunachie, A. Duncan, N. J. Easom, M. Edwards, N. J. Edwards, F. Edwards, O. M. E. Muhanna, S. C. Elias, B. Ellison-Handley, M. J. Elmore, M. R. English, A. Esmail, Y. M. Essack, M. Farooq, S. Fedosyuk, S. Felle, S. Ferguson, C. F. D. Silva, S. Field, R. Fisher, J. Fletcher, H. Fofie, H. Fok, K. J. Ford, R. Fothergill, J. Fowler, P. H. Fraiman, E. Francis, M. M. Franco, J. Frater, M. S. Freire, S. H. Fry, S. Fudge, R. F. Filho, J. Furze, M. Fuskova, P. Galian-Rubio, H. Garlant, M. Gavrila, K. A. Gibbons, C. Gilbride, H. Gill, K. Godwin, K. Gokani, M. L. F. Gonçalves, I. G. Gonzalez, J. Goodall, J. Goodwin, A. Goondiwala, K. Gordon-Quayle, G. Gorini, A. Goyanna, J. Grab, L. Gracie, J. Green, N. Greenwood, J. Greffrath, M. M. Groenewald, A. Gunawardene, G. Gupta, M. Hackett, B. Hallis, M. Hamaluba, E. Hamilton, J. Hamlyn, D. Hammersley, A. T. Hanrath, B. Hanumunthadu, S. A. Harris, C. Harris, T. D. Harrison, D. Harrison, T. A. Harris-Wright, T. C. Hart, B. Hartnell, J. Haughney, S. Hawkins, L. Y. Hayano, I. Head, P. T. Heath, J. A. Henry, M. H. Herrera, D. B. Hettle, C. Higa, J. Hill, G. Hodges, S. Hodgson, E. Horne, M. M. Hou, C. F. Houlihan, E. Howe, N. Howell, J. Humphreys, H. E. Humphries, K. Hurley, C. Huson, C. Hyams, A. Hyder-Wright, S. Ikram, A. Ishwarbhai, P. Iveson, V. Iyer, F. Jackson, S. Jackson, S. Jaumdally, H. Jeffers, N. Jesudason, C. Jones, C. Jones, K. Jones, E. Jones, M. R. Jorge, A. Joshi, E. A. Júnior, R. Kailath, F. Kana, A. Kar, K. Karampatsas, M. Kasanyinga, L. Kay, J. Keen, J. K. Wright, E. J. Kelly, D. Kelly, D. M. Kelly, S. Kelly, D. Kerr, L. Khan, B. Khozoee, A. Khurana, S. Kidd, A. Killen, J. Kinch, P. Kinch, L. D. King, T. B. King, L. Kingham, P. Klenerman, D. M. Kluczna, F. Knapper, J. C. Knight, D. Knott, S. Koleva, P. M. Lages, M. Lang, G. Lang, C. W. Larkworthy, J. P. Larwood, R. Law, A. M. Lawrie, E. M. Lazarus, A. Leach, E. A. Lees, A. Lelliott, N.-M. Lemm, A. E. R. Lessa, S. Leung, Y. Li, A. M. Lias, K. Liatsikos, A. Linder, S. Lipworth, S. Liu, X. Liu, A. Lloyd, S. Lloyd, L. Loew, R. L. Ramon, L. B. Lora, K. G. Luz, J. C. MacDonald, G. MacGregor, M. Madhavan, D. O. Mainwaring, E. Makambwa, R. Makinson, M. Malahleha, R. Malamatsho, G. Mallett, N. Manning, K. Mansatta, T. Maoko, S. Marinou, E. Marlow, G. N. Marques, P. Marriott, R. P. Marshall, J. L. Marshall, M. Masenya, M. Masilela, S. K. Masters, M. Mathew, H. Matlebjane, K. Matshidiso, O. Mazur, A. Mazzella, H. McCaughan, J. McEwan, J. McGlashan, L. McInroy, N. McRobert, S. McSwiggan, C. Megson, S. Mehdipour, W. Meijs, R. N. Mendonça, A. J. Mentzer, A. C. F. Mesquita, P. Miralhes, N. Mirtorabi, C. Mitton, S. Mnyakeni, F. Moghaddas, K. Molapo, M. Moloi, M. Moore, M. Moran, E. Morey,

R. Morgans, S. J. Morris, S. Morris, H. Morrison, F. Morselli, G. Morshead, R. Morter, L. Mottay, A. Moultrie, N. Moyo, M. Mpelembue, S. Msomi, Y. Mugodi, E. Mukhopadhyay, J. Muller, A. Munro, S. Murphy, P. Mweu, C. Myerscough, G. Naik, K. Naker, E. Nastouli, B. Ndlovu, E. Nikolaou, C. Njenga, H. C. Noal, A. Noé, G. Novaes, F. L. Nugent, G. L. A. Nunes, K. O'Brien, D. O'Connor, S. Oelofse, B. Oguti, V. Olchawski, N. J. Oldfield, M. G. Oliveira, C. Oliveira, I. S. Q. Oliveira, A. Oommen-Jose, A. Oosthuizen, P. O'Reilly, P. J. O'Reilly, P. Osborne, D. R. Owen, L. Owen, D. Owens, N. Owino, M. Pacurar, B. V. Paiva, E. M. Palhares, S. Palmer, H. M. R. Parracho, K. Parsons, D. Patel, B. Patel, F. Patel, M. Patrick-Smith, R. O. Payne, Y. Peng, E. J. Penn, A. Pennington, M. P. P. Alvarez, B. P. P. Stuchi, A. L. Perez, T. Perinpanathan, J. Perring, R. Perumal, S. Y. Petkar, T. Philip, J. Phillips, M. K. Phohu, L. Pickup, S. Pieterse, J. M. Pinheiro, J. Piper, D. Pipini, M. Plank, S. Plant, S. Pollard, J. Pooley, A. Pooran, I. Poulton, C. Powers, F. B. Presa, D. A. Price, V. Price, M. R. Primeira, P. C. Proud, S. Provstgaard-Morys, S. Pueschel, D. Pulido, S. Quaid, R. Rabara, K. Radia, D. Rajapaska, T. Rajeswaran, L. Ramos, A. S. F. Ramos, F. R. Lopez, T. Rampling, J. Rand, H. Ratcliffe, T. Rawlinson, D. Rea, B. Rees, M. Resuello-Dauti, E. R. Pabon, S. Rhead, T. Riaz, M. Ricamara, A. Richards, A. Richter, N. Ritchie, A. J. Ritchie, A. J. Robbins, H. Roberts, R. E. Robinson, S. Roche, C. Rollier, L. Rose, A. L. R. Russell, L. Rossouw, S. Royal, I. Rudiansyah, K. Ryalls, C. Sabine, S. Saich, J. C. Sale, A. M. Salman, N. Salvador, S. Salvador, M. D. Sampaio, A. D. Samson, A. Sanchez-Gonzalez, H. Sanders, K. Sanders, E. Santos, M. F. S. Guerra, I. Satti, J. E. Saunders, C. Saunders, A. B. A. Sayed, I. S. van der Loeff, A. B. Schmid, E. Schofield, G. R. Screaton, S. Seddiqi, R. R. Segireddy, R. Senger, S. Serrano, I. Shaik, H. R. Sharpe, K. Sharrocks, R. Shaw, A. Shea, E. Sheehan, A. Shepherd, F. Shiham, S. E. Silk, L. Silva-Reyes, L. B. T. Silveira, M. B. Silveira, N. Singh, J. Sinha, D. T. Skelly, D. C. Smith, N. Smith, H. E. Smith, D. J. Smith, C. C. Smith, A. S. Soares, C. Solórzano, G. L. Sorio, K. Sorley, T. Sosa-Rodriguez, C. M. Souza, B. S. Souza, A. R. Souza, T. S. Lopez, L. Sowole, A. J. Spencer, L. Spoors, L. Stafford, I. Stamford, R. Stein, L. Stockdale, L. V. Stockwell, L. H. Strickland, A. Stuart, A. Sturdy, N. Sutton, A. Szigeti, A. Tahiri-Alaoui, R. Tanner, C. Taoushanis, A. W. Tarr, R. Tarrant, K. Taylor, U. Taylor, I. J. Taylor, J. Taylor, R. te Water Naude, K. Templeton, Y. Themistocleous, A. Themistocleous, M. Thomas, K. Thomas, T. M. Thomas, A. Thombrayil, J. Thompson, F. Thompson, A. Thompson, A. Thompson, K. Thompson, V. Thornton-Jones, L. H. Thotusi, P. J. Tighe, L. A. Tinoco, G. F. Tiongson, B. Tladinyane, M. Tomasicchio, A. Tomic, S. Tonks, J. Towner, N. Tran, J. A. Tree, G. Trillana, C. Trinham, R. Trivett, A. Truby, B. L. Tsheko, P. Tubb, A. Turabi, R. Turner, C. Turner, N. Turner, B. Tyagi, M. Ulaszewska, B. R. Underwood, S. van Eck, R. Varughese, D. Verbart, M. K. Verheul, I. Vichos, T. A. Vieira, G. Walker, L. Walker, M. E. Wand, T. Wardell, G. M. Warimwe, S. C. Warren, B. Watkins, M. E. Watson, E. Watson, S. Webb, A. Webster, J. Welch, Z. Wellbelove, J. H. Wells, A. J. West, B. White, C. White, R. White, P. Williams, R. L. Williams, S. Willingham, R. Winslow, D. Woods, M. Woodyer, A. T. Worth, D. Wright, M. Wroblewska, A. Yao, Y. T. N. Yim, M. B. Zambrano, R. L. Zimmer, D. Zizi, and P. Zuidewind. Single-dose administration and the influence of the timing of the booster dose on immunogenicity and efficacy of ChAdOx1 nCoV-19 (AZD1222) vaccine: a pooled analysis of four randomised trials. *The Lancet*, 397(10277):881–891, mar 2021. doi:10.1016/s0140-6736(21)00432-3.

[109] J. Sadoff, G. Gray, A. Vandebosch, V. Cárdenas, G. Shukarev, B. Grinsztejn, P. A. Goepfert, C. Truyers, H. Fennema, B. Spiessens, K. Offergeld, G. Scheper, K. L. Taylor, M. L. Robb, J. Treanor, D. H. Barouch, J. Stoddard, M. F. Ryser, M. A. Marovich, K. M. Neuzil, L. Corey, N. Cauwenberghs, T. Tanner, K. Hardt, J. Ruiz-Guiñazú, M. L. Gars, H. Schuitemaker, J. V. Hoof, F. Struyf, and M. Douoguih. Safety and efficacy

of single-dose ad26.COV2.s vaccine against covid-19. *New England Journal of Medicine*, 384(23):2187–2201, jun 2021. doi:10.1056/nejmoa2101544.

[110] V. P. Chavda, R. Bezbaruah, D. Valu, B. Patel, A. Kumar, S. Prasad, B. B. Kakoti, A. Kaushik, and M. Jesawadawala. Adenoviral vector-based vaccine platform for COVID-19: Current status. *Vaccines*, 11(2):432, feb 2023. doi:10.3390/vaccines11020432.

[111] B. Sanders, M. Koldijk, and H. Schuitemaker. Inactivated viral vaccines. In *Vaccine Analysis: Strategies, Principles, and Control*, pages 45–80. Springer Berlin Heidelberg, nov 2014. doi:10.1007/978-3-662-45024-6_2.

[112] European Medicines Agency. Ema recommends valneva's covid-19 vaccine for authorisation in the eu. https://www.ema.europa.eu/en/news/ema-recommends-valnevas-covid-19-vaccine-authorisation-eu. Accessed: 2023-04-12.

[113] R. Lazarus, B. Querton, I. C. Ramljak, S. Dewasthaly, J. C. Jaramillo, K. Dubischar, M. Krammer, P. Weisova, R. Hochreiter, S. Eder-Lingelbach, C. Taucher, A. Finn, C. Bethune, M. Boffito, M. Bula, F. M. Burns, R. Clark, D. Dasyam, S. Drysdale, S. Faust, E. Gkrania-Klotsas, C. Green, H. Hassanin, P. Heath, A. Heer, T. Helliwell, A. Hormis, P. Kalra, R. Lazarus, E. Moran, J. Ndikum, I. Page, D. Price, N. Probert, M. Ramjee, T. Rampling, H. S. Randeva, S. Ryder, J. Steer, E. Thompson, and D. Torku. Immunogenicity and safety of an inactivated whole-virus COVID-19 vaccine (VLA2001) compared with the adenoviral vector vaccine ChAdOx1-s in adults in the UK (COV-COMPARE): interim analysis of a randomised, controlled, phase 3, immunobridging trial. *The Lancet Infectious Diseases*, 22(12):1716–1727, dec 2022. doi:10.1016/s1473-3099(22)00502-3.

[114] J.-H. Tian, N. Patel, R. Haupt, H. Zhou, S. Weston, H. Hammond, J. Logue, A. D. Portnoff, J. Norton, M. Guebre-Xabier, B. Zhou, K. Jacobson, S. Maciejewski, R. Khatoon, M. Wisniewska, W. Moffitt, S. Kluepfel-Stahl, B. Ekechukwu, J. Papin, S. Boddapati, C. J. Wong, P. A. Piedra, M. B. Frieman, M. J. Massare, L. Fries, K. L. Bengtsson, L. Stertman, L. Ellingsworth, G. Glenn, and G. Smith. SARS-CoV-2 spike glycoprotein vaccine candidate NVX-CoV2373 immunogenicity in baboons and protection in mice. *Nature Communications*, 12(1), jan 2021. doi:10.1038/s41467-020-20653-8.

[115] J. N. Bhiman, S. I. Richardson, B. E. Lambson, P. Kgagudi, N. Mzindle, H. Kaldine, C. Crowther, G. Gray, L.-G. Bekker, A. Koen, L. Fairlie, L. Fouche, Q. Bhorat, K. Dheda, M. Tameris, M. Masilela, Z. Hoosain, N. Singh, S. Hanley, M. Archary, C. Louw, C. Grobbelaar, U. Lalloo, N. Joseph, G. Kruger, V. Shinde, C. Bennett, G. M. Glenn, S. A. Madhi, and P. L. M. and. Novavax NVX-COV2373 triggers neutralization of omicron sub-lineages. *Scientific Reports*, 13(1), jan 2023. doi:10.1038/s41598-023-27698-x.

[116] J. Wei, K. B. Pouwels, N. Stoesser, P. C. Matthews, I. Diamond, R. Studley, E. Rourke, D. Cook, J. I. Bell, J. N. Newton, J. Farrar, A. Howarth, B. D. Marsden, S. Hoosdally, E. Y. Jones, D. I. Stuart, D. W. Crook, T. E. A. Peto, A. S. Walker, D. W. Eyre, T. Thomas, D. Ayoubkhani, R. Black, A. Felton, M. Crees, J. Jones, L. Lloyd, E. Sutherland, E. Pritchard, K.-D. Vihta, G. Doherty, J. Kavanagh, K. K. Chau, S. B. Hatch, D. Ebner, L. M. Ferreira, T. Christott, W. Dejnirattisai, J. Mongkolsapaya, S. Cameron, P. Tamblin-Hopper, M. Wolna, R. Brown, R. Cornall, G. Screaton, K. Lythgoe, D. Bonsall, T. Golubchik, H. Fryer, S. Cox, K. Paddon, T. James, T. House, J. Robotham, P. Birrell, H. Jordan, T. Sheppard, G. Athey, D. Moody, L. Curry, P. Brereton, I. Jarvis, A. Godsmark, G. Morris, B. Mallick, P. Eeles, J. Hay, H. VanSteenhouse, J. Lee, S. White, T. Evans, L. Bloemberg, K. Allison, A. Pandya, S. Davis, D. I. Conway, M. MacLeod, and

C. C. and. Antibody responses and correlates of protection in the general population after two doses of the ChAdOx1 or BNT162b2 vaccines. *Nature Medicine*, 28(5):1072–1082, feb 2022. doi:10.1038/s41591-022-01721-6.

[117] F. Krammer. A correlate of protection for SARS-CoV-2 vaccines is urgently needed. *Nature Medicine*, 27(7):1147–1148, jul 2021. doi:10.1038/s41591-021-01432-4.

[118] B. Keshavarz, N. E. Richards, L. J. Workman, J. Patel, L. M. Muehling, G. Canderan, D. D. Murphy, S. G. Brovero, S. M. Ailsworth, W. H. Eschenbacher, E. C. McGowan, B. J. Mann, M. R. Nelson, A. Kadl, J. A. Woodfolk, T. A. Platts-Mills, and J. M. Wilson. Trajectory of IgG to SARS-CoV-2 after vaccination with BNT162b2 or mRNA-1273 in an employee cohort and comparison with natural infection. *Frontiers in Immunology*, 13, mar 2022. doi:10.3389/fimmu.2022.850987.

[119] J. J. Lau, S. M. S. Cheng, K. Leung, C. K. Lee, A. Hachim, L. C. H. Tsang, K. W. H. Yam, S. Chaothai, K. K. H. Kwan, Z. Y. H. Chai, T. H. K. Lo, M. Mori, C. Wu, S. A. Valkenburg, G. K. Amarasinghe, E. H. Y. Lau, D. S. C. Hui, G. M. Leung, M. Peiris, and J. T. Wu. Real-world COVID-19 vaccine effectiveness against the omicron BA.2 variant in a SARS-CoV-2 infection-naive population. *Nature Medicine*, 29(2):348–357, jan 2023. doi:10.1038/s41591-023-02219-5.

[120] H. F. Tseng, B. K. Ackerson, Y. Luo, L. S. Sy, C. A. Talarico, Y. Tian, K. J. Bruxvoort, J. E. Tubert, A. Florea, J. H. Ku, G. S. Lee, S. K. Choi, H. S. Takhar, M. Aragones, and L. Qian. Effectiveness of mRNA-1273 against SARS-CoV-2 omicron and delta variants. *Nature Medicine*, 28(5):1063–1071, feb 2022. doi:10.1038/s41591-022-01753-y.

[121] F. C. M. Kirsebom, N. Andrews, R. Sachdeva, J. Stowe, M. Ramsay, and J. L. Bernal. Effectiveness of ChAdOx1-s COVID-19 booster vaccination against the omicron and delta variants in england. *Nature Communications*, 13(1), dec 2022. doi:10.1038/s41467-022-35168-7.

[122] A. W. D. Edridge, J. Kaczorowska, A. C. R. Hoste, M. Bakker, M. Klein, K. Loens, M. F. Jebbink, A. Matser, C. M. Kinsella, P. Rueda, M. Ieven, H. Goossens, M. Prins, P. Sastre, M. Deijs, and L. van der Hoek. Seasonal coronavirus protective immunity is short-lasting. *Nature Medicine*, 26(11):1691–1693, sep 2020. doi:10.1038/s41591-020-1083-1.

[123] FDA. Covid-19 convalescent plasma. https://www.covid19treatmentguidelines.nih.gov/therapies/antivirals-including-antibody-products/covid-19-convalescent-plasma/#:~:text=In%20August%202020%2C%20the%20Food,hospitalized%20patients%20with%20COVID%2D19, 2022. Accessed: 2023-04-12.

[124] V. Piechotta, C. Iannizzi, K. L. Chai, S. J. Valk, C. Kimber, E. Dorando, I. Monsef, E. M. Wood, A. A. Lamikanra, D. J. Roberts, Z. McQuilten, C. So-Osman, L. J. Estcourt, and N. Skoetz. Convalescent plasma or hyperimmune immunoglobulin for people with COVID-19: a living systematic review. *Cochrane Database of Systematic Reviews*, 2021(5), may 2021. doi:10.1002/14651858.cd013600.pub4.

[125] P. Janiaud, C. Axfors, A. M. Schmitt, V. Gloy, F. Ebrahimi, M. Hepprich, E. R. Smith, N. A. Haber, N. Khanna, D. Moher, S. N. Goodman, J. P. A. Ioannidis, and L. G. Hemkens. Association of convalescent plasma treatment with clinical outcomes in patients with COVID-19. *JAMA*, 325(12):1185, mar 2021. doi:10.1001/jama.2021.2747.

[126] WHO. Who recommends against the use of convalescent plasma to treat covid-19. https://www.who.int/news/item/07-12-2021-who-recommends-against-the-use-of-convalescent-plasma-to-treat-covid-19, 2021. Accessed: 2023-04-12.

[127] S. Mulangu, L. E. Dodd, R. T. Davey, O. T. Mbaya, M. Proschan, D. Mukadi, M. L. Manzo, D. Nzolo, A. T. Oloma, A. Ibanda, R. Ali, S. Coulibaly, A. C. Levine, R. Grais, J. Diaz, H. C. Lane, J.-J. Muyembe-Tamfum, and the PALM Writing Group. A randomized, controlled trial of ebola virus disease therapeutics. *New England Journal of Medicine*, 381(24):2293–2303, dec 2019. doi:10.1056/nejmoa1910993.

[128] T. Andabaka, J. W. Nickerson, M. X. Rojas-Reyes, J. D. Rueda, V. B. Vrca, and B. Barsic. Monoclonal antibody for reducing the risk of respiratory syncytial virus infection in children. *Cochrane Database of Systematic Reviews*, apr 2013. doi:10.1002/14651858.cd006602.pub4.

[129] T. F. Rogers, F. Zhao, D. Huang, N. Beutler, A. Burns, W. ting He, O. Limbo, C. Smith, G. Song, J. Woehl, L. Yang, R. K. Abbott, S. Callaghan, E. Garcia, J. Hurtado, M. Parren, L. Peng, S. Ramirez, J. Ricketts, M. J. Ricciardi, S. A. Rawlings, N. C. Wu, M. Yuan, D. M. Smith, D. Nemazee, J. R. Teijaro, J. E. Voss, I. A. Wilson, R. Andrabi, B. Briney, E. Landais, D. Sok, J. G. Jardine, and D. R. Burton. Isolation of potent SARS-CoV-2 neutralizing antibodies and protection from disease in a small animal model. *Science*, 369(6506):956–963, aug 2020. doi:10.1126/science.abc7520.

[130] L. Liu, S. Iketani, Y. Guo, J. F.-W. Chan, M. Wang, L. Liu, Y. Luo, H. Chu, Y. Huang, M. S. Nair, J. Yu, K. K.-H. Chik, T. T.-T. Yuen, C. Yoon, K. K.-W. To, H. Chen, M. T. Yin, M. E. Sobieszczyk, Y. Huang, H. H. Wang, Z. Sheng, K.-Y. Yuen, and D. D. Ho. Striking antibody evasion manifested by the omicron variant of SARS-CoV-2. *Nature*, 602(7898):676–681, dec 2021. doi:10.1038/s41586-021-04388-0.

[131] D. Focosi, S. McConnell, A. Casadevall, E. Cappello, G. Valdiserra, and M. Tuccori. Monoclonal antibody therapies against SARS-CoV-2. *The Lancet Infectious Diseases*, 22(11):e311–e326, nov 2022. doi:10.1016/s1473-3099(22)00311-5.

[132] Y. Liu, Y. Yu, Y. Zhao, and D. He. Reduction in the infection fatality rate of omicron variant compared with previous variants in south africa. *International Journal of Infectious Diseases*, 120:146–149, jul 2022. doi:10.1016/j.ijid.2022.04.029.

[133] C. J. Burrell, C. R. Howard, and F. A. Murphy. Antiviral chemotherapy. In *Fenner and White's Medical Virology*, pages 169–183. Elsevier, 2017. doi:10.1016/b978-0-12-375156-0.00012-6.

[134] European Medicines Agency. Veklury. https://www.ema.europa.eu/en/medicines/human/EPAR/veklury, 2020. Accessed: 2023-04-12.

[135] European Medicines Agency. Paxlovid. https://www.ema.europa.eu/en/medicines/human/EPAR/paxlovid, 2022. Accessed: 2023-04-12.

[136] European Medicines Agency. Lagevrio. https://www.ema.europa.eu/en/medicines/human/summaries-opinion/lagevrio, 2023. Accessed: 2023-04-12.

[137] J. Grein, N. Ohmagari, D. Shin, G. Diaz, E. Asperges, A. Castagna, T. Feldt, G. Green, M. L. Green, F.-X. Lescure, E. Nicastri, R. Oda, K. Yo, E. Quiros-Roldan, A. Studemeister, J. Redinski, S. Ahmed, J. Bernett, D. Chelliah, D. Chen, S. Chihara, S. H. Cohen, J. Cunningham, A. D. Monforte, S. Ismail, H. Kato, G. Lapadula, E. L'Her, T. Maeno, S. Majumder, M. Massari, M. Mora-Rillo, Y. Mutoh, D. Nguyen, E. Verweij, A. Zoufaly, A. O. Osinusi, A. DeZure, Y. Zhao, L. Zhong, A. Chokkalingam, E. Elboudwarej, L. Telep, L. Timbs, I. Henne, S. Sellers, H. Cao, S. K. Tan, L. Winterbourne, P. Desai, R. Mera, A. Gaggar, R. P. Myers, D. M. Brainard, R. Childs, and T. Flanigan. Compassionate use of remdesivir for patients with severe covid-19. *New England Journal of Medicine*, 382(24):2327–2336, jun 2020. doi:10.1056/nejmoa2007016.

[138] R. L. Gottlieb, C. E. Vaca, R. Paredes, J. Mera, B. J. Webb, G. Perez, G. Oguchi, P. Ryan, B. U. Nielsen, M. Brown, A. Hidalgo, Y. Sachdeva, S. Mittal, O. Osiyemi, J. Skarbinski, K. Juneja, R. H. Hyland, A. Osinusi, S. Chen, G. Camus, M. Abdelghany, S. Davies, N. Behenna-Renton, F. Duff, F. M. Marty, M. J. Katz, A. A. Ginde, S. M. Brown, J. T. Schiffer, and J. A. Hill. Early remdesivir to prevent progression to severe covid-19 in outpatients. *New England Journal of Medicine*, 386(4):305–315, jan 2022. doi:10.1056/nejmoa2116846.

[139] K. Dobrowolska, D. Zarebska-Michaluk, M. Brzdek, P. Rzymski, M. Rogalska, A. Moniuszko-Malinowska, D. Kozielewicz, M. Hawro, M. Rorat, K. Sikorska, J. Jaroszewicz, J. Kowalska, and R. Flisiak. Retrospective analysis of the effectiveness of remdesivir in COVID-19 treatment during periods dominated by delta and omicron SARS-CoV-2 variants in clinical settings. *Journal of Clinical Medicine*, 12(6):2371, mar 2023. doi:10.3390/jcm12062371.

[140] R. Arbel, Y. W. Sagy, M. Hoshen, E. Battat, G. Lavie, R. Sergienko, M. Friger, J. G. Waxman, N. Dagan, R. Balicer, Y. Ben-Shlomo, A. Peretz, S. Yaron, D. Serby, A. Hammerman, and D. Netzer. Nirmatrelvir use and severe covid-19 outcomes during the omicron surge. *New England Journal of Medicine*, 387(9):790–798, sep 2022. doi:10.1056/nejmoa2204919.

[141] A. J. Bernal, M. M. G. da Silva, D. B. Musungaie, E. Kovalchuk, A. Gonzalez, V. D. Reyes, A. Martín-Quirós, Y. Caraco, A. Williams-Diaz, M. L. Brown, J. Du, A. Pedley, C. Assaid, J. Strizki, J. A. Grobler, H. H. Shamsuddin, R. Tipping, H. Wan, A. Paschke, J. R. Butterton, M. G. Johnson, and C. D. Anda. Molnupiravir for oral treatment of covid-19 in nonhospitalized patients. *New England Journal of Medicine*, 386(6):509–520, feb 2022. doi:10.1056/nejmoa2116044.

[142] C. C. Butler, F. D. R. Hobbs, O. A. Gbinigie, N. M. Rahman, G. Hayward, D. B. Richards, J. Dorward, D. M. Lowe, J. F. Standing, J. Breuer, S. Khoo, S. Petrou, K. Hood, J. S. Nguyen-Van-Tam, M. G. Patel, B. R. Saville, J. Marion, E. Ogburn, J. Allen, H. Rutter, N. Francis, N. P. B. Thomas, P. Evans, M. Dobson, T.-A. Madden, J. Holmes, V. Harris, M. E. Png, M. Lown, O. van Hecke, M. A. Detry, C. T. Saunders, M. Fitzgerald, N. S. Berry, L. Mwandigha, U. Galal, S. Mort, B. D. Jani, N. D. Hart, H. Ahmed, D. Butler, M. McKenna, J. Chalk, L. Lavallee, E. Hadley, L. Cureton, M. Benysek, M. Andersson, M. Coates, S. Barrett, C. Bateman, J. C. Davies, I. Raymundo-Wood, A. Ustianowski, A. Carson-Stevens, L.-M. Yu, P. Little, A. A. Agyeman, T. Ahmed, D. Allcock, A. Beltran-Martinez, O. E. Benedict, N. Bird, L. Brennan, J. Brown, G. Burns, M. Butler, Z. Cheng, R. Danson, N. de Kare-Silver, D. Dhasmana, J. Dickson, S. Engamba, S. Fisher, R. Fox, E. Frost, R. Gaunt, S. Ghosh, I. Gilkar, A. Goodman, S. Granier, A. Howell, I. Hussain, S. Hutchinson, M. Imlach, G. Irving, N. Jacobsen, J. Kennard, U. Khan, K. Knox, C. Krasucki, T. Law, R. Lee, N. Lester, D. Lewis, J. Lunn, C. I. Mackintosh, M. Mathukia, P. Moore, S. Morton, D. Murphy, R. Nally, C. Ndukauba, O. Ogundapo, H. Okeke, A. Patel, K. Patel, R. Penfold, S. Poonian, O. Popoola, A. Pora, V. Prasad, R. Prasad, O. Razzaq, S. Richardson, S. Royal, A. Safa, S. Sehdev, T. Sevenoaks, D. Shah, A. Sheikh, V. Short, B. S. Sidhu, I. Singh, Y. Soni, C. Thalasselis, P. Wilson, D. Wingfield, M. Wong, M. N. J. Woodall, N. Wooding, S. Woods, J. Yong, F. Yongblah, and A. Zafar. Molnupiravir plus usual care versus usual care alone as early treatment for adults with COVID-19 at increased risk of adverse outcomes (PANORAMIC): an open-label, platform-adaptive randomised controlled trial. *The Lancet*, 401(10373):281–293, jan 2023. doi:10.1016/s0140-6736(22)02597-1.

[143] L. Vangeel, W. Chiu, S. D. Jonghe, P. Maes, B. Slechten, J. Raymenants, E. André, P. Leyssen, J. Neyts, and D. Jochmans. Remdesivir, molnupiravir and nirmatrelvir remain active against SARS-CoV-2 omicron and other variants of concern. *Antiviral Research*, 198:105252, feb 2022. doi:10.1016/j.antiviral.2022.105252.

[144] T. Kaeuferle, R. Krauss, F. Blaeschke, S. Willier, and T. Feuchtinger. Strategies of adoptive t -cell transfer to treat refractory viral infections post allogeneic stem cell transplantation. *Journal of Hematology & Oncology*, 12(1), feb 2019. doi:10.1186/s13045-019-0701-1.

[145] M. Kalos and C. H. June. Adoptive t cell transfer for cancer immunotherapy in the era of synthetic biology. *Immunity*, 39(1):49–60, jul 2013. doi:10.1016/j.immuni.2013.07.002.

[146] A. Bonifacius, S. Tischer-Zimmermann, M. M. Santamorena, P. Mausberg, J. Schenk, S. Koch, J. Barnstorf-Brandes, N. Gödecke, J. Martens, L. Goudeva, M. Verboom, J. Wittig, B. Maecker-Kolhoff, H. Baurmann, C. Clark, O. Brauns, M. Simon, P. Lang, O. A. Cornely, M. Hallek, R. Blasczyk, D. Seiferling, P. Köhler, and B. Eiz-Vesper. Rapid manufacturing of highly cytotoxic clinical-grade SARS-CoV-2-specific t cell products covering SARS-CoV-2 and its variants for adoptive t cell therapy. *Frontiers in Bioengineering and Biotechnology*, 10, apr 2022. doi:10.3389/fbioe.2022.867042.

[147] G. Liu, H. Chen, X. Cao, L. Jia, W. Rui, H. Zheng, D. Huang, F. Liu, Y. Liu, X. Zhao, P. Lu, and X. Lin. Efficacy of pp65-specific tcr-t cell therapy in treating cytomegalovirus infection after hematopoietic stem cell transplantation. *American Journal of Hematology*, 97(11):1453–1463, sep 2022. doi:10.1002/ajh.26708.

[148] M. Hiltensperger and A. M. Krackhardt. Current and future concepts for the generation and application of genetically engineered CAR-t and TCR-t cells. *Frontiers in Immunology*, 14, mar 2023. doi:10.3389/fimmu.2023.1121030.

[149] K. Schober, T. R. Müller, F. Gökmen, S. Grassmann, M. Effenberger, M. Poltorak, C. Stemberger, K. Schumann, T. L. Roth, A. Marson, and D. H. Busch. Orthotopic replacement of t-cell receptor α- and β-chains with preservation of near-physiological t-cell function. *Nature Biomedical Engineering*, 3(12):974–984, jun 2019. doi:10.1038/s41551-019-0409-0.

[150] The Royal Swedish Academy of Sciences. Press release. genetic scissors: a tool for rewriting the code of life. https://www.nobelprize.org/prizes/chemistry/2020/press-release/, 2020. Accessed: 2023-04-12.

[151] J. A. Doudna and E. Charpentier. The new frontier of genome engineering with CRISPR-cas9. *Science*, 346(6213), nov 2014. doi:10.1126/science.1258096.

[152] K. Schumann, S. Lin, E. Boyer, D. R. Simeonov, M. Subramaniam, R. E. Gate, G. E. Haliburton, C. J. Ye, J. A. Bluestone, J. A. Doudna, and A. Marson. Generation of knock-in primary human t cells using cas9 ribonucleoproteins. *Proceedings of the National Academy of Sciences*, 112(33):10437–10442, jul 2015. doi:10.1073/pnas.1512503112.

[153] C. J. Cohen, Y. F. Li, M. El-Gamil, P. F. Robbins, S. A. Rosenberg, and R. A. Morgan. Enhanced antitumor activity of t cells engineered to express t-cell receptors with a second disulfide bond. *Cancer Research*, 67(8):3898–3903, apr 2007. doi:10.1158/0008-5472.can-06-3986.

[154] C. Moosmann, T. R. Müller, D. H. Busch, and K. Schober. Orthotopic t-cell receptor replacement in primary human t cells using CRISPR-cas9-mediated homology-directed repair. *STAR Protocols*, 3(1):101031, mar 2022. doi:10.1016/j.xpro.2021.101031.

[155] L. M. Mateyka, V. Grass, A. Pichlmair, D. H. Busch, and E. D'Ippolito. Sars-cov-2 cd8+ t cell killing assays using replicating viruses and transgenic antigens. *STAR Protocols*, 3(4):101699, dec 2022. doi:10.1016/j.xpro.2022.101699.

[156] T. R. Müller, S. Jarosch, M. Hammel, J. Leube, S. Grassmann, B. Bernard, M. Effenberger, I. Andrä, M. Z. Chaudhry, T. Käuferle, A. Malo, L. Cicin-Sain, P. Steinberger, T. Feuchtinger, U. Protzer, K. Schumann, M. Neuenhahn, K. Schober, and D. H. Busch. Targeted t cell receptor gene editing provides predictable t cell product function for immunotherapy. *Cell Reports Medicine*, 2(8):100374, aug 2021. doi:10.1016/j.xcrm.2021.100374.

[157] E. A. Stadtmauer, J. A. Fraietta, M. M. Davis, A. D. Cohen, K. L. Weber, E. Lancaster, P. A. Mangan, I. Kulikovskaya, M. Gupta, F. Chen, L. Tian, V. E. Gonzalez, J. Xu, I. young Jung, J. J. Melenhorst, G. Plesa, J. Shea, T. Matlawski, A. Cervini, A. L. Gaymon, S. Desjardins, A. Lamontagne, J. Salas-Mckee, A. Fesnak, D. L. Siegel, B. L. Levine, J. K. Jadlowsky, R. M. Young, A. Chew, W.-T. Hwang, E. O. Hexner, B. M. Carreno, C. L. Nobles, F. D. Bushman, K. R. Parker, Y. Qi, A. T. Satpathy, H. Y. Chang, Y. Zhao, S. F. Lacey, and C. H. June. CRISPR-engineered t cells in patients with refractory cancer. *Science*, 367(6481), feb 2020. doi:10.1126/science.aba7365.

[158] S. P. Foy, K. Jacoby, D. A. Bota, T. Hunter, Z. Pan, E. Stawiski, Y. Ma, W. Lu, S. Peng, C. L. Wang, B. Yuen, O. Dalmas, K. Heeringa, B. Sennino, A. Conroy, M. T. Bethune, I. Mende, W. White, M. Kukreja, S. Gunturu, E. Humphrey, A. Hussaini, D. An, A. J. Litterman, B. B. Quach, A. H. C. Ng, Y. Lu, C. Smith, K. M. Campbell, D. Anaya, L. Skrdlant, E. Y.-H. Huang, V. Mendoza, J. Mathur, L. Dengler, B. Purandare, R. Moot, M. C. Yi, R. Funke, A. Sibley, T. Stallings-Schmitt, D. Y. Oh, B. Chmielowski, M. Abedi, Y. Yuan, J. A. Sosman, S. M. Lee, A. J. Schoenfeld, D. Baltimore, J. R. Heath, A. Franzusoff, A. Ribas, A. V. Rao, and S. J. Mandl. Non-viral precision t cell receptor replacement for personalized cell therapy. *Nature*, 615(7953):687–696, nov 2022. doi:10.1038/s41586-022-05531-1.

[159] A. D. Nahmad, E. Reuveni, E. Goldschmidt, T. Tenne, M. Liberman, M. Horovitz-Fried, R. Khosravi, H. Kobo, E. Reinstein, A. Madi, U. Ben-David, and A. Barzel. Frequent aneuploidy in primary human t cells after CRISPR–cas9 cleavage. *Nature Biotechnology*, 40(12):1807–1813, jun 2022. doi:10.1038/s41587-022-01377-0.

[160] M. P. Tan, A. B. Gerry, J. E. Brewer, L. Melchiori, J. S. Bridgeman, A. D. Bennett, N. J. Pumphrey, B. K. Jakobsen, D. A. Price, K. Ladell, and A. K. Sewell. T cell receptor binding affinity governs the functional profile of cancer-specific cd8+ t cells. *Clinical and Experimental Immunology*, 180(2):255–270, apr 2015. doi:10.1111/cei.12570.

[161] S. N. Khilko, M. T. Jelonek, M. Corr, L. F. Boyd, A. L. Bothwell, and D. H. Margulies. Measuring interactions of MHC class i molecules using surface plasmon resonance. *Journal of Immunological Methods*, 183(1):77–94, jun 1995. doi:10.1016/0022-1759(95)00033-7.

[162] M. Knabel, T. J. Franz, M. Schiemann, A. Wulf, B. Villmow, B. Schmidt, H. Bernhard, H. Wagner, and D. H. Busch. Reversible MHC multimer staining for functional isolation of t-cell populations and effective adoptive transfer. *Nature Medicine*, 8(6):631–637, jun 2002. doi:10.1038/nm0602-631.

[163] M. Nauerth, B. Weißbrich, R. Knall, T. Franz, G. Dössinger, J. Bet, P. J. Paszkiewicz, L. Pfeifer, M. Bunse, W. Uckert, R. Holtappels, D. Gillert-Marien, M. Neuenhahn, A. Krackhardt, M. J. Reddehase, S. R. Riddell, and D. H. Busch. Tcr-ligand koff rate

correlates with the protective capacity of antigen-specific cd8+ t cells for adoptive transfer. *Science Translational Medicine*, 5(192), jul 2013. doi:10.1126/scitranslmed.3005958.

[164] D. Campillo-Davo, M. Versteven, G. Roex, H. D. Reu, S. van der Heijden, S. Anguille, Z. N. Berneman, V. F. I. V. Tendeloo, and E. Lion. Rapid assessment of functional avidity of tumor-specific t cell receptors using an antigen-presenting tumor cell line electroporated with full-length tumor antigen mRNA. *Cancers*, 12(2):256, jan 2020. doi:10.3390/cancers12020256.

[165] M. P. Poltorak, P. Graef, C. Tschulik, M. Wagner, V. Cletiu, S. Dreher, B. Borjan, S. P. Fraessle, M. Effenberger, M. Turk, D. H. Busch, J. Plitzko, D. G. Kugler, S. Ragan, T. Schmidt, C. Stemberger, and L. Germeroth. Expamers: a new technology to control t cell activation. *Scientific Reports*, 10(1), oct 2020. doi:10.1038/s41598-020-74595-8.

[166] M. Effenberger, A. Stengl, K. Schober, M. Gerget, M. Kampick, T. R. Müller, D. Schumacher, J. Helma, H. Leonhardt, and D. H. Busch. FLEXamers: A double tag for universal generation of versatile peptide-MHC multimers. *The Journal of Immunology*, 202(7):2164–2171, apr 2019. doi:10.4049/jimmunol.1801435.

[167] D. H. Busch, I. M. Pilip, S. Vijh, and E. G. Pamer. Coordinate regulation of complex t cell populations responding to bacterial infection. *Immunity*, 8(3):353–362, mar 1998. doi:10.1016/s1074-7613(00)80540-3.

[168] S. Jutz, J. Leitner, K. Schmetterer, I. Doel-Perez, O. Majdic, K. Grabmeier-Pfistershammer, W. Paster, J. B. Huppa, and P. Steinberger. Assessment of costimulation and coinhibition in a triple parameter t cell reporter line: Simultaneous measurement of NF-κb, NFAT and AP-1. *Journal of Immunological Methods*, 430:10–20, mar 2016. doi:10.1016/j.jim.2016.01.007.

[169] M. D. Luecken and F. J. Theis. Current best practices in single-cell RNA-seq analysis: a tutorial. *Molecular Systems Biology*, 15(6), jun 2019. doi:10.15252/msb.20188746.

[170] F. A. Wolf, P. Angerer, and F. J. Theis. SCANPY: large-scale single-cell gene expression data analysis. *Genome Biology*, 19(1), feb 2018. doi:10.1186/s13059-017-1382-0.

[171] J. Xu, C. Falconer, Q. Nguyen, J. Crawford, B. D. McKinnon, S. Mortlock, A. Senabouth, S. Andersen, H. S. Chiu, L. Jiang, N. J. Palpant, J. Yang, M. D. Mueller, A. W. Hewitt, A. Pébay, G. W. Montgomery, J. E. Powell, and L. J. Coin. Genotype-free demultiplexing of pooled single-cell RNA-seq. *Genome Biology*, 20(1), dec 2019. doi:10.1186/s13059-019-1852-7.

[172] H. Heaton, A. M. Talman, A. Knights, M. Imaz, D. J. Gaffney, R. Durbin, M. Hemberg, and M. K. N. Lawniczak. Souporcell: robust clustering of single-cell RNA-seq data by genotype without reference genotypes. *Nature Methods*, 17(6):615–620, may 2020. doi:10.1038/s41592-020-0820-1.

[173] G. Sturm, T. Szabo, G. Fotakis, M. Haider, D. Rieder, Z. Trajanoski, and F. Finotello. Scirpy: a scanpy extension for analyzing single-cell t-cell receptor-sequencing data. *Bioinformatics*, 36(18):4817–4818, jul 2020. doi:10.1093/bioinformatics/btaa611.

[174] H.-L. J. Oh, A. Chia, C. X. L. Chang, H. N. Leong, K. L. Ling, G. M. Grotenbreg, A. J. Gehring, Y. J. Tan, and A. Bertoletti. Engineering t cells specific for a dominant severe acute respiratory syndrome coronavirus CD8 t cell epitope. *Journal of Virology*, 85(20):10464–10471, oct 2011. doi:10.1128/jvi.05039-11.

[175] F. F. Gonzalez-Galarza, A. McCabe, E. J. M. dos Santos, J. Jones, L. Takeshita, N. D. Ortega-Rivera, G. M. D. Cid-Pavon, K. Ramsbottom, G. Ghattaoraya, A. Alfirevic, D. Middleton, and A. R. Jones. Allele frequency net database (AFND) 2020 update: gold-standard data classification, open access genotype data and new query tools. *Nucleic Acids Research*, nov 2019. doi:10.1093/nar/gkz1029.

[176] V. A. Traag, L. Waltman, and N. J. van Eck. From louvain to leiden: guaranteeing well-connected communities. *Scientific Reports*, 9(1), mar 2019. doi:10.1038/s41598-019-41695-z.

[177] L. M. Mateyka, P. M. Strobl, S. Jarosch, S. J. C. Scheu, D. H. Busch, and E. D'Ippolito. Gene signatures of t-cell activation can serve as predictors of functionality for SARS-CoV-2-specific t-cell receptors. *Vaccines*, 10(10):1617, sep 2022. doi:10.3390/vaccines10101617.

[178] T. R. Müller, C. Schuler, M. Hammel, A. Köhler, S. Jutz, J. Leitner, K. Schober, D. H. Busch, and P. Steinberger. A t-cell reporter platform for high-throughput and reliable investigation of TCR function and biology. *Clinical & Translational Immunology*, 9(11), jan 2020. doi:10.1002/cti2.1216.

[179] M. B. Leick, H. Silva, I. Scarfò, R. Larson, B. D. Choi, A. A. Bouffard, K. Gallagher, A. Schmidts, S. R. Bailey, M. C. Kann, M. Jan, M. Wehrli, K. Grauwet, N. Horick, M. J. Frigault, and M. V. Maus. Non-cleavable hinge enhances avidity and expansion of CAR-t cells for acute myeloid leukemia. *Cancer Cell*, 40(5):494–508.e5, may 2022. doi:10.1016/j.ccell.2022.04.001.

[180] N. Balneger, L. A. M. Cornelissen, M. Wassink, S. J. Moons, T. J. Boltje, Y. E. Bar-Ephraim, K. K. Das, J. N. Søndergaard, C. Büll, and G. J. Adema. Sialic acid blockade in dendritic cells enhances cd8+ t cell responses by facilitating high-avidity interactions. *Cellular and Molecular Life Sciences*, 79(2), jan 2022. doi:10.1007/s00018-021-04027-x.

[181] J. M. Dan, J. Mateus, Y. Kato, K. M. Hastie, E. D. Yu, C. E. Faliti, A. Grifoni, S. I. Ramirez, S. Haupt, A. Frazier, C. Nakao, V. Rayaprolu, S. A. Rawlings, B. Peters, F. Krammer, V. Simon, E. O. Saphire, D. M. Smith, D. Weiskopf, A. Sette, and S. Crotty. Immunological memory to SARS-CoV-2 assessed for up to 8 months after infection. *Science*, 371(6529), feb 2021. doi:10.1126/science.abf4063.

[182] L. Guo, G. Wang, Y. Wang, Q. Zhang, L. Ren, X. Gu, T. Huang, J. Zhong, Y. Wang, X. Wang, L. Huang, L. Xu, C. Wang, L. Chen, X. Xiao, Y. Peng, J. C. Knight, T. Dong, B. Cao, and J. Wang. SARS-CoV-2-specific antibody and t-cell responses 1 year after infection in people recovered from COVID-19: a longitudinal cohort study. *The Lancet Microbe*, 3(5):e348–e356, may 2022. doi:10.1016/s2666-5247(22)00036-2.

[183] M. D. Rosenstein, A. W. de Visser, L. G. Visser, and A. H. E. Roukens. Long-term immunity after a single yellow fever vaccination in travelers vaccinated at 60 years or older: A 10-year follow-up study. *Journal of Travel Medicine*, 28(8), aug 2021. doi:10.1093/jtm/taab126.

[184] J. J. Ott, G. Irving, and S. T. Wiersma. Long-term protective effects of hepatitis a vaccines. a systematic review. *Vaccine*, 31(1):3–11, dec 2012. doi:10.1016/j.vaccine.2012.04.104.

[185] S. T. Tan, A. T. Kwan, I. Rodríguez-Barraquer, B. J. Singer, H. J. Park, J. A. Lewnard, D. Sears, and N. C. Lo. Infectiousness of SARS-CoV-2 breakthrough infections and reinfections during the omicron wave. *Nature Medicine*, 29(2):358–365, jan 2023. doi:10.1038/s41591-022-02138-x.

[186] A. Bertoletti, N. L. Bert, and A. T. Tan. SARS-CoV-2-specific t cells in the changing landscape of the COVID-19 pandemic. *Immunity*, 55(10):1764–1778, oct 2022. doi:10.1016/j.immuni.2022.08.008.

[187] S. J. Choi, D.-U. Kim, J. Y. Noh, S. Kim, S.-H. Park, H. W. Jeong, and E.-C. Shin. T cell epitopes in SARS-CoV-2 proteins are substantially conserved in the omicron variant. *Cellular & Molecular Immunology*, 19(3):447–448, jan 2022. doi:10.1038/s41423-022-00838-5.

[188] S. M. Murray, A. M. Ansari, J. Frater, P. Klenerman, S. Dunachie, E. Barnes, and A. Ogbe. The impact of pre-existing cross-reactive immunity on SARS-CoV-2 infection and vaccine responses. *Nature Reviews Immunology*, dec 2022. doi:10.1038/s41577-022-00809-x.

[189] I. Schulien, J. Kemming, V. Oberhardt, K. Wild, L. M. Seidel, S. Killmer, Sagar, F. Daul, M. S. Lago, A. Decker, H. Luxenburger, B. Binder, D. Bettinger, O. Sogukpinar, S. Rieg, M. Panning, D. Huzly, M. Schwemmle, G. Kochs, C. F. Waller, A. Nieters, D. Duerschmied, F. Emmerich, H. E. Mei, A. R. Schulz, S. Llewellyn-Lacey, D. A. Price, T. Boettler, B. Bengsch, R. Thimme, M. Hofmann, and C. Neumann-Haefelin. Characterization of pre-existing and induced sars-cov-2-specific cd8+ t cells. *Nature Medicine*, 27(1):78–85, nov 2020. doi:10.1038/s41591-020-01143-2.

[190] Y. Peng, A. J. Mentzer, G. Liu, X. Yao, Z. Yin, D. Dong, W. Dejnirattisai, T. Rostron, P. Supasa, C. Liu, C. López-Camacho, J. Slon-Campos, Y. Zhao, D. I. Stuart, G. C. Paesen, J. M. Grimes, A. A. Antson, O. W. Bayfield, D. E. D. P. Hawkins, D.-S. Ker, B. Wang, L. Turtle, K. Subramaniam, P. Thomson, P. Zhang, C. Dold, J. Ratcliff, P. Simmonds, T. de Silva, P. Sopp, D. Wellington, U. Rajapaksa, Y.-L. Chen, M. Salio, G. Napolitani, W. Paes, P. Borrow, B. M. Kessler, J. W. Fry, N. F. Schwabe, M. G. Semple, J. K. Baillie, S. C. Moore, P. J. M. Openshaw, M. A. Ansari, S. Dunachie, E. Barnes, J. Frater, G. Kerr, P. Goulder, T. Lockett, R. Levin, Y. Zhang, R. Jing, L.-P. Ho, E. Barnes, D. Dong, T. Dong, S. Dunachie, J. Frater, P. Goulder, G. Kerr, P. Klenerman, G. Liu, A. McMichael, G. Napolitani, G. Ogg, Y. Peng, M. Salio, X. Yao, Z. Yin, J. K. Baillie, P. Klenerman, A. J. Mentzer, S. C. Moore, P. J. M. Openshaw, M. G. Semple, D. I. Stuart, L. Turtle, R. J. Cornall, C. P. Conlon, P. Klenerman, G. R. Screaton, J. Mongkolsapaya, A. McMichael, J. C. Knight, G. Ogg, T. Dong, and and. Broad and strong memory cd4+ and cd8+ t cells induced by sars-cov-2 in uk convalescent individuals following covid-19. *Nature Immunology*, 21(11):1336–1345, sep 2020. doi:10.1038/s41590-020-0782-6.

[191] T. Sekine, A. Perez-Potti, O. Rivera-Ballesteros, K. Strålin, J.-B. Gorin, A. Olsson, S. Llewellyn-Lacey, H. Kamal, G. Bogdanovic, S. Muschiol, D. J. Wullimann, T. Kammann, J. Emgård, T. Parrot, E. Folkesson, O. Rooyackers, L. I. Eriksson, J.-I. Henter, A. Sönnerborg, T. Allander, J. Albert, M. Nielsen, J. Klingström, S. Gredmark-Russ, N. K. Björkström, J. K. Sandberg, D. A. Price, H.-G. Ljunggren, S. Aleman, M. Buggert, M. Akber, L. Berglin, H. Bergsten, S. Brighenti, D. Brownlie, M. Butrym, B. Chambers, P. Chen, M. C. Jeannin, J. Grip, A. C. Gomez, L. Dillner, I. D. Lozano, M. Dzidic, M. F. Tullberg, A. Färnert, H. Glans, A. Haroun-Izquierdo, E. Henriksson, L. Hertwig, S. Kalsum, E. Kokkinou, E. Kvedaraite, M. Loreti, M. Lourda, K. Maleki, K.-J. Malmberg, N. Marquardt, C. Maucourant, J. Michaelsson, J. Mjösberg, K. Moll, J. Muva, J. Mårtensson, P. Nauclér, A. Norrby-Teglund, L. P. Medina, B. Persson, L. Radler, E. Ringqvist, J. T. Sandberg, E. Sohlberg, T. Soini, M. Svensson, J. Tynell, R. Varnaite, A. V. Kries, and C. Unge. Robust t cell immunity in convalescent individuals with asymptomatic or mild COVID-19. *Cell*, 183(1):158–168.e14, oct 2020. doi:10.1016/j.cell.2020.08.017.

[192] J. van den Dijssel, R. R. Hagen, R. de Jongh, M. Steenhuis, T. Rispens, D. M. Geerdes, J. Y. Mok, A. H. Kragten, M. C. Duurland, N. J. Verstegen, S. M. van Ham, W. J. van Esch, K. P. van Gisbergen, P. Hombrink, A. ten Brinke, and C. E. van de Sandt. Parallel detection of sars-cov-2 epitopes reveals dynamic immunodominance profiles of cd8+ t memory cells in convalescent covid-19 donors. *Clinical & Translational Immunology*, 11(10), jan 2022. doi:10.1002/cti2.1423.

[193] A. P. Ferretti, T. Kula, Y. Wang, D. M. Nguyen, A. Weinheimer, G. S. Dunlap, Q. Xu, N. Nabilsi, C. R. Perullo, A. W. Cristofaro, H. J. Whitton, A. Virbasius, K. J. Olivier, L. R. Buckner, A. T. Alistar, E. D. Whitman, S. A. Bertino, S. Chattopadhyay, and G. MacBeath. Unbiased screens show cd8+ t cells of covid-19 patients recognize shared epitopes in sars-cov-2 that largely reside outside the spike protein. *Immunity*, 53(5):1095–1107.e3, nov 2020. doi:10.1016/j.immuni.2020.10.006.

[194] J. R. Habel, T. H. O. Nguyen, C. E. van de Sandt, J. A. Juno, P. Chaurasia, K. Wragg, M. Koutsakos, L. Hensen, X. Jia, B. Chua, W. Zhang, H.-X. Tan, K. L. Flanagan, D. L. Doolan, J. Torresi, W. Chen, L. M. Wakim, A. C. Cheng, P. C. Doherty, J. Petersen, J. Rossjohn, A. K. Wheatley, S. J. Kent, L. C. Rowntree, and K. Kedzierska. Suboptimal sars-cov-2specific cd8+ t cell response associated with the prominent hla-a*02:01 phenotype. *Proceedings of the National Academy of Sciences*, 117(39):24384–24391, sep 2020. doi:10.1073/pnas.2015486117.

[195] U. Sahin, A. Muik, I. Vogler, E. Derhovanessian, L. M. Kranz, M. Vormehr, J. Quandt, N. Bidmon, A. Ulges, A. Baum, K. E. Pascal, D. Maurus, S. Brachtendorf, V. Lörks, J. Sikorski, P. Koch, R. Hilker, D. Becker, A.-K. Eller, J. Grützner, M. Tonigold, C. Boesler, C. Rosenbaum, L. Heesen, M.-C. Kühnle, A. Poran, J. Z. Dong, U. Luxemburger, A. Kemmer-Brück, D. Langer, M. Bexon, S. Bolte, T. Palanche, A. Schultz, S. Baumann, A. J. Mahiny, G. Boros, J. Reinholz, G. T. Szabó, K. Karikó, P.-Y. Shi, C. Fontes-Garfias, J. L. Perez, M. Cutler, D. Cooper, C. A. Kyratsous, P. R. Dormitzer, K. U. Jansen, and Özlem Türeci. BNT162b2 vaccine induces neutralizing antibodies and poly-specific t cells in humans. *Nature*, 595(7868):572–577, may 2021. doi:10.1038/s41586-021-03653-6.

[196] D. Kim, J.-Y. Lee, J.-S. Yang, J. W. Kim, V. N. Kim, and H. Chang. The architecture of SARS-CoV-2 transcriptome. *Cell*, 181(4):914–921.e10, may 2020. doi:10.1016/j.cell.2020.04.011.

[197] R. A. Khailany, M. Safdar, and M. Ozaslan. Genomic characterization of a novel SARS-CoV-2. *Gene Reports*, 19:100682, jun 2020. doi:10.1016/j.genrep.2020.100682.

[198] T. H. Nguyen, L. C. Rowntree, J. Petersen, B. Y. Chua, L. Hensen, L. Kedzierski, C. E. van de Sandt, P. Chaurasia, H.-X. Tan, J. R. Habel, W. Zhang, L. F. Allen, L. Earnest, K. Y. Mak, J. A. Juno, K. Wragg, F. L. Mordant, F. Amanat, F. Krammer, N. A. Mifsud, D. L. Doolan, K. L. Flanagan, S. Sonda, J. Kaur, L. M. Wakim, G. P. Westall, F. James, E. Mouhtouris, C. L. Gordon, N. E. Holmes, O. C. Smibert, J. A. Trubiano, A. C. Cheng, P. Harcourt, P. Clifton, J. C. Crawford, P. G. Thomas, A. K. Wheatley, S. J. Kent, J. Rossjohn, J. Torresi, and K. Kedzierska. Cd8+ t cells specific for an immunodominant sars-cov-2 nucleocapsid epitope display high naive precursor frequency and tcr promiscuity. *Immunity*, 54(5):1066–1082.e5, may 2021. doi:10.1016/j.immuni.2021.04.009.

[199] L. C. Rowntree, T. H. Nguyen, L. Kedzierski, M. R. Neeland, J. Petersen, J. C. Crawford, L. F. Allen, E. B. Clemens, B. Chua, H. A. McQuilten, A. A. Minervina, M. V. Pogorelyy, P. Chaurasia, H.-X. Tan, A. K. Wheatley, X. Jia, F. Amanat, F. Krammer, E. K. Allen, S. Sonda, K. L. Flanagan, J. Jumarang, P. S. Pannaraj, P. V. Licciardi, S. J. Kent, K. A.

Bond, D. A. Williamson, J. Rossjohn, P. G. Thomas, S. Tosif, N. W. Crawford, C. E. van de Sandt, and K. Kedzierska. Sars-cov-2-specific t cell memory with common tcr$\alpha\beta$ motifs is established in unvaccinated children who seroconvert after infection. *Immunity*, 55(7):1299–1315.e4, jul 2022. doi:10.1016/j.immuni.2022.06.003.

[200] A. A. Minervina, M. V. Pogorelyy, A. M. Kirk, J. C. Crawford, E. K. Allen, C.-H. Chou, R. C. Mettelman, K. J. Allison, C.-Y. Lin, D. C. Brice, X. Zhu, K. Vegesana, G. Wu, S. Trivedi, P. Kottapalli, D. Darnell, S. McNeely, S. R. Olsen, S. Schultz-Cherry, J. H. Estepp, A. Gaur, J. Hoffman, M. Mori, L. Tang, E. Tuomanen, R. Webby, H. Hakim, R. T. Hayden, D. R. Hijano, R. Bajracharya, W. Awad, L.-A. V. de Velde, B. L. Clark, T. L. Wilson, A. Souquette, A. Castellaw, R. H. Dallas, J. Hodges, A. Gowen, J. Russell-Bell, J. Sparks, D. E. Wittman, T. P. Fabrizio, S. Cherry, E. K. Roubidoux, V. Cortez, P. Freiden, N. Wohlgemuth, K. Whitt, M. A. McGargill, J. Wolf, and P. G. T. and. Sars-cov-2 antigen exposure history shapes phenotypes and specificity of memory cd8+ t cells. *Nature Immunology*, 23(5):781–790, apr 2022. doi:10.1038/s41590-022-01184-4.

[201] D. S. Fischer, M. Ansari, K. I. Wagner, S. Jarosch, Y. Huang, C. H. Mayr, M. Strunz, N. J. Lang, E. D'Ippolito, M. Hammel, L. Mateyka, S. Weber, L. S. Wolff, K. Witter, I. E. Fernandez, G. Leuschner, K. Milger, M. Frankenberger, L. Nowak, K. Heinig-Menhard, I. Koch, M. G. Stoleriu, A. Hilgendorff, J. Behr, A. Pichlmair, B. Schubert, F. J. Theis, D. H. Busch, H. B. Schiller, and K. Schober. Single-cell RNA sequencing reveals ex vivo signatures of SARS-CoV-2-reactive t cells through 'reverse phenotyping'. *Nature Communications*, 12(1), jul 2021. doi:10.1038/s41467-021-24730-4.

[202] K. Shimizu, T. Iyoda, A. Sanpei, H. Nakazato, M. Okada, S. Ueda, M. Kato-Murayama, K. Murayama, M. Shirouzu, N. Harada, M. Hidaka, and S. ichiro Fujii. Identification of TCR repertoires in functionally competent cytotoxic t cells cross-reactive to SARS-CoV-2. *Communications Biology*, 4(1), dec 2021. doi:10.1038/s42003-021-02885-6.

[203] A. S. Shomuradova, M. S. Vagida, S. A. Sheetikov, K. V. Zornikova, D. Kiryukhin, A. Titov, I. O. Peshkova, A. Khmelevskaya, D. V. Dianov, M. Malasheva, A. Shmelev, Y. Serdyuk, D. V. Bagaev, A. Pivnyuk, D. S. Shcherbinin, A. V. Maleeva, N. T. Shakirova, A. Pilunov, D. B. Malko, E. G. Khamaganova, B. Biderman, A. Ivanov, M. Shugay, and G. A. Efimov. SARS-CoV-2 epitopes are recognized by a public and diverse repertoire of human t cell receptors. *Immunity*, 53(6):1245–1257.e5, dec 2020. doi:10.1016/j.immuni.2020.11.004.

[204] E. S. Ford, K. Mayer-Blackwell, L. Jing, A. M. Sholukh, R. S. Germain, E. L. Bossard, H. Xie, T. H. Pulliam, S. Jani, S. Selke, C. J. Burrow, C. L. McClurkan, A. Wald, M. R. Holbrook, B. Eaton, E. Eudy, M. Murphy, E. Postnikova, H. S. Robins, R. Elyanow, R. M. Gittelman, M. Ecsedi, E. Wilcox, A. G. Chapuis, A. Fiore-Gartland, and D. M. Koelle. Cd8+ t cell clonotypes from prior sars-cov-2 infection predominate during the cellular immune response to mrna vaccination. oct 2022. doi:10.21203/rs.3.rs-2146712/v1.

[205] J. K. Whitmire, J. T. Tan, and J. L. Whitton. Interferon-γ acts directly on cd8+ t cells to increase their abundance during virus infection. *Journal of Experimental Medicine*, 201(7):1053–1059, apr 2005. doi:10.1084/jem.20041463.

[206] S. Ghassemi, S. Nunez-Cruz, R. S. O'Connor, J. A. Fraietta, P. R. Patel, J. Scholler, D. M. Barrett, S. M. Lundh, M. M. Davis, F. Bedoya, C. Zhang, J. Leferovich, S. F. Lacey, B. L. Levine, S. A. Grupp, C. H. June, J. J. Melenhorst, and M. C. Milone. Reducing ex vivo culture improves the antileukemic activity of chimeric antigen receptor (car) t cells. *Cancer Immunology Research*, 6(9):1100–1109, sep 2018. doi:10.1158/2326-6066.cir-17-0405.

[207] A. Purcarea, S. Jarosch, J. Barton, S. Grassmann, L. Pachmayr, E. D'Ippolito, M. Hammel, A. Hochholzer, K. I. Wagner, J. H. van den Berg, V. R. Buchholz, J. B. A. G. Haanen, D. H. Busch, and K. Schober. Signatures of recent activation identify a circulating t cell compartment containing tumor-specific antigen receptors with high avidity. *Science Immunology*, 7(74), aug 2022. doi:10.1126/sciimmunol.abm2077.

[208] M. Boutet, Z. Benet, E. Guillen, C. Koch, S. M. Soudja, F. Delahaye, D. Fooksman, and G. Lauvau. Memory cd8+ t cells mediate early pathogen-specific protection via localized delivery of chemokines and ifnγ to clusters of monocytes. *Science Advances*, 7(36), sep 2021. doi:10.1126/sciadv.abf9975.

[209] N. Arase, A. Takeuchi, M. Unno, S. Hirano, T. Yokosuka, H. Arase, and T. Saito. Heterotypic interaction of crtam with necl2 induces cell adhesion on activated nk cells and cd8+ t cells. *International Immunology*, 17(9):1227–1237, aug 2005. doi:10.1093/intimm/dxh299.

[210] R. Jin, J. Hao, J. Yu, P. Wang, E. R. Sauter, and B. Li. Role of FABP5 in t cell lipid metabolism and function in the tumor microenvironment. *Cancers*, 15(3):657, jan 2023. doi:10.3390/cancers15030657.

[211] K. Toriyama, M. Kuwahara, H. Kondoh, T. Mikawa, N. Takemori, A. Konishi, T. Yorozuya, T. Yamada, T. Soga, A. Shiraishi, and M. Yamashita. T cell-specific deletion of pgam1 reveals a critical role for glycolysis in t cell responses. *Communications Biology*, 3(1), jul 2020. doi:10.1038/s42003-020-01122-w.

[212] J. Liu, M. Xu, Z. Wu, Y. Yang, S. Yuan, J. Liang, and H. Zhu. Low expression of RILPL2 predicts poor prognosis and correlates with immune infiltration in endometrial carcinoma. *Frontiers in Molecular Biosciences*, 8, may 2021. doi:10.3389/fmolb.2021.670893.

[213] X. Fu, L. Tao, A. Rivera, S. Williamson, X.-T. Song, N. Ahmed, and X. Zhang. A simple and sensitive method for measuring tumor-specific t cell cytotoxicity. *PLoS ONE*, 5(7):e11867, jul 2010. doi:10.1371/journal.pone.0011867.

[214] S. Lorenzo-Herrero, C. Sordo-Bahamonde, S. Gonzalez, and A. López-Soto. CD107a degranulation assay to evaluate immune cell antitumor activity. In *Methods in Molecular Biology*, pages 119–130. Springer New York, nov 2018. doi:10.1007/978-1-4939-8885-3_7.

A Publications

Parts of this thesis have previously been published.

First-author publications

- **L. M. Mateyka***, P. M. Strobl*, S. Jarosch*, S. J. C. Scheu, D. H. Busch, and E. D'Ippolito. Gene signatures of T-cell activation can serve as predictors of functionality for SARS-CoV-2-specific T-cell receptors. Vaccines, 10(10):1617, sep 2022. doi: 10.3390/vaccines10101617.
- **L. M. Mateyka***, V. Grass*, A. Pichlmair, D. H. Busch, and E. D'Ippolito. SARS-CoV-2 CD8+ T cell killing assays using replicating viruses and transgenic antigens. STAR Protocols, 3(4):101699, dec 2022. doi:10.1016/j.xpro.2022.101699.
- K. I. Wagner*, **L. M. Mateyka***, S. Jarosch*, V. Grass, S. Weber, K. Schober, M. Hammel, T. Burrell, B. Kalali, H. Poppert, H. Beyer, S. Schambeck, S. Holdenrieder, A. Strötges-Achatz, V. Haselmann, M. Neumaier, J. Erber, A. Priller, S. Yazici, H. Roggendorf, M. Odendahl, T. Tonn, A. Dick, K. Witter, H. Mijočević, U. Protzer, P. A. Knolle, A. Pichlmair, C. S. Crowell, M. Gerhard, E. D'Ippolito, and D. H. Busch. Recruitment of highly cytotoxic CD8+ T cell receptors in mild SARS-CoV-2 infection. Cell Reports, 38(2):110214, jan 2022. doi:10.1016/j.celrep.2021.110214.

  * These authors contributed equally.

Collaborations

- S. E. Schambeck, **L. M. Mateyka**, T. Burrell, N. Graf, I. Brill, T. Stark, U. Protzer, D. H. Busch, M. Gerhard, H. Riehl, and H. Poppert. Two-year follow-up on chemosensory dysfunction and adaptive immune response after infection with SARS-CoV-2 in a cohort of 44 healthcare workers. Life, 12(10):1556, oct 2022. doi:10.3390/life12101556.
- E. Gaitzsch, V. Passerini, E. Khatamzas, C. D. Strobl, M. Muenchhoff, C. Scherer, A. Osterman, M. Heide, A. Reischer, M. Subklewe, A. Leutbecher, B. Tast, A. Ruhle, T. Weiglein, S.-S. Stecher, H. J. Stemmler, M. Dreyling, P. Girl, E. Georgi, R. Wölfel, **L. Mateyka**, E. D'Ippolito, K. Schober, D. H. Busch, J. Kager, C. D. Spinner, M. Treiber, S. Rasch, T. Lahmer, R. Iakoubov, J. Schneider, U. Protzer, C. Winter, J. Ruland, M. Quante, O. T. Keppler, M. von Bergwelt-Baildon, J. Hellmuth, and O. Weigert. COVID-19 in patients receiving CD20-depleting immunochemotherapy for B-cell lymphoma. HemaSphere, 5(7):e603, jun 2021. doi:10.1097/hs9.0000000000000603.
- D. S. Fischer, M. Ansari, K. I. Wagner, S. Jarosch, Y. Huang, C. H. Mayr, M. Strunz, N. J. Lang, E. D'Ippolito, M. Hammel, **L. Mateyka**, S. Weber, L. S. Wolff, K. Witter, I. E. Fernandez, G. Leuschner, K. Milger, M. Frankenberger, L. Nowak, K. Heinig-Menhard, I. Koch, M. G. Stoleriu, A. Hilgendorff, J. Behr, A. Pichlmair, B. Schubert, F. J. Theis,

D. H. Busch, H. B. Schiller, and K. Schober. Single-cell RNA sequencing reveals ex vivo signatures of SARS-CoV-2-reactive T cells through 'reverse phenotyping'. Nature Communications, 12(1), jul 2021. doi:10.1038/s41467-021-24730-4.

Conference Abstract

74th Mosbacher Kolloquium "Immune Engineering - from Molecules to Therapeutic Approaches", Mosbach, Germany

- **L. M. Mateyka**, K. I. Wagner, S. Jarosch, P. M. Strobl, V. Grass, A. Pichlmair, E. D'Ippolito, and D. H. Busch. "Gene expression signatures can predict SARS-CoV-2 T cell receptor functionality". Mosbacher Kolloquium, mar 2023.

Keystone Symposia on Molecular and Cellular Biology, "Viral Immunity: Basic Mechanisms and Therapeutic Applications", Keystone CO, USA

- **L. M. Mateyka**, K. I. Wagner, S. Jarosch, V. Grass, S. Weber, M. Hammel, A. Pichlmair, C. S. Crowell, M. Gerhard, E. D'Ippolito, and D. H. Busch. Recruitment of highly cytotoxic CD8+ T cell receptors in mild SARS-CoV-2 infection. Keystone Symposia, jun 2022.

International Conference on Lymphocyte Engineering, Munich, Germany

- **L. M. Mateyka**, K. I. Wagner, S. Jarosch, V. Grass, S. Weber, M. Hammel, A. Pichlmair, C. S. Crowell, M. Gerhard, E. D'Ippolito, and D. H. Busch. Identification of highly functional and cytotoxic SARS-CoV-2-specific CD8+ T cells by orthotopic TCR replacement engineering. Human Gene Therapy, 33(7-8):A19, apr 2022. doi:10.1089/hum.2022.29200.abstracts.

B Acknowledgements

The Institute for Medical Microbiology, Immunology and Hygiene at the TUM has provided me with a very collaborative and scientifically stimulating environment. I would like to take this opportunity to achnowledge the many people who have contributed to my work and supported me during my time here.

First and foremost, I would like to thank my doctor father, Prof. Dr. Dirk Busch, who gave me the opportunity to start working in his laboratory when the COVID-19 pandemic hit Germany. With his continuous guidance and scientific input, he supervised the projects I was involved in. I would also like to thank my PhD supervisors, Prof. Dr. Jürgen Ruland and Prof. Dr. Kathrin Schumann, who have monitored my progress over the years and provided valuable feedback and confirmation that I was on the right track.

Next, I would like to emphasize Dr. Elvira D'Ippolito, who has been a great mentor from the beginning when I joined the lab until the writing of my thesis. By providing the right amount of supervision at the right time, she not only supported me when needed, but also gave me the freedom to develop my own ideas and become more independent. I would also like to mention PD Dr. Kilian Schober, who initiated some successful collaborations in the first months of my time in the laboratory.

I would like to thank the whole AG Busch and especially some members who made my time in the laboratory unforgettable and enjoyable. First of all, I would like to mention Karolin Wagner, who gave me a warm welcome into the laboratory even under the difficult starting conditions, when curfew and social distancing complicated our lives. Working with you on the SARS-CoV-2 project was a real pleasure. With all those early ICCS, early breakfasts and coffee breaks, we quickly became friends, which made working on a project together so much more fun. Sebastian Jarosch joined the SARS-CoV-2 team a little later for data analysis, and his contributions were crucial for the successful completion of these projects. Even when you were busy with other projects and deadlines, you always took the time to analyze data and revise figures. I would also like to thank Simone Weber, who was part of the SARS-CoV-2 team in the early days and who joined the project with great dedication and motivation.

A special thanks goes to some graduate students who created a great lab environment and always had time for a coffee in the afternoon or a beer in the evening to talk about science and personal lives, Sabrina Wagner, Andreas aka Andrew Carr, Linda Warmuth, Jack Barton, Pascal Winterhalter, Adrian Straub, Sebastian Scheu, and Mortimer Svec. I would like to thank our technical assistants, Monika Hammel, Anna Hochholzer, Noomen Hamed, Laura Valentiner, Andrea Werner, and Füsun Gökmen, for their continuous technical support and for keeping the laboratory running. In particular, Monika Hammel's expertise in single-cell RNA sequencing and sample preparation was crucial to this work. I would also like to thank my master's and bachelor's students, Philipp Strobl, Linus Wollenweber, Paul Wätzig, Nina Dieminger and Milan Ziesmer, who joined me on parts of my project over the years and who stood out for their high motivation and dedication. They generated valuable data for the project and gave me the opportunity to develop my own mentoring skills.

I would like to thank all the members of the cell sorting facility, especially Immanuel Andrä and Corinne Angerpointer, Lynette Henkel, Dharshini Raju, and Katharina Hofmann for providing the high purity cell sorts that were essential for this work. The virus killing assay would not have

been possible without the help of our collaborators at AG Pichlmair and especially Dr. Vincent Grass, who generously shared his expertise with us. Special thanks also go to all the patients and donors who kindly donated blood samples at the Helios Clinic West Munich, German Heart Center Munich, and the University Medicine Mannheim, and to all those involved in the study design and sample collection.

While all of my colleagues and collaborators have been instrumental in advancing my scientific progress, this work would not have been possible without the strong support network of friends and family.

I would like to express my special gratitude to my boyfriend Flo for his continuous support during the experimental part but also during the writing part of my thesis. Thank you for understanding the long working hours and weekend laboratory visits. Especially during the writing of my thesis you were my rock. Thank you for your endless patience and calmness and for always believing in me.

A big thank you also goes out to my friends Moe, Guiseppe and Maike, who always provided enough distraction from work when needed. Last but not least, I would like to thank my family for their love and support over the years and for never doubting me. My parents' support has kept me grounded and given me the mental strength to continue on this journey. A special thank you also goes to my sister Julia and her boyfriend Christoph for their understanding of my work schedule and for joining me in many activities outside of the laboratory.

Thank you.